

THÈSE EN COTUTELLE PRÉSENTÉE  
POUR OBTENIR LE GRADE DE

DOCTEUR DE  
L'UNIVERSITÉ DE BORDEAUX  
ET DE L'UNIVERSITÉ DE VALLADOLID

ÉCOLE DOCTORALE DES SCIENCES CHIMIQUES

ÉCOLE DOCTORALE UVA

SPÉCIALITÉ POLYMÈRES

Par Javier PINTO SANZ

**Fabrication et Caractérisation de Polymères Micro et  
Nano Cellulaires à partir de Polymères  
Nanostructurés à base PMMA**

Sous la direction de Michel DUMON  
Et de Miguel Ángel RODRÍGUEZ PÉREZ

Soutenue le 7 mai 2014

Membres du jury:

M. VIGNOLES, Gérard L. Prof. Dr. Université de Bordeaux  
M. SOLÓRZANO, Eusebio Dr. Universidad de Valladolid  
M. Velasco, José Ignacio Prof. Dr. Universidad Politécnica de Cataluña  
M. GRANDE, Daniel Dr. CNRS, Université Paris Est  
M. COSTEUX, Stéphane Dr. The Dow Chemical Company

Examineur  
Examineur  
Rapporteur  
Rapporteur  
Examineur



TESIS DOCTORAL EN COTUTELA PRESENTADA  
PARA OPTAR AL GRADO DE

DOCTOR DE  
LA UNIVERSIDAD DE VALLADOLID  
Y DE LA UNIVERSIDAD DE BORDEAUX

ÉCOLE DOCTORALE DES SCIENCES CHIMIQUES

ESCUELA DOCTORAL UVA

DOCTORADO EN FÍSICA

Por Javier PINTO SANZ

**Fabricación y Caracterización de Materiales  
Poliméricos Submicrocelulares a partir de Polímeros  
Nanoestructurados**

Dirigida por:  
Prof. Dr. Miguel Ángel RODRÍGUEZ PÉREZ  
Prof. Dr. Michel DUMON





**Titre :** Fabrication et Caractérisation de Polymères Micro et Nano Cellulaires à partir de Polymères Nanostructurés à base PMMA.

**Résumé :**

Cette thèse porte sur la production et l'étude des mousses de polymères micro ou nano poreux et de nano mousses à partir de matériaux à base de PMMA (poly(méthyl méthacrylate)) par dissolution et moussage avec CO<sub>2</sub>.

Plusieurs techniques expérimentales ont été améliorées ou adaptées afin de fournir de précieuses informations sur les des systèmes étudiés.

La nanostructuration des mélanges solides denses à base de PMMA est induite par l'addition d'un copolymère à blocs (MAM, poly(méthyl méthacrylate)-co-poly(butylacrylate)-copolymère(méthyl méthacrylate)). Les structures cellulaires des mousses produites à partir de ces mélanges ont été caractérisés et expliquées ; on a démontré que la nanostructuration agit comme un modèle de la structure cellulaire, permettant l'obtention d'un large éventail de structures cellulaires et en particulier des nanocellular mousses.

De plus il est démontré que les paramètres du procédé, tels que la pression et la température, permettent la différenciation entre deux voies de moussage ; ceux-ci ont une influence significative sur les caractéristiques finales des mousses de PMMA seul, mais pas sur les mélanges PMMA/MAM. Les mousses dans ces mélanges présentent un mécanisme de nucléation hétérogène contrôlée par la nanostructuration, ce qui permet d'éviter l'influence des paramètres de traitement dans la nucléation de la cellule. En outre, certains mélanges de PMMA/MAM présentent également une remarquable stabilité de leur morphologie au cours de la croissance cellulaire, ce qui évite l'effondrement cellulaire et la coalescence.

Enfin, on a étudié l'influence sur les propriétés de las mousses de la transition entre les structures micro-cellulaires et les structures nano-cellulaires ; une nette diminution de la conductivité thermique en raison de l'effet de Knudsen, et une augmentation notable de la température de transition vitreuse en raison de l'isolement des chaînes de polymères dans les parois de la cellule, sans noter d'influence sur le module de Young.

**Mots clés :** mousse polymère nanoporous, copolymère à blocs, nucleation hétérogène, moussage pour dissolution de gaz, polymères nanostructurés.

**Título:** Fabricación y Caracterización de Materiales Poliméricos Submicrocelulares a partir de Polímeros Nanoestructurados.

**Resumen:**

Esta tesis se centra en la producción y estudio de espumas poliméricas nanocelulares producidas a partir de materiales basados en PMMA (poli(metil metacrilato)), mediante la técnica de espumado por disolución de gas usando CO<sub>2</sub>.

Debido a la novedad de este campo de investigación ha sido necesario mejorar o adaptar varias técnicas experimentales para obtener la información necesaria de los sistemas bajo estudio.

Se han caracterizado y relacionado la nanoestructuración de mezclas basadas en PMMA, inducida por la adición de un copolímero de bloque (MAM, poli(metil metacrilato)-co-poli(butil acrilato)-co-poli(metil metacrilato)), y la estructura celular de las espumas producidas a partir de esas mezclas; obteniéndose que la nanoestructuración actúa como patrón para la estructura celular, permitiendo obtener una amplia variedad de estructuras celulares y en particular de estructuras nanocelulares.

Se ha demostrado que los parámetros de procesado, como la presión y temperatura, permiten diferenciar entre dos rutas de espumado y presentan una influencia significativa en las características finales de las espumas de PMMA puro, pero no en las mezclas de PMMA/MAM. Estas mezclas presentan un mecanismo de nucleación heterogénea controlado por la nanoestructuración, que evita que los parámetros de procesado influyan en el proceso de nucleación de las celdas. Además, algunas mezclas de PMMA/MAM también presentan una alta estabilidad durante el crecimiento de las celdas, evitando el colapso de la estructura celular y la coalescencia.

Finalmente, se ha estudiado la influencia en las propiedades de las espumas de la transición entre el rango microcelular y el rango nanocelular; obteniéndose que hay una clara influencia sobre la conductividad térmica, que decrece en las espumas nanocelulares debido al efecto Knudsen, y sobre la temperatura de transición vítrea, que se incrementa debido al confinamiento de las cadenas poliméricas en las paredes de las celdas, pero no sobre el módulo de Young.

**Palabras clave:** espumas poliméricas nanocelulares, copolímero de bloque, nucleación heterogénea, espumado por disolución de gas, polímeros nanoestructurados

**Title:** Fabrication and Characterization of Nanocellular Polymeric Materials from Nanostructured Polymers.

**Abstract:**

This dissertation focuses on the production and study of nanocellular foams from PMMA-based (poly(methyl methacrylate)) materials by CO<sub>2</sub> gas dissolution foaming.

Due to the novelty of this research field several experimental techniques have been improved or adapted in order to provide valuable information from the systems under study.

Nanostructuration of PMMA-based blends induced by the addition of a block copolymer (MAM, poly(methyl methacrylate)-b-poly(butyl acrylate)-b-poly(methyl methacrylate)) and the cellular structure of the foams produced from these blends have been characterized and related; obtaining that the nanostructuration acts as a pattern for the cellular structure, allowing obtaining a wide range of cellular structures and in particular nanocellular foams.

It is demonstrated that processing parameters, such as pressure and temperature, allow differentiating between two foaming routes; and present a significant influence on the foaming process and final characteristics of neat PMMA foams, but not on PMMA/MAM blends. PMMA/MAM blends present a heterogeneous nucleation mechanism controlled by the nanostructuration that avoid the influence of the processing parameters in the cell nucleation. In addition, some PMMA/MAM blends also present a high stability during the cell growth, avoiding the cellular collapse and coalescence.

Finally, it has been studied the influence on the foams properties of the transition between the microcellular and the nanocellular ranges; obtaining that there is a clear influence on the thermal conductivity, which decreases in nanocellular foams due to the Knudsen effect, and the glass transition temperature, which increases in nanocellular foams due to the confinement of the polymer chains in the cell walls, but not on the Young's modulus.

**Keywords:** polymeric nanofoam, block copolymer, heterogeneous nucleation, gas dissolution foaming, nanostructured polymers.



## **Unités de recherche / Centros de investigación**

LCPO Laboratoire Chimie des Polymères Organiques, UMR CNRS 5629.

Université de Bordeaux

ENSCBP, avenue Pey Berland, 33 607 Pessac, France

[www.lcpo.fr](http://www.lcpo.fr)

CellMat Laboratory, Departamento de Física de la Materia Condensada,  
Cristalografía y Mineralogía, Facultad de Ciencias, Universidad de  
Valladolid

Paseo Belén, nº 7, 47 001 Valladolid, España

[www.cellmat.es](http://www.cellmat.es)



*“Pero daré a conocer lo poco que he aprendido para que alguien mejor que yo pueda atisbar la verdad y, en su obra, pueda probar y criticar mi error. Así, me regocijaré a pesar de todo de haber sido un medio a través del cual salga a la luz la verdad”.*

*“But I shall let the little I have learnt go forth into the day in order that someone better than I may guess the truth, and in his work may prove and rebuke my error. At this I shall rejoice that I was yet a means whereby this truth has come to light”.*

ALBRECHT DÜRER (ALBERTO DURERO)





## Contents

<b>Contents .....</b>	<b>i</b>
<b>Résumé en français .....</b>	<b>F-1</b>
<b>F.1 Introduction .....</b>	<b>F-3</b>
<b>F.2 Objectifs .....</b>	<b>F-6</b>
<b>F.3 Structure de cette thèse .....</b>	<b>F-7</b>
<b>F.4 Avantages de mélanges structurés amorphes pour nano mousses .....</b>	<b>F-10</b>
<b>F.5 Résultats principaux .....</b>	<b>F-10</b>
<b>F.6 Références .....</b>	<b>F-11</b>
<b>Resumen en español .....</b>	<b>S-1</b>
<b>S.1 Introducción .....</b>	<b>S-3</b>
<b>S.2 Marco de la tesis .....</b>	<b>S-7</b>
<b>S.3 Objetivos .....</b>	<b>S-8</b>
<b>S.4 Estructura de esta tesis .....</b>	<b>S-11</b>
<b>S.5 Principales resultados .....</b>	<b>S-19</b>
<b>S.6 Referencias .....</b>	<b>S-20</b>
<b>0. Introduction .....</b>	<b>1</b>
<b>0.1 Introduction .....</b>	<b>3</b>
<b>0.2 Framework of this thesis .....</b>	<b>5</b>
<b>0.3 Summary of the state of the art .....</b>	<b>7</b>
0.3.1 Nanocellular polymer foams .....	7
0.3.2 Gas dissolution process .....	9
0.3.3 Nanocellular polymer foams produced by CO <sub>2</sub> gas dissolution foaming ....	11
0.3.4 Properties of nanocellular polymer foams .....	15
<b>0.4 Objectives .....</b>	<b>16</b>

0.5 Structure of this thesis .....	18
0.6 Advantages of amorphous structured blends for nanofoams .....	26
0.7 References .....	28
 <b>Chapter I. Experimental techniques .....</b>	<b>37</b>
<b>I.1 Non-standard characterization techniques .....</b>	<b>39</b>
<b>I.1.1 Nanostructuration characterization .....</b>	<b>39</b>
<i>I.1.1.1 SEM .....</i>	<i>40</i>
<i>I.1.1.2 AFM .....</i>	<i>40</i>
<i>I.1.1.3 TEM .....</i>	<i>43</i>
<b>I.1.2 Cellular structure characterization .....</b>	<b>46</b>
<i>“Characterization of Cellular Structure Based on User-Interactive Image Analysis Procedures” .....</i>	<i>47</i>
<b>I.1.3 Density homogeneity of foamed samples .....</b>	<b>68</b>
<i>I.1.3.1 X-ray imaging fundamentals .....</i>	<i>69</i>
<i>I.1.3.2 Matter-beam interaction .....</i>	<i>70</i>
<i>I.1.3.3 Microfocus X-ray system at CellMat .....</i>	<i>71</i>
<i>I.1.3.4 Determination of density profiles of polymeric foams by X-ray radiography .....</i>	<i>75</i>
<b>I.1.4 Thermal conductivity of foams .....</b>	<b>76</b>
<i>I.1.4.1 An introduction to the TPS method .....</i>	<i>76</i>
<i>I.1.4.2 Experimental procedure .....</i>	<i>77</i>
<b>I. 2 References .....</b>	<b>80</b>
 <b>Chapter II. PMMA/MAM blends and foams production and consequent nanostructuration and cellular structure .....</b>	<b>83</b>
<b>II.1 Materials .....</b>	<b>85</b>
<b>II.1.1 Poly(methyl methacrylate) (PMMA) .....</b>	<b>85</b>
<b>II.1.2 Poly(methyl methacrylate)-co-poly(butyl acrylate)-co-poly(methyl methacrylate (MAM) .....</b>	<b>86</b>
<b>II.1.3 Literature summary on neat block copolymers (BCP) .....</b>	<b>87</b>
<b>II.1.4 Literature summary on blends of block copolymers (BCP + epoxy systems) .....</b>	<b>87</b>

II.2 Blends production route .....	88
II.3 Morphology analysis of PMMA/MAM dense solid blends by AFM .....	89
II.4 Morphology analysis of PMMA/MAM dense solid blends by TEM .....	91
II.5 Comparison between AFM and TEM results .....	96
II.5.1 Low MAM content .....	96
II.5.2 Medium MAM content .....	97
II.5.3 High MAM content .....	97
II.6 Foams production route .....	99
II.7 Nanostructuration evolution due to CO <sub>2</sub> saturation .....	101
II.7.1 Effect of CO <sub>2</sub> annealing on final morphology .....	104
II.8 Cellular structures of PMMA/MAM foams: general description and evolutions .....	106
II.8.1 Presence of solid skin-foamed core structure .....	106
II.8.2 Homogeneity along directions .....	107
II.8.3 Anisotropy of cells .....	110
II.8.4 Cellular structure of different MAM content foams, evolution of cells morphology with the saturation temperature .....	112
II.8.5 Influence of saturation CO <sub>2</sub> pressure .....	117
II.9 References .....	121
 Chapter III. Relationship between PMMA/MAM blends nanostructures and cellular structures. Foaming mechanisms .....	 123
<i>“Nanocellular CO<sub>2</sub> foaming of PMMA assisted by block copolymer nanostructuration”</i> .....	130
<i>“Block Copolymers Self-Assembly Allows Obtaining Tunable Micro or Nanoporous Membranes or Depth Filters Based on PMMA; Fabrication Method and Nanostructures”</i> .....	138
<i>“Solid Skin Characterization of PMMA/MAM Foams Fabricated by Gas Dissolution Foaming over a Range of Pressures”</i> .....	146

<b>Chapter IV. Influence of temperature on the foaming processes, mechanisms, and foams structures .....</b>	<b>151</b>
<b>IV.1 Influence of the CO<sub>2</sub> saturation temperature on foaming process, morphology and density of PMMA/MAM foams .....</b>	<b>154</b>
<i>“Temperature Influence and CO<sub>2</sub> Transport in Foaming Processes of Poly(methyl methacrylate)-Block Copolymer Nanocellular and Microcellular Foams” .....</i>	<i>156</i>
<b>IV.2 Influence of the foaming temperature and post-foaming on the morphology and density of PMMA/MAM foams .....</b>	<b>177</b>
<b>IV.2.1 Post-foaming vs. two-step foaming .....</b>	<b>178</b>
<b>IV.2.2 Comparison of PMMA and PMMA/MAM post-foaming .....</b>	<b>179</b>
<b>IV.3 Conclusions .....</b>	<b>182</b>
 <b>Chapter V. Transition between microcellular and nanocellular foams; consequences on mechanical and thermal properties .....</b>	 <b>183</b>
<i>“Low Density Nanocellular Foams Produced by High-Pressure Carbon Dioxide” .....</i>	<i>184</i>
<b>V.1 Young’s Modulus .....</b>	<b>194</b>
<b>V.2 Glass Transition Temperature .....</b>	<b>197</b>
<b>V.3 Thermal Conductivity .....</b>	<b>202</b>
<i>“Thermal Conductivity Transition between Microcellular and Nanocellular Polymeric Foams: Experimental Validation of the Knudsen Effect” .....</i>	<i>206</i>
<b>V.4 References .....</b>	<b>212</b>
 <b>Conclusions and Perspectives .....</b>	 <b>213</b>
<b>Improved experimental techniques or technological progress for characterization .....</b>	<b>215</b>
<b>Production of nanocellular foams .....</b>	<b>216</b>
<b>Understanding of the foaming mechanisms .....</b>	<b>217</b>
<b>Properties of PMMA/MAM foams .....</b>	<b>219</b>
<b>Future Perspectives .....</b>	<b>220</b>

## *Résumé en français*



## Résumé en français

### F.1 Introduction

L'Union Européenne, dans la définition d'objectifs 2014-2020 (*Horizon 2020*) [3], définit l'une de ses priorités de la recherche en science des matériaux : “*Manufacturing and control of nanoporous materials*”. La phrase suivante précise l'objectif, “*a constantly growing interest in nanostructured porous materials, thanks to the many applications that can benefit from controlled porosity at the nanoscale*”. Ainsi pour accroître les applications des matériaux poreux [4], outre le gain de masse, les nano et micro mousses de polymère ont des potentielles applications nombreuses dans la thermique [12], l'absorption de chocs, la filtration [17], la catalyse [18], l'optique, l'acoustique [13].

Notre travail contribue à ces objectifs et est intitulé “*Fabrication et Caractérisation de Polymères Micro et Nano Cellulaires à partir de Polymères Nanostructurés à base PMMA*”.

Cet travail fut initié au LCPO lors d'un projet ANR 2008 -2012, *Listrac* (Light Structures and Composites), qui a produit et étudié de point de vue mécanique, une gamme de matériaux cellulaires de taille de porosités variable pour l'absorption de chocs et d'impacts (sécurité passive). Une des familles de polymères étudiés est à base de mélanges d'un homopolymère PMMA avec un copolymère à blocs acrylique. Le procédé d'élaboration est le moussage physique par CO<sub>2</sub>.

Le travail de cette thèse prolonge et approfondit l'étude de ce système. Il généralise le concept de nano et micro mousses en milieu CO<sub>2</sub> à partir de polymères nanostructurés; notamment l'effet du taux de copolymère, les relations entre les nano structures initiales et les porosités, les mécanismes de moussage, les propriétés mécaniques et thermiques.

Le manuscrit est composé d'une introduction –chapitre 0- décrivant le cadre du travail, l'état de l'art, les objectifs, un synopsis, les articulations des chapitres, les principales avancées technologiques et scientifiques, puis de 5 chapitres -I à V- correspondant à des publications acceptées, et une conclusion. Cette collaboration entre deux laboratoires, CellMat Laboratory (Condensed Matter Physics Department, Universidad de Valladolid, España) et le Laboratoire de Chimie des Polymères Organiques (LCPO, Université de Bordeaux, France) fait l'objet d'une convention de cotutelle de thèse avec double diplôme. La thèse est écrite entièrement en anglais. Des liens entre les publications sont toujours faits et chaque chapitre a sa propre bibliographie.

Le choix d'un homopolymère se porte sur un polymère amorphe, non formulé, le poly(méthylméthacrylate) (PMMA) et un copolymère tri-blocs contenant deux blocs PMMA et un bloc polybutylacrylate (le poly(méthylméthacrylate)-co-poly(butylacrylate)-co-poly(méthyl méthacrylate, MAM), celui-ci donne une nano structuration quel que soit le taux de copolymère dans le PMMA

homopolymère, avec des morphologies diverses à l'échelle nanométrique : micelles, core-shells, lamelles, worms. Ce copolymère tri blocs (MAM) est choisi en ayant un bloc CO<sub>2</sub>-phile élastomère, il a déjà été utilisé à un taux de 10% (massique) dans le P MMA pour générer des mousses de taille « sous micronique » et dans certains cas nanométriques [52].

La fabrication et l'étude de polymères nanocellulaires à l'état de films est connue, soit à partir d'empreinte de nanostructures (pattern-transfer [16, 79-81]) ou par dégradation ou dissolution sélective de blocs [16, 80-87]. D'autre part, la bibliographie montre que le moussage par un agent chimique traditionnel ne peut pas générer des nano mousses.

Le moussage par dissolution de gaz sous haute pression (CO<sub>2</sub>, N<sub>2</sub>) est encore assez peu connu [81, 88-90] mais apparaît comme une technique très efficace, peu onéreuse et « verte », notamment le CO<sub>2</sub> (ayant une excellente capacité de diffusion à l'état supercritique (31° C and 7.3 MPa)).

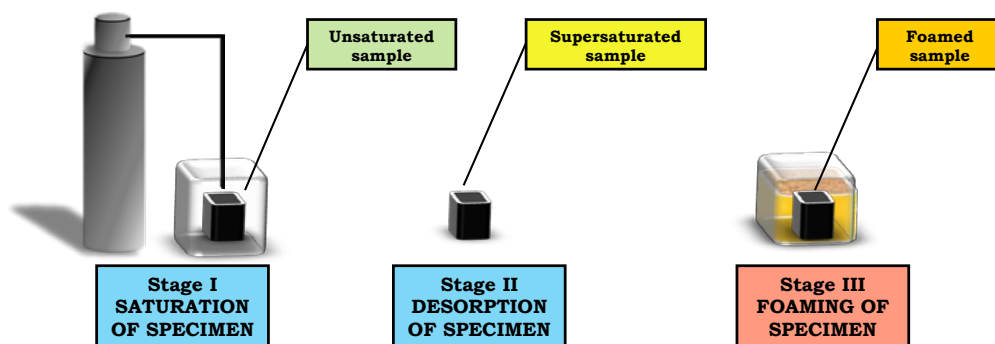


Figure F.1 : schéma des étapes de moussage par dissolution de gaz

Le moussage se déroule selon les étapes suivantes (Figure F.1) :

- étape I. Saturation du polymère.
- étape II. Désorption du gaz, détente de pression.
- étape III. Moussage à une température supérieure ou proche de la  $T_g$  du polymère plastifié ( $T_{g, effective}$ ).

Si la détente en pression déclenche la nucléation de bulles, le procédé est appelé *one-step* or *batch foaming* [66, 89] (cas d'une température proche de  $T_g$  ou au-dessus).

Si le milieu est vitreux, l'expansion se fait lors d'un chauffage au-dessus de  $T_{g, eff}$  qui amorce le moussage; le procédé est appelé *two-step* or *solid state foaming* [72].

Les nano mousses demandent une densité de nucléation importante ( $N_o$ , nombre de noyaux par cm<sup>3</sup> de polymère dense), classiquement  $10^{14}$ - $10^{15}$  noyaux/cm<sup>3</sup>. Les paramètres du procédé ( $T^{sat}$ , la Pression de saturation et la vitesse de détente [89, 96, 102]) contrôlent essentiellement la nucléation pour des matériaux homogènes comme le montre la figure ci-dessous (Figure F.2).



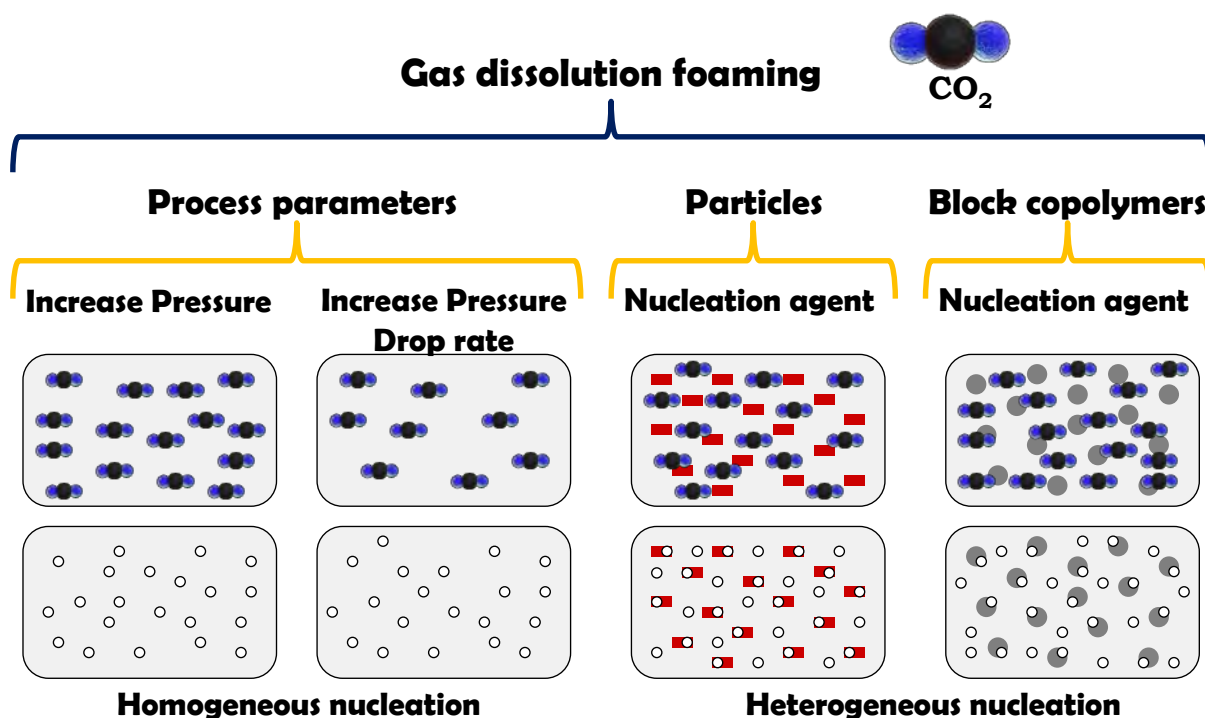


Figure F.2 : Possibilités de nucléation homogène et hétérogène

Pour des matériaux hétérogènes, dans un gaz tel que  $\text{CO}_2$ , l'addition de *particules* (talc, oxyde de titane, kaolin, nanosilice, MMT) accroît la nucléation, ceci selon la taille des particules [108]. Par exemple, Siripurapu et al. [109] propose des films nanocellulaires de PMMA avec des silices de diamètre moyen 10-12 nm) et du  $\text{CO}_2$  à 34,5 MPa.

D'autre part, des *copolymères à blocs* (de type A-B ou A-B-A) [113] permettraient la formation de nanostructures qui sont des noyaux potentiels et des sites de nucléation pour les cellules de vide. De plus, si les blocs sont  $\text{CO}_2$ -philes, les nanostructures sont des réservoirs de  $\text{CO}_2$  pour la croissance des cellules [108]. Cependant les cellules ne sont pas toutes nanocellulaires, comme le cas du polystyrène-b-poly(diméthylsiloxane), ou du PMMA-b-PFOMA (poly(1,1-dihydroperfluorooctyl méthacrylate) [109].

Yokoyama et al. [115] montre des densités de cellules d'environ  $10^{16}$  cellules/cm<sup>3</sup>) sur des copolymères polystyrène-b-poly(perfluorooctyl éthylméthacrylate) (PS-b-PFMA). Yokoyama and Sugiyama [118] ont utilisé des copolymères polystyrène-b-poly(perfluorooctyl propyloxy styrène) (PS-b-PFS).

## F.2 Objectifs

Notre démarche est décrite par le schéma suivant (Figure F.3) :

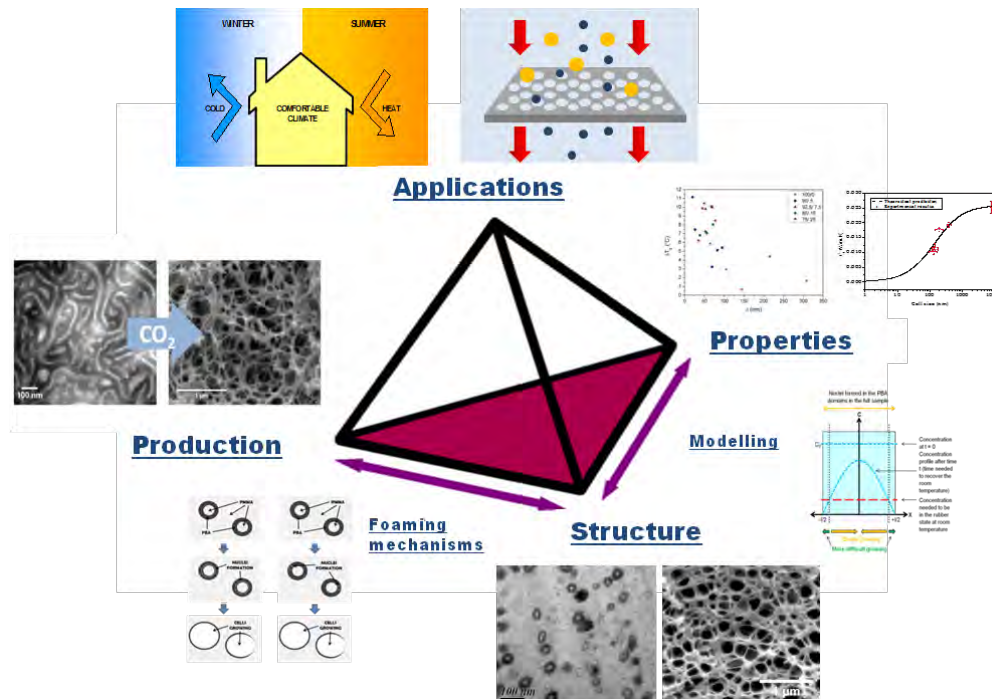


Figure F.3 : Tétraèdre de notre recherche et inter relations

Ainsi nous proposons de :

- 1) Développer une gamme de mousses polymères nanométriques sur toutes les concentrations de MAM à partir des mélanges PMMA/MAM et d'en caractériser les nano structures initiales et les cellules finales.
- 2) Avoir une compréhension des mécanismes de moussage de polymères dans  $\text{CO}_2$ , en particulier en milieu hétérogène c'est-à-dire en présence d'un copolymère à blocs.
- 3) Etudier la transition entre mousses microcellulaire et nanocellulaire, en particulier sur les propriétés mécaniques et thermiques.

Du point de vue technologique, nous recherchons des matériaux d'accès facile, capables de se nanostructurer dans toutes les conditions de procédés (extrusion / injection / gonflement dans une enceinte  $\text{CO}_2$ ); des mousses de densité réduite (~50% de la densité du matériau précurseur dense) et des structures nano cellulaires variées, ceci avec des matériaux de grande diffusion et de production industrielle.

Du *point de vue scientifique*, nous voulons répondre aux questions suivantes :

- la nucléation est-elle homogène ou hétérogène (ou une combinaison des deux) ?
- peut-on découpler les mécanismes ?
- la nanostructure du solide dense est-elle répliquable dans les mousses par CO<sub>2</sub> ?
- quel est le rôle du copolymère et d'un bloc souple CO<sub>2</sub>-phile dans la nucléation et la croissance ?
- quelle est l'influence des paramètres du procédé (T, P, dP/dt) en présence de copolymère ?

### **F.3 Structure de cette thèse**

Les objectifs décrits dans la section précédente sont abordés à travers cinq chapitres, comme indiqué dans le schéma suivant (Figure F.4). Outre les publications incluses dans chaque chapitre peuvent être trouvés dans le Table F-1.

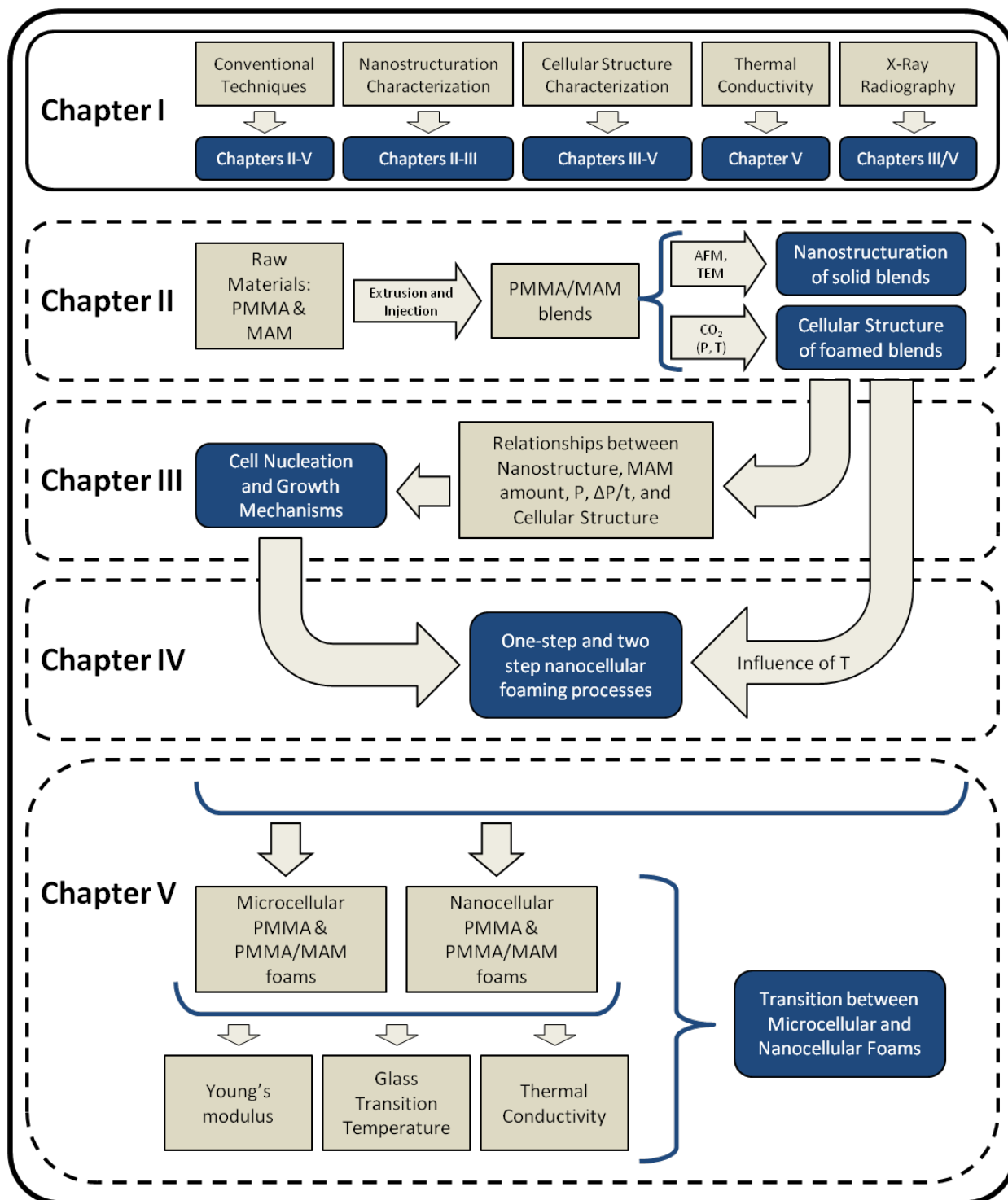


Figure F.4: Schéma de la structure de la thèse et des chapitres I à V

**Table F-1: Publications incluses dans les chapitres où le doctorant est l'auteur principal**

Publications acceptées dans des revues internationales	Chapitre
J. A. Reglero, M. Dumon, J. Pinto, M. A. Rodriguez-Perez <b>Low Density Nanocellular Foams Produced by High-Pressure Carbon Dioxide</b> <i>Macromolecular Materials and Engineering</i> 296, 752-759 (2011)	V
J. Pinto, S. Pardo-Alonso, E. Solórzano, M. A. Rodriguez-Perez, M. Dumon, J. A. de Saja <b>Solid Skin Characterization of PMMA/MAM Foams Fabricated by Gas Dissolution Foaming over a Range of Pressures</b> <i>Defect and Diffusion Forum vols. 326-328</i> , 434-439 (2012)	III
J. Pinto, E. Solórzano, M. A. Rodriguez-Perez, J. A. de Saja <b>Characterization of Cellular Structure Based on User-Interactive Image Analysis Procedures</b> <i>Journal of Cellular Plastics</i> 49, 6, 554-574 (2013)	I
J. Pinto, M. Dumon, M. Pedros, J. Reglero, M. A. Rodriguez-Perez <b>Nanocellular CO<sub>2</sub> foaming of PMMA assisted by block copolymer nanostructuration</b> <i>Chemical Engineering Journal</i> (2014) DOI: 10.1016/j.cej.2014.01.021	III
J. Pinto, M. Dumon, M. A. Rodriguez-Perez, R. García, C. Dietz <b>Block Copolymers Self-Assembly Allows Obtaining Tunable Micro or Nanoporous Membranes or Depth Filters Based on PMMA; Fabrication Method and Nanostructures</b> <i>The Journal of Physical Chemistry C</i> 118, 9, 4656-4663 (2014)	III
J. Pinto, J. Reglero-Ruiz, M. Dumon, M. A. Rodriguez-Perez <b>Temperature Influence and CO<sub>2</sub> Transport in Foaming Processes of Poly(methyl methacrylate)-Block Copolymer Nanocellular and Microcellular Foams</b> <i>Journal of Supercritical Fluids</i> (soumis)	IV

### F.4 Avantages des mélanges structurés amorphes pour nano mousses

Nous avons étudié et montré la nano structuration du MAM dans le PMMA quel que soit le taux de MAM et quel que soit le procédé de mélanges (extrusion / injection), on peut ainsi envisager une échelle semi industrielle.

Des mousses ouvertes ou fermées selon le taux de MAM, à l'état massique (bulk) sur des échantillons épais, sont obtenues. Les densités sont de l'ordre de 0.4 à 0.6 g/cm<sup>3</sup>, sur une gamme large de pressions de saturation (10 à 30 MPa).

La nucléation est complètement hétérogène, contrôlée par le bloc souple PBA. L'efficacité de nucléation est proche de 1 (rapport du nombre de noyaux des cellules des mousses sur le nombre d'objets dispersés du matériau dense).

La croissance est contrôlée par la plastification de la phase PMMA, on peut éviter la coalescence par la sélection des paramètres de procédé de moussage.

Une transition entre mousses micro et nano cellulaires est mise en évidence, en particulier sur la conductivité thermique.

### F.5 Résultats principaux

Des mélanges PMMA/MAM nano structurés se révèlent d'excellents matériaux modèles et robustes pour la production de polymères nano cellulaires.

Les morphologies ou la structuration ou l'autoassemblage à l'état dense dépend du taux massique de MAM et montrent des objets micellaires / core shells, à lamellaires / worm like ou quasi co continus.

La dissolution de gaz dans ces mélanges conduit toujours à des nano ou micro mousses. Les quantités de CO<sub>2</sub> dans le MAM, le PBA et le PMMA ont été évaluées.

Les polymères seuls ne montrent des nano mousses qu'avec un choix étroit de conditions de moussage (i.e. à haute pression et proche ou en dessous de la température ambiante); alors que les mélanges PMMA/MAM sont robustes et des nano mousses sont possibles sur la gamme complète de pressions (de 10 à 30 MPa) et des températures jusqu'à 50° C.

Les cellules de vides (les pores) peuvent être fermées ou ouvertes ou allongées ou co continues. Le recuit sous CO<sub>2</sub> permet l'homogénéisation de ces nano structures cellulaires.

La nucléation uniquement hétérogène est due à la dispersion d'objets et s'explique par la dispersion du bloc PolyButylAcrylate (PBA), sa plus grande CO<sub>2</sub>-philie que le PMMA ainsi que son état

caoutchoutique tout au long du moussage. Aussi les paramètres de procédé (i.e. pression de saturation et température, vitesse de détente) sont peu opérants, ce qui est un avantage technologique important.

Les domaines de PBA constituent donc les noyaux pour la nucléation des cellules, chaque nano objet devient un pore; et la coque (le “shell”) apparaît plus spécifiquement gonflée par le CO<sub>2</sub> et de diamètre interne comparable à celui de la taille des noyaux nécessaires à la nucléation.

Néanmoins si la quantité de MAM (donc de PBA) augmente l'absorption de CO<sub>2</sub> dans le mélange, elle entraîne aussi la diffusion plus rapide du CO<sub>2</sub> hors de la matrice, surtout dans les structures co-continues.

La présence de copolymère permet de découpler la nucléation et la croissance des cellules. En effet, ici, la croissance est gouvernée par la plastification de la phase PMMA et s'arrête à la vitrification de cette phase (dans matrice ou dans les blocs).

La mesure de certaines propriétés thermomécaniques montre des effets de la transition micro – nano cellulaires. Ainsi la T<sub>g</sub> est augmentée de 8 à 12 °C, ce qui est attribué à l'effet des très faibles épaisseurs des parois des cellules qui réduit la mobilité des chaînes. Le module est augmenté ; cet effet n'est pas relié explicitement à un effet de taille mais plus à une meilleure homogénéité macroscopique des mousses et à un effet de « renforcement structural ».

La réduction de la conductivité thermique par l'effet Knudsen est montrée expérimentalement pour une des premières fois dans une mousse polymère lorsque l'on transite d'une micro à une nano mousse.

## F.6 Références

Les références citées dans ce résumé peuvent être trouvées dans la section 0.7.





## *Resumen en español*



## Resumen en español

### S.1 Introducción

El conocimiento humano y el desarrollo tecnológico no han crecido de manera constante desde el comienzo de la civilización. Al contrario, muchas áreas científicas y técnicas evolucionan de manera exponencial [1, 2]. De hecho, se estima que más del 90% del conocimiento científico ha sido desarrollado desde el final de la II Guerra Mundial en 1945. Esta afirmación es válida prácticamente para cada campo científico, y en lo que respecta a la Ciencia de Materiales presenta dos lecturas complementarias.

Por una parte, los avances en este campo permiten desarrollar nuevos materiales con propiedades únicas, o bien mejorar las propiedades o rutas de producción de materiales de uso común, ampliando de esa forma su rango de aplicación o inclusive dando lugar a aplicaciones completamente nuevas para dichos materiales. Por otra parte los avances en otras ramas de la ciencia y el desarrollo de nuevas tecnologías frecuentemente requieren de nuevos o mejorados materiales para poder llevarse a cabo, y especialmente para poder llevar a cabo la transición desde su producción en laboratorio hasta ser capaces de suponer un impacto significativo sobre la sociedad. Debido a esta dualidad la Ciencia de Materiales es una de las principales áreas de interés tanto de organismos públicos de investigación como de centros de investigación privados.

De hecho, la Unión Europea (UE) estableció en diciembre de 2013 los objetivos de investigación del programa “Horizonte 2020” (Horizonte 2020, el programa de Investigación e Innovación de la UE para el periodo 2014-2020) [3], entre los que se encuentran múltiples objetivos centrados en la Ciencia de Materiales. En particular, dentro de esos objetivos una de las prioridades de la UE es la “*Producción y control de materiales nanoporosos*”. La UE refleja así este tema “*creciente interés en materiales porosos nanoestructurados, debido a las múltiples aplicaciones que pueden beneficiarse de una porosidad controlada en la nanoescala*”.

La presente tesis titulada “***Fabricación y Caracterización de Materiales Poliméricos Submicrocelulares a partir de Polímeros Nanoestructurados***” se encuadra por tanto dentro de este campo de investigación prioritario, en la actualidad y en el futuro, para la UE.

De manera general los materiales espumados, o espumas, son un tipo de materiales porosos (es decir, con una fase sólida y una fase gaseosa). La palabra espuma es habitualmente utilizada para clasificar materiales de baja densidad relativa (independientemente de su tamaño de poro) producidos mediante procesos o técnicas de espumado, que implican la introducción y expansión de la fase gaseosa en dicho sólido. La producción de espumas tiene como finalidad mejorar las propiedades de materiales conocidos, o bien incrementar el rango de sus potenciales aplicaciones [4]. Además de ofrecer una reducción de la

densidad del material de partida (obteniendo así piezas más ligeras para unas mismas dimensiones/aplicación), los materiales porosos y espumas pueden presentar mejores propiedades que los materiales sólidos en diferentes áreas/aplicaciones, como por ejemplo: menor conductividad térmica, mejor absorción de impactos, absorción acústica, etc.

Sin embargo los materiales porosos no pueden considerarse una invención de la humanidad, la naturaleza ha utilizado ampliamente esta aproximación durante la evolución de la vida sobre la Tierra, siendo posible encontrar materiales en estructuras vivas (vegetales o animales) con estructuras porosas, como por ejemplo la madera, corcho, las esponjas marinas, o los huesos de diferentes especies de vertebrados [5]. Pero reproducir estas estructuras vivas por medios artificiales dista mucho de ser simple. Las estructuras de organismos vivos se desarrollan con la estrategia denominada “*bottom-up*” (“de abajo a arriba”), con las células del organismo organizándose para formar la estructura, y respondiendo a las demandas externas a las que esa estructura es sometida. Por ejemplo, la estructura de los huesos humanos (Figura 0.1, izquierda) se organiza para proveer el soporte necesario al cuerpo humano, y puede reforzarse si esas demandas se incrementan (como por ejemplo con el ejercicio físico).

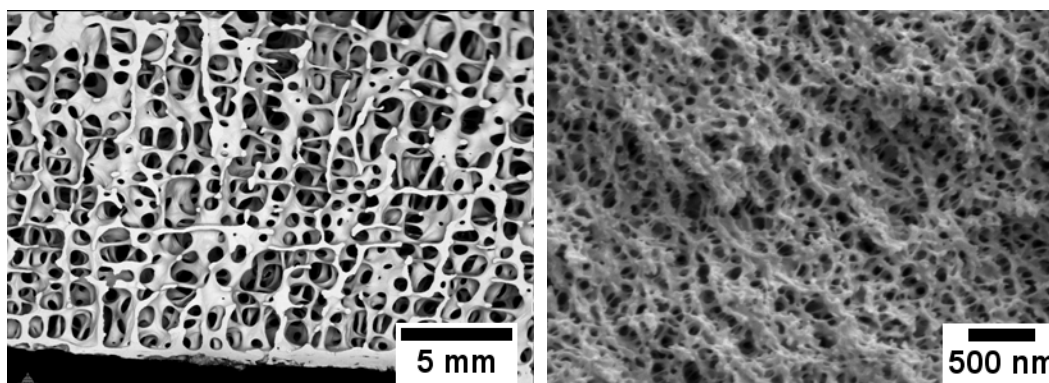


**Figura 0.1: Estructura porosa de un hueso humano (izquierda) y estructura porosa de una espuma polimérica nanocelular (derecha)**

Actualmente es posible fabricar materiales celulares a partir de múltiples materiales de partida, como líquidos, polímeros, metales, cerámicas, etc. [6-10]. Estos materiales pueden presentar propiedades mecánicas y densidades relativas bajas que les permiten encontrar aplicación en empaquetamiento, industria aeronáutica, industria del automóvil, industria naval, turbinas aerogeneradoras, etc. [11]. Otras aplicaciones de importancia de estos materiales se encuentran en el aislamiento térmico [12], aislamiento acústico [13], así como en su uso como *scaffolds* (materiales que sirven como “andamio” para el crecimiento de tejidos vivos) [14-16], filtros [17] y en procesos de catálisis debido a su estructura y su elevada área específica superficial [18].

La producción de espumas ha experimentado una progresión significativa con el desarrollo de la Nanotecnología. Este concepto fue primeramente introducido por el premio Nobel Richard P. Feynman

en 1959 en su conferencia “*There’s Plenty of Room at the Bottom*”. Tal y como Feynman predijo (y otros investigadores como Norio Taniguchi, quien propuso el término “*nano-tecnología*”) gracias a la manipulación de la materia a escala atómica, molecular, o supramolecular comenzó una nueva era en la Ciencia de Materiales.

Correspondientemente, varias de las actuales fronteras en la investigación en espumas poliméricas son la adición de nanopartículas (con el fin de modificar el proceso de espumado o para mejorar/modificar la estructura y propiedades de la espuma), y la producción de espumas poliméricas con estructuras celulares en el rango nanométrico ( $1\text{ nm} = 10^{-9}\text{ m}$ ) con porosidades intermedias o elevadas (densidades medias o bajas). Debido al enorme interés de este campo, hemos centrado este trabajo de investigación en la producción y comprensión de espumas poliméricas nanocelulares, utilizando para ello una aproximación “*bottom-up*” basada en la auto-organización de copolímeros de bloque como patrón de las estructuras nanocelulares. La Figura 0.1 (derecha) muestra la estructura típica de una de las espumas nanocelulares producidas en esta investigación.

La fabricación de polímeros nanoporosos a partir de films poliméricos es bien conocida, ya sea mediante el empleo de nanoestructuras (técnicas de transferencia de patrones [16, 79-81]) o mediante la degradación o disolución selectiva de bloques [16, 80-87]. Por otra parte, la bibliografía muestra que no es posible obtener materiales nanocelulares mediante el empleo de técnicas de espumado empleando un agente de espumado químico.

Por el contrario, el proceso de espumado por disolución de gas a altas presiones (típicamente  $\text{N}_2$  o  $\text{CO}_2$ ) es quizás menos conocido [81, 88-90], pero es una técnica versátil, eficaz, barata y medioambientalmente sostenible, especialmente cuando se emplea  $\text{CO}_2$  (que presenta una excelente capacidad de difusión en el estado supercrítico (por encima de  $31^\circ\text{C}$  y  $7.3\text{ MPa}$ )) y con el potencial de crear polímeros nanocelulares.

El espumado mediante disolución de gas está compuesto de tres etapas (Figura 0.2):



Figura 0.2: Esquema del proceso de disolución de gas

- Etapa I: Saturación del polímero bajo presión.
- Etapa II: Desorción del gas tras liberar la presión.
- Etapa III: Espumado a una temperatura superior o cercana a la temperatura de transición vítrea efectiva del polímero plastificado ( $T_{g,ef}$ ).

Si la nucleación de las celdas se produce durante la liberación de la presión el proceso es calificado como un proceso de espumado en una etapa [66, 89] (también conocido como *batch foaming*), para lo cual la temperatura del polímero durante el proceso de liberación de la presión deberá ser próxima o superior a su  $T_{g,ef}$ .

Por el contrario, si durante la liberación de la presión el polímero se encuentra en estado vítreo será necesario llevar a cabo el proceso de espumado en una segunda etapa, calentando la muestra polimérica saturada de gas a una temperatura cercana o superior a su  $T_{g,ef}$ . En este caso el proceso de espumado será de dos etapas [72] (también conocido como *solid state foaming*).

La producción de polímeros nanocelulares mediante el proceso de espumado por disolución de gas requiere alcanzar una densidad de nucleación muy elevada ( $N_0$ , número de núcleos por  $\text{cm}^3$  de la muestra sin espumar), típicamente con valores de orden de  $10^{14}$ - $10^{15}$  núcleos/ $\text{cm}^3$ . Existen diversas aproximaciones para incrementar la densidad de nucleación como se muestra en la Figura 0.3.

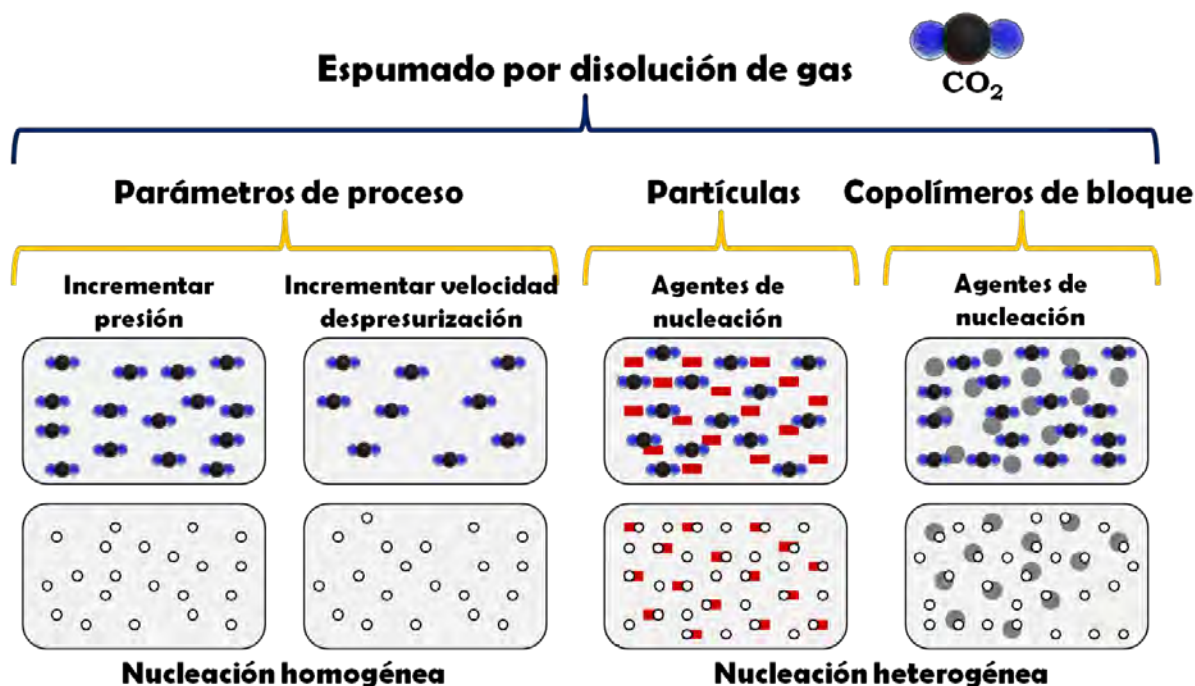


Figure 0.3: Métodos para incrementar la densidad de nucleación en los procesos de espumados por disolución de gas

En materiales que presentan un mecanismo de **nucleación homogénea** la densidad de nucleación está controlada por los parámetros del proceso de espumado (principalmente la presión de saturación y la velocidad de liberación de la presión) [89, 96, 102].

Mientras que en los materiales que presentan mecanismos de **nucleación heterogénea** es posible incrementar la tasa de nucleación mediante la adición de partículas (talco, óxido de titanio, caolín, nanosílicas, etc.), siempre y cuando dichas partículas estén bien dispersadas en la matriz polimérica y tengan un tamaño apropiado (del mismo orden o superior al radio crítico de nucleación del sistema polímero/gas) [108]. Por ejemplo, Sripurapu et al. [109] obtuvieron films nanocelulares de PMMA mediante la adición de nanopartículas de sílice con diámetros en torno a 10-12 nm, con presiones de saturación de CO<sub>2</sub> de 34.5 MPa.

También es posible incrementar la nucleación heterogénea mediante el uso de copolímeros de bloque (de tipo A-B o A-B-A, siendo A y B diferentes cadenas poliméricas) [113]. Estos copolímeros permiten la formación de nanoestructuras en la matriz polimérica, que pueden actuar como puntos de nucleación para las celdas. Adicionalmente, si alguno de los bloques del copolímero presenta afinidad por el CO<sub>2</sub> las nanoestructuras podrán almacenar más gas para inducir el crecimiento de las celdas [108].

Siguiendo este procedimiento pueden encontrarse en la bibliografía espumas nanocelulares obtenidas a partir de films de copolímeros de poliestireno-b-poli(dimetilsiloxano) o de PMMA-b-PFOMA (PFOMA, poli(1,1-dihidroperfluorooctil metacrilato)) [109]. Sin embargo estas espumas presentan densidades relativas muy elevadas (en torno a 0.98), y es necesario evitar la difusión del gas a través de las superficies del film durante la liberación de la presión.

Al inicio de esta investigación los mejores resultados obtenidos mediante el empleo de copolímeros habían sido obtenidos por Yokoyama et al. [115] y Yokoyama y Sugiyama [118], que obtuvieron densidades de nucleación cercanas a los 10<sup>16</sup> nucleos/cm<sup>3</sup>, a partir de films delgados de PS-b-PFMA (poliestireno-b-poli(perfluorooctil metacrilato)) y PS-b-PFS (poliestireno-b-poli(perfluorooctil propiloxi estireno)), presentando en ambos casos los bloques fluorados una mayor afinidad por el CO<sub>2</sub> que la matriz de poliestireno. Estos autores necesitaban llevar a cabo un enfriamiento de la muestra tras la liberación de la presión para preservar la estructura nanocelular, obteniendo de esa manera tamaños de celda en torno a los 15-30 nm, con una eficiencia de nucleación baja (es decir, con una densidad de nucleación significativamente inferior a la de densidad de nanodominios), y densidades relativas generalmente altas (cercanas a 1).

### S.2 Marco de la tesis

Este trabajo es el resultado de la colaboración entre dos laboratorios de investigación, el Laboratorio de Materiales Celulares (CellMat, Departamento de Física de la Materia Condensada, Universidad de Valladolid, España) y el Laboratorio de Química de Polímeros Orgánicos (LCPO, Universidad de Burdeos, Francia). Dicha colaboración se estableció mediante la firma de un acuerdo de cotutela de la tesis entre ambas instituciones, siendo dicha tesis financiada por el Ministerio Español de Educación (programa FPU, referencia AP2008-03603).

La actividad del grupo CellMat comenzó en 1999 con la tesis doctoral de Miguel Ángel Rodríguez Pérez [19]. A partir de entonces, bajo la dirección del profesor Miguel Ángel Rodríguez y del profesor José Antonio de Saja se han desarrollado trece tesis doctorales y se han publicado en torno a 150 artículos en revistas internacionales en el ámbito de los materiales celulares [20-31]. En la actualidad CellMat mantiene cinco líneas de investigación principales: espumas microcelulares y nanocelulares [47-49], nanocomposites celulares [50-53], espumas a partir de bioplásticos [54-56], espumas metálicas [57-60], y desarrollo de nuevas técnicas experimentales y dispositivos para el estudio de los mecanismos de espumado [61-64].

El laboratorio LCPO fue creado en 1985 por el profesor M. Fontanille, siendo actualmente dirigido por el profesor Henri Cramail. LCPO es uno de los principales centros de investigación sobre polímeros en Francia y Europa, con una calificación A<sup>+</sup> desde 2009. Su producción científica se encuentra en torno a 80 publicaciones/año en revistas internacionales, entre 7 y 10 patentes cada año, y desarrolla en la actualidad 7 proyectos de investigación europeos y 20 proyectos de investigación nacionales.

### S.3 Objetivos

Los objetivos generales de este trabajo son estudiar la producción, los mecanismos de espumado, y las propiedades de polímeros nanocelulares obtenidos a partir de mezclas de PMMA (poli(metil metacrilato)) y MAM (copolímero de bloque compuesto por un bloque de PMMA, un bloque de PBA (poli(butil acrilato)) y otro bloque de PMMA). Este sistema polímero/copolímero no ha sido estudiado sistemáticamente con anterioridad como precursor de materiales espumados, de manera que se ha llevado a cabo un estudio completo sobre el espumado de estos materiales.

Tradicionalmente existen cuatro principales áreas de interés en el estudio de un nuevo material celular: su ruta de producción, su estructura celular, sus propiedades, y sus potenciales aplicaciones. Esos aspectos están fuertemente interrelacionados, tal y como muestra el tetraedro de la Figura 0.4.



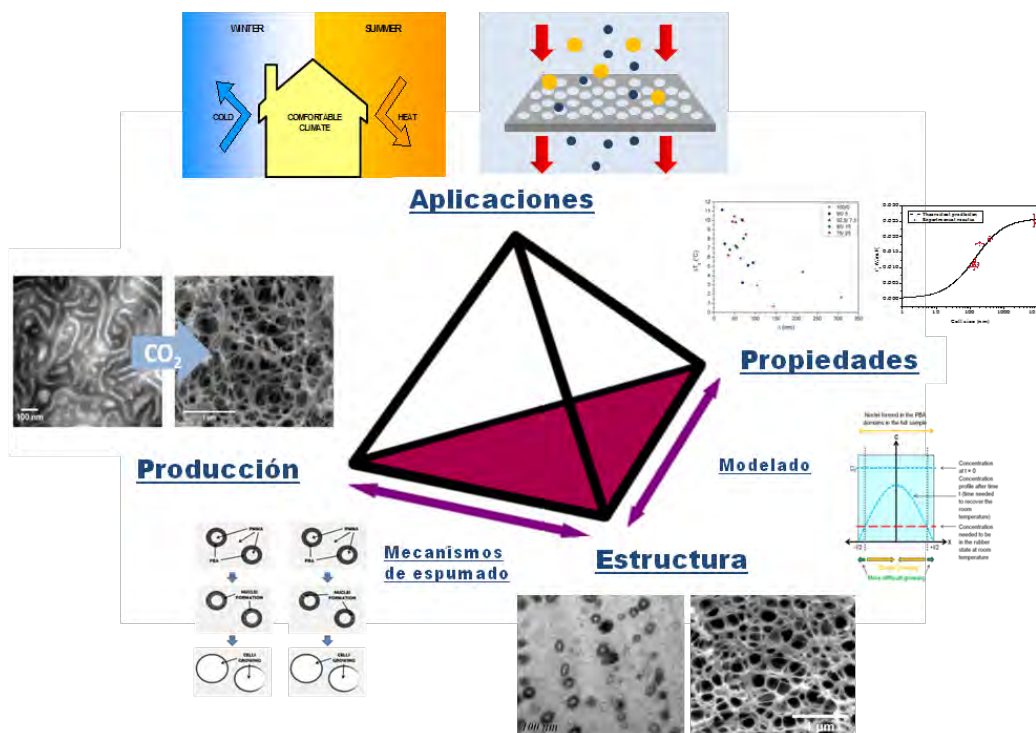


**Figura 0.4: Tetraedro de la ciencia de los materiales y sus inter-relaciones para los materiales espumados**

Nuestra investigación se ha centrado especialmente en la base del tetraedro, intentando producir conocimiento científico sobre estos materiales que pueda permitir encontrar aplicaciones de interés. Por tanto, los tres principales objetivos técnicos pueden resumirse como sigue:

1. Solventar algunas de las principales desventajas o limitaciones de las actuales estrategias de producción utilizadas para obtener espumas poliméricas nanocelulares (“Producción”).
2. Proporcionar una mejor comprensión de los mecanismos de espumado involucrados en la producción de espumas poliméricas nanocelulares. Para ello se analizará la estructura celular de los materiales fabricados y su relación con la morfología de los precursores utilizados para el espumado y con los parámetros de procesado (“Producción ↔ Estructura”).
3. Estudiar si existe una transición en las propiedades de estos materiales cuando el tamaño celular pasa del rango microcelular al rango nanocelular (“Propiedades”).

Aunque los principales objetivos se hayan centrado en estas tres áreas a lo largo de los distintos capítulos se describen algunas potenciales aplicaciones de estos materiales, así como del conocimiento generado.

Asimismo se han definido objetivos parciales dentro de los objetivos principales, de cara a definir precisamente el enfoque y la extensión de cada uno de ellos.

Desde el punto de vista de la técnica de producción queremos obtener espumas poliméricas nanocelulares con los siguientes requisitos:

- Los materiales de partida deben ser fácilmente accesibles, sin una síntesis excesivamente compleja y preferiblemente ser polímeros comerciales.
- Las mezclas sólidas polímero/copolímero deben presentar una autoestructuración mediante auto-organización.
- La ruta de producción debe ser escalable industrialmente, evitando requerimientos como presiones de saturación excepcionalmente elevadas, velocidades de despresurización extremadamente altas, enfriamiento de la muestra tras la liberación de la presión, etc.
- Debe obtenerse una reducción de la densidad significativa (por encima del 50%), manteniéndose intacta la estructura nanocelular.

Desde el punto de vista científico, en torno a los mecanismos de espumado el trabajo se ha centrado en las siguientes cuestiones:

- ¿El proceso de nucleación es homogéneo o heterogéneo? (O una combinación de ambos mecanismos). ¿Esos mecanismos pueden ser identificados de manera independiente?
- ¿Está la nanoestructura de las muestras sólidas relacionada con la estructura celular de las muestras espumadas?
- ¿Cuál es el papel del bloque blando del copolímero MAM en los procesos de nucleación y crecimiento de las celdas?
- ¿Cuál es el papel de la matriz de PMMA en los procesos de nucleación y crecimiento de las celdas?
- ¿Cuál es la influencia del porcentaje de MAM y la morfología de las nanoestructuras en la densidad y estructura celular de las espumas de PMMA/MAM?
- ¿Cuál es la influencia de los parámetros de procesamiento (presión de saturación de  $\text{CO}_2$  y temperatura de saturación) en las espumas de PMMA/MAM?

Y finalmente, hemos centrado parte de nuestra investigación en determinar la influencia de la reducción del tamaño celular, desde el rango micrométrico al nanométrico, sobre las siguientes propiedades:

- Conductividad térmica: se espera que la conductividad térmica de la fase gaseosa de las espumas nanocelulares sea menor que la de las espumas microcelulares debido al efecto Knudsen [124].
- Temperatura de transición vítrea de la matriz polimérica: la temperatura de transición vítrea en films delgados puede incrementarse debido al confinamiento de las cadenas poliméricas [126]. Por tanto, los polímeros nanocelulares podrían presentar un efecto similar debido al bajo espesor de las paredes y aristas de las celdas.
- Módulo de Young: en espumas microcelulares de PMMA se ha descrito una mejora de sus propiedades mecánicas (módulo de Young entre otras) con la reducción del tamaño de celda [127]. Se espera por tanto que las espumas nanocelulares puedan presentar mejores propiedades mecánicas que las espumas microcelulares [78].

#### S.4 Estructura de la tesis

El trabajo de investigación presentado en esta tesis se ha realizado en el marco de un acuerdo de cotutela entre dos universidades de diferentes países. Además esta tesis se presenta para optar al grado de *Doctor con mención Internacional*. Por ambos motivos el cuerpo principal de la tesis está redactado en inglés. Adicionalmente, de acuerdo con las normativas específicas de la universidad de cotutela se incluyen dos resúmenes de la tesis, uno en francés y otro en español.

Además, esta tesis está escrita como *compendio de publicaciones*. Incluyendo seis artículos enviados a revistas internacionales (uno de ellos todavía pendiente de ser aceptado) y un proceeding de una comunicación oral en un congreso internacional. Adicionalmente, se han incluido algunos resultados no publicados para proporcionar una mejor comprensión del trabajo y para alcanzar los objetivos previamente definidos. La Tabla 0-1 muestra los artículos incluidos en la tesis, indicando en que capítulo se encuentran.

Otras publicaciones en revistas con proceso de revisión por pares, contribuciones a congresos internacionales (relativas a la tesis u otros campos de investigación), estancias de investigación en otras instituciones, y la participación en proyectos de investigación durante los últimos cuatro años (en ámbitos diferentes a las espumas basadas en PMMA) se muestran en las tablas 0-2, 0-3, 0-4, 0-5 y 0-6, respectivamente.

La tesis está dividida en seis capítulos, incluyendo la siguiente información:

El capítulo 1 introduce las técnicas experimentales utilizadas en este trabajo. Las técnicas convencionales son enumeradas, mientras que las técnicas no convencionales (algunas de ellas desarrolladas dentro de esta investigación) son descritas en detalle.

El capítulo 2 describe los materiales de partida, PMMA y MAM, y las rutas de producción de las mezclas de PMMA/MAM y de las espumas. La morfología de la nanoestructuración de las mezclas sólidas de PMMA/MAM y la estructura celular de las espumas fabricadas son estudiadas y descritas en este capítulo.

El capítulo 3 define las relaciones entre la nanoestructuración de los precursores de PMMA/MAM y la estructura de las espumas obtenidas mediante espumado por disolución de gas ( $\text{CO}_2$ ). Además se analizan el *proceso de nucleación* y la influencia de la *presión de saturación* y el *contenido de MAM* en la estructura celular. A partir de estas relaciones se describen los procesos de nucleación y crecimiento de las celdas para estos materiales.

El capítulo 4 proporciona información sobre el papel de la *temperatura de saturación* y la de *post-espumado* en el proceso de espumado de las mezclas de PMMA/MAM. Determinándose el límite entre procesos de espumado de una y dos etapas, y proporcionándose una descripción de ambos procesos teniendo en cuenta los mecanismos de nucleación de las mezclas de PMMA/MAM previamente descritos.

El capítulo 5 estudia las propiedades de las espumas nanocelulares comparadas con las propiedades de espumas microporosas de la misma composición química. Este capítulo se divide en tres secciones, correspondientes al estudio de la conductividad térmica, la temperatura de transición vítrea, y el módulo de Young.

El último capítulo recoge las principales conclusiones de este trabajo, e incluye sugerencias para la continuación de esta línea de investigación en el futuro.

Con el ánimo de proporcionar una mejor comprensión de la estructura de la tesis y las relaciones entre los diferentes capítulos se ha incluido el esquema de la Figura 0.5.

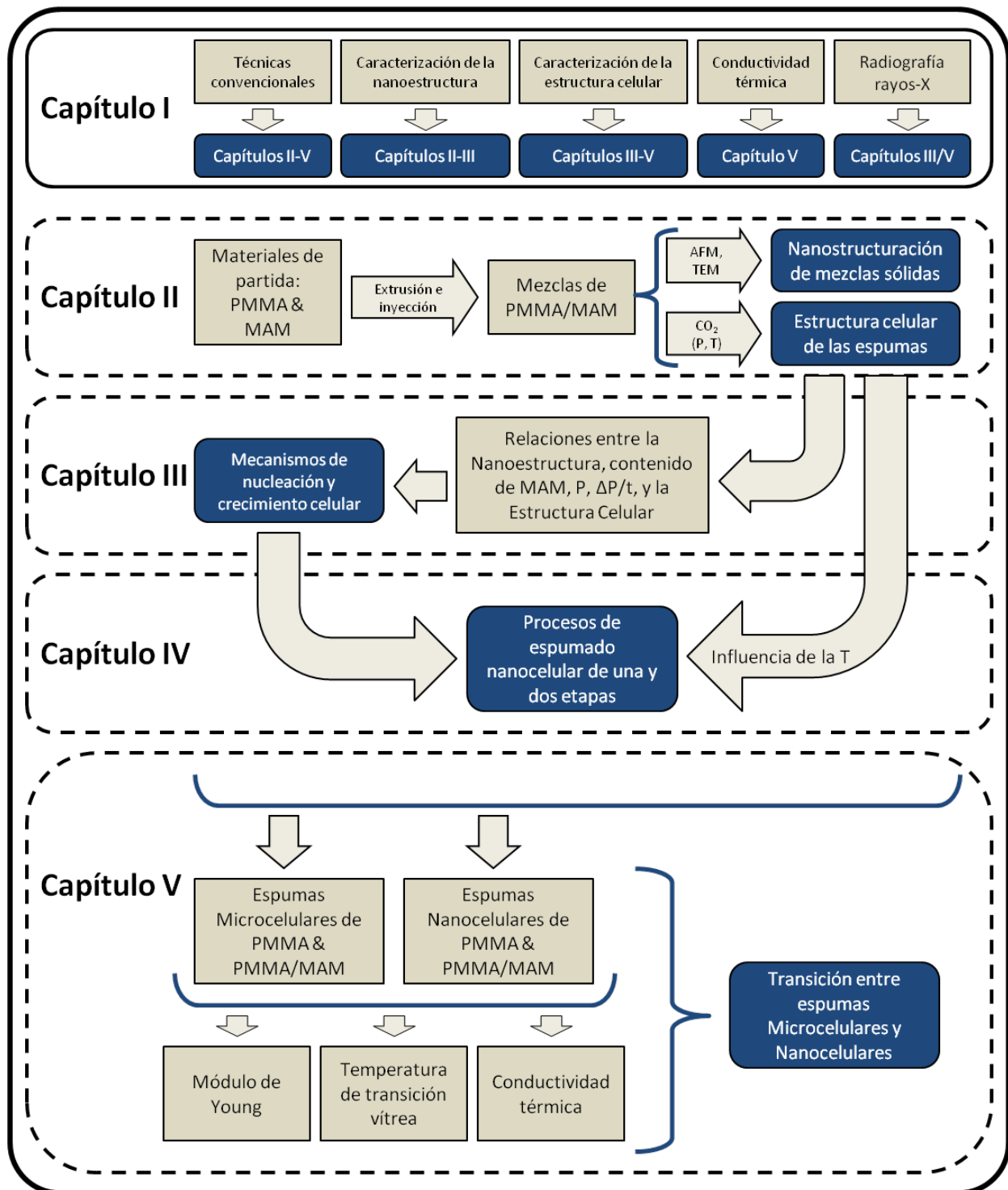


Figura 0.5: Esquema de la estructura de la tesis

Tabla 0-1: Publicaciones en revistas internacionales incluidas en la tesis

Publicaciones enviadas a revistas internacionales	Capítulo
J. A. Reglero, M. Dumon, J. Pinto, M. A. Rodríguez-Perez <b>Low Density Nanocellular Foams Produced by High-Pressure Carbon Dioxide</b> <i>Macromolecular Materials and Engineering</i> 296, 752-759 (2011)	V
J. Pinto, S. Pardo-Alonso, E. Solórzano, M. A. Rodríguez-Perez, M. Dumon, J. A. de Saja <b>Solid Skin Characterization of PMMA/MAM Foams Fabricated by Gas Dissolution Foaming over a Range of Pressures</b> <i>Defect and Diffusion Forum vols.</i> 326-328, 434-439 (2012)	III
J. Pinto, E. Solórzano, M. A. Rodríguez-Perez, J. A. de Saja <b>Characterization of Cellular Structure Based on User-Interactive Image Analysis Procedures</b> <i>Journal of Cellular Plastics</i> 49, 6, 554-574 (2013)	I
J. Pinto, M. Dumon, M. Pedros, J. Reglero, M. A. Rodríguez-Perez <b>Nanocellular CO<sub>2</sub> foaming of PMMA assisted by block copolymer nanostructuration</b> <i>Chemical Engineering Journal</i> 243C, 428-435 (2014)	III
J. Pinto, M. Dumon, M. A. Rodríguez-Perez, R. García, C. Dietz <b>Block Copolymers Self-Assembly Allows Obtaining Tunable Micro or Nanoporous Membranes or Depth Filters Based on PMMA; Fabrication Method and Nanostructures</b> <i>The Journal of Physical Chemistry C</i> 118, 9, 4656-4663 (2014)	III
J. Pinto, J. Reglero-Ruiz, M. Dumon, M. A. Rodríguez-Perez <b>Temperature Influence and CO<sub>2</sub> Transport in Foaming Processes of Poly(methyl methacrylate)-Block Copolymer Nanocellular and Microcellular Foams</b> <i>Journal of Supercritical Fluids</i> (pendiente de aceptación)	IV

Tabla 0-2: Otras publicaciones en revistas internacionales

Otras publicaciones enviadas a revistas internacionales
M. Dumon, J. A. Reglero-Ruiz, J. Pinto, M. A. Rodriguez-Perez, J. M. Tallon, M. Pedros, P. Viot <b>Block Copolymer-Assisted Microcellular Supercritical CO<sub>2</sub> Foaming of Polymers and Blends</b> <i>Cellular Polymers</i> 31, 207-222 (2012)
E. Solórzano, J. Pinto, S. Pardo-Alonso, F. García-Moreno, M. A. Rodriguez-Perez <b>Application of a Microfocus X-Ray Imaging Apparatus to the Study of Cellular Polymers</b> <i>Polymer Testing</i> 32, 321-329 (2012)
B. Notario, J. Pinto, E. Solórzano, J. Escudero, J. Martín de León, D. Velasco, M. A. Rodriguez-Perez <b>In-Situ Optical Analysis of Structural Changes in Polyactic Acid (PLA) during Gas Dissolution Process</b> <i>Defect and Diffusion Forum</i> (aceptado, pendiente de publicación)

Tabla 0-3: Contribuciones en congresos internacionales relativas a la tesis

Contribuciones en congresos internacionales relativas a la tesis
<p>J. Pinto, M. A. Rodríguez-Perez, J. A. de Saja</p> <p><b>Development of an Image J Macro to Characterize the Cellular Structure of Polymeric Foams</b></p> <p><b>Póster.</b> <i>XI Reunión del Grupo Especializado de Polímeros (GEP), Valladolid (Spain) (2009)</i></p>
<p>J. Pinto, S. Pardo, E. Solórzano, M. A. Rodríguez-Perez, M. Dumon, J. A. de Saja</p> <p><b>Solid Skin Characterization of PMMA/MAM Foams Fabricated by Gas Dissolution Foaming over a Range of Pressures</b></p> <p><b>Oral.</b> <i>DSL 2011, Algarve (Portugal) (2011)</i></p>
<p>J. Pinto, M. A. Rodríguez-Perez, J. A. de Saja, M. Dumon, R. García, C. Dietz</p> <p><b>Relationship Between the Nano-Structured Morphology of PMMA/MAM Blends and the Nanocellular Structure of Foams Produced from these Materials</b></p> <p><b>Oral.</b> <i>FOAMS 2011, Iselin (New Jersey, USA) (2011)</i></p>
<p>M. A. Rodríguez-Perez, J. Pinto, M. Dumon</p> <p><b>From Micro to Nanocellular Polymeric Materials</b></p> <p><b>Invited Lecture.</b> <i>PPS Conference, Niagara Falls (Canada) (2012)</i></p>
<p>J. Pinto, E. Solórzano, M. A. Rodríguez-Perez, J. A. de Saja, M. Dumon</p> <p><b>Thermal Conductivity Transition between Microcellular and Nanocellular Polymeric Foams: Experimental Validation of the Knudsen Effect</b></p> <p><b>Oral.</b> <i>FOAMS 2012, Barcelona (Spain) (2012)</i></p>
<p>M. A. Rodríguez-Perez, J. Pinto, J. Escudero, A. Lopez-Gil, E. Solórzano, C. Saiz-Arroyo, S. Estravís, S. Pardo-Alonso</p> <p><b>Nano-strategies applied to the production of cellular polymers with improved cellular structure and properties</b></p> <p><b>Keynote Lecture.</b> <i>CellMat Conference, Dresden (Germany) (2012)</i></p>
<p>J. Pinto, M. Dumon, M. A. Rodríguez-Perez</p> <p><b>Development of Nanocellular Foams by Gas Physical Foaming</b></p> <p><b>Poster.</b> <i>FOAMS 2013, Seattle (USA) (2013)</i></p>
<p>J. Pinto, E. Solórzano, M. A. Rodríguez-Perez, M. Dumon</p> <p><b>Nanocellular Foams Fabrication Assisted by Nanostructuration Pattern: Understanding the Heterogeneous Nucleation Mechanism</b></p> <p><b>Oral.</b> <i>FOAMS 2013, Seattle (USA) (2013)</i></p>



Tabla 0-4: Otras comunicaciones en congresos internacionales

Otras comunicaciones en congresos internacionales
<p>J. Escudero, J. Pinto, E. Solórzano, M. A. Rodríguez-Perez, J. A. de Saja</p> <p><b>Structural Foams vs. Conventional Foams: Structural Characterization and Mechanical Behavior</b></p> <p><b>Oral.</b> <i>XI Reunión del Grupo Especializado de Polímeros (GEP), Valladolid (Spain) (2009)</i></p>
<p>M. A. Martínez, J. Abenojar, M. A. Rodríguez-Perez, J. Pinto, S. Estravis, J. Ecenero, E. Aldanondo, P. Álvarez</p> <p><b>Unión de Espumas de Poliolefina y Poliuretano al Aluminio: Ensayos de Adhesión y su Modelización</b></p> <p><b>Póster.</b> <i>X Congreso de Adhesión y Adhesivos, Alicante (Spain) (2009)</i></p>
<p>P. Álvarez, A. Echeverría, M. M. Petite, M. A. Rodríguez-Perez, J. Pinto, S. Estravis, M. A. Martínez, J. Abenojar</p> <p><b>Fabricación, Caracterización y Modelización de Paneles Sándwich Compuestos por Cores de Espumas de Polietileno y Poliuretano y Pielas de Aluminio</b></p> <p><b>Póster.</b> <i>Comatcomp 09, San Sebastian (Spain) (2009)</i></p>
<p>E. Solórzano, M. A. Rodríguez-Perez, J. Pinto, F. García-Moreno, J. A. de Saja</p> <p><b>A Novel Procedure to in-situ Analyze the Foamability of Thermoplastic Foams using Optical Expandometry and X-Ray Radioscopy</b></p> <p><b>Oral.</b> <i>Blowing Agents 2010, Köln (Germany) (2010)</i></p>
<p>E. Solórzano, J. Escudero, J. Pinto, J. A. de Saja, M. A. Rodríguez-Perez</p> <p><b>Gas Diffusion and Other Physical Mechanisms Involved in the Production of Structural Foams</b></p> <p><b>Oral.</b> <i>DSL 2010, Paris (France) (2010)</i></p>
<p>M. A. Rodríguez-Perez, E. Solórzano, J. Pinto, J. A. de Saja</p> <p><b>A Novel Method to Analyze the Foamability of Polymer Systems using in-situ Optical Expandometry and X-Ray Radioscopy</b></p> <p><b>Oral.</b> <i>FOAMS 2011, Seattle (USA) (2010)</i></p>
<p>E. Solórzano, J. Pinto, F. García-Moreno, M. A. Rodríguez-Perez</p> <p><b>ImageJ: Multifunctional Analysis in Materials Science</b></p> <p><b>Oral.</b> <i>ImageJ User and Developer Conference, Mondor les Bains (Luxembourg) (2010)</i></p>
<p>M. Dumon, J. A. Reglero-Ruiz, J. M. Tallon, M. Pedros, E. Cloutet, J. Pinto, P. Viot</p> <p><b>Behavior of block copolymers in supercritical CO<sub>2</sub> and microcellular foaming of polymer blends</b></p> <p><b>Oral</b> <i>DSL 2011, Algarve (Portugal) (2011)</i></p>

E. Solórzano, J. Pinto, S. Pardo, M. A. Rodríguez-Perez, J. A. de Saja

**X-Ray Radioscopy In-Situ Monitoring of Diffusion Mechanism Occurring during the Production of Structural Foams by Free Foaming**

**Oral.** *DSL 2011, Algarve (Portugal) (2011)*

E. Solórzano, J. Escudero, J. Pinto, M. A. Rodríguez-Perez, J. A. de Saja

**Evolution of Polymers during the Gas Dissolution Process**

**Oral.** *DSL 2011, Algarve (Portugal) (2011)*

M. A. Rodríguez-Perez, J. Escudero, J. Pinto E. Solórzano

**Production of Structural Foams using Free Foaming. In-situ Analysis of the Foaming Process**

**Oral.** *FOAMS 2011, Iselin (New Jersey, USA) (2011)*

M. Dumon, J. A. Reglero-Ruiz, E. Cloutet, J. Pinto, M. A. Rodríguez-Perez, P. Viot

**Block copolymer-assisted microcellular supercritical CO<sub>2</sub> foaming of polymers and blends**

**Oral.** *Blowing Agents and Foaming Processes, Berlin (Germany) (2012)*

E. Solórzano, S. Pardo-Alonso, J. Pinto, M. A. Rodríguez-Perez

**Polymer Foaming Processes and Related Physics: Monitorization by X-Ray Radioscopy**

**Oral.** *FOAMS 2012, Barcelona (Spain) (2012)*

M. Dumon, P. Viot, J. A. Reglero-Ruiz, L. Maheo, G. Ciclia, O. Mondain Monvai, V. Schmitt, A. Chirazi, J. Pinto, M. A. Rodríguez-Perez

**Fabrication of Calibrated Micro-Foams, Structures and Mechanical Properties**

**Oral.** *FOAMS 2012, Barcelona (Spain) (2012)*

B. Notario, J. Pinto, E. Solórzano, J. Escudero, J. Martín-de León, D. Velasco, M. A. Rodríguez-Perez

**In-Situ Optical Analysis of Structural Changes in Amorphous Polymers during the Gas Dissolution Process**

**Oral.** *DSL 2013, Madrid (Spain) (2013)*

Tabla 0-5: Estancias en otros centros de investigación

Estancias en otros centros de investigación
Dos semanas en el Instituto de Microelectrónica (CSIC) de Madrid (Spain) en 2009 <b>Objetivo: Aprendizaje del uso de Atomic Force Microscopy (AFM)</b>
Una semana en la Technical University of Berlin (Germany) en 2010 <b>Objetivo: Aprendizaje de técnicas de análisis de imagen</b>
Tres meses en el Microcellular Plastics Laboratory (Mechanical Engineering Department) de la University of Washington (USA) en 2011 <b>Objetivo: Producción de materiales celulares basados en HDPE y x-HDPE mediante espumado por disolución de gas (CO<sub>2</sub>)</b>

Tabla 0-6: Participación en otros proyectos de investigación financiados en los últimos 4 años

Proyectos de investigación financiados
FP7 Comisión Europea. <b>NANCORE 214148</b>
Agencia Espacial Europea. <b>MAP AO-99-075</b>
Ministerio de Ciencia e Innovación (Programa Nacional de Materiales). <b>MAT2009-14001-C02-01</b>
Ministerio de Ciencia e Innovación (Programa Nacional de Materiales). <b>MAT2012-34901</b>
Junta de Castilla y León. <b>VA174A12-2</b>
Junta de Castilla y León. <b>VA035U13</b>

## S.5 Principales resultados

A continuación se van a introducir las principales conclusiones obtenidas en este trabajo de investigación:

- Las mezclas de PMMA/MAM nanoestructuradas se han mostrado como excelentes materiales para la producción de materiales poliméricos nanocelulares. Siendo estos materiales de partida comerciales y de fácil acceso.
- Las morfologías de la nanoestructuración auto-organizada de las mezclas sólidas de PMMA/MAM dependen del contenido de MAM, mostrando desde objetos micelares, a estructuras tipo gusano o lamelares. Además esta nanoestructuración bien definida se presenta después de los procesos de extrusión e inyección (procesos industrialmente escalables).

- Se han obtenido de manera controlada espumas nanocelulares con dos morfologías diferentes claramente definidas (celda cerrada y celda abierta). El tipo de estructura celular puede elegirse ajustando el contenido del copolímero de bloque en las mezclas de PMMA/MAM.
- Se han obtenido espumas nanocelulares a partir de muestras sólidas de varios milímetros de espesor con tiempos de saturación de 24 horas.
- Se han obtenido espumas nanocelulares con significativas reducciones de densidad (densidades relativas desde 0.4 a 0.6).
- Se han obtenido espumas nanocelulares con presiones de  $\text{CO}_2$  no excesivamente altas, ni por medio de velocidades de despresurización extremadamente altas, ni necesitando enfriar la muestra tras la liberación de la presión.
- El proceso de nucleación de las celdas en las mezclas de PMMA/MAM es completamente heterogéneo. Estando controlado por el bloque blando y con mayor afinidad por el  $\text{CO}_2$  del MAM. La eficiencia de nucleación (la relación entre el número de núcleos de celdas y el número de nanoestructuras dispersas) es cercana a la unidad.
- El crecimiento de las celdas es controlado por la plastificación de la matriz de PMMA, siendo posible prevenir la coalescencia de las celdas mediante una apropiada selección de las condiciones de procesado.
- Como consecuencia de los dos resultados previos, es posible obtener espumas nanocelulares a partir de mezclas de PMMA/MAM en un amplio rango de presiones de saturación, desde 10 a 30 MPa.
- Se ha encontrado una clara transición entre las espumas microcelulares y nanocelulares de PMMA/MAM en cuanto a los valores de la conductividad térmica y la temperatura de transición vítrea se refiere.

## S.6 Referencias

Las referencias citadas en este resumen pueden encontrarse en la sección 0.7.

# *Introduction*



## 0.1 Introduction

Human knowledge and technological development have not kept a steady growth since the advent of civilization; on the contrary, several scientific and technological fields have increased in an exponential way [1, 2]. In fact, it is estimated that more than 90 % of the scientific knowledge has been developed since the end of the II World War in 1945. This affirmation virtually applies for every single scientific field, and in the Materials Science field has two main implications.

On one side, advances on this field allow developing new materials with unique properties, or improving the properties or production routes of known materials. On the other side, advances on other scientific fields and development of new technological devices usually require new or tailored materials with specific properties. Due to this duality, Materials Science is one of the main fields of interest of both public and private research organizations.

The European Union (EU) established in December 2013 the research objectives of the program “*Horizon 2020*” (Horizon 2020, the EU Research and Innovation program for the period 2014-2020)[3]. Inside the materials science field one of the priorities will be the “*Manufacturing and control of nanoporous materials*”. EU refers “*a constantly growing interest in nanostructured porous materials, thanks to the many applications that can benefit from controlled porosity at the nanoscale*”.

The present thesis entitled “***Fabrication and Characterization of Nanocellular Polymeric Materials from Nanostructured Polymers***” is part of this priority research field for the EU present and next period.

Generally speaking, foams belong to porous materials; the word “foam” is often used to name relatively low density materials (irrespective of the pore size) and is related to the production process or technique (use of an expansion method). But production of foams (i.e. porous/cellular materials) is one approach to improve several properties of known materials, or to increase the range of their potential applications [4]. Indeed if mass gain is both a technical and society concern, porous materials and foams do offer additional properties (thermal, shock absorption, filtration, catalysis, optical, acoustical, etc.).

Nature also used this approach during the evolution of life in Earth, and it is possible to find materials in living organisms (vegetables or animals) with a porous structure, such as wood, cork, sponges or bones of different species [5]. However, reproducing living structures by artificial means is never simple. Structures of living materials are built in a “bottom-up” way, with the individual living cells organizing themselves, and responding to the external demands. For instance, structure of the human bones (Figure 0.1, left) is organized to provide support to the human body, and can be reinforced if the support demands are increased (e.g. by physical exercise).

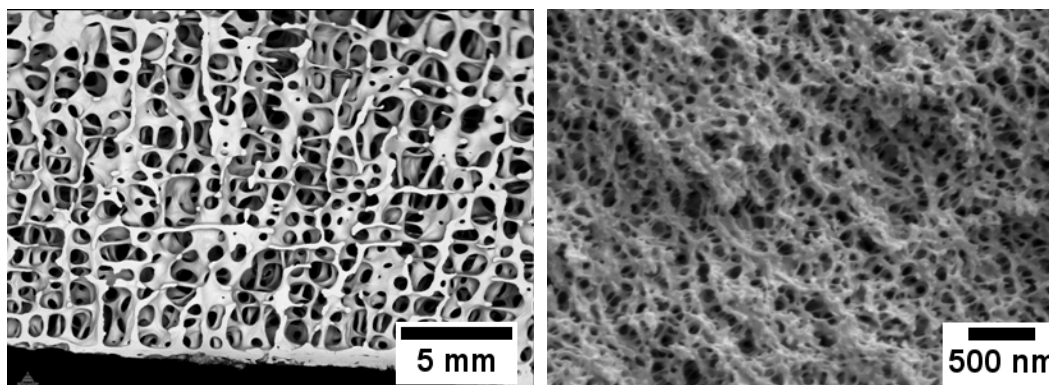


**Figure 0.1: Porous structure of a human bone (left) and porous structure of a nanocellular polymeric foam (right)**

Nowadays foams can be manufactured from several different materials, such as liquids, polymers, metals, ceramics, et c. [6-10]. Applications of manufactured foams due to their mechanical properties and low relative density are found in packaging, aeronautic industry, automotive industry, shipbuilding industry, wind turbines, etc. [11]. Other important applications of this kind of materials are their use in thermal insulation [12], acoustic insulation [13], and their use as scaffolds [14-16] and filtration [17] and catalysis processes due to their structure and high specific surface area [18].

The production of foams has experienced a significant progression with the development of Nanotechnology. This concept was firstly introduced by the Nobel Prize Richard P. Feynman in 1959 in his talk “*There’s Plenty of Room at the Bottom*”. As Feynman predicted (and other scientists like Norio Taniguchi, who introduced the term “*nano-technology*”) with the manipulation of matter at an atomic, molecular or supramolecular scale began a new era for Materials Science.

Accordingly, some of the current frontiers in polymer foams research are the addition of nanoparticles (to modify the foaming process or to enhance/modify the structure and properties of the foam) and the production of polymers with cellular structures in the nanometric range at medium to high void fractions (i.e. medium to low densities). Due to the enormous interest of this field, we focus this research work in the production and understanding of polymer nanofoams, using a “*bottom-up*” approach with the self-assembly of block copolymers as a pattern of the nanocellular structures. Figure 0.1 (right) shows the typical structure of one of the nanocellular foams produced in this research.

This introducing chapter (*Chapter 0*) is divided into five sections. First is a description of the scientific framework where this work was carried out. Secondly, an overall view of the state of the art on nanocellular polymeric foams is provided. Then, the scope and objectives are described. Also, an explanation about the body of the manuscript, its organization and a global schematic view of the



investigation are included. Finally, the main novelties and contributions of this work to the field of nanocellular polymeric foams field are enumerated.

## 0.2 Framework of this thesis

This investigation is the result of the collaboration between two research laboratories, CellMat Laboratory (Condensed Matter Physics Department, University of Valladolid, Spain) and the Laboratoire de Chimie des Polymères Organiques (LCPO, University of Bordeaux 1, France). The collaboration was established by the signature of a thesis co-tutelle agreement between both institutions. The scholarship is granted by the Spanish Ministry of Education (FPU program, AP2008-03603).

Activity of CellMat Laboratory started on 1999 with the PhD thesis of Miguel Ángel Rodríguez-Pérez [19]. Thenceforth, under the direction of Prof. Dr. Miguel Ángel Rodríguez-Pérez and Prof. Dr. José Antonio de Saja thirteen PhD theses and about 150 journal papers have been published on cellular materials [20-31]. Research activity of CellMat began with the characterization of polymeric foams based on polyolefins [32-46]. After a few years the research topics were extended to the production of polymeric foams both by chemical and physical blowing agents. In 2002 a new research line in metal foams was introduced [25, 26]. Finally, in the last years significant efforts have been done in the development of non-conventional characterization techniques and experimental devices, with the aim to provide a better understanding of the mechanisms taking place during the foaming process.

Nowadays CellMat sustain five main research lines: microcellular and sub-microcellular foams [47-49], cellular nanocomposites [50-53], bioplastic foams [54-56], metallic foams [57-60], and development of new experimental techniques and devices [61-64].

LCPO (Laboratoire de Chimie des Polymères Organiques) belongs to CNRS (Centre National de la Recherche Scientifique, UMR unit n° 5629) and is a university laboratory of Université of Bordeaux and of Institut Polytechnique de Bordeaux (IPB, the pool of engineering schools of Bordeaux). It comprises 42 permanent people in 5 categories (researchers, teachers, technicians, engineers and administration), and more than 70 non-permanent people (Ph. Ds, post-docs, internships). It is located at Ecole Nationale Supérieure de Chimie, de Biologie et de Physique (ENSCBP) (2000 m<sup>2</sup>) and at Université de Bordeaux (1300 m<sup>2</sup>).

LCPO was created in 1985 by Prof. M. Fontanille, and is now supervised by Prof. H. Cramail. LCPO is one of first polymer center in France and Europe, with an A<sup>+</sup> mark since 2009. Scientific production is

around 80 publications/year in international journals; 7 to 10 patents/year; 7 european and more than 20 national ongoing projects.

Original scope of the research on LCPO is synthesis and organic chemistry of polymers, with now four main research lines: Polymerization Catalysis & Macromolecular Design, Biopolymers & Bio-sourced Polymers, Polymer Self-Assembly & Life Sciences and Polymer Electronic Materials & Devices. Scientific objectives are to develop new functional polymers for sustainable development, health or energy through green technologies and macromolecular engineering.

Particularly, LCPO has been working with CO<sub>2</sub> as a reaction dispersant medium for the synthesis of polyurethane and silicone particles when a first research line on cellular polymers was launched by Prof. Dr. M. Dumon and Dr. J. A. Reglero (postdoc) between 2009-2011 in an ANR project 2009-2012, named *Listrac* (Light Structures and Composites), ANR is the Agence National de la Recherche; the project developed basic knowledge on various cellular polymer materials based on PMMA or PS for shock absorbers in passive safety devices, one class being PMMA blend foams in the presence of di and tri block acrylic copolymers. In this framework, different foam synthesis routes were studied in terms of varying the porous structures and the consequent mechanical behavior. The aim was also to propose new models in order to describe, understand, and model their mechanical behavior as a function of the materials structure. The elaboration routes were the technique of HIPE-emulsions in order to template foams above the micrometric range (CRPP laboratory), and supercritical CO<sub>2</sub>-foaming to generate foams around and below the micrometric range (LCPO).

Thus the *Listrac* work was focused in the production of foams from nanostructured polymer-copolymer blends by gas dissolution foaming, using CO<sub>2</sub> as physical blowing agent.

In order to provide an academic work, neat unformulated (or as little as possible), unfilled, uncharged commodity amorphous polymers as polystyrene (PS) and poly(methyl methacrylate) (PMMA) [49, 65-69] were chosen because these polymers are homogeneous at the nanometer level

Then nanostructuration of these amorphous polymers is coupled, which is well known in the field of polymer blends, compatibilization and reinforcement. The field of self-assembly, nanostructuration, nano patterning is well known with di/tri block copolymers and abundant literature exists (we will not give a review on this field in Chapter 0, but a summary can be found in Chapter II). Polymer nanostructuration consists in dispersing a second separated phase at the nanometer level; the phase being ordered at either nano or micro ranges as micelles, core-shells, lamella, and worm-like. The choice is such that the second phase is compatible enough to leave the precursor blend material transparent before foaming.

In this manuscript nanostructuring of PMMA is induced by the addition of a tri block acrylic copolymers with a CO<sub>2</sub>-philic block, with the aim to increase the gas sorption and increase the nucleation ratio of these foams. In 2010 Dr. José Antonio Reglero started to study (poly(methyl methacrylate)-co-poly(butyl acrylate)-co-poly(methyl methacrylate)) (MAM) [49], and discovered that blends of PMMA and a 10% of weight (wt%) of MAM could produce well-defined nanocellular foams. The collaboration between LCPO and CellMat was established in 2010-2011 and the present thesis was carried out with the aim to continue, extend, and amplify this initial work with PMMA/MAM blends.

Apart from choosing the precursor, the foaming technique or the process has a great importance. Physical (inert gas blowing) or chemical techniques (e.g. CBA chemical blowing agents by thermal decomposition) are the two main industrial processes for bulk polymer foams.

Also among the chemical techniques, are other less productive methods by selective degradation or extraction of one phase in a matrix. It can be called templating techniques or pattern-transfer techniques (e.g. high  $T_g$  polymers). Among physical foaming techniques, the gas dissolution technique coupled with a pattern-transfer technique is promising for nanofoams. We will comment these techniques in the next paragraph.

### 0.3 Summary of the state of the art

In the present section prior knowledge on the production and properties of nanocellular polymeric foams is briefly presented. Up to date literature on this topic and on other specific topics (image analysis, cell size calculation, thermal conductivity, etc.) can be found in the journal articles included in the corresponding chapters. It is important to mention that there has been a significant evolution of this topic and an increase of the papers published in the last three years.

#### 0.3.1 Nanocellular polymer foams

Cellular materials are two-phase structures composed of a continuous solid/liquid phase and either continuous or discontinuous gaseous phase [4, 6, 8, 9]. As explained before it is possible to find a large variety of materials with a cellular structure (polymers, wood, metals, ceramics, etc.). Cellular structures can be classified according to their topology; on one hand would be the open cell foams, which show continuity of the gas and solid phases, and on the other hand would be the closed cell foams in which the gas is enclosed in the pores (i.e. continuous solid phase and discontinuous gas phase).

Another classification of foams, and in particular of polymer foams, can be done in terms of their average cell size. For instance, conventional polymer foams present cell sizes larger than 100  $\mu\text{m}$ , whereas

microcellular polymer foams present cell sizes in the order of  $10\ \mu\text{m}$ . Microcellular polymers and corresponding technologies have been under development since the early 1980s [70-72]; these materials show significant improvements of compressive and bending strength, impact strength and fatigue life, etc.; for example, microcellular plastics exhibit higher Charpy impact strength, toughness, fatigue life, thermal stability, light reflectivity, and lower thermal conductivity than unfomed plastics, and much better mechanical properties than conventional foams [73-76]. Continuing with the classification of polymer foams in terms of their average cell size the next group of foams is the nanocellular polymers, with cell sizes under the micron.

Then, nanocellular polymer foams (i.e. nanocellular polymers produced by foaming processes) (Figure 0.2) are two-phase materials composed by a polymeric matrix and a cellular structure with nanometric pores filled by gas (either individual pores or connected ones). Just as microcellular foams present better properties than conventional foams, it is expected that nanocellular foams will present enhanced properties due to their lower cell size. For instance, they could have better mechanical properties, such as better toughness, higher impact energies, and strain to failure [77]; also, they could present an improved thermal insulation behavior due to the Knudsen effect [78]. More details about the expected properties of nanocellular polymer foams will be provided in the last section of this literature survey.

The terms “nanoporous polymer” and “nanocellular polymer foams” often refer to different materials, and literature surveys give different papers if inquiring both keywords. However among nanocellular polymer foams produced by foaming processes, rather few (a few tens) papers are given in the last 10 years. More papers are found about nanoporous polymers in high  $T_g$  matrices or biopolymers (e.g. see papers of Antonietti, Hentze, Hillmyer, Hedrick, etc.) and we will not give a complete survey but only the following remarks.

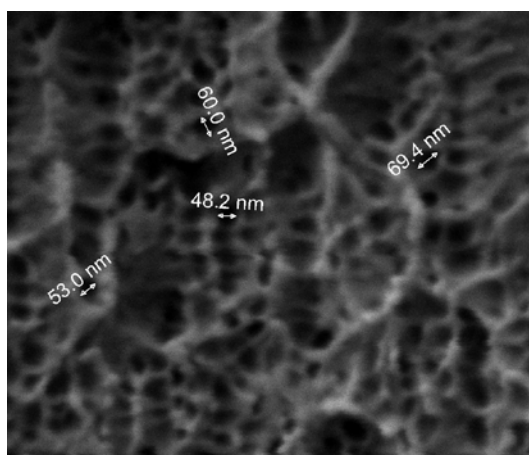


**Figure 0.2: Typical cellular structure of a PMMA/MAM nanocellular foam**

Fabrication of thin film nanocellular polymeric materials was often carried out from nanostructured polymers by pattern-transfer techniques [16, 79-81] or by the selective removal of one of the blocks in nanostructured block neat copolymers. This route was been employed generally in high- $T_g$  polymers/co-polymers by thermal degradation of one part of the polymer/co-polymer or in co-polymers by the use of organic solvents to remove one of the co-polymer phases [16, 80-87]. The traditional foaming chemical process (using chemical blowing agents, CBA) is not suitable to our knowledge to provide nanofoams.

Another promising technique used to produce polymeric foams is gas dissolution foaming process and in particular the high-pressure or supercritical  $\text{CO}_2$  gas dissolution foaming, where  $\text{CO}_2$  is used as a physical blowing agent [81, 88-90]. Also, this gas is one of the best options for this kind of process because of its excellent characteristics of diffusion in the supercritical state, and the relatively mild conditions to reach this state ( $31^\circ\text{C}$  and  $7.3\text{ MPa}$ ). Last but not least, carbon dioxide is a *green* solvent that can be removed without residue or production of any pollutant compound [91, 92].

### 0.3.2 Gas dissolution foaming process

Gas dissolution foaming consists of the following steps (Figure 0.3) [93]:

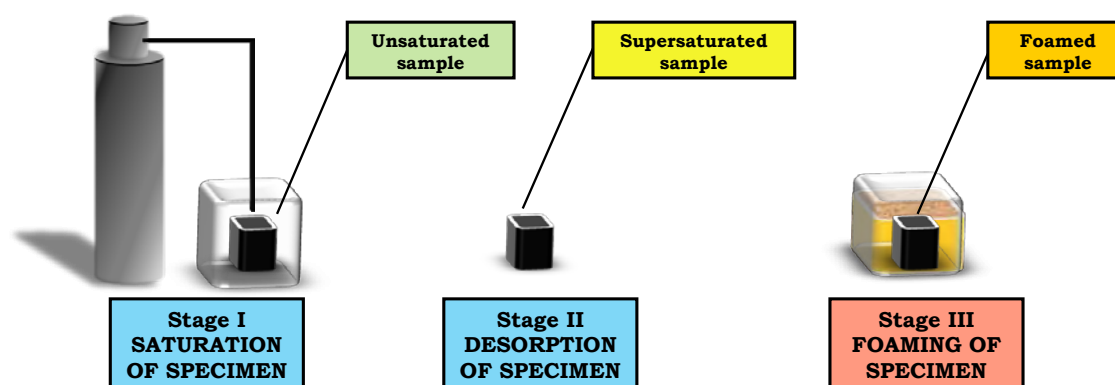


Figure 0.3: Gas dissolution foaming process scheme

- Stage I. Saturation Stage: a polymer is introduced into a pressure vessel under a controlled gas pressure and temperature. During this stage the gas diffuses into the polymer, occupying the gas molecules the free space between the polymer chains [94, 95]. This stage usually ends when the polymer sample is completely saturated (i.e. it reaches the maximum amount of gas that can absorb at the pressure and temperature under study).
- Stage II. Desorption Stage: gas pressure is released, then the sample enters into a supersaturated state. The polymer starts to release the excess of gas, either by diffusion to the outside or by the

formation of discontinuities/voids inside the matrix. These voids will act as nuclei for the cells formation [96, 97].

- Stage III. Foaming Stage: when the saturated sample reaches a temperature over or close to its glass transition temperature ( $T_g$ ) the nuclei previously formed can grow into cells. Cell growing is promoted by the pressure difference between the gas inside the sample and the external pressure. As a consequence of the increment of the cell size the sample presents a macroscopic expansion and, consequently, a density reduction. Final cell size is controlled by the magnitude of the pressure inside the sample, and the viscoelastic properties of the polymeric matrix at the foaming temperature (depending on these properties the polymer will show more or less opposition to the cell growth). Other factor that can influence the final cell size is the phenomena of coalescence, whereby several cells can collapse into one single cell [98].

Furthermore, the plasticization effect of the  $\text{CO}_2$  on amorphous polymers decreases the effective value of the glass transition temperature ( $T_{g,ef}$ ) [99-101]. The relationships between this effective glass transition temperature and the temperature of the saturation stage allows differentiating two main gas types of processes.

On one hand, when the saturation temperature is higher than the effective glass transition temperature of the polymer (i.e. the polymer is in the rubbery state at the end of the saturation stage) the foaming occurs during the pressure release, being the foaming triggered by the pressure difference. This process is called *one-step* or *batch foaming* [66, 89]. In this foaming process the desorption stage disappears, then, after the pressure release the cell nucleation and growth processes take place immediately one after another.

On the other hand, at saturation temperatures lower than the effective glass transition temperature of the polymer (i.e. the polymer is in the glassy state at the end of the saturation stage) the foaming process will be triggered in a second stage by heating the sample over its  $T_{g,ef}$ . This process is usually called *two-step* or *solid state foaming* [72].

Development of polymer nanocellular foams by gas dissolution foaming requires reaching very high cell nucleation densities ( $N_o$ , number of nuclei/cells per cubic centimeter of the unfoamed material) and reduced coalescence.

Coalescence can be avoided, or maintained without significant influence, by an appropriate selection of the polymer matrix and selection of the foaming temperature in comparison with the effective glass transition temperature.

Main difficulty of foaming processes to produce nanocellular structures resides in the thermodynamics of the polymer-gas systems. Formation of nanometric cells leads to a huge increment of the interfacial

(surface) area and the interfacial (surface) free energy. Moreover, the nucleation mechanisms of the cells are also governed by thermodynamics; in gas dissolution foaming processes the abrupt modification of the process parameters (pressure or temperature) reduces the gas solubility into the polymer, inducing gas phase segregation and a new disposal of the gas into cells that will tend to reduce the free energy of the foaming systems. After the nucleation process, each nucleus should overcome an energy barrier to become into a cell (Gibbs free energy barrier). This energy barrier on homogeneous polymers (i.e. one phase polymers without particles or impurities) depends on the surface tension of the polymer matrix in the presence of  $\text{CO}_2$  and the pressure difference between the bubble and the bulk (related to the  $\text{CO}_2$  concentration); whereas in heterogeneous polymers (i.e. several phases or with particles or impurities) the dispersed particles or phases can provide potential nucleation sites with lower energy barrier than the surrounding polymeric matrix (more details about cell nucleation mechanisms can be found in the articles included in Chapter III).

### 0.3.3 Nanocellular polymer foams produced by $\text{CO}_2$ gas dissolution foaming

Several approaches were used to promote the cells nucleation up to the desired levels (typically higher than  $10^{14}$ - $10^{15}$  nuclei/ $\text{cm}^3$ ) using  $\text{CO}_2$  gas dissolution foaming processes, depending on the nucleation mechanisms involved.

On **homogeneous materials** (i.e. systems with a homogeneous nucleation) there are two approaches to promote the nucleation (Figure 0.4) by varying the processing parameters [89, 96, 102]. Saturation pressure controls the amount of gas molecules dissolved into the polymer sample, being directly related to the  $\text{CO}_2$  uptake. Increasing the amount of gas molecules into the polymer will enhance the probability of aggregation between molecules to produce a nucleus/bubble, and consequently, the nucleation density. Therefore, a higher nucleation ratio can be promoted by increasing the saturation pressure.

The other processing parameter that can enhance the nucleation is the pressure drop rate during the pressure release. Higher pressure drop rates produce higher thermodynamic instability, and therefore a higher probability of nuclei formation.

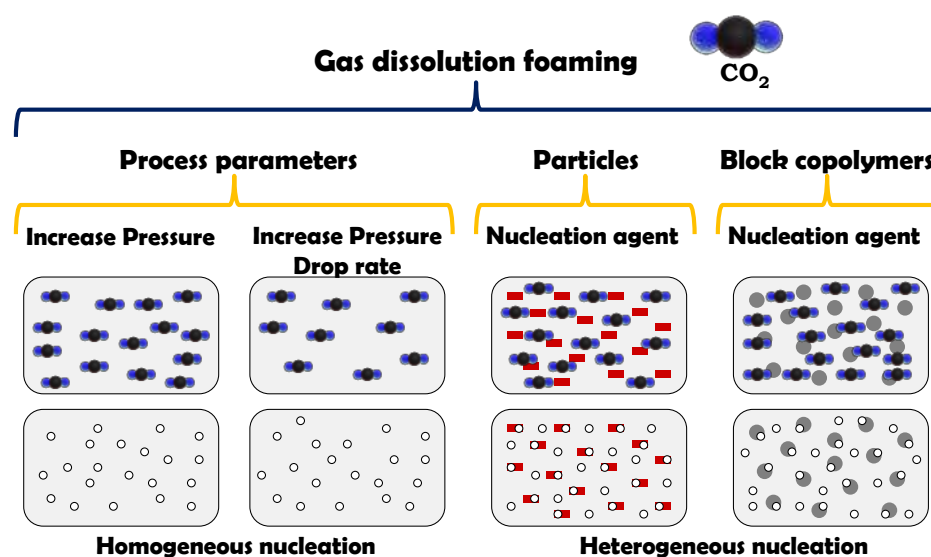


**Figure 0.4: Methods to enhance the cell nucleation in gas dissolution foaming processes**

Some nanocellular polymer foams have been produced following these approaches from homogeneous polymers thin films, obtaining nanocellular foams with high relative densities ( $\rho_r > 0.4$ ).

Krause et al. [103, 104] obtained bicontinuous nanoporous structures from polyetherimide (PEI), polyethersulfone (PES), polyimide (PI), and PSU/PI blends (PSU, bisphenol A polysulfone) films with a saturation stage carried out at room temperature (RT) and about 5 MPa, quick pressure release and a foaming stage carried out at high temperatures (100-260°C). PEI allowed obtaining pore sizes about 50 nm and relative densities about 0.55; PES foams reached pore sizes about 30 nm and relative densities about 0.59; PI foams presented pore sizes on the order of 20-50 nm and relative densities about 0.65; finally, foaming of PSU/PI blends resulted in foams with pore size about 500 nm and relative densities between 0.5 and 0.65.

Miller et al. [105] found similar results with PEI from samples produced by compression molding and long saturation times at RT and 5 MPa. They obtained open cell foams with cell sizes with cell sizes between 30 and 120 nm and relative densities from 0.7 to 0.48, carrying out the foaming stage at temperatures from 145 to 180°C.

Nawaby et al. [106] study the retrograde behavior of amorphous acrylonitrile-butadiene-styrene copolymers (ABS) and syndiotactic poly(methyl methacrylate) (sPMMA); due to this particular behavior they produced nanocellular foams from these materials at saturation temperatures of 0°C and saturation pressure of 3.4 MPa. ABS foamed at 60°C (after the pressure release) presented a cell size about 470 nm and a relative density of 0.74; whereas PMMA foamed at 90°C (after the pressure release) presented a cell size about 800 nm and a relative density of 0.2.



Janani et al. [107] designed a specific high-pressure system able to produce an instantaneous pressure release (about 300 MPa/sec) and quench the sample just after the pressure release in order to preserve the cellular structure induced by the pressure release (avoiding coalescence). Using this system they produced foams from polystyrene (PS) in a temperature range of 90-180° C and pressure of 25 MPa, obtaining cell sizes near to the nanometric range (between 500 nm and 1  $\mu$ m) and relative densities about 0.5.

**Heterogeneous materials** (i.e. systems in which a heterogeneous nucleation takes place) offer other two main approaches to increase the nucleation independently of the processing parameters.

On the one hand, addition of particles to the polymer (such as talc, titanium oxide, kaolin, nanosilica, and other nanoparticles) can increase the nucleation ratio. Particles should be well dispersed to increase the potential nucleation sites (individual particles volumetric density should be of the same order, or higher, than the desired nucleation density). Also, size of the individual particles is a main issue, they should present a size of the same order of magnitude, or higher, than the critical nucleation radius of the polymer-CO<sub>2</sub> system [108].

Siripurapu et al. [109] obtained nanocellular PMMA foamed films with cell sizes about 400 nm and high relative densities (about 0.98) by the addition of nanosilica particles (mean diameter 10-12 nm) using CO<sub>2</sub> saturation pressures up to 34.5 MPa.

Fujimoto et al. [110] and Ema et al. [111] reduced the average cell size of polyactide-based foams up to 200 nm by the addition of nanoclays (montmorillonite (MMT)) with saturation pressures between 10 to 24 MPa. Relative density of the obtained nanocellular foams took values about 0.44.

Urbanczyk et al. [112] also added MMT to poly(styrene-co-acrylonitrile) (SAN) obtaining foams with cell sizes between the nanometric and micrometric scales at saturation pressures up to 30 MPa. They found that the addition of MMT allow decreasing the average cell size from values near 1  $\mu$ m to values below 500 nm, but at the same time the relative density of the foam is increased from 0.23 to 0.65. Moreover, they concluded that influence of the nanoclays on the nucleation process is small in comparison with the influence of the saturation parameters.

On the other hand, additional nucleation sites or interfaces to promote nucleation can be generated by heterogeneous polymer/polymer or polymer/block copolymer blends (either A-B diblock or A-B-A triblock copolymers) [113]. Well chosen block or random copolymers are readily miscible with their corresponding homopolymer, and can lead to the formation of nanostructures. Low contents of copolymer (< 15 wt%) can self-assemble into a large number of spherical micelles (up to 10<sup>13</sup>-10<sup>14</sup> micelles/cm<sup>3</sup>) that can act as nucleation sites. In addition, the use of CO<sub>2</sub>-philic blocks can increase the effectiveness of these

nanostructures as nucleating agents, becoming CO<sub>2</sub> reservoirs. The main difficulty of this approach lies in the selection and synthesis of the block copolymers.

Spitael et al. [108] found the first evidences about the influence of block copolymer micelles with a CO<sub>2</sub>-philic block as nucleation agent with block ends of polystyrene (PS) and polystyrene-block-poly(dimethylsiloxane) diblock copolymer (PS-*b*-PDMS); however, nucleation increment was not enough to produce nanocellular structures. They suggested that the influence of the block copolymer micelles on the nucleation can be enhanced by using block copolymers that produce micelle cores with higher CO<sub>2</sub>-philicity and lower surface tensions than the surrounding polymer matrix.

Siripurapu et al. [109] obtained microcellular foams with enhanced nucleation from films of blends of PMMA and PMMA-*b*-PDMS, and nanocellular foams with cell sizes between 100-300 nm and high relative densities about 0.98 from blends of PMMA and PMMA-*b*-PFOMA (poly(1,1-dihydroperfluorooctyl methacrylate)); both materials were foamed using a constrained gas dissolution foaming process, avoiding the gas diffusion through the films surface [114].

Yokoyama et al. [115] produced nanocellular foams with very high cell densities (i.e. 10<sup>16</sup> cells/cm<sup>3</sup>), cell sizes between 10-30 nm, and relative density of 0.5 from monoliths of polystyrene-block-poly(perfluorooctylethyl methacrylate) (PS-*b*-PFMA); they found that a quench of the films to 0° C before the pressure release and a slow pressure release rate are needed to obtain nanofoams from this copolymer. Li et al. [116, 117] followed the same procedure with thin and thick films of PS-*b*-PFMA to produce nanocellular foams at 10 MPa, obtaining cell sizes about 15-30 nm and relative densities about 0.8-0.9. Yokoyama and Sugiyama [118] extended this route to polystyrene-block-poly(perfluorooctylpropyloxy styrene) (PS-*b*-PFS), obtaining similar results as PS-*b*-PFMA. Research of Yokoyama's group with fluorinated block copolymers found that the nanostructured fluorinated CO<sub>2</sub>-philic domains acts as nucleation sites, with a nucleation efficiency significantly lower than one (i.e. cell density is significantly lower than the nanodomains density). The frozen PS matrix (due to the temperature quench before the pressure release) controls the cell size and avoids coalescence (without the temperature quench the nanocellular structure disappears), obtaining average cell sizes about 20 nm and high relative densities near 1.

Nemoto et al. [119, 120] produced foams with micrometric and nanometric cellular structures from blends of poly(propylene) (PP) and thermoplastics polystyrene elastomers (TPS, specifically hydrogenated polystyrene-block-polybutadiene-block-polystyrene rubber, and hydrogenated polystyrene-block-polyisoprene-block-polystyrene) or a propylene-block-ethylene copolymer (PER); best results were obtained in PP/TPS thin films saturated at 20 MPa, leading to cellular structures with an average cell size about 200-400 nm and relative densities about 0.75.

Otsuka et al. [121] produced nanocellular foams from blends of PS/PMMA; the morphology of PMMA is in a form of nanoscale nodules, acting as nucleants agent. At high pressure drop rates and low temperatures they obtain cellular structures with 40-50 nm of average diameter, cell density of  $8.5 \times 10^{14}$  cells/cm<sup>3</sup>, and therefore a relative density of 0.94.

Wang et al. [122] controlled the cell size of thin films of aromatic poly(aryl ether)s (PAE) by modifying the parameters of a two-step foaming process, obtaining nanoporous co-continuous structures (i.e. open cell) with short desorption stages (i.e. time between the saturation stage (at 20 MPa) and the foaming stage) in order to preserve high CO<sub>2</sub> concentration. They obtained pore sizes between 50 and 500 nm, and relative densities down to 0.4.

Finally, Nemoto et al. [123] produced nanocellular foams from immiscible blends of poly(ether ether ketone) and poly(ether imide) (PEEK/PEI). They found that cell nucleation and growth were highly controlled in the PEI domains, obtaining cell sizes about 100 nm but without a significant foam macroscopic expansion ratio.

### 0.3.4 Properties of nanocellular polymer foams

Although it is commonly expected that nanocellular polymer foams will present improved properties than conventional or microcellular foams, there is just little evidence that this may be true. Main limitation to characterize several properties of nanocellular foams is the production of sufficiently large samples that can be subjected to standard test protocols.

Miller and Kumar [77] compared the mechanical properties of microcellular (cells in 2-5  $\mu$ m range) and nanocellular (cells in the 50-100 nm range) PEI foams produced by CO<sub>2</sub> gas dissolution foaming [105], in a range of relative densities comprised between 0.75 and 0.9. They found that nanofoams showed a significantly higher strain to failure, with an improvement of the modulus of toughness up to 350% compared to microcellular foams. Also, they found a brittle-to-ductile transition in nanofoams, resulting in better response under impact tests, with impact energies up to 600% higher than the microcellular foams. Moreover, they found an increment of the  $T_g$  of the polymer matrix, related to the confinement of the polymer chains inside the thick cell walls.

No evidences of improved thermal insulation behavior of nanocellular polymer foams can be found in the literature. However, this behavior has been proved on analogous structures. Schmidt et al. [78] measured the thermal conductivity of porous materials obtained by cross-linking reactions, templated either by microemulsions and colloidal particles. These porous materials present open cell structure with cell sizes about 100-200 nm and relative densities lower than 0.15. Contribution of the gaseous phase was found

lower in nanocellular materials than in microcellular ones, due to the Knudsen effect [124], resulting in a lower total thermal conductivity for nanocellular materials.

Finally, it has been speculated that nanofoams produced from amorphous polymers with a well-defined cell structure with cell sizes under the wavelength of the visible radiation could be transparent. In fact, there are strong evidences about this behavior on aerogels; however, production of aerogels with high transparency requires pore/particle sizes of the order of the tenth of the light wavelength (i.e. below 40 nm) and extremely low relative densities (typically below  $0.05 \text{ g/cm}^3$ ). These requirements are far away from the actual status on the production of nanofoams, and therefore the production of transparent nanofoams will be extremely difficult [125].

### 0.4 Objectives

This work aims at studying the production and foaming mechanisms of nanocellular polymer foams from blends of PMMA and MAM. This polymer/co-polymer system was not systematically studied before as a foam precursor, and therefore a complete and novel study about the foaming of the PMMA/MAM system has been carried out. Traditionally, there are four main topics on the study of a new cellular material: its production route, its cellular structure, its properties and its potential applications. These topics are strongly interrelated, as the materials tetrahedron of Figure 0.5 shows.

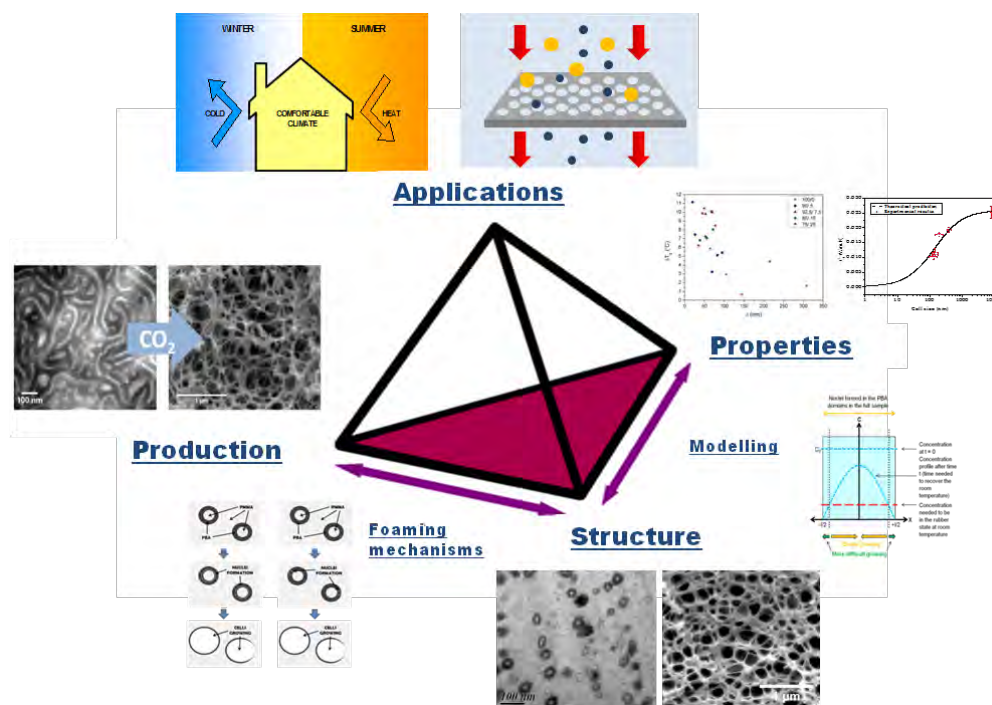


**Figure 0.5: Tetrahedron of research areas and their relationships for foamed materials**

Our research has been focused on the base of the tetrahedron, trying to produce valuable scientific knowledge about these materials that could allow finding applications. Then, the three main scientific and technical objectives are as follows:

1. To overcome some of the main disadvantages or limitations of the current production strategies used to produce nanocellular polymer foams (“Production”).
2. To provide a better understanding of the foaming mechanisms involved in the production of nanocellular foams and to analyze the cellular structure of the produced materials and its relation with the morphology of the precursors used for foaming and the production parameters (“Production  $\Leftrightarrow$  Structure”).
3. To study the property transition between microcellular and nanocellular foams (“Properties”).

Although the main objectives of this research have been focused on these three areas, some potential applications of these nanocellular foams and the generated knowledge are discussed in the journal articles included in the following chapters.

Some partial objectives have been defined inside each of the main objectives to define precisely the scope and extent of each of them.

From the production and technical point of view, we aim at obtaining nanocellular foams with the following requisites:

- Raw polymers should be easily accessible, without a very complex synthesis and preferably being commercial polymers.
- Solid blends should show a self-assembly nanostructuration.
- Production routes should be industrially scalable, avoiding requirements as exceptionally high saturation pressures, extremely high pressure release rates, quenching of the sample before/after pressure release, etc.
- Significant density reduction (over 50%) should be obtained keeping the nanocellular structure.

From the scientific point of view, about the foaming mechanisms the work has been focused on answering the following questions:

- Is the nucleation process homogeneous or heterogeneous? (Or a combination of both mechanisms). Can these mechanisms be identified and decoupled?
- Is the nanostructure of solid blends related to the cellular structure of foams?
- What is the role of the soft-block of the MAM copolymer in the nucleation and cell growth processes?
- What is the role of the PMMA matrix in the nucleation and cell growth processes?
- What is the influence of the MAM amount and morphology on PMMA/MAM foams?
- What is the influence of the processing parameters (saturation CO<sub>2</sub> pressure and temperature) on PMMA/MAM foams?

And finally, we have focused part of the research on determining the influence of the reduction of the cellular size from the micrometric to the nanometric range on the following properties:

- Thermal conductivity: It is expected that a significant decrease of the thermal conductivity of the gaseous phase when the pore size falls in the nanometric range, due to an effect known as Knudsen Effect [124].
- Glass transition temperature of the polymer matrix: Glass transition temperature of thin films can increase due to the confinement of the polymer chains [126]. Nanocellular foams can present a similar effect due to the low thickness of their cell walls and edges.
- Young's modulus: In microcellular PMMA foams, enhancement of the mechanical properties with the reduction of the cell size has been described [127]. Also, it is expected that nanocellular foams can present better mechanical properties than microcellular foams [78].

### 0.5 Structure of this thesis

The research presented on this thesis has been done in the frame of a co-tutelle agreement between two universities from different countries. Also this thesis is presented to obtain the degree of *Doctor in Philosophy (Ph. D.)* with an *International Mention*. Then, for both reasons the main body of the thesis is

written in English. In addition, according to the specific regulations of the co-tutelle agreement a summary of the thesis is included, both in French and Spanish.

This thesis is written as a *compendium of publications*. Six regular papers sent to international journals (one of them still pending for acceptance) and one proceeding from an oral communication in an international conference have been included. In addition, some unpublished results have been included in several chapters in order to provide a better understanding of the work and reach the objectives previously defined. Table 0-1 summarizes the papers included in this thesis, with their enclosing chapter in the right column.

Other peer-reviewed publications, contributions to international conferences (related to the thesis and on other topics), research stages in other institutions, and participation in research projects during the last four years (out of the direct scope of PMMA blends) are summarized in tables 0-2, 0-3, 0-4, 0-5 and 0-6 respectively.

The manuscript is divided into six chapters including the following information:

Chapter 1 introduces the experimental techniques used in this work. Standard techniques are enumerated, while non-usual techniques (some of them developed or adapted for this research) are further described.

Chapter 2 describes the raw polymers, PMMA and MAM, and the production route of PMMA/MAM solid blends and foams. Nanostructuration of PMMA/MAM solid blends (morphologies) and cellular structure of the obtained foams are studied and described in this chapter.

Chapter 3 defines the relationships between the nanostructuration of PMMA/MAM solid precursors and the cellular structure of foams obtained by CO<sub>2</sub> gas dissolution foaming. In addition, the influence of the *saturation pressure and MAM amount* on the final cellular structure and *nucleation process* are discussed. From these previous relationships nucleation and cell growth mechanisms are described for these materials.

Chapter 4 provides information about the role of the *saturation temperature* and the *post-foaming temperature* in the foaming process of PMMA/MAM blends. The boundary between a one-step and a modified two-step foaming processes are determined, and a description of both foaming processes taking into account the nucleation mechanism of PMMA/MAM foams is proposed.

Chapter 5 studies the properties of the nanocellular foams compared to the properties of microcellular foams. This chapter is divided in three sections, corresponding to the study of the thermal conductivity, the study of the glass transition temperature and the study of the Young's modulus.

Last chapter collects the main conclusions of this work, and includes several research topics for future research.

To provide a better understanding of the thesis structure a schematic view can be found in Figure 0.6.

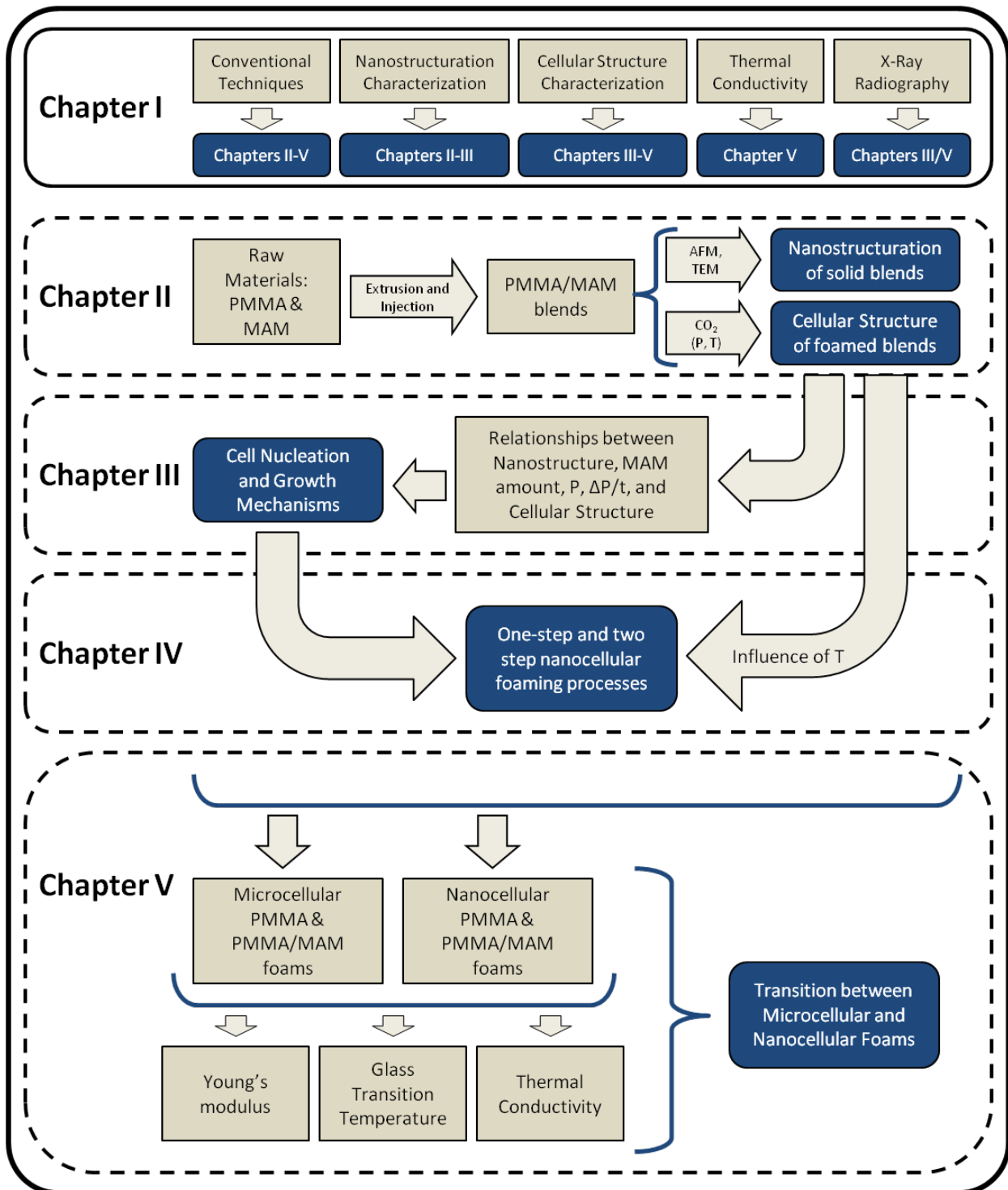


Figure 0.6: Scheme of the thesis structure



**Table 0-1: Publications in international journals included in this dissertation; the Ph.D is main author or main participant.**

Publications submitted to international journals	Chapter
J. A. Reglero, M. Dumon, J. Pinto, M. A. Rodriguez-Perez <b>Low Density Nanocellular Foams Produced by High-Pressure Carbon Dioxide</b> <i>Macromolecular Materials and Engineering</i> 296, 752-759 (2011)	V
J. Pinto, S. Pardo-Alonso, E. Solórzano, M. A. Rodriguez-Perez, M. Dumon, J. A. de Saja <b>Solid Skin Characterization of PMMA/MAM Foams Fabricated by Gas Dissolution Foaming over a Range of Pressures</b> <i>Defect and Diffusion Forum vols. 326-328, 434-439 (2012)</i>	III
J. Pinto, E. Solórzano, M. A. Rodriguez-Perez, J. A. de Saja <b>Characterization of Cellular Structure Based on User-Interactive Image Analysis Procedures</b> <i>Journal of Cellular Plastics</i> 49, 6, 554-574 (2013)	I
J. Pinto, M. Dumon, M. Pedros, J. Reglero, M. A. Rodriguez-Perez <b>Nanocellular CO<sub>2</sub> foaming of PMMA assisted by block copolymer nanostructuration</b> <i>Chemical Engineering Journal</i> 243C, 428-435 (2014)	III
J. Pinto, M. Dumon, M. A. Rodriguez-Perez, R. García, C. Dietz <b>Block Copolymers Self-Assembly Allows Obtaining Tunable Micro or Nanoporous Membranes or Depth Filters Based on PMMA; Fabrication Method and Nanostructures</b> <i>The Journal of Physical Chemistry C</i> 118, 9, 4656-4663 (2014)	III
J. Pinto, J. Reglero-Ruiz, M. Dumon, M. A. Rodriguez-Perez <b>Temperature Influence and CO<sub>2</sub> Transport in Foaming Processes of Poly(methyl methacrylate)-Block Copolymer Nanocellular and Microcellular Foams</b> <i>Journal of Supercritical Fluids</i> (acceptance pending)	IV

**Table 0-2: Other publications in international journals; the Ph.D is coauthor.**

Other publications submitted to international journals
M. Dumon, J. A. Reglero-Ruiz, J. Pinto, M. A. Rodriguez-Perez, J. M. Tallon, M. Pedros, P. Viot <b>Block Copolymer-Assisted Microcellular Supercritical CO<sub>2</sub> Foaming of Polymers and Blends</b> <i>Cellular Polymers 31, 207-222 (2012)</i>
E. Solórzano, J. Pinto, S. Pardo-Alonso, F. García-Moreno, M. A. Rodriguez-Perez <b>Application of a Microfocus X-Ray Imaging Apparatus to the Study of Cellular Polymers</b> <i>Polymer Testing 32, 321-329 (2012)</i>
B. Notario, J. Pinto, E. Solórzano, J. Escudero, J. Martín de León, D. Velasco, M. A. Rodriguez-Perez <b>In-Situ Optical Analysis of Structural Changes in Polyactic Acid (PLA) during Gas Dissolution Process</b> <i>Defect and Diffusion Forum (accepted, pending publication)</i>

**Table 0-3: Communications in international conferences related to the thesis work**

Communications presented in international conferences related to the thesis
<p>J. Pinto, M. A. Rodriguez-Perez, J. A. de Saja</p> <p><b>Development of an Image J Macro to Characterize the Cellular Structure of Polymeric Foams</b></p> <p><b>Poster.</b> <i>XI Reunión del Grupo Especializado de Polímeros (GEP), Valladolid (Spain) (2009)</i></p>
<p>J. Pinto, S. Pardo, E. Solórzano, M. A. Rodriguez-Perez, M. Dumon, J. A. de Saja</p> <p><b>Solid Skin Characterization of PMMA/MAM Foams Fabricated by Gas Dissolution Foaming over a Range of Pressures</b></p> <p><b>Oral.</b> <i>DSL 2011, Algarve (Portugal) (2011)</i></p>
<p>J. Pinto, M. A. Rodriguez-Perez, J. A. de Saja, M. Dumon, R. García, C. Dietz</p> <p><b>Relationship Between the Nano-Structured Morphology of PMMA/MAM Blends and the Nanocellular Structure of Foams Produced from these Materials</b></p> <p><b>Oral.</b> <i>FOAMS 2011, Iselin (New Jersey, USA) (2011)</i></p>
<p>M. A. Rodriguez-Perez, J. Pinto, M. Dumon</p> <p><b>From Micro to Nanocellular Polymeric Materials</b></p> <p><b>Invited Lecture.</b> <i>PPS Conference, Niagara Falls (Canada) (2012)</i></p>
<p>J. Pinto, E. Solórzano, M. A. Rodriguez-Perez, J. A. de Saja, M. Dumon</p> <p><b>Thermal Conductivity Transition between Microcellular and Nanocellular Polymeric Foams: Experimental Validation of the Knudsen Effect</b></p> <p><b>Oral.</b> <i>FOAMS 2012, Barcelona (Spain) (2012)</i></p>
<p>M. A. Rodriguez-Perez, J. Pinto, J. Escudero, A. Lopez-Gil, E. Solórzano, C. Saiz-Arroyo, S. Estravís, S. Pardo-Alonso</p> <p><b>Nano-strategies applied to the production of cellular polymers with improved cellular structure and properties</b></p> <p><b>Keynote Lecture.</b> <i>CellMat Conference, Dresden (Germany) (2012)</i></p>
<p>J. Pinto, M. Dumon, M. A. Rodriguez-Perez</p> <p><b>Development of Nanocellular Foams by Gas Physical Foaming</b></p> <p><b>Poster.</b> <i>FOAMS 2013, Seattle (USA) (2013)</i></p>
<p>J. Pinto, E. Solórzano, M. A. Rodriguez-Perez, M. Dumon</p> <p><b>Nanocellular Foams Fabrication Assisted by Nanostructuration Pattern: Understanding the Heterogeneous Nucleation Mechanism</b></p> <p><b>Oral.</b> <i>FOAMS 2013, Seattle (USA) (2013)</i></p>

Table 0-4: Other communications in international conferences

Other communications presented in international conferences	
J. Escudero, J. Pinto, E. Solórzano, M. A. Rodríguez-Perez, J. A. de Saja	
<b>Structural Foams vs. Conventional Foams: Structural Characterization and Mechanical Behavior</b>	
<b>Oral.</b> <i>XI Reunión del Grupo Especializado de Polímeros (GEP), Valladolid (Spain) (2009)</i>	
M. A. Martínez, J. Abenojar, M. A. Rodríguez-Perez, J. Pinto, S. Estravis, J. Ecenero, E. Aldanondo, P. Álvarez	
<b>Unión de Espumas de Poliolefina y Poliuretano al Aluminio: Ensayos de Adhesión y su Modelización</b>	
<b>Poster.</b> <i>X Congreso de Adhesión y Adhesivos, Alicante (Spain) (2009)</i>	
P. Álvarez, A. Echeverría, M. M. Petite, M. A. Rodríguez-Perez, J. Pinto, S. Estravis, M. A. Martínez, J. Abenojar	
<b>Fabricación, Caracterización y Modelización de Paneles Sándwich Compuestos por Cores de Espumas de Polietileno y Poliuretano y Pieles de Aluminio</b>	
<b>Poster.</b> <i>Comatcomp 09, San Sebastian (Spain) (2009)</i>	
E. Solórzano, M. A. Rodríguez-Perez, J. Pinto, F. García-Moreno, J. A. de Saja	
<b>A Novel Procedure to in-situ Analyze the Foamability of Thermoplastic Foams using Optical Expandometry and X-Ray Radioscopy</b>	
<b>Oral.</b> <i>Blowing Agents 2010, Köln (Germany) (2010)</i>	
E. Solórzano, J. Escudero, J. Pinto, J. A. de Saja, M. A. Rodríguez-Perez	
<b>Gas Diffusion and Other Physical Mechanisms Involved in the Production of Structural Foams</b>	
<b>Oral.</b> <i>DSL 2010, Paris (France) (2010)</i>	
M. A. Rodríguez-Perez, E. Solórzano, J. Pinto, J. A. de Saja	
<b>A Novel Method to Analyze the Foamability of Polymer Systems using in-situ Optical Expandometry and X-Ray Radioscopy</b>	
<b>Oral.</b> <i>FOAMS 2011, Seattle (USA) (2010)</i>	
E. Solórzano, J. Pinto, F. García-Moreno, M. A. Rodríguez-Perez	
<b>ImageJ: Multifunctional Analysis in Materials Science</b>	
<b>Oral.</b> <i>ImageJ User and Developer Conference, Mondor les Bains (Luxembourg) (2010)</i>	
M. Dumon, J. A. Reglero-Ruiz, J. M. Tallon, M. Pedros, E. Cloutet, J. Pinto, P. Viot	
<b>Behavior of block copolymers in supercritical CO<sub>2</sub> and microcellular foaming of polymer blends</b>	
<b>Oral</b> <i>DSL 2011, Algarve (Portugal) (2011)</i>	

E. Solórzano, J. Pinto, S. Pardo, M. A. Rodriguez-Perez, J. A. de Saja

**X-Ray Radioscopy In-Situ Monitoring of Diffusion Mechanism Occurring during the Production of Structural Foams by Free Foaming**

**Oral.** *DSL 2011, Algarve (Portugal) (2011)*

E. Solórzano, J. Escudero, J. Pinto, M. A. Rodriguez-Perez, J. A. de Saja

**Evolution of Polymers during the Gas Dissolution Process**

**Oral.** *DSL 2011, Algarve (Portugal) (2011)*

M. A. Rodriguez-Perez, J. Escudero, J. Pinto E. Solórzano

**Production of Structural Foams using Free Foaming. In-situ Analysis of the Foaming Process**

**Oral.** *FOAMS 2011, Iselin (New Jersey, USA) (2011)*

M. Dumon, J. A. Reglero-Ruiz, E. Cloutet, J. Pinto, M. A. Rodriguez-Perez, P. Viot

**Block copolymer-assisted microcellular supercritical CO<sub>2</sub> foaming of polymers and blends**

**Oral.** *Blowing Agents and Foaming Processes, Berlin (Germany) (2012)*

E. Solórzano, S. Pardo-Alonso, J. Pinto, M. A. Rodriguez-Perez

**Polymer Foaming Processes and Related Physics: Monitorization by X-Ray Radioscopy**

**Oral.** *FOAMS 2012, Barcelona (Spain) (2012)*

M. Dumon, P. Viot, J. A. Reglero-Ruiz, L. Maheo, G. Ciclia, O. Mondain Monvai, V. Schmitt, A. Chirazi, J. Pinto, M. A. Rodriguez-Perez

**Fabrication of Calibrated Micro-Foams, Structures and Mechanical Properties**

**Oral.** *FOAMS 2012, Barcelona (Spain) (2012)*

B. Notario, J. Pinto, E. Solórzano, J. Escudero, J. Martín-de León, D. Velasco, M. A. Rodriguez-Perez

**In-Situ Optical Analysis of Structural Changes in Amorphous Polymers during the Gas Dissolution Process**

**Oral.** *DSL 2013, Madrid (Spain) (2013)*

**Table 0-5: Stages in other research institutions**

<b>Stages in other research institutions</b>
Two weeks in the Instituto de Microelectrónica (CSIC) of Madrid (Spain) in 2009 <b>Topic: Training on Atomic Force Microscopy (AFM)</b>
One week in the Technical University of Berlin (Germany) in 2010 <b>Topic: Training on Image Analysis Techniques</b>
Three months in the Microcellular Plastics Laboratory (Mechanical Engineering Department) of the University of Washington (USA) in 2011 <b>Topic: Production of cellular materials based on HDPE and x-HDPE by CO<sub>2</sub> solid state foaming</b>

**Table 0-6: Participation to other research funded projects in the course of the 4 years**

<b>Research funded projects</b>
FP7 European Commission. <b>NANCORE 214148</b>
European Spatial Agency. <b>MAP AO-99-075</b>
Ministerio de Ciencia e Innovación (National Materials Program). <b>MAT2009-14001-C02-01</b>
Ministerio de Ciencia e Innovación (National Materials Program). <b>MAT2012-34901</b>
Junta of Castile and Leon. <b>VA174A12-2</b>
Junta of Castile and Leon. <b>VA035U13</b>

## 0.6 Advantages of amorphous structured blends for nanofoams

To conclude this introduction the major novelties or advantages of amorphous structured blends for the production of nanofoams introduced by this work over the literature are pointing out:

- The initial precursor materials for the production of nanocellular foams are commercial, easily accessible and well defined polymers.
- PMMA/MAM blends present a well-defined nanostructuration after extrusion/injection processes (industrially scalable processes).

- Two different morphologies of nanocellular foams (open and closed structures), are obtained in a controlled way by adjusting the amount of block copolymer from the same PMMA/MAM system.
- Nanocellular foams have been obtained from bulk samples of several millimeters of thickness with saturation times of 24 hours.
- Nanocellular polymer foams with significant density reduction have been produced (relative densities from 0.4 to 0.6).
- Nanocellular foams have been produced with medium-high, but not extremely high saturation pressures and pressure release rates, and without quenching of the polymer before/after the depressurization.
- Cells nucleation process is completely heterogeneous, being controlled by the soft and CO<sub>2</sub>-philic block of the PMMA/MAM blends. Nucleation efficiency (ratio between the number of cell nuclei and the number of dispersed nanostructured) is close to one.
- Cells growth process is completely controlled by the plasticization of the PMMA matrix, being able to avoid the coalescence phenomena with an appropriate selection of the processing conditions.
- As a consequence of the two previous statements, nanocellular foams from PMMA/MAM can be produced in a wide range of saturation pressures, from 10 to 30 MPa.
- A clear transition between the micro and nanocellular foams have been found on the thermal conductivity and glass transition temperature of PMMA/MAM foams.

## 0.7 References

1. Moore, G.E., *Cramming more components onto integrated circuits*. Electronics, 1965. **38**(8): 114-117.
2. Carlson, R., *The Proliferation of Biological Technologies*. Biosecurity and Bioterrorism: Biodefense Strategy, Practice, and Science, 2003. **1**(3): 203-214.
3. EU, E.U. *Horizon 2020. Work Programme 2014 -2015*. 2013; Available from: [http://ec.europa.eu/research/participants/data/ref/h2020/wp/2014\\_2015/main/h2020-wp1415-leit-nmp\\_en.pdf](http://ec.europa.eu/research/participants/data/ref/h2020/wp/2014_2015/main/h2020-wp1415-leit-nmp_en.pdf).
4. Gibson, L.J. and M.F. Ashby, *Cellular Solids: Structure and Properties*. 2nd ed 1997, Cambridge: Cambridge University Press.
5. Gibson, L.J., M.F. Ashby, and B.A. Harley, *Cellular Materials in Nature and Medicine* 2010, Cambridge, U.K.: Cambridge University Press.
6. Weaire, D. and S. Hutzler, *The Physics of Foams* 1999, Oxford, U.K.: Oxford University Press.
7. Davies, G.J. and S. Zhen, *Metallic foams: their production, properties and applications*. Journal of Materials Science, 1983. **18**(7): 1899-1911.
8. Klempner, D., V. Sendjarević, and R.M. Aseeva, *Handbook of Polymeric Foams and Foam Technology* 2004, Munich: Hanser Publishers. 612.
9. Eaves, D., *Handbook of Polymer Foams* 2004: Rapra Technology. 189-193.
10. Bhaduri, S.B., *Science and technology of ceramic foams*. Advanced Performance Materials, 1994. **1**(3): 205-220.
11. Solórzano, E. and M.A. Rodríguez-Perez, *Polymer Foams*, in *Structural Materials and Processes in Transportation*, M. Busse, A.S. Herrmann, K. Kayvantash, and D. Lehmhus, Editors. 2013, Wiley-VCH: Weinheim (Germany).
12. Papadopoulos, A.M., *State of the art in thermal insulation materials and aims for future developments*. Energy and Buildings, 2005. **37**(1): 77-86.
13. Díez-Gutiérrez, S., M.A. Rodríguez-Perez, M. Machimbarranea, J. González, and J.A. De Saja, *Technical Note. Impact Sound Reduction of Crosslinked and non-Crosslinked Polyethylene Foams in Suspended Concrete Floor Structures*. Journal of Building and Acoustics, 2003. **10**(3): 261-271.
14. Ghosh, S., V. Gutierrez, C. Fernández, M.A. Rodríguez-Perez, J.C. Viana, R.L. Reis, and J.F. Mano, *Dynamic mechanical behavior of starch-based scaffolds in dry and physiologically simulated conditions: effect of porosity and pore size*. Acta biomaterialia, 2008. **4**(4): 950-959.
15. Prabakaran, M., M.A. Rodríguez-Perez, J.A. de Saja, and J.F. Mano, *Preparation and characterization of poly(L-lactic acid)-chitosan hybrid scaffolds with drug release capability*. Journal of biomedical materials research. Part B, Applied biomaterials, 2007. **81**(2): 427-434.
16. Hentze, H.P. and M. Antonietti, *Porous polymers and resins for biotechnological and biomedical applications*. Reviews in molecular biotechnology, 2002. **90**(1): 27-53.
17. Ulbricht, M., *Advanced functional polymer membranes*. Polymer, 2006. **47**(7): 2217-2262.



18. Twigg, M.V. and J.T. Richardson, *Theory and Applications of Ceramic Foam Catalysts*. Chemical Engineering Research and Design, 2002. **80**(2): 183-189.
19. Rodriguez-Perez, M.A., *Propiedades Térmicas y Mecánicas de Espumas de Poliolefinas*, 1998, Universidad de Valladolid.
20. Almanza, O., *Caracterización y Modelización de las Propiedades Térmicas y Mecánicas en Espumas de Poliolefinas*, 2000, Universidad de Valladolid.
21. Arcos y Rabado, L.O., *Propiedades Térmicas y Mecánicas de Espumas de Poliolefinas Fabricadas en un Proceso de Moldeo por Compresión*, 2002, Universidad de Valladolid.
22. Ruiz-Herrero, J.L., *Impacto y Fluencia de Espumas con Base Polietileno*, 2004, Universidad de Valladolid.
23. González-Peña, J.I., *Efecto de los Tratamientos Térmicos en Bloques de Espuma de Polietileno de Baja Densidad Producidos Mediante Moldeo por Compresión*, 2006, Universidad de Valladolid.
24. Álvarez-Laínez, M., *Propiedades Térmicas, Mecánicas y Acústicas de Espumas de Poliolefina de Celda Abierta*, 2007, Universidad de Valladolid.
25. Reglero Ruiz, J.A., *Manufacture and characterization of aluminium foams: Applications in the aeronautical sector*, 2007, Universidad de Valladolid.
26. Solórzano, E., *Aluminium foams: Foaming process, cellular structure & properties*, 2008, Universidad de Valladolid.
27. Hidalgo-González, F., *Diseño Optimizado de los Parámetros de Proceso de Fabricación de Espuma de Poliolefina Reticulada mediante Moldeo por Compresión*, 2008, Universidad de Valladolid.
28. Román-Lorza, S., *Fabrication and characterization of flame retardant halogen free polyolefin based cellular materials*, 2010, Universidad de Valladolid.
29. Campo-Arnáiz, R., *Aplicación de Técnicas Espectroscópicas al Estudio de la Morfología Polimérica, Propiedades Térmicas y de Emisión de Espumas de Baja Densidad con Base Poliolefina*, 2011, Universidad de Valladolid.
30. Saiz-Arroyo, C., *Fabricación de materiales celulares mejorados basados en poliolefinas. Relación procesado-composición-estructura-propiedades*, 2012, Universidad de Valladolid.
31. Lobos Martín, J., *Improving the stiffness and strength of porous materials by enhancement of the matrix microstructure and cellular morphology*, 2013, Universidad de Valladolid.
32. Velasco, J.I., A.B. Martínez, D. Arencón, M.A.R. Pérez, and J.A.D. Saja, *Application of instrumented falling dart impact to the mechanical characterization of thermoplastic foams*. Journal of materials science, 1999. **34**(3): 431-438.
33. Rodriguez-Perez, M.A., J.L. Ruiz-Herrero, E. Solórzano, and J.A. De Saja, *Gas diffusion in polyolefin foams during creep tests. Effect on impact behaviour and recovery after creep*. Cellular polymers, 2006. **25**(4): 221-236.
34. Rodríguez-Pérez, M.A., A. Duijsens, and J.A. De Saja, *Effect of addition of EVA on the technical properties of extruded foam profiles of low-density polyethylene/EVA blends*. Journal of Applied Polymer Science, 1998. **68**(8): 1237-1244.

35. Rodríguez-Pérez, M. A., S. Díez-Gutiérrez, and J. A. De Saja, *The recovery behavior of crosslinked closed cell polyolefin foams*. Polymer Engineering & Science, 1998. **38**(5): 831-837.
36. Rodriguez-Perez, M.A. and J.A. De Saja, *The effect of blending on the physical properties of crosslinked closed cell polyethylene foams*. Cellular polymers, 1999. **18**(1): 1-20.
37. Rodríguez-Pérez, M.A., R.A. Campo-Arnáiz, R.F. Aroca, and J.A. de Saja, *Characterisation of the matrix polymer morphology of polyolefins foams by Raman spectroscopy*. Polymer, 2005. **46**(26): 12093-12102.
38. Rodriguez-Perez, M.A., M. Álvarez-Láinez, and J.A. de Saja, *Microstructure and physical properties of open-cell polyolefin foams*. Journal of Applied Polymer Science, 2009. **114**(2): 1176-1186.
39. Rodríguez-Pérez, M.A., O. Alonso, J. Souto, and J.A. de Saja, *Thermal conductivity of physically crosslinked closed cell polyolefin foams*. Polymer Testing, 1997. **16**(3): 287-298.
40. Rodriguez-Perez, M. A., O. Almanza, J. L. Ruiz-Herrero, and J.A. De Saja, *The Effect of Processing on the Structure and Properties of Crosslinked Closed Cell Polyethylene Foams*. Cellular polymers, 2008. **27**(3): 179-200.
41. Rodríguez-Pérez, M. A., O. Almanza, and J.A. De Saja, *Anomalous thickness increase in crosslinked closed cell polyolefin foams during heat treatments*. Journal of Applied Polymer Science, 1999. **73**(14): 2825-2835.
42. Mills, N. J. and M. A. Rodriguez-Perez, *Modelling the gas-loss creep mechanism in EVA foam from running shoes*. Cellular polymers, 2001. **20**(2): 79-100.
43. Alvarez-Lainez, M., M.A. Rodriguez-Perez, and J.A. De Saja, *Thermal conductivity of open-cell polyolefin foams*. Journal of Polymer Science Part B: Polymer Physics, 2008. **46**(2): 212-221.
44. Almanza, O., M.A. Rodríguez-Pérez, and J.A. de Saja, *The microstructure of polyethylene foams produced by a nitrogen solution process*. Polymer, 2001. **42**(16): 7117-7126.
45. Almanza, O., M.A. Rodríguez-Pérez, B. Chernev, J.A. de Saja, and P. Zipper, *Comparative study on the lamellar structure of polyethylene foams*. European Polymer Journal, 2005. **41**(3): 599-609.
46. Almanza, O., L. O. Arcos y Rábago, M. A. Rodríguez-Pérez, A. González, and J. A. de Saja, *Structure-Property Relationships in Polyolefin Foams*. Journal of Macromolecular Science, Part B, 2001. **40**(3-4): 603-613.
47. Rodriguez-Perez, M.A., J. Lobos, C.A. Perez-Muñoz, and J.A.d. Saja, *Mechanical Response of Polyethylene Foams with High Densities and Cell Sizes in the Microcellular Range*. Journal of Cellular Plastics, 2009. **45**(5): 389-403.
48. Rodríguez Pérez, M.Á., J. Lobos Martín, C. Pérez Muñoz, J.A.d. Saja Sáez, L.M. González Gutierrez, and M.A.d. Carpio, *Mechanical Behaviour at Low Strains of LDPE Foams with Cell Sizes in the Microcellular Range: Advantages of Using these Materials in Structural Elements*. Cellular polymers, 2008. **27**(6): 347-362.
49. Reglero Ruiz, J. A., C. Saiz-Arroyo, M. Dumon, M. A. Rodríguez-Perez, and L. González, *Production, cellular structure and thermal conductivity of microcellular (methyl methacrylate)-(butyl acrylate)-(methyl methacrylate) triblock copolymers*. Polymer international, 2011. **60**(1): 146-152.

50. Verdejo, R., C. Saiz-Arroyo, J. Carretero-Gonzalez, F. Barroso-Bujans, M.A. Rodriguez-Perez, and M.A. Lopez-Manchado, *Physical properties of silicone foams filled with carbon nanotubes and functionalized graphene sheets*. European Polymer Journal, 2008. **44**(9): 2790-2797.
51. Velasco, J.I., M. Antunes, O. Ayyad, C. Saiz-Arroyo, M.A. Rodríguez-Pérez, F. Hidalgo, and J.A. de Saja, *Foams based on low density polyethylene/hectorite nanocomposites: Thermal stability and thermo-mechanical properties*. Journal of Applied Polymer Science, 2007. **105**(3): 1658-1667.
52. Román-Lorza, S., M.A. Rodríguez-Perez, J.A.D.S. Sáez, and J. Zurro, *Cellular Structure of EVA/ATH Halogen-free Flame-retardant Foams*. Journal of Cellular Plastics, 2010. **46**(3): 259-279.
53. Ma, Y., R. Pyrz, M.A. Rodríguez-Perez, J. Escudero, J.C. Rauhe, and X. Su, *X-ray Microtomographic Study of Nanoclay-Polypropylene Foams*. Cellular polymers, 2011. **30**(3): 95-109.
54. Wang, Y., M.A. Rodríguez-Perez, R.L. Reis, and J.F. Mano, *Thermal and Thermomechanical Behaviour of Polycaprolactone and Starch/Polycaprolactone Blends for Biomedical Applications*. Macromolecular Materials and Engineering, 2005. **290**(8): 792-801.
55. Simoes, R.d., M.a. Rodriguez-Perez, J.a. De Saja, and C.j.l. Constantino, *Tailoring the structural properties of P(VDF) and P(VDF-TrFE) by using natural polymers as additives*. Polymer Engineering & Science, 2009. **49**(11): 2150-2157.
56. Rodriguez-Perez, M.a., R.d. Simoes, S. Roman-Lorza, M. Alvarez-Lainez, C. Montoya-Mesa, C.j.l. Constantino, and J.a. de Saja, *Foaming of EVA/starch blends: Characterization of the structure, physical properties, and biodegradability*. Polymer Engineering & Science, 2012. **52**(1): 62-70.
57. Solórzano, E., M.A. Rodríguez-Perez, J.A. Reglero, and J.A. de Saja, *Mechanical Behaviour of Internal Reinforced Aluminium Foams*. Advanced Engineering Materials, 2007. **9**(11): 955-958.
58. Solórzano, E., M.A. Rodríguez-Perez, and J.A. de Saja, *Thermal Conductivity of Cellular Metals Measured by the Transient Plane Source Method*. Advanced Engineering Materials, 2008. **10**(4): 371-377.
59. Lázaro, J., E. Solórzano, J.A.d. Saja, and M.A. Rodríguez-Pérez, *Early anisotropic expansion of aluminium foam precursors*. Journal of materials science, 2013. **48**(14): 5036-5046.
60. Garcia-Moreno, F., E. Solórzano, and J. Banhart, *Kinetics of coalescence in liquid aluminium foams*. Soft Matter, 2011. **7**(19): 9216-9223.
61. Solórzano, E., J. Pinto, S. Pardo, F. Garcia-Moreno, and M.A. Rodríguez-Perez, *Application of a microfocus X-ray imaging apparatus to the study of cellular polymers*. Polymer Testing, 2013. **32**(2): 321-329.
62. Solórzano, E., S. Pardo-Alonso, J.A.d. Saja, and M.A. Rodríguez-Perez, *X-ray radiography in-situ studies in thermoplastic polymer foams*. Colloids and Surfaces A: Physicochemical and Engineering Aspects, 2013. **438**: 167-173.
63. Solórzano, E., M. Antunes, C. Saiz-Arroyo, M.A. Rodríguez-Pérez, J.I. Velasco, and J.A. de Saja, *Optical expandometry: A technique to analyze the expansion kinetics of chemically blown thermoplastic foams*. Journal of Applied Polymer Science, 2012. **125**(2): 1059-1067.

64. Pardo-Alonso, S., E. Solórzano, L. Brabant, P. Vanderniepen, M. Dierick, L. Van Hoorebeke, and M.A. Rodríguez-Pérez, *3D Analysis of the progressive modification of the cellular architecture in polyurethane nanocomposite foams via X-ray microtomography*. European Polymer Journal, 2013. **49**(5): 999-1006.
65. Reglero Ruiz, J.A., P. Viot, and M. Dumon, *Foaming Behaviour and Compressive Properties of Microcellular Nanostructured Polystyrene*. Cellular polymers, 2009. **28**(6): 363-385.
66. Reglero Ruiz, J.A., P. Viot, and M. Dumon, *Microcellular foaming of polymethylmethacrylate in a batch supercritical CO<sub>2</sub> process: Effect of microstructure on compression behavior*. Journal of Applied Polymer Science, 2010. **118**(1): 320-331.
67. Ruiz, J.A.R., J. Marc-Tallon, M. Pedros, and M. Dumon, *Two-step microcellular foaming of amorphous polymers in supercritical CO<sub>2</sub>*. The Journal of Supercritical Fluids, 2011. **57**(1): 87-94.
68. Ruiz, J.A.R., M. Pedros, J.-M. Tallon, and M. Dumon, *Micro and nano cellular amorphous polymers (PMMA, PS) in supercritical CO<sub>2</sub> assisted by nanostructured CO<sub>2</sub>-philic block copolymers – One step foaming process*. The Journal of Supercritical Fluids, 2011. **58**(1): 168-176.
69. Reglero, J.A., P. Viot, and M. Dumon, *Foaming of amorphous polymers and blends in supercritical CO<sub>2</sub>: Solubility versus block copolymers addition*. Journal of Cellular Plastics, 2011. **47**(6): 535-548.
70. Martini-Vvedensky, J.E., N.P. Suh, and F.A. Waldman, *Microcellular closed cell foams and their method of manufacture*, 1984, Massachusetts Institute Of Technology.
71. Kumar, V., *Process Synthesis for Manufacturing Microcellular Thermoplastic Parts*, 1988, Massachusetts Institute of Technology.
72. Kumar, V. and N.P. Suh, *A process for making microcellular thermoplastic parts*. Polymer Engineering & Science, 1990. **30**(20): 1323-1329.
73. Shimbo, M., I. Higashitani, and Y. Miyano, *Mechanism of Strength Improvement of Foamed Plastics Having Fine Cell*. Journal of Cellular Plastics, 2007. **43**(2): 157-167.
74. Nadella, K. and V. Kumar, *Tensile and Flexural Properties of Solid-State Microcellular Abs Panels*, in *Experimental Analysis of Nano and Engineering Materials and Structures*, E.E. Gdoutos, Editor 2007, Springer Netherlands. 765-766.
75. Kumar, V., K.A. Seeler, M. VanderWel, and J. Weller, *Experimental Characterization of the Tensile Behavior of Microcellular Polycarbonate Foams*. Journal of Engineering Materials and Technology, 1994. **116**(4): 439-445.
76. Kumar, V., J.E. Weller, M. Ma, R. Montecillo, and R.R. Kwapisz, *The effect of additives on microcellular PVC foams: Part II. Tensile behaviour*. Cellular polymers, 1998. **17**(5): 350-361.
77. Miller, D. and V. Kumar, *Microcellular and nanocellular solid-state polyetherimide (PEI) foams using sub-critical carbon dioxide II. Tensile and impact properties*. Polymer, 2011. **52**(13): 2910-2919.
78. Schmidt, D., V.I. Raman, C. Egger, C. du Fresne, and V. Schädler, *Templated cross-linking reactions for designing nanoporous materials*. Materials Science and Engineering: C, 2007. **27**(5-8): 1487-1490.

79. Madou, M. J., *Fundamentals of Microfabrication: The Science of Miniaturization*, Second Edition 2002, Boca Raton: CRC. 776.
80. Hillmyer, M.A., *Nanoporous materials from block copolymer precursors*, in *Block Copolymers II* 2005, Springer. 137-181.
81. Olson, D.A., L. Chen, and M.A. Hillmyer, *Templating Nanoporous Polymers with Ordered Block Copolymers*. Chemistry of materials, 2007. **20**(3): 869-890.
82. Hedrick, J.L., R.D. Miller, C.J. Hawker, K.R. Carter, W. Volksen, D.Y. Yoon, and M. Trolls\aaas, *Templating Nanoporosity in Thin-Film Dielectric Insulators*. Advanced Materials, 1998. **10**(13): 1049-1053.
83. Hentze, H.P. and M. Antonietti, *Template synthesis of porous organic polymers*. Current Opinion in Solid State and Materials Science, 2001. **5**(4): 343-353.
84. Jackson, E.A. and M.A. Hillmyer, *Nanoporous membranes derived from block copolymers: From drug delivery to water filtration*. ACS nano, 2010. **4**(7): 3548-3553.
85. Hedrick, J.L., K.R. Carter, J.W. Labadie, R.D. Miller, W. Volksen, C.J. Hawker, D.Y. Yoon, T.P. Russell, J.E. McGrath, and R.M. Biber, *Nanoporous polyimides*, in *Progress in Polyimide Chemistry II* 1999, Springer. 1-43.
86. Lazzari, M. and M.A. López-Quintela, *Block copolymers as a tool for nanomaterial fabrication*. Advanced Materials, 2003. **15**(19): 1583-1594.
87. Park, C., J. Yoon, and E.L. Thomas, *Enabling nanotechnology with self-assembled block copolymer patterns*. Polymer, 2003. **44**(22): 6725-6760.
88. Kazarian, S.G., *Polymer Processing with Supercritical Fluids*. Polymer Science, Series C, 2000. **42**(1): 78-101.
89. Tsivintzelis, I., A.G. Angelopoulou, and C. Panayiotou, *Foaming of polymers with supercritical CO<sub>2</sub>: An experimental and theoretical study*. Polymer, 2007. **48**(20): 5928-5939.
90. Reverchon, E. and J. Cardea, *Production of controlled polymeric foams by supercritical CO<sub>2</sub>*. Journal of Supercritical Fluids, 2007. **40**: 144-152.
91. Jacobs, L.J.M., M.F. Kemmere, and J.T.F. Keurentjes, *Sustainable polymer foaming using high pressure carbon dioxide: a review on fundamentals, processes and applications*. Green Chemistry, 2008. **10**(7): 731-738.
92. Wells, S.L. and J. DeSimone, *CO<sub>2</sub> technology platform: an important tool for environmental problem solving*. Angewandte Chemie International Edition, 2001. **40**(3): 518-527.
93. Kumar, V. and J. Weller, *Production of microcellular polycarbonate using carbon dioxide for bubble nucleation*. Journal of engineering for industry, 1994. **116**(4): 413-420.
94. Vieth, W.R. and K.J. Sladek, *A model for diffusion in a glassy polymer*. Journal of Colloid Science, 1965. **20**(9): 1014-1033.
95. Crank, J., *The Mathematics of Diffusion* 1956, London, England: Oxford University Press. 244.
96. Goel, S.K. and E.J. Beckman, *Generation of microcellular polymeric foams using supercritical carbon dioxide. I: Effect of pressure and temperature on nucleation*. Polymer Engineering & Science, 1994. **34**(14): 1137-1147.

97. Colton, J.S., *Nucleation of Microcellular Foam: Theory and Practice*. Polymer Engineering & Science, 1987. **34**(14): 1137-1147.
98. Goel, S.K. and E.J. Beckman, *Generation of microcellular polymeric foams using supercritical carbon dioxide. II: Cell growth and skin formation*. Polymer Engineering & Science, 1994. **34**(14): 1148-1156.
99. Zhang, Z. and Y.P. Handa, *An in-situ study of plasticization of polymers by high-pressure gases*. Journal of Polymer Science Part B: Polymer Physics, 1998. **36**(6): 977-982.
100. Dong H wang, Y. and S. Woon C ha, *The relationship between gas absorption and the glass transition temperature in a batch microcellular foaming process*. Polymer Testing, 2002. **21**(3): 269-275.
101. Alessi, P., A. Cortesi, I. Kikic, and F. Vecchione, *Plasticization of polymers with supercritical carbon dioxide: Experimental determination of glass-transition temperatures*. Journal of Applied Polymer Science, 2003. **88**(9): 2189-2193.
102. Guo, Q., J. Wang, and C.B. Park, *A Microcellular Foaming Simulation System with a High Pressure-Drop Rate*. Industrial & Engineering Chemistry Research, 2006. **45**(18): 6153-6161.
103. Krause, B., H.J.P. Sijbesma, P. Mönöklü, N.F.A. Van der Vegt, and M. Wessling, *Bicontinuous nanoporous polymers by carbon dioxide foaming*. Macromolecules, 2001. **34**(25): 8792-8801.
104. Krause, B., K. Diekmann, N.F.A. Van der Vegt, and M. Wessling, *Open nanoporous morphologies from polymeric blends by carbon dioxide foaming*. Macromolecules, 2002. **35**(5): 1738-1745.
105. Miller, D., P. Chatchaisucha, and V. Kumar, *Microcellular and nanocellular solid-state polyetherimide (PEI) foams using sub-critical carbon dioxide I. Processing and structure*. Polymer, 2009. **50**(23): 5576-5584.
106. Nawaby, A., Y.P. Handa, X. Liao, Y. Yoshitaka, and M. Tomohiro, *Polymer-CO<sub>2</sub> systems exhibiting retrograde behavior and formation of nanofoams*. Polymer international, 2007. **56**(1): 67-73.
107. Janani, H. and M.H.N. Famili, *Investigation of a strategy for well controlled inducement of microcellular and nanocellular morphologies in polymers*. Polymer Engineering & Science, 2010. **50**(8): 1558-1570.
108. Spitzel, P., C.W. Macosko, and R.B. McClurg, *Block copolymer micelles for nucleation of microcellular thermoplastic foams*. Macromolecules, 2004. **37**(18): 6874-6882.
109. Siripurapu, S., J.M. DeSimone, S.A. Khan, and R.J. Spontak, *Controlled foaming of polymer films through restricted surface diffusion and the addition of nanosilica particles or CO<sub>2</sub>-philic surfactants*. Macromolecules, 2005. **38**(6): 2271-2280.
110. Fujimoto, Y., S.S. Ray, M. Okamoto, A. Ogami, K. Yamada, and K. Ueda, *Well-Controlled Biodegradable Nanocomposite Foams: From Microcellular to Nanocellular*. Macromolecular rapid communications, 2003. **24**(7): 457-461.
111. Ema, Y., M. Ikeya, and M. Okamoto, *Foam processing and cellular structure of polylactide-based nanocomposites*. Polymer, 2006. **47**(15): 5350-5359.

112. Urbanczyk, L., C. Calberg, C. Detrembleur, C. Jérôme, and M. Alexandre, *Batch foaming of SAN/clay nanocomposites with  $\text{scCO}_2$ : A very tunable way of controlling the cellular morphology*. *Polymer*, 2010. **51**(15): 3520-3531.
113. Ruckdäschel, H., P. Gutmann, V. Altstädt, H. Schmalz, and A.H.E. Müller, *Foaming of microstructured and nanostructured polymer blends*, in *Complex Macromolecular Systems 2010*, Springer. 199-252.
114. Siripurapu, S., J.A. Coughlan, R.J. Spontak, and S.A. Khan, *Surface-constrained foaming of polymer thin films with supercritical carbon dioxide*. *Macromolecules*, 2004. **37**(26): 9872-9879.
115. Yokoyama, B.H., L. Li, T. Nemoto, and K. Sugiyama, *Tunable nanocellular polymeric monoliths using fluorinated block copolymer templates and supercritical carbon dioxide*. *Advanced Materials*, 2004. **16**(17): 1542-1546.
116. Li, L., H. Yokoyama, T. Nemoto, and K. Sugiyama, *Facile fabrication of nanocellular block copolymer thin films using supercritical carbon dioxide*. *Advanced Materials*, 2004. **16**(14): 1226-1229.
117. Li, L., T. Nemoto, K. Sugiyama, and H. Yokoyama,  *$\text{CO}_2$  foaming in thin films of block copolymer containing fluorinated blocks*. *Macromolecules*, 2006. **39**(14): 4746-4755.
118. Yokoyama, H. and K. Sugiyama, *Nanocellular structures in block copolymers with  $\text{CO}_2$ -philic blocks using  $\text{CO}_2$  as a blowing agent: Crossover from micro-to nanocellular structures with depressurization temperature*. *Macromolecules*, 2005. **38**(25): 10516-10522.
119. Nemoto, T., J. Takagi, and M. Ohshima, *Control of Bubble Size and Location in Nano-/Microscale Cellular Poly(propylene)/Rubber Blend Foams*. *Macromolecular Materials and Engineering*, 2008. **293**(7): 574-580.
120. Nemoto, T., J. Takagi, and M. Ohshima, *Nanoscale Cellular Foams from a Poly(propylene)-Rubber Blend*. *Macromolecular Materials and Engineering*, 2008. **293**(12): 991-998.
121. Otsuka, T., K. Taki, and M. Ohshima, *Nanocellular Foams of PS/PMMA Polymer Blends*. *Macromolecular Materials and Engineering*, 2008. **293**(1): 78-82.
122. Wang, D., W. Jiang, H. Gao, and Z. Jiang, *Controlling cellular morphology by supercritical carbon dioxide*. *Journal of Applied Polymer Science*, 2009. **111**(4): 2116-2126.
123. Nemoto, T., J. Takagi, and M. Ohshima, *Nanocellular foams—cell structure difference between immiscible and miscible PEEK/PEI polymer blends*. *Polymer Engineering & Science*, 2010. **50**(12): 2408-2416.
124. Lu, X., R. Caps, J. Fricke, C.T. Alviso, and R.W. Pekala, *Correlation between structure and thermal conductivity of organic aerogels*. *Journal of Non-Crystalline Solids*, 1995. **188**(3): 226-234.
125. Pajonk, G.M., *Transparent silica aerogels*. *Journal of Non-Crystalline Solids*, 1998. **225**: 307-314.
126. Roth, C.B. and J.R. Dutcher, *Glass transition and chain mobility in thin polymer films*. *Journal of Electroanalytical Chemistry*, 2005. **584**(1): 13-22.
127. Jo, C., J. Fu, and H.E. Naguib, *Constitutive modeling for mechanical behavior of PMMA microcellular foams*. *Polymer*, 2005. **46**(25): 11896-11903.





# ***Chapter I:***

## ***Experimental techniques***



## Chapter I. Experimental techniques

Several experimental techniques were used to characterize the solid samples, the foaming process, the CO<sub>2</sub>-polymer interactions, the cellular structure and properties of foams described in this dissertation. Table I-1 lists them in order to provide a general view of the characterizing methods used. Each publication briefly describes the techniques employed, however, in this chapter further explanations, about some non-conventional techniques developed, improved or adapted in this work, are provided.

**Table I-1: Experimental techniques employed in this work and chapter in which they are used**

Experimental technique	Chapter
Size-exclusion chromatography (SEC)	II
Transmission electron microcopy (TEM)	II-III
Atomic force microscopy (AFM)	II-III
Scanning electron microscopy (SEM)	II-V
Differential scanning calorimetry (DSC)	II-V
Archimedes densimetry	II-V
CO <sub>2</sub> uptake gravimetric measurement	III-IV
Cell structure characterization assisted by software	III-V
X-ray radiography	III & V
Dynamic mechanical analysis (DMA)	V
Thermal conductimetry: Transient plane source (TPS)	V

### I.1 Non-standard characterization techniques

One of the main challenges found during this work was the selection of appropriate techniques to characterize the solid and foamed samples, and some of their properties. In the present section the techniques used for the characterization of nanostructuration in solid blends (SEM, AFM and TEM), the cellular structure of foamed blends (using a specific software developed in this work), the density distribution of foamed samples (x-ray radiography) and the thermal conductivity of nanocellular foams (TPS) are detailed.

#### I.1.1 Nanostructuration characterization

As explained in the introduction the main scope of this work is the production of nanocellular foams from nanostructured precursors. Therefore, a detailed characterization of the nanostructuration is essential. This

important topic was covered using three techniques: SEM, AFM and TEM. General details about these techniques are well known. Therefore, the following explanations are focused on the specific protocols or operation modes used to study the nanostructuration of our samples.

### *1.1.1.1 SEM*

First attempts to study the nanostructuration of PMMA/MAM blends were carried out by SEM. Injected samples of PMMA/MAM were cut by microtome and then stained with ruthenium tetroxide ( $\text{RuO}_4$ ). Microtoming was done at room temperature with low PBA amount samples, and at cryogenic conditions with medium-to-high PBA amount samples. Staining protocol is described below. [1]

- A 2 % solution of  $\text{RuO}_4$  is prepared by adding 0.2 g of  $\text{RuO}_4$  to 10 ml of a 50/50 mixture between distilled water and concentrated commercial bleach at 9.6 % of active chlorine.
- Thin samples (cut by microtome) were collected on cooper grids.
- 4 droplets of  $\text{RuO}_4$  solution are placed in a Petri dish, and the cooper grid with the samples is placed nearby.
- Samples are exposed to the  $\text{RuO}_4$  solution vapors during 1-2 minutes.
- Samples are rinsed and dried ( $\text{RuO}_4$  is neutralized by sodium bisulfate and then rinsed with water), being ready for SEM observations.

Although this staining protocol was developed for TEM observations [1] our first attempts with SEM observations on 90/10 PMMA/MAM blends seemed to show the nanostructuration [2].

However, results obtained by this method presented poor reproducibility and questionable accuracy. Therefore this technique was discarded in the beginning of this work and other options were studied.

### *1.1.1.2 AFM*

AFM experiences were carried out using a Multimode AFM (Veeco Instruments) in the Instituto of Microelectrónica de Madrid (INM, CSIC) with the help of Dr. Christian Dietz and Dr. Ricardo García.

Identification of polymer phases can be done with the AFM operating in the amplitude modulation mode (tapping mode AFM) [3]. Using AFM in this mode the topography, tip oscillation amplitude, and the phase shift signals are recorded. From this data polymer phases can be well identified in the AFM phase

images. These images show a better contrast on polymer blends than the topography images because they detect changes in the energy dissipated by the AFM tip [4].

AFM images were obtained from PMMA/MAM blends on flat surfaces obtained by cutting with a microtome using a glass knife. Microtoming was done at room temperature with low PBA amount samples, and at cryogenic conditions with medium-high PBA amount samples ( $-50^{\circ}\text{C}$ ). Samples obtained by this procedure present surfaces with differences in height lower than 100 nm, being suitable to the AFM technique.

Main issue using this technique is the correct identification of the polymer phases. Although the better contrast is presented on AFM phase images, the information of the three channels is needed (topography, amplitude and phase) to reach a correct interpretation of the AFM images.

Figure I.1 shows the AFM images (from left to right, topography, amplitude and phase) and the recorded signal values corresponding to the selected profile (in gray over the images) of a neat PMMA sample. And figure I.2 shows the same information from a PMMA/MAM blend.

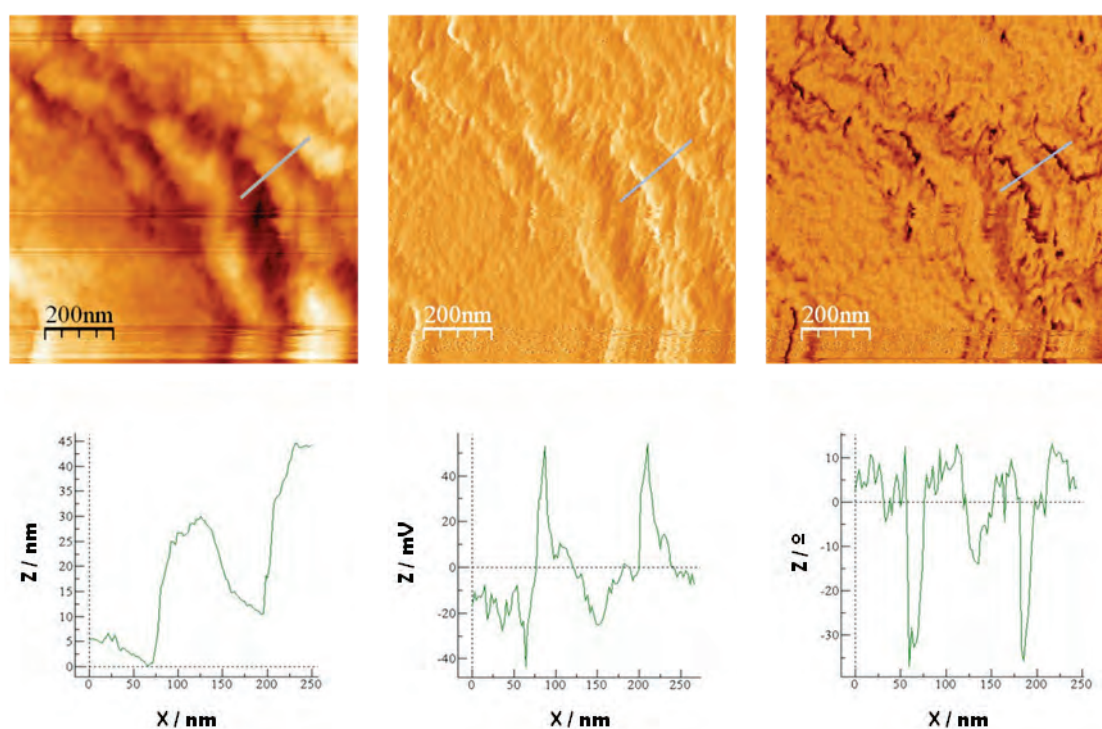


**Figure I.1: AFM topographic (left), amplitude (middle) and phase (right) images of neat PMMA (up) and signals values (down) corresponding to the selected profile (in gray over the images).**

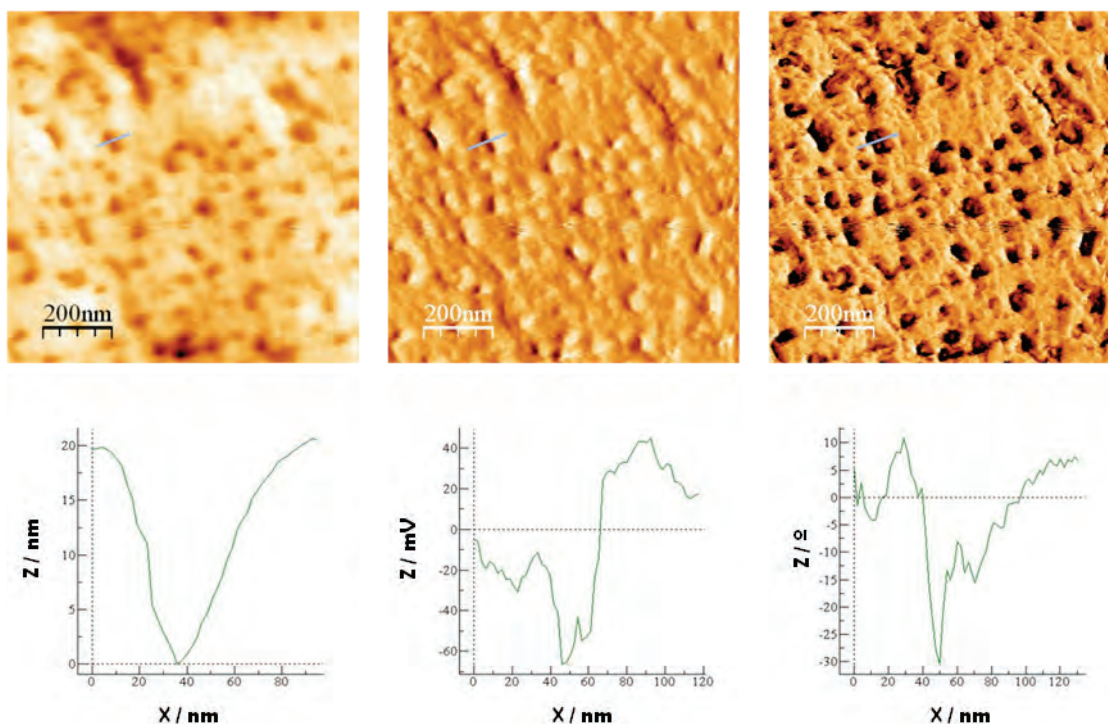


**Figure I.1: AFM topographic (left), amplitude (middle) and phase (right) images of PMMA/MAM blend (up) and signals values (down) corresponding to the selected profile (in gray over the images).**

AFM phase images from both materials show areas with high contrast (i.e., areas presenting significant different phase shift). Also, in both cases these areas correspond to signals of, apparently, lower height in the topography image. So, to identify if these areas are just voids or a different polymeric phase (a softer one that allows a little indentation of the surface) the information of the amplitude signal is required. When the AFM tip reaches a void the amplitude is increased (tip loss contact with the sample's surface and then its oscillation amplitude is increased), whereas the phase shift is decreased. On the contrary, when the AFM tip reaches a different polymeric phase, in our case the soft-block PBA, the change on the amplitude signal has the same behavior as the phase signal; both are decreased due to the changes in the tip-sample interactions between the PMMA and the PBA phases. Therefore, high contrast areas of the figure 1 correspond to voids in the samples surfaces, and high contrast areas of the figure 2 correspond to a different polymeric phase.

Accurate identification of the PBA phase on AFM phase images allows measuring some parameters of the nanostructuration. On one side, the area fraction filled by the nanostructures can be determined by image analysis procedures. Contrast between the PBA and PMMA phases allows quantifying independently the area of each phase, and therefore obtaining the nanostructuration area fraction.

On the other side, AFM phase images of blends with dispersed nanodomains allow quantifying the volumetric density of domains ( $N_n$ , domains/cm<sup>3</sup>) and the average diameter of the domains. Volumetric density of domains can be obtained using Eq. I-1.

$$N_n = \left( \frac{n}{A} \right)^{3/2} \quad \text{[I-1]}$$

Where  $n$  is the number of dispersed domains observed in the AFM phase image and  $A$  is the area of the image in cm<sup>2</sup>. Average diameter of the domains can be obtained by measuring the diameter of several domains (about 100), or by obtaining the average diameter from the measured area and density of domains (assuming spherical domains).

### 1.1.3 TEM

Last technique used to study the nanostructuration of PMMA/MAM blends is the transmission electron microscopy. TEM (model Hitachi H7650 with Orius camera) experiences were carried out in the Bordeaux Imaging Center BIC (Université Bordeaux Segalen) with the help of Dr. Etienne Gontier, Dr. Soizic Lacampagne and Dr. Melina Petrel.

In the case of PMMA-MAM blends, two acrylate polymers need to be differentiated, i.e. poly(butyl acrylate) (PBA) from poly(methyl methacrylate) (PMMA), even two different PMMA's might be differentiated (blocks from matrix).

TEM imaging of similar polymers is often difficult, phosphotungstic acid (PTA) staining is one solution suggested for organic polymers and copolymers by Harris et al. [5]. Structural features were revealed (core-shell particles, blends, amphiphilic block copolymers).

Phosphotungstic acid (PTA) is a good contrasting staining agent *at nanometric levels* in polyethylacrylate-polyhydroxyethylacrylate (PEA-PHEA) interpenetrating networks [6] or poly(methyl methacrylate)-co-polyacrylonitrile (PMMA-PAN) composite particles or epoxy-acrylate particles [7].

Generally PTA is known to react with or to graft to chemical functions such as OH, COOH, NH [8]. For example, polyamides (PA) are very well contrasted by PTA in PA-PMMA blends; PA appears dark due to the NH groups while PMMA appears light grey. In PEA-PHEA blends, PHEA is stained due to the OH groups while PEA is not stained by PTA and appears white.

In PMMA-PAN systems, PTA interacts selectively with PAN and PMMA is not stained in the composite particles.

In the epoxy-acrylate latex particles where the acrylate cores are composed of butylacrylate (BA) – methylmethacrylate (MMA) -styrene random copolymers, only the epoxy shell is stained. The styrene-acrylate core is not affected by PTA.

In sequentially synthesized BA/MMA/epoxy latex particles, the three layered structure is evidenced by PTA showing a black shell, a black epoxy core and a light grey middle MMA layer. In another work, dealing with BA-MMA particles [9] where BA and MMA are homopolymers, only the BA cores are stained by PTA. Authors claim that the solubility (or maybe the differential swelling capacity) difference in water and ester could be the reason for PTA selective staining but no mechanism is explained, and all the explanations remain unclear.

Therefore, PMMA alone does not seem to be stained by PTA whatever the pH conditions (acidic or neutral) [7, 9].

For Maiez et al. [10], in PMMA-DMA-PBA BCP's, PBA is white in the presence of  $\text{RuO}_4$  while PMMA-DMA copolymer is dark (stained). As a strong oxidant  $\text{RuO}_4$  is supposed to bind to carbon double bonds (unsaturated, aromatic compounds) but also to ester, alcohol, amine functions. Thus PBA is said to be stained in certain conditions by  $\text{RuO}_4$  [11]. Nevertheless PMMA is not stained neither by  $\text{RuO}_4$  (nor  $\text{OsO}_4$ ).

In our case, it was checked that classical ruthenium oxide is not suitable to contrast the MAM copolymer neither the PMMA-MAM blends as dense materials (there is a very poor contrast, no distinction of an inner structure).

Dronet et al. [8] and Ruzette et al. [1] show MAM micrographs where PMMA is said to be colored by PTA (grey or black) and PBA appears white. They claim that PTA binds to amide (Dronet), but also to methacrylate ester functions (thus PMMA is grey) while it does not bind to acrylate esters (thus PBA is white).

As a conclusion the selective staining power of PTA seems to depend on reactivity (grafting), solubility, hydrophobicity of the nano structure and maybe on the surrounding phases. Another hypothesis for preferred staining is the preferential swelling of soft materials or soft phases with alkyl groups (such as the poly(butyl acrylate) areas) by benzyl alcohol from the PBA solution, therefore enabling a better staining.

If the contrasting effect of PTA is proved, the precise assessment of the PBA and PMMA phases is sometimes contradictory. Nevertheless, nano structures are always proved (or revealed) by PTA staining.



In our particular situation of two non reactive polyacrylate blends, no chemical reactive functions are available; if our case can be related to some previous cases found in literature, we could expect that PTA staining may contrast PBA selectively and not or little PMMA.

Therefore, the TEM preparation protocol applied on PMMA/MAM samples can be summarized as follows:

- Thin cuts (60-70 nm) of the solid PMMA/MAM samples are obtained by microtome carried out at -50° C with a diamond knife.
- Cuts are deposited on formvar cooper grids and treated by a water solution with 2 % in weight of phosphotungstic acid (PTA) + 2 % in weight of benzyl alcohol during 2 minutes at 60° C. Benzyl alcohol apparently acts as a dyeing assistant [1].
- Samples are rinsed and dried.

Following this procedure, PTA staining of TEM samples seems to be the best method to determine the nanostructuration of solid PMMA/MAM samples.

TEM micrographs obtained by this procedure allow obtaining the same parameters of the nanostructure than AFM phase images. Fraction area can be obtained in the same way by image analysis procedures, and also the volumetric density and average diameter of dispersed domains. From TEM micrographs the volumetric density of dispersed domains can be calculated using Eq. II-2.

$$N_n = \frac{n}{V} \quad \text{[I-2]}$$

Where  $V$  the volume of the sample in  $\text{cm}^3$  (calculated from the area of the image and the thickness of the TEM sample) and  $n$  is the number of core-shell nodules observed in a TEM image. As TEM image is a two-dimensional projection of the three-dimensional structure of the sample some assumptions are needed to estimate the number of nanosized domains. Completely black structures in TEM images are assumed to be core-shell structures completely contained in the sample and counted as units, and structures with a dark shell and gray core are assumed to be core-shell nodules partially contained in the sample, because the gray core is due to the absence of the lower or upper part of the dark shell (not contained in the sample), and counted as halves.

In addition some attempts to determine the nanostructuration of foamed samples were carried out. Foamed samples were stiffened to allow the cutting by microtome and avoid damage to the nanocellular structure. With this aim, voids were filled by a TEM-contrasting liquid hardening formulation, composed

by a crosslinking solution (formulation remains confidential and not publishable). This solution is allowed to fill the voids without solubilization of PMMA, and the overall system gelifies and hardens rapidly (< 30 minutes). After this procedure, the TEM foamed samples were prepared following the same protocol than the solid ones.

### I.1.2 Cellular structure characterization

Characterization of the cellular structure is one of the main issues on the study of cellular materials. Consequently, there are several methods to measure the main parameters such as average cell size, cells anisotropy, cells density, cells nucleation density or cell size distribution.

For nanocellular foams the characterization of the cellular structure is based on micrographs obtained by high resolution scanning electron microscopy. Other techniques such as tomography have not yet been developed enough to characterize these materials (spatial resolution is not as high as needed for these materials).

However, neither the standard nor the theoretical existent methods based on micrographs allow obtaining a complete and quick characterization. Due to this time-consuming manual measurements are usually needed to complete the characterization.

First journal article including in this dissertation is focused on this topic. It was published in **Journal of Cellular Plastics Vol. 49 (2013)** with the title “*Characterization of the cellular structure based on user-interactive image analysis procedures*”. This publication is focused on the development of a specific software to characterize the cellular structure from foam’s micrographs. This software is based on image analysis procedures and the introduction of some steps that require interaction of the software user with the software, avoiding the main problems associated to automatic image analysis procedures. Results obtained using this software are presented and compared to the results obtained from three other methods commonly used in the literature. From this comparison the developed software presents the best relationship between the number of parameters provided, the accuracy of the measurement and the time consumed (less than 3 minutes per micrograph). Due to the clear advantages of this method and its accuracy, this software became the standard cellular structure characterization method in CellMat Laboratory.

It should be noticed that all the results showed in this paper are from microcellular materials. These materials were selected in order to provide broader test conditions to the software (different cell size distributions, number of cells per image, different anisotropies, etc.) and not for their average cell size. Nonetheless, characterization of the nanocellular structures showed in this dissertation was carried out using this software.

# Characterization of the cellular structure based on user-interactive image analysis procedures

Javier Pinto, Eusebio Solórzano,  
Miguel Angel Rodriguez-Perez and  
Jose Antonio de Saja

## Abstract

This work addresses the development of a novel user-interactive image analysis computed technique to determine the main characteristics of the cellular structure of cellular materials with any density, morphology, and/or cell size from micrographs obtained from any source—scanning electron microscopy, optical microscopy, etc. The specific analyzed parameters are cell size (mean cell diameter), cell anisotropy, cell size distribution, and cell density. A comparison with several conventionally used methods is also presented in this work. The development of such application offers a quick (<3 min per micrograph) and complete characterization of the cellular structure, with reproducible results and good agreement with the typical manual measurement methods.

## Keywords

Foams, cell size, cellular materials, cellular structure, image analysis

## Introduction

Nowadays, the fabrication and characterization of cellular materials has gained significant interest, considering technical, environmental, and cost-saving issues. On one hand, cellular materials cover a wide range of densities and, usually, it is possible to custom-design any particular foam (basically selecting the final material density) to fulfill the requirements of any specific application. On the other hand,

---

Faculty of Sciences University of Valladolid, Valladolid, Spain

### Corresponding author:

Javier Pinto, Cellular Materials Laboratory (CellMat), Condensed Matter Physics Department, University of Valladolid, Paseo de Belén no. 7, Valladolid 47011, Spain.

Email: jpinto@fmc.uva.es

this type of materials presents good specific mechanical properties, such as high elastic modulus or energy absorption,<sup>1–3</sup> combined with improved thermal and acoustic insulation properties due to their cellular structure.<sup>4–8</sup>

It is well known that the properties of cellular materials depend on both the properties of the solid matrix and characteristics such as density and cellular architecture.<sup>1</sup> Cellular morphology becomes fundamental in the particular case of thermal and acoustic properties, in which a combination of diverse morphological and topological aspects controls the final response of the cellular material.<sup>4–8</sup> Among the mentioned key aspects (matrix, density, and cell architecture), the characterization of the cellular structure presents several practical difficulties that standard methods hardly solve.

According to the literature, there is not a well-defined unique method to determine the previous parameters using a reasonable user time. The only accepted method within the American Society for Testing and Materials (ASTM) standards is the intersections methods (see further details in section 2.3.2),<sup>9–11</sup> but it does not offer accurate results in medium or high density cellular materials, because it does not take into account the cell wall thickness. Another remarkable lack of this standard is that only the average values are obtained but not its distribution<sup>12</sup> (e.g. bimodal cell size distributions cannot be quantified).

Using modifications of the intersections method, not recognized in the ASTM standard, is possible to calculate the cell average anisotropy ratio, and obtain better results in medium-high density foams measuring chord lengths.<sup>10</sup> This method could be applied over images of the cellular structure obtained by scanning electron microscopy (SEM), or optical microscopy. However, these modifications cannot determine other parameters such as the cell size distribution, and in fact it is needed to measure each cell manually to obtain this distribution.

With the aim of developing an automatic method to determine the cell size distribution, there are several papers in the literature based on image analysis. One option is to control the process of binarization of each image, assuring that each cell is properly segmented,<sup>10,13,14</sup> but this is a tedious and in general a non-reproducible process. Other option is trying to improve the contrast between the cells and the polymeric matrix, to allow an automatic recognition of the cells by image analysis software. In some cases, a very thin cut of the sample is used (thickness lower than average cell size) to obtain images with an appropriate contrast.<sup>9,15–17</sup> This method has the disadvantage of requiring a difficult sample preparation, especially when the foams have cell sizes in the micrometer or submicrometer range, therefore this method cannot be generalized. Alternatively, ink staining on a cut foam surface has also been used.<sup>9,18</sup>

From all the revised methods, manual ones offer the general inconvenience of a tedious methodology and/or incomplete cellular morphology determination. Alternatively, the automatic methods may offer imprecise results due to the inhomogeneous contrast of cell walls that seriously complicates the binarization step, which is fundamental for the later individual cell recognition. Furthermore, the methods mentioned here use the image from a foam section and, therefore, the

obtained value is two-dimensional needing for a theoretical correction that may assume inexact hypothesis.

Alternatively several methods that aimed to determine/estimate the three-dimensional cell size can be found in the literature, most of them based on information obtained in a 2D image. It is possible to obtain the three-dimensional cell size from theoretical calculations, using as key parameters the cells per unit area in a SEM image and macroscopic values such as the densities of cellular and solid materials.<sup>19–22</sup> The average cell size and the cell size distribution can be obtained by stereological methods using complex theoretical expressions.<sup>21,23–25</sup> Also, the three-dimensional cell size can be obtained from the 2D value with a theoretical correction factor.<sup>9,10</sup> Finally, the only method allowing a direct 3D analysis of cellular materials is the computed microtomography ( $\mu$ CT). X-ray or optical  $\mu$ CT have been successfully used to reconstruct the internal structure of porous solids. Nevertheless, optical tomography presents severe technical difficulties,<sup>26–28</sup> and so X-ray tomography is the merely used technique for cellular materials 3D analysis. This technique offers a direct measurement of an extremely wide number of morphological and topological variables associated to the cellular structure, but specific and expensive equipment, as well as long data processing time usually under expensive software licenses,<sup>10,18,25,29,30</sup> are needed.

In summary, the usual inexpensive methods to characterize the cellular structure do not offer a good ratio between the accuracy of the results and the invested time to obtain them. Alternatively, the 3D methods X-ray tomography need for rather long user times and expensive equipment to obtain precise 3D values. As an alternative, the method described in this work is a novel “hybrid method,” in which both automatic and manual methodologies are used, and a complete set of accurate results are obtained in short times.

It is important to remark that the proposed method provides a complete characterization of the cellular structure (average cell size, cell size distribution, anisotropy coefficient, and cell density), of any cellular material in all the density range. Also, this method has been developed under FIJI/ImageJ,<sup>31</sup> a public domain Java image processing software. An appropriate combination of image processing routines, small user’s assistance, and the implementation of theoretical expressions, provides a useful application which could be widely used in the characterization of cellular materials.

## Materials and methods

### *Materials selection*

Four different types of polymeric foams have been characterized in this work. Polyurethane and epoxy thermosets foams with significant different densities and significant different cellular structures have been studied. Additionally, two different polypropylene thermoplastic foams have been analyzed. All these materials

were produced at CellMat Laboratory. The different materials have been selected to show the ability of the developed method to characterize images with a very large number of cells, or structures including bimodal cell size distributions. The main characteristics of these materials can be found in Table 1.

### Samples preparation

Materials preparation is a key process to preserve cellular structure without producing any kind of tearing, breaking, or cell deformation. To this end, foams were immersed in liquid nitrogen for 10 min till they reached a temperature below their  $T_g$ , and subsequently fractured. In a second step, a thin layer of Au (20 nm) is evaporated over the exposed fractured cellular structure to make it electrically conductive, thus allowing the SEM observation. A scanning electron microscope model JSM-820 from Jeol, Japan, was used to obtain the micrographs (imaging conditions are 20 kV and  $10^{-9}$ – $10^{-10}$  A. SEM images were digitalized with resolution of  $1024 \times 700$  pixels<sup>2</sup>). Figure 1 shows characteristic micrographs of each material.

### Characterization methods

In this section, the characterization methods used in the paper are described.

**Manual overlay method (reference method).** This method consists in the manual drawing of an overlay for each individual cell contour. This method can be considered as very accurate and will be used as a *reference* for the comparative presented in next sections, this is because the major source of inaccuracy, the binarization process, is very accurate after overlaying the cellular structure. The obtained overlay is analyzed using FIJI/ImageJ quantification module. The average two-dimensional cell size ( $\bar{\phi}_{2D}$ ), the cell size distribution, the anisotropy ratio of each cell, and the average anisotropy ratio ( $A_{y/x}$ ) were analyzed by using this methodology.

**Intersections method.** This method is defined in the ASTM D3576-04 (2010) Standards.<sup>9</sup> A grid with equispaced lines in two perpendicular directions ( $m$

**Table 1.** Main characteristics of the employed foams.

Matrix	$\rho_{\text{foam}}$ (kg/m <sup>3</sup> )	$\rho_{\text{solid}}$ (kg/m <sup>3</sup> )	Foaming process
Polyurethane (PU)	50	1200	Reactive foaming
Epoxy resin	230	1000	Reactive foaming
Polypropylene-1 (PP-1)	200	920	Chemical foaming
Polypropylene-2 (PP-2)	180	910	Chemical foaming

vertical lines of length  $h$  and  $l$  horizontal lines of length  $w$ ) is overlaid in each micrograph. For each line, the number of cells intercepted ( $n_i, n_j$ ) is counted and the line length ( $h$  or  $w$ ) is known. From these values, it is possible to obtain the average chord length of the cells ( $\Phi_{1D-i}, \Phi_{1D-j}$ , i.e., a one-dimensional value), dividing the line length by the number of cells. The average cell size value can be obtained using this procedure over every line with the equation (1), where  $M$  is the magnification value of the micrograph and it is used the standard three-dimensional or two-dimensional correction factor (1.623 and 1.273, see section on ASTM standard correction factor) to calculate the reference three-dimensional or two-dimensional average cell size ( $\bar{\phi}_{3D}$  and  $\bar{\phi}_{2D}$ ) (equation (1)).

$$\bar{\phi}_{3D} = \frac{\sum_{i,j}^{m,l} \phi_{1D-ij}}{m+l} \cdot M \cdot 1.623 \quad (1a)$$

$$\bar{\phi}_{2D} = \frac{\sum_{i,j}^{m,l} \phi_{1D-ij}}{m+l} \cdot M \cdot 1.273 \quad (1b)$$

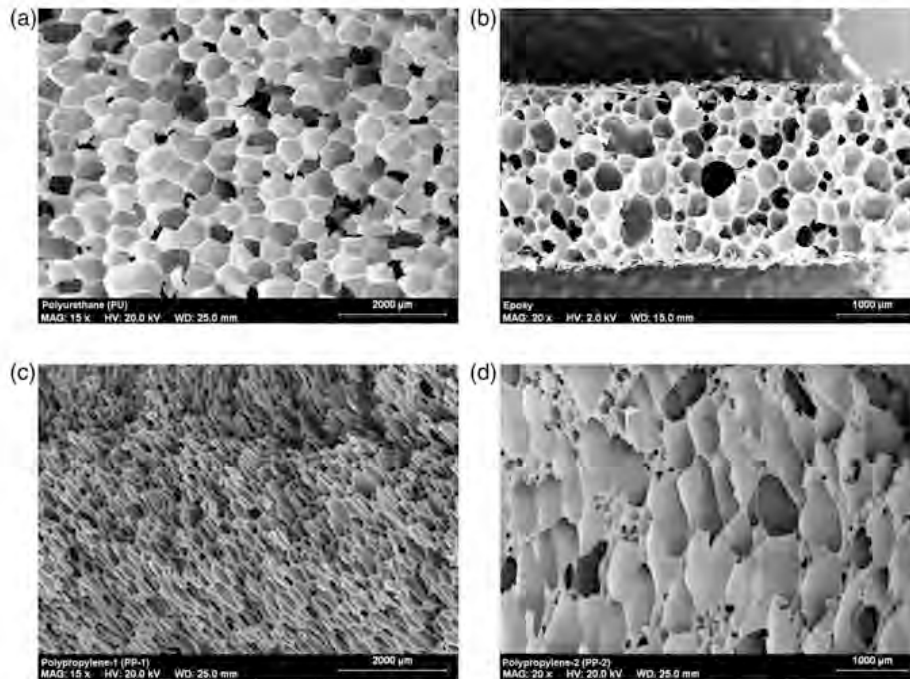


**Figure 1.** SEM Images which will be characterized with the different methods proposed: (a) PU, (b) Epoxy, (c) PP-1, and (d) PP-2.

Also, this method provides the average anisotropy ratio ( $A_{y/x}$ ) between the two directions measured ( $x$  and  $y$ ) (equation (2)).

$$A_{y/x} = \frac{\sum_{i=1}^m \phi_{1D-i}}{\sum_{j=1}^l \phi_{1D-j}} \quad (2)$$

The main disadvantages of this method are its low accuracy for medium-high density foams due to the cell wall thickness which is not taken into account, and that the cell size distribution is not provided. Some attempts, not registered in the ASTM standards, have been proposed to improve this method. The accuracy for medium-high density foams can be increased using as a correction factor the void fraction value (porosity), which accounts for the pores area reduction and the consequent effective pore size due to thicker walls. Alternatively, more precise cell size distributions can be obtained by measuring the chord length of each cell along the reference grid lines,<sup>10</sup> but this is a very time-consuming process.

*Kumar's theoretical approximation.* In this method,<sup>19–22</sup> no direct measurements of cell dimensions over the micrograph are required, only the image area ( $A$ ) and the total number of cells ( $n$ ) contained are measured. From these values and the magnification factor of the micrograph ( $M$ ), the cell density ( $N_v$ , number of cells per cubic centimeter of the foamed material) can be calculated (equation (3)).

$$N_v = [(nM^2)/A]^{3/2} \quad (3)$$

It is known that the volume fraction of voids ( $V_f$ ) can be obtained from the cell density ( $N_v$ ) and the average cell size ( $\bar{\phi}_{3D}$ ), assuming spherical cells (equation (4)).

$$V_f = \frac{\pi \bar{\phi}_{3D}^3}{6} N_v \quad (4)$$

Furthermore, the volume fraction of voids ( $V_f$ ) can be calculated from the density of the foamed and solid material ( $\rho_{\text{foam}}$  and  $\rho_{\text{solid}}$ ) (equation (5)). Therefore, by measuring these densities it is possible to obtain the average cell size, assuming spherical cells, using equation (6).

$$V_f = 1 - \frac{\rho_{\text{foam}}}{\rho_{\text{solid}}} \quad (5)$$

$$\bar{\phi}_{3D} = \left[ \frac{1}{N_v} \cdot \frac{6}{\pi} \cdot \left( 1 - \frac{\rho_{\text{foam}}}{\rho_{\text{solid}}} \right) \right]^{1/3} \quad (6)$$



This method also provides an expression to estimate the cell nucleation density ( $N_o$ , number of cells per cubic centimeter of the solid material), assuming that coalescence phenomena did not occur during processing stage (equation (7)).

$$N_o = \frac{N_v}{1 - V_f} \quad (7)$$

It is important to remark that the application of this method presents two important sources of inaccuracy. On one hand, this method only provides completely accurate results in foams with spherical cells. On the other hand, the determination of the exact number of cells ( $n$ ) in the area ( $A$ ) of one micrograph<sup>20</sup> is not trivial, because some cells located near the limits of the micrograph could be incomplete. One option to avoid this problem is counting the incomplete cells as halves.<sup>20</sup>

This method is implemented as a complementary method in the developed image analysis application, as will be explained later.

*User-interactive image analysis.* As mentioned earlier, one of the main characteristics of the developed application is the implication of user cognition capabilities. The interaction between user and application avoids mistakes in the cells binarization and recognition, allowing to obtain accurate results. This interaction does not involve a high time consumption and the benefits obtained are substantial in terms of accuracy.

A schematic flow diagram of the application is shown in Figure 2, summarizing the description of the process. The first step is the binarization of the micrographs, in the general process the image contrast is enhanced and a *median* filter is applied to reduce the noise of the image and preserve edges, then a *convolve* filter (a type of derivative filter) is applied to obtain an image where the edges are revealed. From this, a binary image of the cell walls is obtained (Figure 3a). This general binarization process works well with different materials, and it can be easily optimized if the results are not good enough.

Every binarized micrograph could present some defects, broken cell walls, and incomplete cells in the image borders. These defects are an important source of inaccuracy for the cellular structure characterization if an automatic cell identification process is used. This is the reason why a user-interactive cell identification process is implemented. It basically consists in a user selecting/validating the cells with no binarization/border defects which later on will be measured (Figure 3(b), right, cells with dots in the center).

Each selected cell is measured following this procedure: first, the application finds the approximate center of the cell. Subsequently, from this point it measures the cell radius in eight different directions (angles), obtaining the two-dimensional cell size, anisotropy ratio and orientation of each cell. From these measurements, the average values are calculated ( $\bar{\phi}_{2D}$  and  $A_{Y/X}$ , respectively).

The application also provides the measured cell size distribution and relevant statistical parameters such as the standard deviation (SD; equation (8)) and the

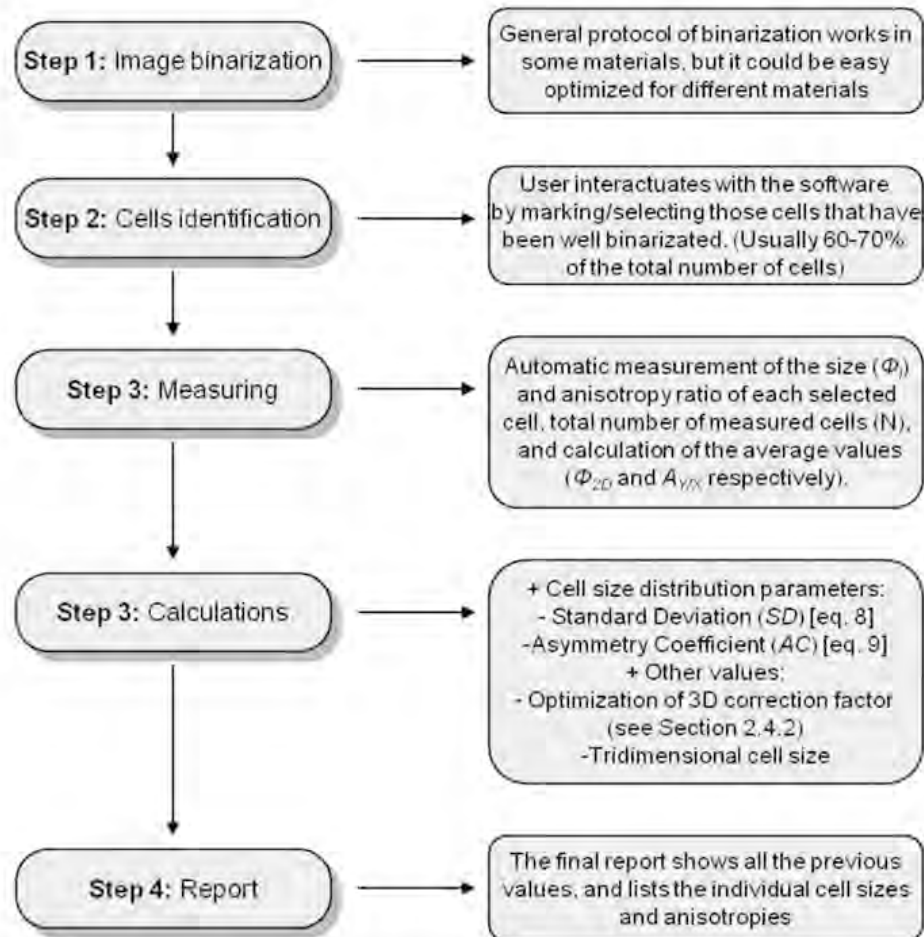


**Figure 2.** Developed application operation flow diagram, each step is briefly explained on the right side.

asymmetry coefficient (AC; equation (9)). The homogeneity of the cell size distribution can be studied using the ratio between the SD and  $\bar{\phi}_{2D}$ . Homogeneous cell distributions presents small values for this ratio, instead heterogeneous distributions which presents values near or higher than one. Asymmetry coefficient provides information on the shape of the distribution; if the coefficient is negative the smallest cells are more separated from the average value than the bigger ones, and vice versa.

$$SD = \sqrt{\frac{\sum_{i=1}^n (\phi_i - \bar{\phi}_{2D})^2}{n - 1}} \quad (8)$$

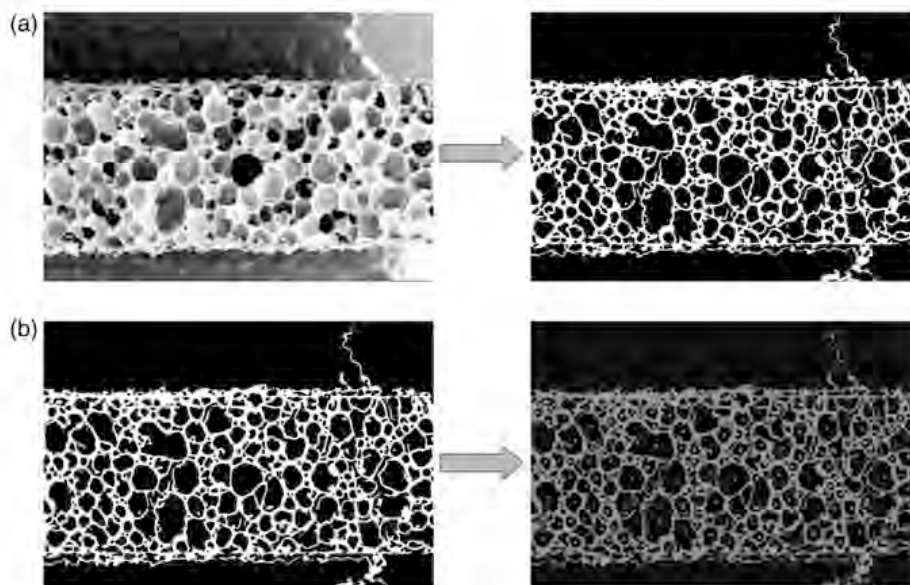


**Figure 3.** Examples of the micrograph processing: (a) Binarization of the image and (b) selection of cells to be analyzed.

$$AC = \frac{\sum_i^n (\phi_i - \phi_{2D})^3}{n \cdot (SD)^3} \quad (9)$$

Finally, the average three-dimensional cell size ( $\bar{\phi}_{3D}$ ) is calculated using the standard correction factor from 2D to 3D (1.273, see section on ASTM standard correction factor). An optimized correction factor (see section on Optimized correction factor) is also calculated by the application.

In addition, Kumar's theoretical approximation is implemented as a complementary characterization method in the application. The combined implementation of both methods allows obtaining a complete report about the cellular structure of any foam in an average time below 3 min.

### *Calculation of three-dimensional cell size*

Some of the methods previously explained need the use of a correction factor to estimate the three-dimensional cell size from bidimensional measurements. This section explains how these factors are calculated.

**ASTM standard correction factor.** The average two-dimensional cell size value is measured directly by the software, and a correction factor is used to obtain the three-dimensional average cell size. In the literature, it is possible to find a process to

obtain a standard correction factor that provides the three-dimensional value from the one-dimensional value.<sup>9</sup>

It is assumed that the cell shape is spherical, and the cell size is relatively uniform. This standard method begins with an average chord length value ( $t$ ) (one-dimensional value) measured over a two-dimensional micrograph.

First, it is necessary to obtain the average two-dimensional size ( $\bar{\phi}_{2D}$ ) from the randomly cells chords.

Thus, this average two-dimensional size must be converted to the average three-dimensional size ( $\bar{\phi}_{3D}$ ). In both cases, the process is the same, and this correction factor can be calculated as follow:

1. The mean value of the ordinates in the first quadrant for any circle  $x^2 + y^2 = r^2$  is:

$$\bar{y} = (1/r) \int_0^r \sqrt{r^2 - x^2} dx = \pi r/4 \quad (10)$$

2. Then, the relationship between  $t$  (one-dimensional value) and  $\bar{\phi}_{2D}$  (two-dimensional value) is:

$$\begin{aligned} t &= \pi \bar{\phi}_{2D}/4 \\ \bar{\phi}_{2D} &= t/0.785 \end{aligned} \quad (11)$$

3. The process is repeated to obtain  $\bar{\phi}_{3D}$  (three-dimensional value) from  $\bar{\phi}_{2D}$  (two-dimensional value):

$$\begin{aligned} \bar{\phi}_{2D} &= \pi \bar{\phi}_{3D}/4 \\ \bar{\phi}_{3D} &= \bar{\phi}_{2D}/0.785 \end{aligned} \quad (12)$$

4. Finally, the relationship between  $t$  (one-dimensional value) and  $\bar{\phi}_{3D}$  (three-dimensional value) is:

$$\bar{\phi}_{3D} = t/(0.785)^2 = t \cdot 1.623 \quad (13)$$

Taking into account this process, the two-dimensional to three-dimensional standard correction factor can be calculated as:

$$\bar{\phi}_{3D} = \bar{\phi}_{2D}/0.785 = \bar{\phi}_{2D} \cdot 1.273 \quad (14)$$

*Optimized correction factor.* A new method aimed to improve the accuracy of the ASTM correction factor has been developed in this work. The standard correction factor assumes that the measured cell sections in the micrograph cover the complete distribution from zero to the maximum diameter.<sup>9</sup> However, smallest sections are not usually detected/measured, thus obtaining measurements of a truncated

distribution of cell-sections which induces the fail of the previous assumption and, this way, the ASTM correction factor will trend to overestimate the cell size. So, an improved method to calculate the correction factor based on the measured cell size distribution is proposed. It works as follow:

1. First, a three-dimensional value is calculated ( $\bar{\phi}_{3D}$ ) using the standard correction factor and the measured *average two-dimensional size* ( $\bar{\phi}_{2D}$ ).

$$\bar{\phi}_{3D} = \bar{\phi}_{2D} \cdot 1.273 \quad (15)$$

2. The average value for the three smallest measured cells is calculated ( $\bar{s}_{2D}$ ), it represents an estimated value for the minimum cell-section measured. Then, this value is normalized by maximum cell-section (equivalent to the average three-dimensional cell size,  $\bar{\phi}_{3D}$ ), obtained in step 1.

$$s = \bar{s}_{2D} / \bar{\phi}_{3D} \quad (16)$$

3. The mean value of the ordinates ( $\bar{y}'$ ) in the first quadrant of a circle (normalized radius, 1) is calculated in the range  $y \in [s, 1]$ . Thus, the new value takes into account only the cells-sections distribution that has been measured (contrary to the calculation of the standard correction factor takes into account the full range  $y \in [0, 1]$ ).
4. A new correction factor ( $cf$ ) is calculated using  $\bar{y}'$ .

$$cf = 1 / \bar{y}' \quad (17)$$

5. A new three-dimensional size value is calculated using  $cf$ .

$$\bar{\phi}_{3D} = \bar{\phi}_{2D} \cdot cf \quad (18)$$

6. The steps 2 to 5 are repeated until the difference between two consecutive three-dimensional values ( $\bar{\phi}_{3D}$ ) is lower than 1%.
7. Finally, an optimized value of the three-dimensional cell size is obtained.

## Results

### Number of analyzed cells

Developed process allows to measure a significant number of cells on each micrograph. Cells recognition can be improved using an appropriate magnification in the

micrograph acquisition. Micrographs showing 150–200 cells allows to measure around a 60–70% of the cells present in the image. While micrographs showing higher number of cells (500–800 cells) complicate the cell recognition, only around of 50% of the cells can be measured. However, in any case the total number of measured cells is high enough to obtain accurate results (Table 2).

### User influence on the results

One of the possible inconveniences of using an interactive measurement process is that the user might become the main source of inaccuracy, and he/she may need previous training and/or experience. To check this influence, five different users have analyzed the same image. The influence of user on the cell selection is showed in Figure 4 where results for the average two-dimensional cell size ( $\phi_{2D}$ ) and anisotropy ratio ( $A_{Y/X}$ ) are exhibited. It is important to mention that the image

**Table 2.** Total number of cells and cells measured on each micrograph.

Foam	Cells	Measured cells	Measured cells (%)
Polyurethane (PU)	149	105	70.5
Epoxy resin	182	115	63.2
Polypropylene-1 (PP-1)	732	406	55.5
Polypropylene-2 (PP-2)	261	109	41.8

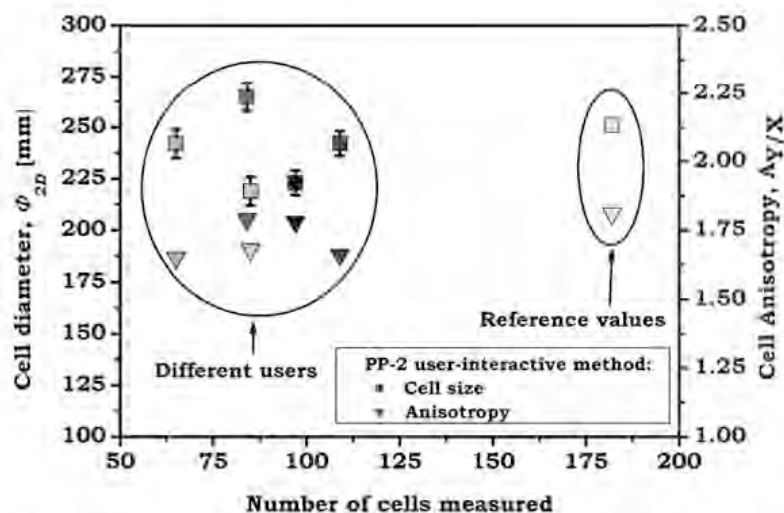


**Figure 4.** Average cell size and anisotropy ratio for five different users, plotted together with the reference values (manual overlay method).

corresponds to sample PP-2, with an inhomogeneous cellular structure (high standard deviation), in order to provide upper variance of user influence.

Results obtained by different non-trained users could reach maximum differences of 10%, but provided results are close to the exact values obtained by the manual overlay method. Therefore, a previous training in the use of the application is not needed to obtain high accurate results.

### Cell size (2D)

The average two-dimensional cell size ( $\bar{\phi}_{2D}$ ) of the four proposed materials could be determined using the overlay method, the intersections method and the developed interactive software application. It is important to remark that both the manual overlay method and the developed software calculate the average 2D cell size from directly measured two-dimensional values, while the intersections method calculates the average two-dimensional cells size from an one-dimensional average value using a correction factor (Eq. (1b)). Results are shown in Figure 5.

In general, the results provided by the developed application are closer to the reference values (provided by the overlay method), than the results provided by the intersections method. It is important to remark that the three methods provided similar results only with images with a very large number of homogeneous cells, such as Polypropylene-1 (PP-1) image, and that the intersections method does not provide accurate results in images with very heterogeneous cells, such as Polypropylene-2 (PP-2) image. Best results are obtained with the application in

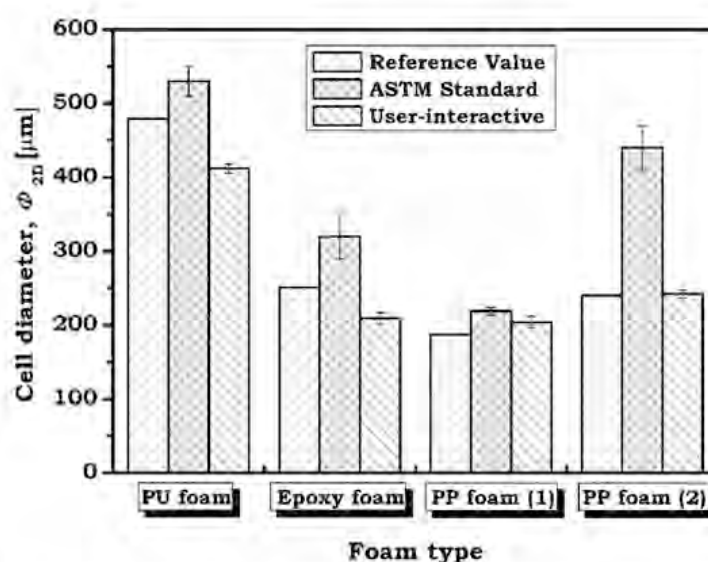


**Figure 5.** Two-dimensional cell size of the four foams obtained by three different methods.

foam images with higher number of cells, PP-1 and PP-2, probably due to statistical considerations.

### Cell size distribution (2D)

Manual overlay method and the developed application both provide results on the cell size distribution. Figure 6 shows the compared histograms of the analyzed images; maximum frequency has been normalized to one for comparison purposes.

Histograms obtained by both methods present a rather good agreement, the shape and general information of the cell size distribution could be obtained with accuracy by the developed application. Moreover, it could be observed that the developed application misses the smallest cells in the four materials analyzed. This effect is expected considering that smallest cells in each image have areas of a few square pixels and are binarized with difficulty. It is important to remark that this effect does not produce an overestimation in the calculation of the three-dimensional cell size, because the three-dimensional correction factor is calculated taking this into account (see section on Optimized correction factor).

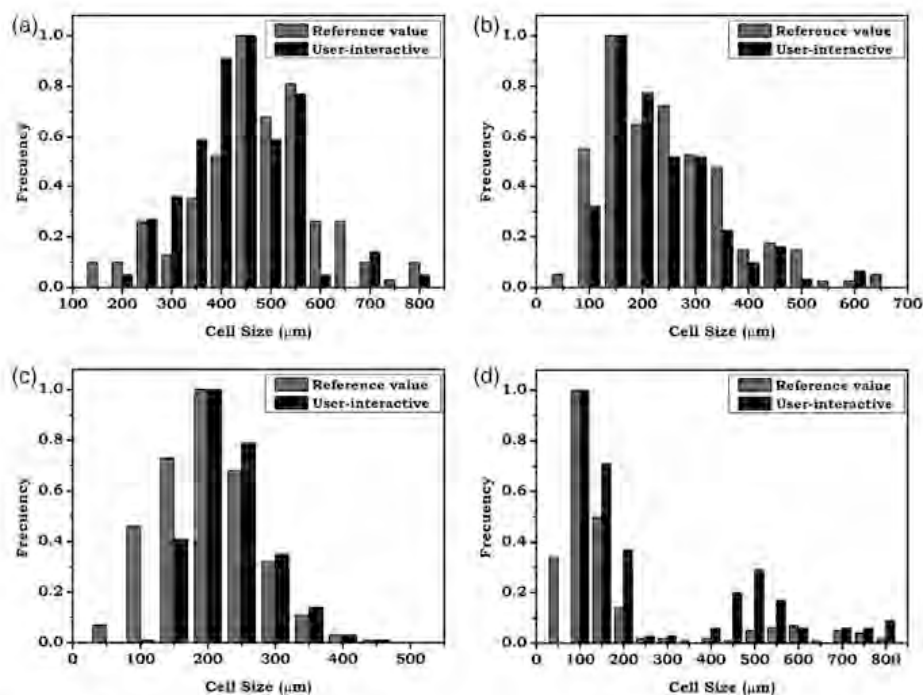


**Figure 6.** Compared cell size distribution for the different materials analyzed. (a) PU, (b) Epoxy, (c) PP-1, and (d) PP-2.



### Three-dimensional cell size estimation

The average three-dimensional cell size ( $\bar{\phi}_{3D}$ ) has also been comparatively analyzed for the proposed materials and methods, similarly to  $\bar{\phi}_{2D}$ , (Figure 7). In this case, Kumar's theoretical method directly provides a three-dimensional cell size, meanwhile the values given by the intersections method and the developed software are calculated using a correction factor. This correction factor used is 1.623 in the case of the intersections, ASTM standard, method (see section on ASTM standard correction factor). On the contrary, the user-interactive application calculates an optimized factor (see section on Optimized correction factor) used to transform the two-dimensional value into a three-dimensional value.

There is no exact reference to compare the results of the average three-dimensional cell size; all the methods provide an estimation of this value (a theoretical assumption is needed), so it is not possible to affirm which one is the most accurate (reference) method. However, it was previously shown that the intersections method provides inaccurate results for the average 2D cell size and thus the 3D value calculated from the 2D one will be less accurate.

### Anisotropy and cell orientation

The results on average cell anisotropy ratio ( $A_{Y/X}$ ,  $Y$  the vertical direction and  $X$  the horizontal one) for the proposed materials analyzed by the three methods are shown in Figure 8.

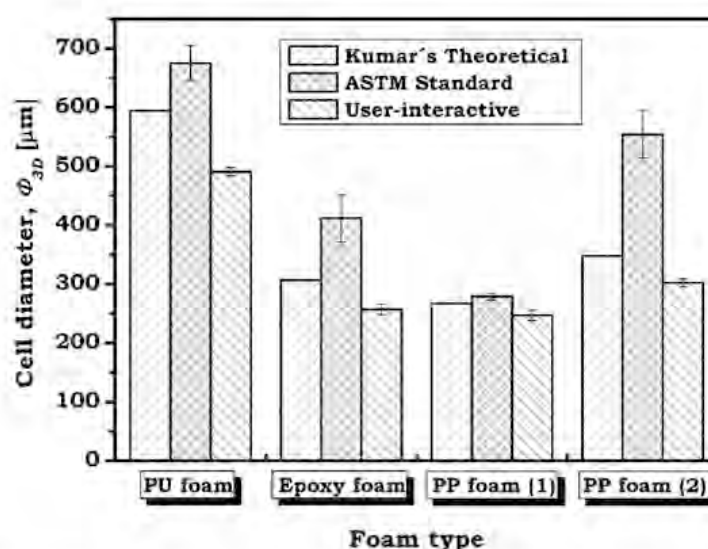


**Figure 7.** Three-dimensional cell size obtained by three different methods.

In this case, the obtained results are very similar, and the average anisotropy ratio ( $A_{Y/X}$ ) could be measured with high accuracy using any method. However, results provided by the intersections method present a higher deviation from the reference value, obtained by the overlay method. On the other hand, the values obtained by the software application match with the reference ones in most cases.

Additionally, the user-interactive application provides useful information on the preferred cell orientation. One of the advantages of this methodology is the possibility of determining the maximum anisotropy direction (angle), and the anisotropy value at that angle. Furthermore, maximum anisotropy and  $A_{Y/X}$  can be correlated as follow:

$$A_{Y/X} = A_{\max} \sin(\alpha_{\max}) \quad (19)$$

Figure 9 shows the orientation distribution of the main axis of cells present in sample PP-2. As it can be observed, this material presents an evident preferred orientation  $\alpha = 135^\circ$  ( $315^\circ$ ) with anisotropy values in that direction reaching values up to 5. Only a few cells are oriented out of the mentioned direction.

#### *Influence of anisotropy on the 3D cell size estimation*

Focusing on the comparative results for the Kumar's theoretical method and the developed software application (Figure 7), it is necessary to take into account that the theoretical method assumed a spherical shape for the cells. Similarly,

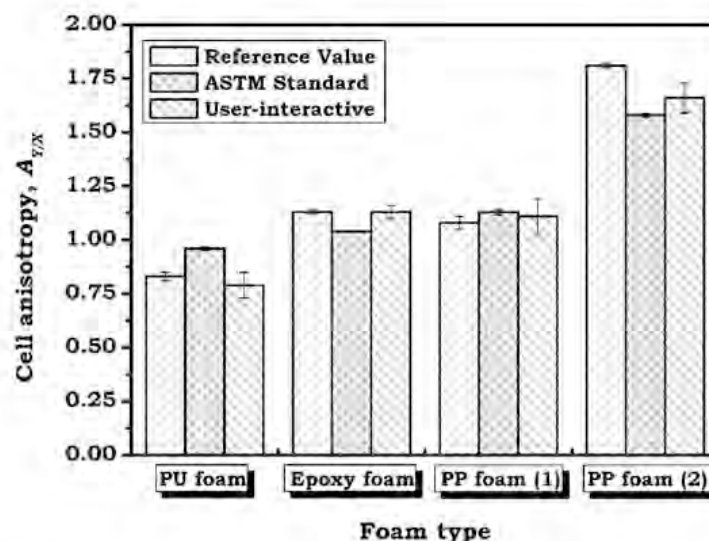


**Figure 8.** Anisotropy ratio for the four analyzed materials obtained by three different methods.

the extrapolation from 2D experimental results to 3D implies the use of a factor that assumes spherical cells, although in this case the factor only modifies an experimental value. Under this assumption, the presence of non-spherical pores will produce an over/underestimation of the expected cell size. Figure 10 shows a comparison of these two methods plotted versus the anisotropy ratio, used at this particular moment as a reference factor to check the compliance of Kumar's method to the experimental results.

As expected, theoretical estimations and experimental results present good agreement when conditions assumed by the theoretical method are matched, i.e. when cells are nearly spherical (anisotropy values near to one). In addition, the agreement between the two values decreases when the average cell anisotropy increases, and therefore the theoretical method cannot provide accurate results. This trend is clear in foams with an usual cells size distribution (monomodal), but not in foams with a bimodal cell size distribution such as PP-2 image, because there are small spherical cells and large cells with high anisotropy, so average values of cell size and anisotropy are not representative values.

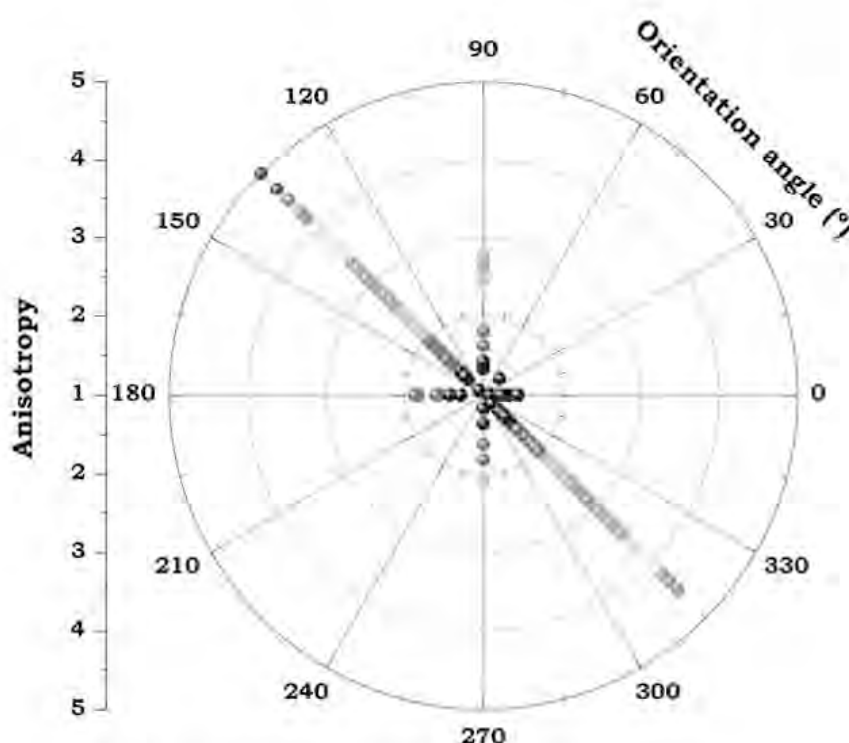


**Figure 9.** Cells main axis orientation angle distribution for PP-1.

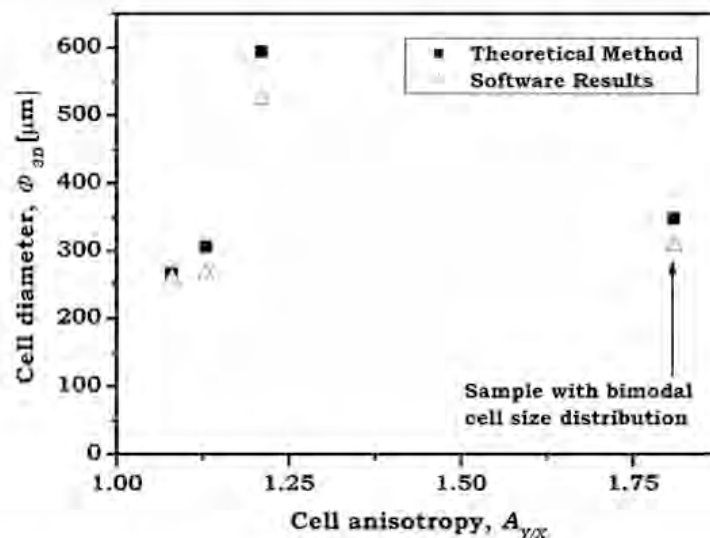


**Figure 10.** Influence of the cell anisotropy on the agreement between theoretical estimations and experimental results.

### Other results

The user-interactive application does not only provide the previous results but also statistical information on the cell size distribution (SD and AC), as well as other foam characteristics associated to the foaming process, such as the cell density and nucleation density values. Statistical data are calculated from the measured cell size distribution using equations (8) and (9), while the cell and nucleation densities are obtained from the previously explained Kumar's theoretical approximation. These results completing the application report are shown in Table 3.

From the observed results it can be assessed that the more homogeneous foam is PP-1, with a SD of 55  $\mu m$  while the more heterogeneous one is PP-2 with a SD of 204  $\mu m$  for a similar average cell size. As it can be also appreciated, results are in perfect agreement with the micrographs (Figure 1). These results can also be correlated to the cell size distribution histograms (Figure 6) which present "tails" to larger cell sizes and, in consequence, positive asymmetry coefficients for every foam. Moreover, the higher asymmetry corresponds to the Epoxy and PP-2 foams, as clearly shown in the histograms.

Obtained values for the cells and nucleation densities are in the expected ranges, taking into account the densities and cells sizes of these cellular materials.

**Table 3.** Other results provided by the developed application.

Foam	$\bar{\phi}_{2D}$ ( $\mu\text{m}$ )	SD ( $\mu\text{m}$ )	AC	$N_v$ (cell/ $\text{cm}^3$ )	$N_o$ (nuclei/ $\text{cm}^3$ )
Polyurethane (PU)	412	106	0.48	$8.7 \times 10^3$	$2.1 \times 10^5$
Epoxy resin	209	102	1.24	$5.1 \times 10^4$	$2.2 \times 10^5$
Polypropylene-1 (PP-1)	204	55	0.75	$7.8 \times 10^4$	$3.6 \times 10^5$
Polypropylene-2 (PP-2)	242	204	1.08	$3.6 \times 10^4$	$1.8 \times 10^5$

## Conclusions

It has been demonstrated that the developed application works properly with SEM images from materials with different cellular structures and densities. Cellular materials of both low and high densities, and cell sizes from nanometers to millimeters can be characterized using this method. The application allows obtaining better results in the characterization of two-dimensional parameters (such cell size and anisotropy ratio) than standard methods. In addition, the cell size distribution obtained presents good agreement with the reference one, and the limitations of the application to measure the smallest cells have been solved with the modification of the correction factor needed to calculate the three-dimensional cell size from a two-dimensional one. Therefore, the application provides a good estimation of the three-dimensional cell size, comparable to the results obtained with widely used theoretical expressions. In addition, it provides useful information not accessible by conventional techniques, such as the direction of preferential anisotropy, the standard deviation, and asymmetry coefficient of the cellular structure.

This new application provides a detailed characterization of the cellular structure of a porous material. The methodology combines a good agreement with the typical manual measurement values, with a short processing time, and due to this it could become an useful application in the cellular materials science.

Developed application and user manual will available soon in the Cellular Materials Laboratory website ([www.cellmat.es](http://www.cellmat.es)).

## Acknowledgements

Financial assistance from MCINN (MAT2009-14001-C02-01), European Spatial Agency (Project MAP AO-99-075), FPU grant AP2008-03603 (J. Pinto), and Juan de la Cierva grant JCI-2011-09775 (E. Solorzano) from the Spanish Ministry of Education is gratefully acknowledged.

## Funding

This research received no specific grant from any funding agency in the public, commercial, or not-for-profit sectors.

## References

1. Gibson LJ and Ashby MF. *Cellular solids: Structure and properties*. 2nd ed. Cambridge: UK, Cambridge University Press, 1997.
2. Rodriguez-Perez MA, Lobos J, Perez-Muñoz CA, et al. Mechanical behaviour at low strains of ldpe foams with cell sizes in the microcellular range: advantages of using these materials in structural elements. *Cell Polym* 2008; 27: 347–362.
3. Rodriguez-Perez MA. The effect of chemical composition, density and cellular structure on the dynamic mechanical response of polyolefin foams. *Cell Polym* 2002; 21: 117–136.
4. Reglero-Ruiz JA, Saiz-Arroyo C, Dumon M, et al. Production, cellular structure and thermal conductivity of microcellular (methyl methacrylate)–(butyl acrylate)–(methyl methacrylate) triblock copolymers. *Polym Int* 2011; 60: 146–152.
5. Rodriguez-Perez MA, Alonso O, Souto J, et al. Thermal conductivity of physically crosslinked closed cell polyolefin foams. *Polym Test* 1997; 16: 287–298.
6. Alvarez-Lainez M, Rodríguez-Perez MA and de Saja JA. Thermal conductivity of open-cell polyolefin foams. *J Polym Sci Polym Phys* 2008; 46: 212–221.
7. Wang X and Lu TJ. Optimized acoustic properties of cellular solids. *J Acoust Soc Am* 1999; 106: 756–765.
8. Cummings A and Beadle SP. Acoustic properties of reticulated plastic foams. *J Sound Vib* 1994; 175: 115–133.
9. ASTM D3576-04. Standard Test Method for Cell Size of Rigid Cellular Plastics, ASTM International: Plastics (II), 2010.
10. Rodriguez Perez. *Thermal and mechanical properties of polyolefin foams*. PhD Thesis, University of Valladolid, Spain, 1998.
11. Sims GLA and Khuniteekool C. Cell size measurement of polymeric foams. *Cell Polym* 1994; 13: 137.
12. Rodriguez-Perez MA, Alonso O, Duijsens A, et al. Thermal expansion of crosslinked closed-cell polyethylene foams. *J Polym Sci Polym Phys* 1998; 36: 2587–2596.
13. Goel SK and Beckman EJ. Generation of microcellular polymeric foams using supercritical carbon dioxide. II: Cell growth and skin formation. *Polym Eng Sci* 1994; 34: 1148–1156.
14. Pourdeyhimi B. Imaging and image analysis applications for plastics. William Andrew Publishing/Plastics Design Library, 1999, pp.241–248.
15. Lewis KM, Kijak I, Reuter KB, et al. An image analysis method for cell-size and cell-size distribution measurement in rigid foams. *J Cell Plast* 1996; 32: 235.
16. Torres MC. *Generation of heterogeneous cellular structures by sonication*. PhD thesis, Heriot-Watt University, Edinburgh, 2008.
17. Schwartz NV and Bomberg MT. Image analysis and the characterization of cellular plastics. *J Build Phys* 1991; 15: 153.
18. Landers R, Venzmer J and Boinowitz T. Methods for Cell Structure Analysis of Polyurethane Foams. In: *Proceedings of the polyurethane conference (API)*, Houston, Texas, 17–19 October 2005.
19. Kumar V. *Process synthesis for manufacturing microcellular thermoplastic parts*. PhD Thesis, Massachusetts Institute of Technology, Cambridge, MA, 1988.
20. Gosselin R and Rodrigue D. Cell morphology analysis of high density polymer foams. *Polym Test* 2005; 24: 1027–1035.

21. Weller JE and Kumar V. Solid-state microcellular polycarbonate foams. I. The steady-state process space using subcritical carbon dioxide. *Polym Eng Sci* 2010; 50: 2160–2169.
22. Reglero JA, Dumon M, Pinto J, et al. Low-density nanocellular foams produced by high-pressure carbon dioxide. *Macromol Mater Eng* 2011; 296: 752–759.
23. Sahagian DL and Proussevitch AA. 3D particle size distributions from 2D observations: stereology for natural applications. *J Volcanol Geotherm Res* 1998; 84: 173–196.
24. Rhodes MB and Khaykin B. Foam characterization and quantitative stereology. *Langmuir* 1986; 2: 643–649.
25. Montminy MD, Tannenbaum AR and Macosko CW. New algorithms for 3-D imaging and analysis of open-celled foams. *J Cell Plast* 2001; 37: 501.
26. Fetterman MR, Tan E, Ying L, et al. Tomographic imaging of foam. *Opt Express* 2000; 7: 186.
27. Monnereau C and Vignes-Adler M. Optical tomography of real three-dimensional foams. *J Colloid Interf Sci* 1998; 202: 45–53.
28. Thomas PD, Darton RC and Whalley PB. Resolving the structure of cellular foams by the use of optical tomography. *Ind Eng Chem Res* 1998; 37: 710–717.
29. Maire E, Colombo P, Adrien J, et al. Characterization of the morphology of cellular ceramics by 3D image processing of X-ray tomography. *J Eur Ceram Soc* 2007; 27: 1973–1981.
30. Maire E, Fazekas A, Salvo L, et al. X-ray tomography applied to the characterization of cellular materials. Related finite element modeling problems. *Compos Sci Technol* 2003; 63: 2431–2443.
31. Abramoff MD, Magalhaes PJ and Ram SJ. Image processing with ImageJ. *Biophotonics Int* 2004; 11: 36–42.

### I.1.3 Density homogeneity of foamed samples

Study of the polymer/fraction of voids spatial distribution on polymeric cellular materials can provide valuable information about the foaming mechanisms of these materials. In addition, the presence of structural defects or inhomogeneities can produce a reduction of the expected properties of these materials (e.g. structural defects can reduce the mechanical properties of a cellular material providing starting points for a mechanical failure).

A main characteristic of the cellular materials produced by solid state foaming is the presence of a foamed core and an outer solid skin. This structure appears due to the changes in the gas concentration profile inside the polymer sample during the desorption stage, and the existence of a minimum gas concentration needed to trigger the homogeneous cell nucleation [12]. Characterization of the solid skin thickness is usually carried out by SEM [12], being necessary to extract samples from the studied foam, and to take a large number of SEM images to obtain an average value. Therefore, study of the core-solid skin structure requires a destructive characterization method.

Also, the presence of internal defects or density inhomogeneities is usually studied by destructive methods. Internal defects can be detected by cutting the sample to reveal the internal structure, and inhomogeneities are studied by measuring the density of several samples extracted from different areas of the studied foam.

An alternative to these destructive methods is the X-ray radiography technique (or X-ray radioscopy technique if the study also has time resolution). Application of these non-destructive techniques to the study of cellular materials is widely studied in the journal article “*Application of a microfocus X-ray imaging apparatus to the study of cellular polymers*” (E. Solórzano, J. Pinto, S. Pardo, F. García-Moreno, M. A. Rodríguez-Perez) published in **Polymer Testing vol. 32 (2013)** [13]. These techniques allow studying the internal structure and density distribution of the samples preserving their integrity. Figure I.3 shows examples of the density distribution determination and internal defects detection over X-ray radiographies of the nanocellular foams of this thesis.



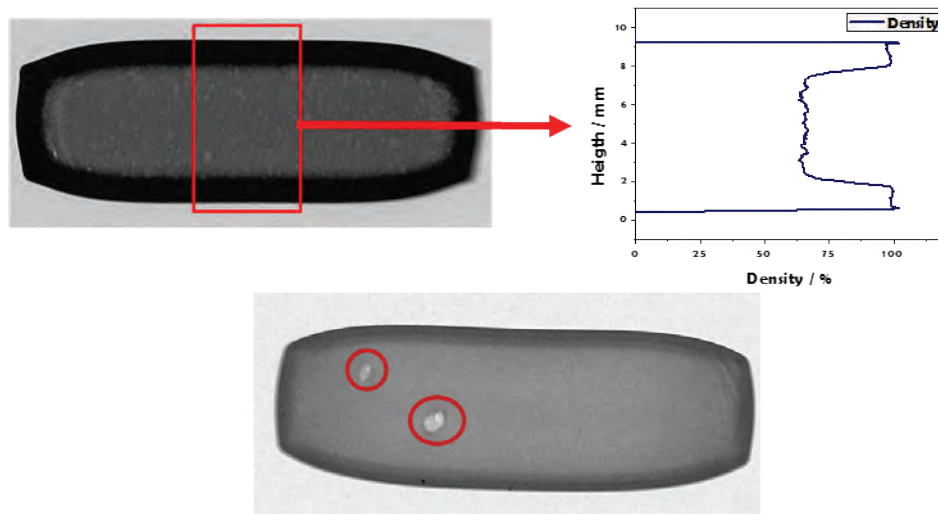


**Figure I.3: Determination of the density distribution profile (up, average density profile is obtained from the region identified with a red rectangle) and detection of internal defects (down, defect are identified with red circles) on polymeric foams by X-ray radiography.**

Basic fundamentals of this technique and a description of the experimental device used on this research are summarized in the following subsections.

#### *1.1.3.1 X-ray imaging fundamentals*

The typical energy of X-rays photons ranges from 100 eV up to 20 MeV (see Figure I.4). Therefore this penetrating radiation seems to be appropriate for obtaining structural information of matter since the distance in between atoms is  $10^{-10}$  m approximately. The penetration power of X-rays is rather high and thus it allows for transmission imaging. However, for imaging purposes the useful energies are 5-150 keV, except in some special cases (industrial processes) where 500 keV can be applied. Too soft X-rays do not penetrate deeply enough and too hard X-rays simply are not absorbed leading to poor contrast

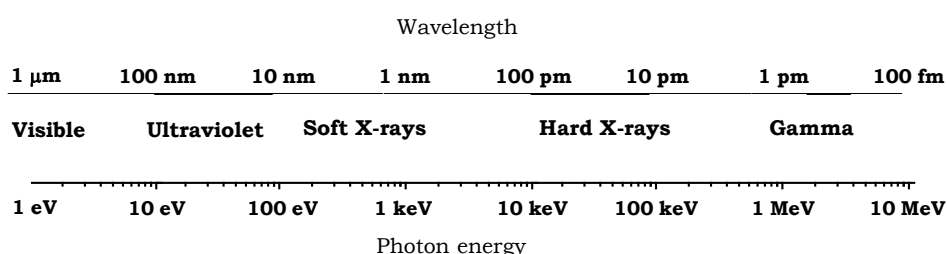


**Figure I.4: Electromagnetic spectrum of energies and wavelengths**

### 1.1.3.2 Matter-beam interaction

X-rays interact with matter in a number of different ways that can be used for imaging: electron photoemission, elastic and inelastic scattering fluorescence (see Figure I.5). Hence, X-ray detection techniques can be classified based on the particle-matter interaction that is used to form the image. Conventional X-ray imaging relies on transmission measurement that is determined by object beam absorption. Photoelectric absorption and inelastic scattering are mainly contributing to absorption. Elastic scattering is also contributing to absorption although it is more related to macroscopic refraction effect.

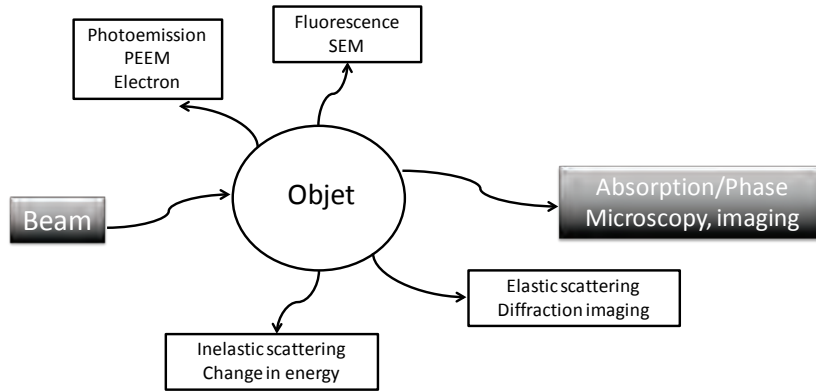


**Figure I.5: X-ray and matter interaction producing elastic and inelastic phenomena as a result**

The physical fundamentals of radiation absorption are based on the Beer-Lambert equation shown in Equation I-3. This expression predicts the attenuation of incident monochromatic (it is usually not true in this simple form for polychromatic beams) X-ray radiation by an exponential function of the linear absorption coefficient ( $\mu$ ), the element concentration ( $c$ ) and the thickness ( $t$ ). Additionally, it is possible to estimate an effective linear attenuation coefficient,  $\mu_{eff}$ , if several elements are contained in the irradiated material and for polychromatic beam, as shown in Eq. I-4. Finally, it is sometimes used more conveniently mass attenuation coefficient by defining  $\mu_m = \mu_{eff}/c$ .

$$I = I_0 e^{-\mu c t} \quad [\text{I-3}]$$

$$I = I_0 e^{-\mu_{eff} c t} \quad [\text{I-4}]$$

The attenuation coefficient,  $\mu$ , also varies with incident radiation wavelengths and energy. It is also important to note that a relationship of the captured intensity (non-absorbed by the material) and the density ( $\rho$ ) can be established. In the specific case of monochromatic beam and pure element, the attenuation coefficient can be further extended and related to atomic number,  $Z$ . High atomic weight ( $Z$ ) materials such as metals will stop X-ray radiation immediately (either by absorbing, reflecting or dispersing it), whereas materials with light molecular weight made for instance from carbon and hydrogen (polymers) will let almost all light to pass. This is shown in Figure I.6. It is also important to comment

that mass attenuation coefficient of elements constituting polymers are much higher for other radiations such as neutrons.

Imaging mainly works on absorption phenomena since we have seen that matter attenuates X-ray radiation. Therefore, in transmission imaging, the transmitted radiation is the information captured by the detection system as 2D image (radiography).

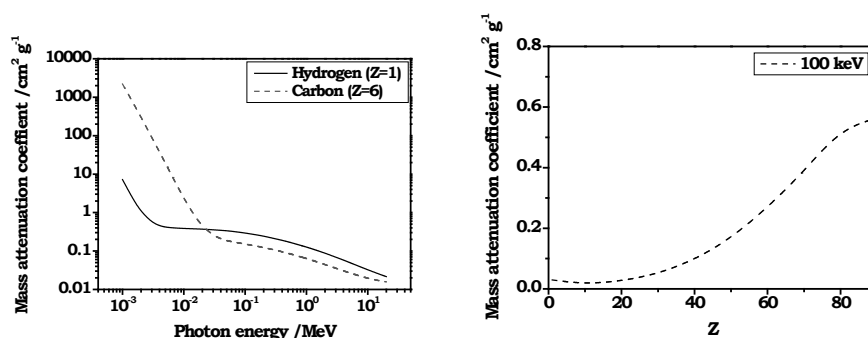


**Figure I.6: Left: attenuation coefficient of elements typically contained in polymers: hydrogen and carbon. Right: attenuation coefficient variation with  $Z$  in the periodic table.**

### *1.1.3.3 Microfocus X-ray system at CellMat*

The X-ray imaging device used in this work has been recently built in CellMat. It is a valuable tool able to obtain information about polymer foaming processes. Both the X-ray tube and the detector needed careful selection since polymers present low X-rays absorption coefficient and foaming is a process evolving rapidly. In this sense low energies of the emitted X-rays are suitable for imaging polymers although detectors are not conceived for low energies. The high sensitivity of the detector response is thus of extreme importance. Moreover, dimensions of cellular structure are in the order of microns and therefore high resolution is also relevant, thus needed small spot focus size and small pixel size in the detector.

#### Microfocus X-ray source L10101:

A closed air-cooled microfocus X-ray source L10101 (Hamamatsu, Japan) is used to produce the X-rays. In this tube an ultrafine electron beam produces X-rays, striking on a tungsten target in high vacuum atmosphere. Then the tungsten surface that is irradiated by the electrons produces X-rays. X-rays come out the source through a Beryllium 150  $\mu\text{m}$ -thick window forming an X-ray conic beam of  $39^\circ$ . The microfocus spot size of 5  $\mu\text{m}$  tends to slightly broaden as electron acceleration voltage or current

increase, up to a maximum of 20  $\mu\text{m}$ . Nevertheless, the spot size remains in its smaller size (i.e. 5  $\mu\text{m}$ ) meanwhile these values keep below 40% of maximum power. The maximum intensity (current) is limited by the produced voltage according to graph in Figure I.7. The technical characteristics are summarized in Table I-2.

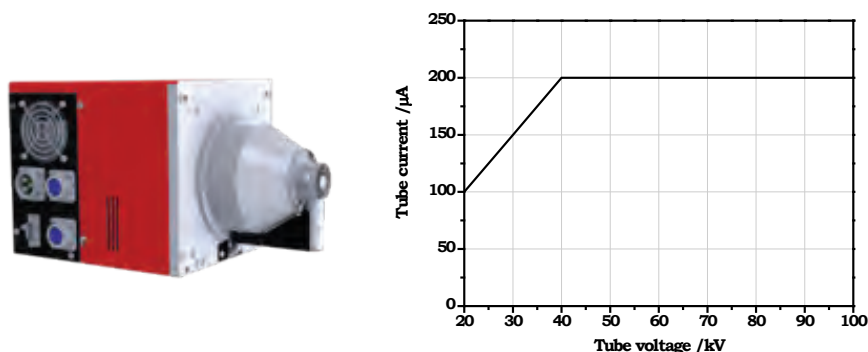


Figure I.7: X-ray tube L10101 from Hamamatsu. Maximum power output curve

Table I-2: Technical characteristics of X-ray tube L10101

Spot size	5-20 $\mu\text{m}$
Voltage	20-100 kV
Current	0-200 $\mu\text{A}$
Maximum power output	20 W

#### Flat panel detector:

The detection system is a flat panel (FP) from Hamamatsu (Japan) C7940DK-02 (Figure I.8). This high resolution detector is composed by a matrix of 2240 x 2344 pixels with a pixel size of 50  $\mu\text{m}$ , i.e. sizing 111.50 x 117.20 mm. The digital output is a 12 bits depth resolution with maximum acquisition velocity up to 9 fps working at 4 x 4 binning mode.

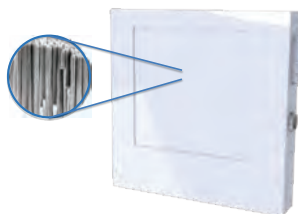
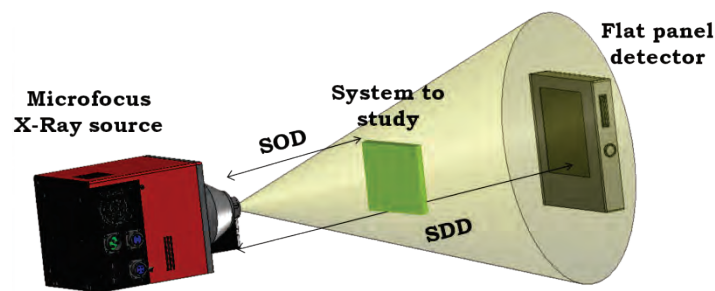


Figure I.8: Flat panel detector and micrograph of CsI needle grow crystals

This flat panel detection technology consists in deposited scintillator material CsI, layer directly in front of a CMOS detector. One of its main advantages yields in the small dimensions of the complete high resolution imaging apparatus. The scintillating material is grown in special needle-like shape in order to improve light transmission in the normal direction and thus reduce photons scattering. It is important that the diameter of the grown needled material is smaller than or similar to the CMOS pixel size, i.e. 50 microns for our particular case.

#### System configuration:

X-ray tube and FP detector are settled on in front of each other inside a X-ray shielded lead cabinet, as seen in Figure I.9. In principle, it is possible to position them at any distance, *SDD*, but in general optimum distances are in the range of 0.3 to 1.2 m. As the beam is cone-spread the more distant the less radiation the FP-detector receives, which, in principle, is positive for its lifetime but reduces image quality since different artifacts effects increase with distance. In this particular device, the box dimensions limit this distance and it was chosen at 580 mm, becoming a compromise distance for all the involved factors. The objects to be imaged can be placed at any position in between the detector and the source. The fact of having diverging (cone-beam) X-ray beam allows for object magnification. Magnification factor (*M*) is a function of the object to source distance (*OSD*) compared to the total distance from the source to the detector (*SDD*). Thus magnification is defined as indicated in Eq. I-5.



**Figure I.9: Magnification scheme obtained thanks to cone-beam geometry**

$$M = \frac{SDD}{OSD} \quad \text{[I-5]}$$

The CellMat device also includes a metric lab-jack mounted on displacement rails for sample positioning, power and thermocouple connections, compressed air, and PID controller (Figure I.10). All these complements are installed in order to facilitate polymer foaming experiments which frequently require temperatures over 200° C inside the shielded cabinet. A thermostat controls inside temperature.

Additionally a pneumatic shutter is placed to avoid unnecessary exposure time of the detector during X-rays source heating up or during long experiments. This extends the life of the flat panel detector and prevents lag undesired effects.

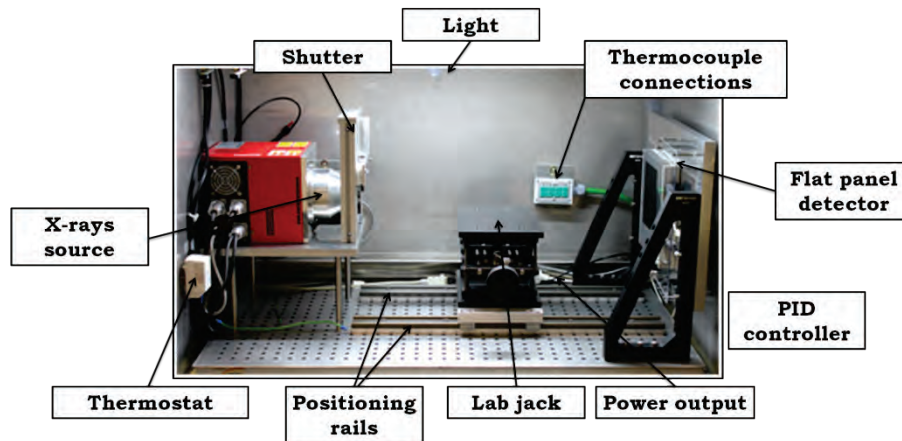


Figure I.10: X-ray device with all complementary connections

#### Acquisition software and hardware:

With respect to the software for controlling the complete imaging device, the X-ray tube has its own control tool (MFX Control Software) which facilitates the warm-up process and the beam emission control. The commercial software HiPic v8.3 from Hamamatsu is used to control the acquisition and store the images (Figure I.11).

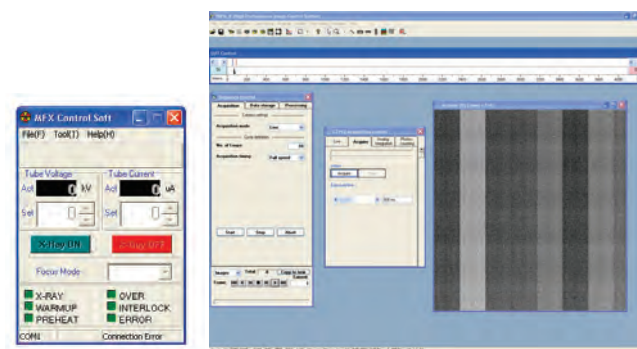


Figure I.11: Hamamatsu software for the X-ray source beam control and the detector acquisition

Complementarily, self-developed software has been programmed under LabView environment (Figure I.12). The main objective is to have an integrated software which controls temperature, X-ray tube, and image acquisition in a single window. The software is programmed based on a states machine workflow. The detector control by Labview is done thanks to SDK library already implemented by Hamamatsu Germany. This library includes the SubVIs necessary to run in a batch mode all the HiPic v8.3 functionalities.

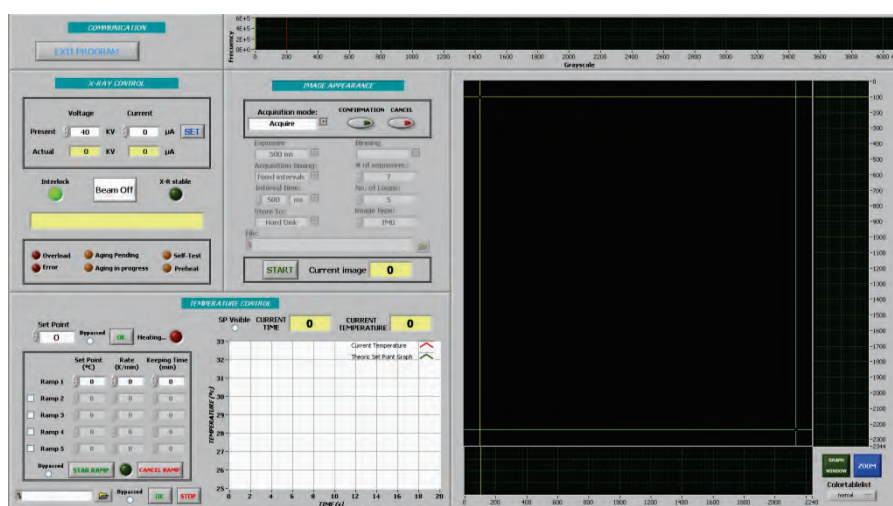


Figure I.12: Integrated control software developed on CellMat

#### 1.1.3.4 Determination of density profiles of polymeric foams by X-ray radiography

Determination of the density profile of polymeric foams requires samples with a homogeneous thickness. Appropriate samples from PMMA and PMMA/MAM foams were obtained using a precision saw (mod. 1000, Isomet) with a thickness about 2 mm.

X-ray radiographies from these samples were taken using the following parameters:  $V = 35$  kV,  $I = 120$   $\mu$ A, and  $t = 1200$  ms ( $V$  and  $I$  are the voltage and current intensity of the X-ray source, and  $t$  is the exposition time of the detector used to take the image). Moreover, a *background* and *brighthfield* images were taken with the same parameters (the *background* is taken with the X-ray source off, while the *brighthfield* is taken without sample and with the X-ray source on) to be used in the correction of the images previous to their analysis.

Density profiles were obtained from the X-ray radiographies using a specific software based on FIJI/ImageJ developed in CellMat Laboratory. Inputs of the software are the average density of the sample (measured independently by Archimedes' method) and the selection of one area of the image filled by the sample, and other area of the image without sample. The software measures the average radiation intensity value from these areas, and relates then with their densities (average density of the sample in the first case, and zero (no sample, just air) in the second case) using expressions derived from Eq. I-3. By this way a calibration between the radiation intensity and the samples density is obtained. Then, using this calibration the software can calculate the density profile of the area of the sample selected to be measured, as Figure I-3 shows. More details can be found in the previously mentioned paper "Application of a microfocus X-ray imaging apparatus to the study of cellular polymers" [13].



### I.1.4 Thermal conductivity of foams

Thermal conductivity of microcellular and nanocellular foams was measured by the Transient Plane Source (TPS) technique using a thermal conductivimeter mod. HDMD (Hotdisk). TPS is a standard technique for thermal properties characterization of different materials (metals, ceramics, polymers, liquids, etc.) [14].

#### I.1.4.1 An introduction to the TPS method

Measurement of thermal conductivity by means of the TPS method has been demonstrated elsewhere [15-21]. The basic principle of this method relies on a plane element which acts both as temperature sensor and heat source. This element consists of an electrically conducting pattern of thin nickel foil ( $10\ \mu\text{m}$ ) spiral-shaped, embedded in an insulation layer usually made of Kapton ( $70\ \mu\text{m}$  thick). The TPS element is located between two samples with both sensor faces in contact with the two surfaces as Figure I.13 depicts. Two samples of similar characteristics are required for this purpose.

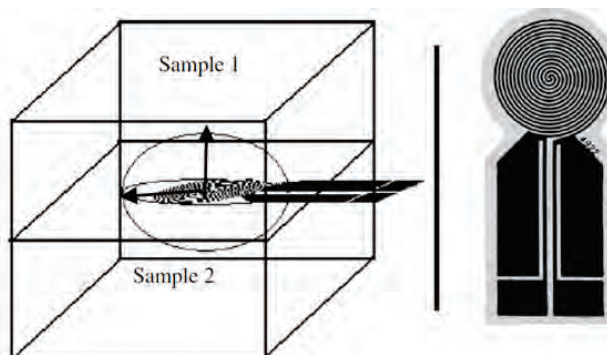


**Figure I.13: Experimental set-up to perform TPS measurements and sensor shape**

This method offers some advantages in comparison with other standard methods, such as fast and easy experiments, wide ranges of measurement temperatures ( $50\ \text{K} < T < 1000\ \text{K}$ ) and thermal conductivities accessible (from  $0.01$  to  $500\ \text{W/m}\cdot\text{K}$ ), measurement can be carried out at atmospheric pressure or under vacuum conditions, marginal effort needed in sample preparation, flexibility in sample size and a possibility to perform local or bulk measurements with only changing the sensor diameter.

It is important to remark that this is a contact method, so special care has to be taken to minimize thermal contact resistance. The good heat transition through two different materials is mainly associated to contact pressure and surface roughness [22, 23].



Moreover, the TPS equipment is able to compensate the heat capacity of the sensor and other thermal delays of the heat flow by introducing a time correction. Nevertheless, it is necessary to suppress the first 20-30 points of each measurement (of a total of 200 points of the heating curve) to eliminate the heat capacity of the sensor that cannot be fully compensated by the time correction [17, 18, 24].

Finally, to avoid residual temperature drifts on the samples, it is necessary to fix a time spam between individual experiments on each specimen.

#### *I.1.4.2 Experimental procedure*

The CellMat TPS device is composed by the TPS sensor, TPS controller unit associated to a computer, a vacuum chamber, rotary vacuum pump (Edwards, mod. RV3 A65201903), and a vacuum sensor (BOC Edwards, mod. WRG-S) (Figure I.14).

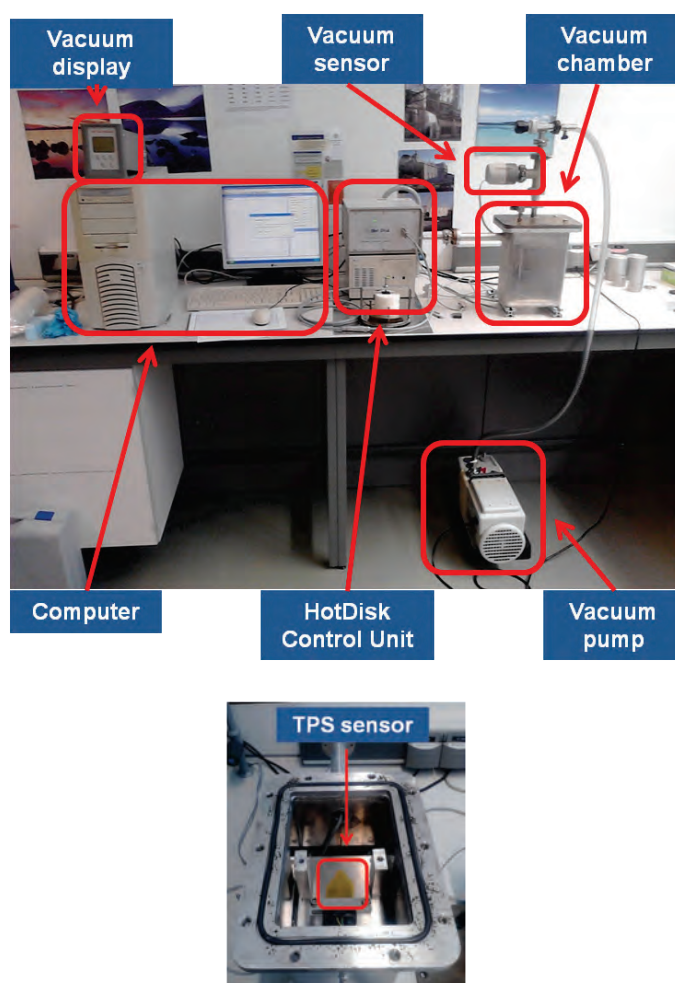


**Figure I.14: General view of the CellMat TPS device (up). Detail of the TPS sensor inside the vacuum chamber (down).**

Samples preparation and measurement were carried out following the next steps:

1° Samples were studied by X-ray radiography to exclude those foams presenting defects or inhomogeneities that could be an important source of inaccuracy in the thermal conductivity measurements.

2° Samples were polished using a polishing machine (mod. LaboPol2-LaboForce3, Struers) equipped with a silicon carbide grinding paper (P 600) to assure an appropriate contact with the sensor faces and to remove the outer solid or densified skin (if any). After polishing, samples had an average thickness about 5 mm.

3° Samples were dried during 4 h at 50° C.

4° Samples were stored at controlled temperature and humidity (23° C and 50% humidity) at least 3 days before the measurements.

5° Samples were placed in the experimental set-up, inside the vacuum chamber, with a constant pressure between the two pieces. After samples placement the vacuum chamber was closed.

6° Samples and experimental set-up were allowed to reach an equilibrium temperature (experiments were carried out in an environment with controlled temperature) before the beginning of the measurements (typically 30 minutes).

7° Measurement parameters (power and time) were adjusted to ensure accurate results. Typical parameters to measure PMMA-based foams are about 0.006 watt and 50 seconds.

8° Samples were measured five times at atmospheric pressure. Time span to avoid temperature drift was fixed on 5 minutes.

9° After the measurement under atmospheric pressure the rotary vacuum pump was activated.

10° After reaching the desired vacuum conditions, samples and experimental set-up were allowed again to reach an equilibrium temperature before the beginning of the measurements (typically 60 minutes).

11° Measurement parameters (power and time) were adjusted to ensure accurate results. It should be noticed that measurement parameters usually change between atmospheric pressure and vacuum conditions. Parameters used at atmospheric pressure can damage the sample and the sensor due to the lower heat dissipation under vacuum conditions. In general, samples under

vacuum conditions require lower power and higher measuring time (e.g., atmospheric pressure:  $w = 0.006$  W and  $t = 50$  s; vacuum:  $w = 0.005$  W and  $t = 60$  s).

12° Samples were measured twelve times at vacuum conditions. Time spam to avoid temperature drift was fixed on 60 minutes. Also these measurements during 12 hours allowed detecting if an evolution of the thermal conductivity occurs (due to a slow and progressive extraction of the gas inside the foam).

13° Thermal conductivities of the samples, both measured at atmospheric pressure and under vacuum conditions, were calculated using the software provided with the TPS device. Calculations were made selecting the “*Standard Analysis*” and neglecting the first 25 measured points to eliminate the heat capacity of the sensor.

14° Taking into account the average cell size and density of the measured foams, their total thermal conductivity ( $\lambda_t$ ) is contributed only by the thermal conductivity through the solid ( $\lambda_s$ ) and gaseous ( $\lambda_g$ ) phases (more details can be found in Chapter V). Measurements carried out at atmospheric pressure allow obtaining  $\lambda_t$ ; whereas measurements under vacuum conditions provide  $\lambda_s$  (assuming that the gas inside the voids of the foam is completely extracted); therefore,  $\lambda_g$  can be calculated from the previous values, obtaining by this way a complete characterization of the thermal conductivity of these foams.

## I.2 References

1. Ruzette, A.-V., S. Tencé-Girault, L. Leibler, F. Chauvin, D. Bertin, O. Guerret and P. Gerard, *Molecular disorder and mesoscopic order in polydisperse acrylic block copolymers prepared by controlled radical polymerization*. *Macromolecules*, 2006. **39**(17): 5804-5814.
2. Reglero Ruiz, J.A., M. Dumon, J. Pinto and M.A. Rodríguez-Pérez, *Low-Density Nanocellular Foams Produced by High-Pressure Carbon Dioxide*. *Macromolecular Materials and Engineering*, 2011. **296**(8): 752-759.
3. Garcia, R. and A. San Paulo, *Attractive and repulsive tip-sample interaction regimes in tapping-mode atomic force microscopy*. *Physical review letters* B, 1999. **60**: 4961-4967.
4. Garcia, R., C.J. Gómez, N.F. Martínez, S. Patil, C. Dietz and R. Margerle, *Identification of Nanoscale Dissipation Processes by Dynamic Atomic Force Microscopy*. *Physical review letters*, 2006. **97**(1): 016103.
5. Harris, J.R., C. Roos, R. Djalali, O. Rheingans, M. Maskos and M. Schmidt, *Application of the negative staining technique to both aqueous and organic solvent solutions of polymer particles*. *Micron*, 1999. **30**(4): 289-298.
6. Ferrer, G.G., M.S. Sánchez, J.L.G. Ribelles, F.J.R. Colomer and M.M. Pradas, *Nanodomains in a hydrophilic-hydrophobic IPN based on poly(2-hydroxyethyl acrylate) and poly(ethyl acrylate)*. *European Polymer Journal*, 2007. **43**(8): 3136-3145.
7. Chen, W., M. Zhu, S. Song, B. Sun, Y. Chen and H.-J.P. Adler, *Morphological Characterization of PMMA/PAN Composite Particles in Nano to Submicro Size*. *Macromolecular Materials and Engineering*, 2005. **290**(7): 669-674.
8. Dronet, S., *Matériaux nanostructurés obtenus par combinaison de polymérisation radicalaire contrôlée et mélangeage réactif*, 2009, Université Pierre et Marie Curie.
9. Li, X.Q., P.Z. Chen and C.H. Pin, *Polymer Materials Science and Engineering*, 1999. **15**: 129.
10. Maiez, S., *Relations entre la structure d'un copolymère à blocs et la nanostructuration d'un polymère réticulé*, 2007, INSA Lyon.
11. Lalande, L., *Structure et mécanismes de microdéformation de polyméthylméthacrylates renforcés au choc*, 2007, Ecole Polytechnique Federale de Lausanne.
12. Kumar, V. and J.E. Weller, *A model for the unfoamed skin on microcellular foams*. *Polymer Engineering & Science*, 1994. **34**(3): 169-173.
13. Solórzano, E., J. Pinto, S. Pardo, F. Garcia-Moreno and M.A. Rodríguez-Pérez, *Application of a microfocus X-ray imaging apparatus to the study of cellular polymers*. *Polymer Testing*, 2013. **32**(2): 321-329.
14. UNE-EN ISO 22007-2, A.C., *Determinación de la conductividad térmica y la difusividad térmica. Parte 2: Método de la fuente de calor plana transitoria (disco caliente)*, in *Plásticos* 2012, AENOR. 23.
15. Solórzano, E., J.A. Reglero, M.A. Rodríguez-Pérez, D. Lehmkus, M. Wichmann and J.A. de Saja, *An experimental study on the thermal conductivity of aluminium foams by using the transient*

- plane source method*. International Journal of Heat and Mass Transfer, 2008. **51**(25–26): 6259-6267.
16. Solórzano, E., M.A. Rodríguez-Pérez and J.A. de Saja, *Thermal Conductivity of Cellular Metals Measured by the Transient Plane Sour Method*. Advanced Engineering Materials, 2008. **10**(4): 371-377.
  17. Gustavsson, M., E. Karawacki and S.E. Gustafsson, *Thermal conductivity, thermal diffusivity and specific heat of thin samples from transient measurements with hot-disk sensors*. Review of Scientific Instruments, 1994. **65**: 3856-3859.
  18. Log, T. and S.E. Gustafsson, *Transient Plane Source (TPS) technique for measuring thermal transport properties of building materials*. Fire Materials, 1995. **19**: 39-43.
  19. Reglero Ruiz, J.A., C. Saiz-Arroyo, M. Dumon, M.A. Rodríguez-Pérez and L. Gonzalez, *Production, cellular structure and thermal conductivity of microcellular (methyl methacrylate)–(butyl acrylate)–(methyl methacrylate) triblock copolymers*. Polymer international, 2011. **60**(1): 146-152.
  20. Almanza, O., M.A. Rodríguez-Pérez and J.A. De Saja, *Applicability of the transient plane source method to measure the thermal conductivity of low-density polyethylene foams*. Journal of Polymer Science Part B: Polymer Physics, 2004. **42**(7): 1226-1234.
  21. Almanza, O., M. Rodríguez-Pérez and J. de Saja, *Measurement of the thermal diffusivity and specific heat capacity of polyethylene foams using the transient plane source technique*. Polymer international, 2004. **53**(12): 2038-2044.
  22. Singhal, V., P.J. Litke, A.F. Black and S.V. Garimella, *An experimentally validated thermo-mechanical model for the prediction of thermal contact conductance*. International journal of heat and mass transfer, 2005. **48**: 5446-5459.
  23. Wolff, E.G. and D.A. Schneider, *Prediction of thermal contact resistance between polished surfaces*. International journal of heat and mass transfer, 1998. **41**: 3469-3482.
  24. Gustafsson, S.E., *Transient Plane Source (TPS) technique for thermal conductivity and thermal diffusivity measurements of solid materials*. Review of Scientific Instruments, 1991. **62**: 797-804.



***Chapter II:***  
***PMMA/MAM blends and foams  
production and consequent  
nanostructuration and cellular  
structure***





## Chapter II. PMMA/MAM blends and foams production and consequent nanostructuration and cellular structure

In this chapter the characteristics of the polymers employed in this work are presented. First, the main properties of PMMA and MAM, and the production route of PMMA/MAM blends are described.

As explained before PMMA/MAM blends present a phase-separated morphology due to self-assembly of incompatible but covalently linked PBA-PMMA blocks (these nano separated regular patterns produce a nanostructuration). For a ll M AM c oncentrations, P MMA/MAM bl ends a re t ransparent a nd different nanostructures are evidenced. A wide selection of micrographs of the PMMA/MAM morphologies by AFM a nd T EM are included i n t his chapter. Morphological c onsiderations a bout t he influence of t he MAM amount on the nanostructuration, homogeneity and anisotropy of injected bulk samples, and the influence of the CO<sub>2</sub> saturation process over the nanostructure are discussed.

Second, t he pr oduction r oute of P MMA/MAM f oams i s explained. F or a ll M AM c oncentrations, PMMA/MAM foams can be pr oduced by gas dissolution foaming a t different pressure and temperature conditions. This c hapter i ncludes a wide s election of S EM micrographs of t he P MMA/MAM c ellular structures, analyzing general aspects of the cellular structure such as the homogeneity, anisotropy, and influence of the CO<sub>2</sub> saturation pressure.

Quantification of the nanostructuration characteristics (% of area of nanodomains, density of dispersed nanodomains), a detailed description of the cellular structure (average cell size, porosity, density of cells), and the relationships between the nanostructure and the cellular structure of the foams can be found in Chapter III.

### II.1 Materials

This r esearch was c arried out us ing P MMA a nd M AM a s raw materials, bo th p olymers a re optically transparent, and were kindly supplied in the form of pellets by Arkema Company (France).

#### II.1.1 Poly(methyl methacrylate) (PMMA)

PMMA is an amorphous polymer, whose chemical formula is shown on Figure II.1.

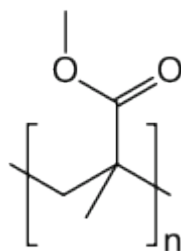


Figure II.1: Chemical formula of PMMA

Particular PMMA in our study is a pure homopolymer (without impact modifier), with a density ( $\rho$ ) of  $1.18 \text{ g/cm}^3$ , glass transition temperature ( $T_g$ ) about  $112^\circ \text{C}$ , and the following characteristics  $M_w \approx 83000 \text{ g/mol}$ ,  $M_n \approx 43000 \text{ g/mol}$ ,  $I_p \approx 1.9$  (molar mass values are related to polystyrene standards).

### II.1.2 Poly(methyl methacrylate)-co-poly(butyl acrylate)-co-poly(methyl methacrylate) (MAM)

MAM copolymers are a family of “ABA” block copolymers synthesized by controlled radical polymerization with a DEPN (N-tert-butyl-N-(1-diethylphosphono-2,2-dimethylpropyl) nitroxide) [1, 2]. They have a rather high dispersity index ( $I_p$  around 1.9 to 2.2), and average molar masses  $65000 \leq M_n \leq 90000 \text{ g/mol}$ . Depending upon the “grade”, the number average molar mass  $M_n$  of the middle Poly(Butyl Acrylate) (PBA) block is ranging from 20 000 to 27000 g/mol with a low dispersity  $I_p \leq 1.2$ . Chemical formula of PBA homopolymer is shown in Figure II.2.  $T_g$  of PBA homopolymer is around  $-45^\circ \text{C}$ .

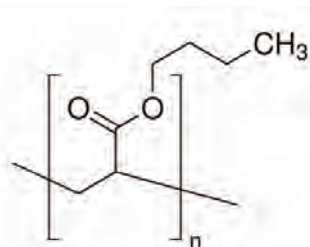


Figure II.2: Chemical formula of PBA

The particular MAM in our study, 36 wt% PBA, has the following characteristics,  $\rho = 1.08 \text{ g/cm}^3$ ,  $M_n^{MAM} \approx 85000 \text{ g/mol}$ ,  $M_w^{MAM} \approx 180000 \text{ g/mol}$ , therefore  $I_p^{MAM} \approx 2$  and  $M_n^{PMMAblock} \approx 27000 \text{ g/mol}$  (molar mass values are related to polystyrene standards).

### II.1.3 Literature summary on neat block copolymers (BCP)

All MAM neat (pure) copolymers after a temperature annealing exhibit lamellar structures at PBA contents between 30 and 40 wt% approximately (equal block length) [3, 4]; and regular curved lamellars with quite a long range development are characterized, their thickness being around 20 to 30 nm.

At PBA contents around 50 %, the PBA-rich phases are cylindrical, and then become micellar above 60 % of PBA. The equilibrium conditions are considered achieved after 48 h annealing at 180° C on films obtained from evaporation of a good solvent solution. The order-disorder temperature ( $T_{ODT}$ , the temperature at which the micro/nano domain structure disappears completely, giving rise to a disordered homogeneous phase) of different MAMs lie well above 120°C [4], i.e. above  $T_g$ 's of both phases. This temperature is probably overcome during a melt blending process. But MAM was observed to be structured even at certain high processing temperatures (180-200°C); and MAM nanostructures are still observed in bulk injected samples without any particular thermal treatment [2, 4-6]. Indeed an advantage of these copolymers is their robustness for self-assembly in several process conditions.

However, if MAM (equal block length, 30-40 wt% PBA) is not annealed, e.g. if the structure is observed directly after injection molding, the structures are poorly defined and worm-like or co-continuous structures are observed on neat MAMs.

In addition, some examples of nanostructuration of polymer/MAM blends can be found in the literature.

### II.1.4 Literature summary on blends of block copolymers (BCP + epoxy systems)

Blends based on MAM-like BCP (with dimethylacrylamide in the PMMA block) were studied in epoxy-amine monomers [7], they exhibit several nano structures: micelles or core-shell nodules which diameter ranges between 25 and 40 nm at low BCP content (< 15-20 wt%), the shell of these nano structures being the one block soluble with the matrix.

The nano structures are of different types: at high BCP contents, they are lamellar (> 75 % MAM), cylindrical micelles or worm-like structures ("elongated micelles") ( $\approx$  40 % MAM), then spherical micelles ( $\approx$  30 % MAM). The average length of worm-like structures is 100 to 200 nm and their thickness lies between 15 and 25 nm.

After thermal polymerization of the reactive epoxy-amine crosslinking systems, the structuration remains but depends on the polymerization temperature: the lower the temperature the more organized is the nano

structure. But the solubility also changes along the reaction (due to molar mass increase) and the more organized structures (i.e. the cylinders) tend to disappear for micelles.

Another example is a blend of two BCP's, di + tri butyl-methylmethacrylate; this blend still shows lamella but the layers are randomly oriented and are thicker than the neat "monodisperse" MAM.

## II.2 Blends production route

Several blends of PMMA/MAM with different MAM amounts (from 5 to 75 wt%) were produced by extrusion using a S camex CE02 single screw extruder (IUT Bordeaux 1, France). The extruder had a diameter of 45 mm and a length/diameter ratio ( $L/D$ ) of 28.

Both materials, PMMA and MAM, were dried in vacuum (680 mm Hg) at 80° C during 4 h prior to the extrusion. Then, they were introduced in the extruder at the appropriate proportions, and processed with a temperature profile from 165° to 225° C and a screw speed of 60 rpm. Pellets from each blend were obtained using a continuous cutting machine operating at the end of the extrusion line.

PMMA/MAM blends generated following this procedure were transparent and macroscopically homogeneous.

Solid samples of neat polymers and PMMA/MAM blends were injection molded. Pellets, both raw materials and blends, were first dried in the same conditions as the extrusion process. Then, dried pellets were injected into bulk pieces (50 x 15 x 3 mm<sup>3</sup>) using a small scale injection molding machine (DSM Xplore). Process parameters were set at 240° C for the melt temperature, 60° C for the mold temperature and 1 MPa during 8 seconds for the injection pressure. Obtained pieces were optically transparent, both for raw materials and blends, and without injection defects.

Main characteristics (density and glass transition temperature) of PMMA/MAM blends are shown on Table II-1. It should be noticed that in our DSC experiments, carried out with a DSC 862 (Mettler) at 10° C/min and N<sub>2</sub> flow of 60 ml/min, temperature range was from 20° to 160° C; thus the  $T_g$  of the PBA (about -50° C) is not detected. Therefore, only the  $T_g$  (midpoint) of the PMMA (mixture of homopolymer and block) is measured.

Table II-1: Density and glass transition temperature ( $T_g$ ) of PMMA/MAM blends

PMMA/MAM wt%	Density / g/cm <sup>3</sup>	$T_g$ / °C
95/5	1.18	115
92.5/7.5	1.17	115
90/10	1.17	115
85/15	1.17	115
80/20	1.16	114
75/25	1.16	113
50/50	1.16	108
25/75	1.14	104

### II.3 Morphology analysis of PMMA/MAM dense solid blends by AFM

PMMA/MAM solid blends with 5, 10, 20, 50 and 75 wt% of MAM were studied by AFM. First topic under study was the homogeneity and possible anisotropy of the nanostructuration along the injected specimens ( $50 \times 15 \times 3 \text{ mm}^3$ ). With this aim two injected samples were selected, one with a low MAM content (90/10) and other with high MAM content (25/75). Then, AFM samples were prepared and studied from each injected specimen. Areas studied on each PMMA/MAM sample, their location on the injected specimen, and nomenclature used to describe the AFM samples are shown in Figure II.3. (V: along injection flow; H: perpendicular to injection flow).

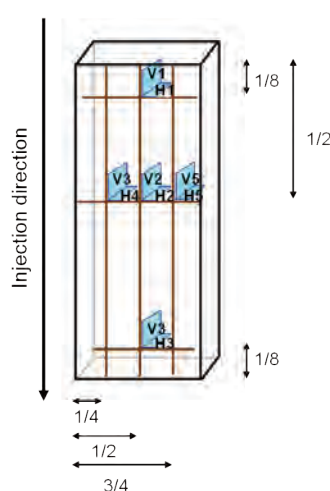
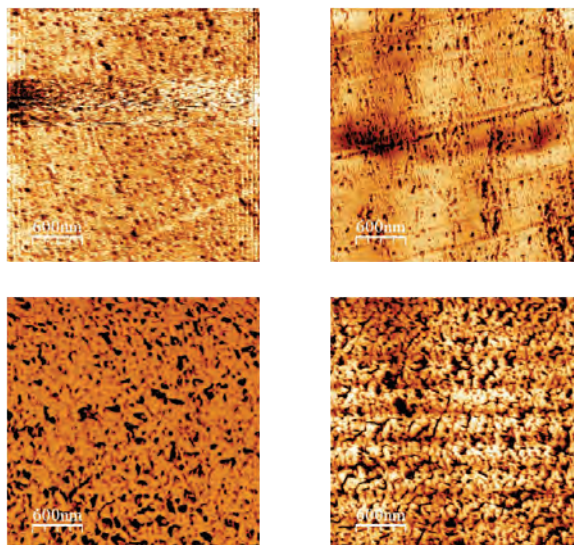


Figure II.3: Location and nomenclature of AFM samples taken from injected samples



**Figure II.4: AFM micrographs from 90/10 (up) and 25/75 (down) PMMA/MAM blends. Samples shown were extracted from the locations H2 (upper left), H1 (upper right), V2 (lower left), V3 (lower right).**

Some examples of AFM images taken in different positions can be found on Figure II.4. This study reveals that nanostructuration of the samples is homogeneous macroscopically along the sample (i.e. the same result is observed in different positions).

However, depending on the MAM amount, the injection process can induce a significant anisotropy of the nanostructures. Samples with MAM amount between 10 and 20 wt% present a strong alignment of the nanostructures along the injection direction. On the contrary, samples with either lower or higher amounts (5, 50 and 75 wt%) seem not exhibit this effect (Figure II.5).

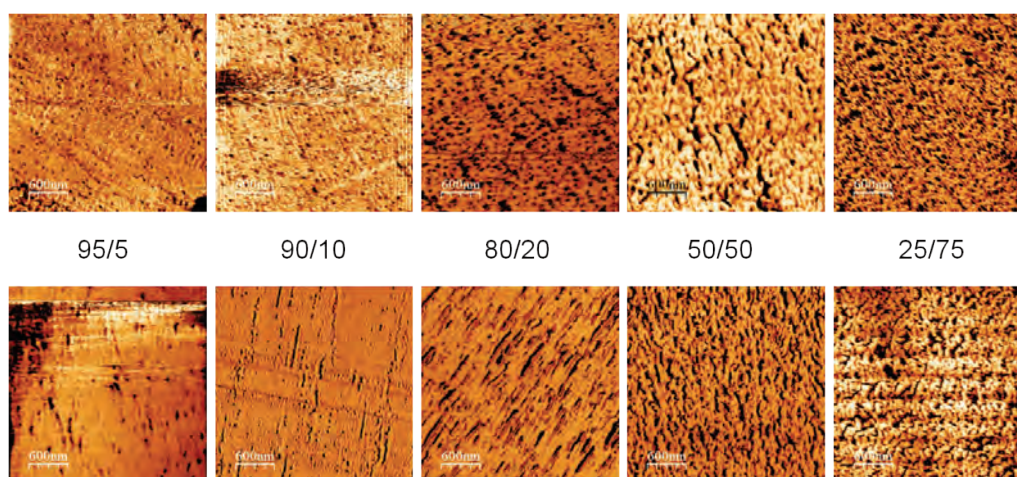


**Figure II.5: AFM micrographs from PMMA blends with MAM amounts between 5 and 75 wt% taken in the plane perpendicular to the injection direction (H, up), and in the plane containing the injection direction (V, down).**

AFM micrographs allow differentiating dispersed nanodomains on blends with low MAM content (from 5 to 20 wt%). Size of the nanodomains seems to increase proportionally to the MAM amount, being in a range between 20 and 50 nm. Also, the nanodomains of 80/20 PMMA/MAM blend present a more pronounced alignment effect than 90/10. It seems that nanodomains of 80/20 are ellipsoids.

Blends with a high MAM content (50 and 75 wt%) present a worm-like nanostructuration on AFM micrographs, with no clear differences between different MAM amounts. It is also not possible to detect alignment effects.

## II.4 Morphology analysis of PMMA/MAM dense solid blends by TEM

MAM and PMMA/MAM solid blends with 5, 10, 25, 50 and 75 wt% of MAM were also studied by TEM.

Neat MAM (Figure II.6) shows the typical long ranged lamellas; some of them are curved (due to an effect of processing).

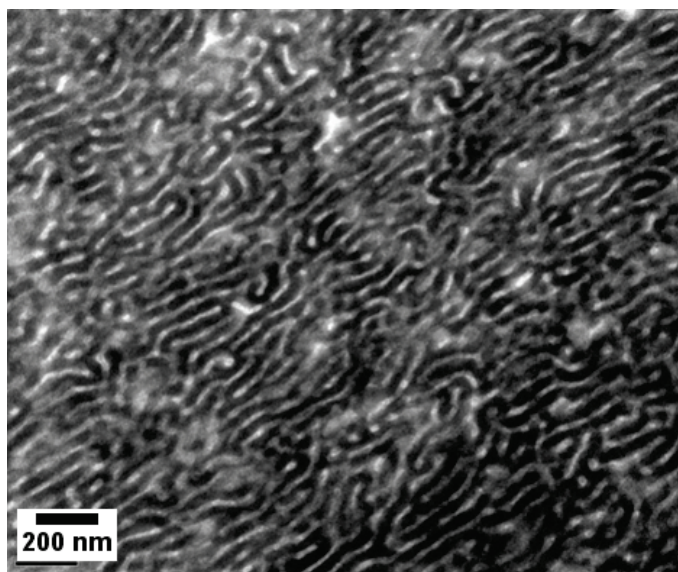


**Figure II.6: TEM micrograph of neat MAM stained by PTA**

PTA staining brings different contrast: white, grey and very dark areas. White “zebra” are observed with thickness below 25 nm thick. In PTA stained samples, the overall dark fraction (black + grey) accounts for much more than 36 % area. Assuming that PTA only stained the PBA phase this excess of dark fraction can be explained as follows.

Measured values about the PBA/dark fraction obtained from a MAM surface micrograph should be about 36 %. However, TEM micrographs show information about the entire volume of the samples, being a



bidimensional projection of three-dimensional information. That implies that in samples with a lamellar nanostructure the micrograph can present higher dark fractions if the nanostructure is not perpendicular to the sample surface (Figure II.7). Also, in samples with dispersed nanostructure the apparent PBA/dark fraction will be higher than expected due to the detection on the TEM micrograph of dispersed nanostructures from different planes of the sample, and not only from the surface.

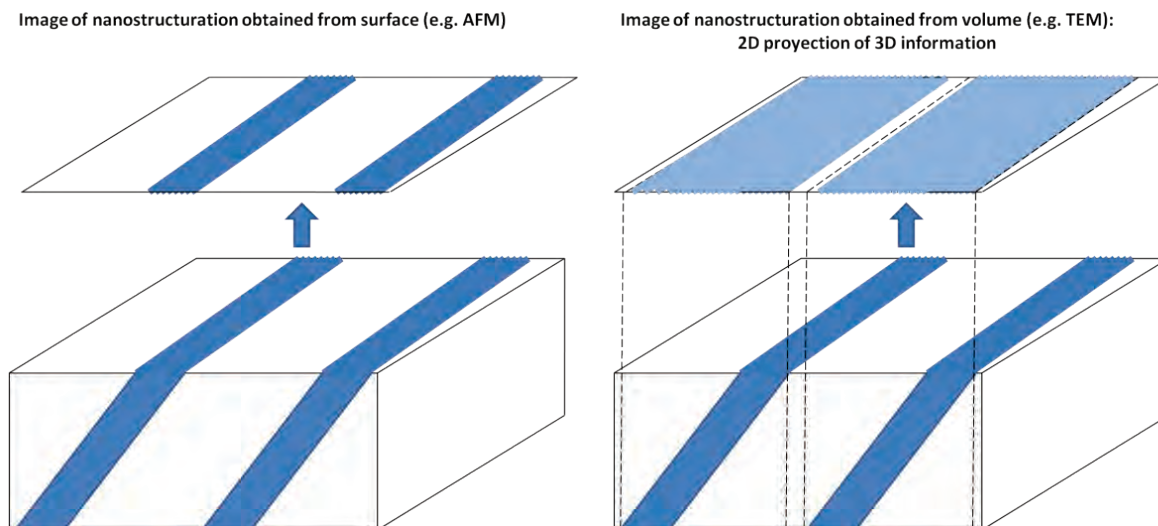


**Figure II.7: Difference between the nanostructure information obtained from a surface (left) and from the entire volume (right) of the sample**

95/5 PMMA/MAM blends (Figure II.8) show regular well dispersed “nodules”, looking core-shell particles or micellar objects with a white core (PMMA), and a black crown (i.e. a shell or layer of PBA); their apparent diameter is 20-25 nm. These nodules are embedded in a “white” matrix (probably homoPMMA+PMMA blocks from MAM). No orientation effect is found.

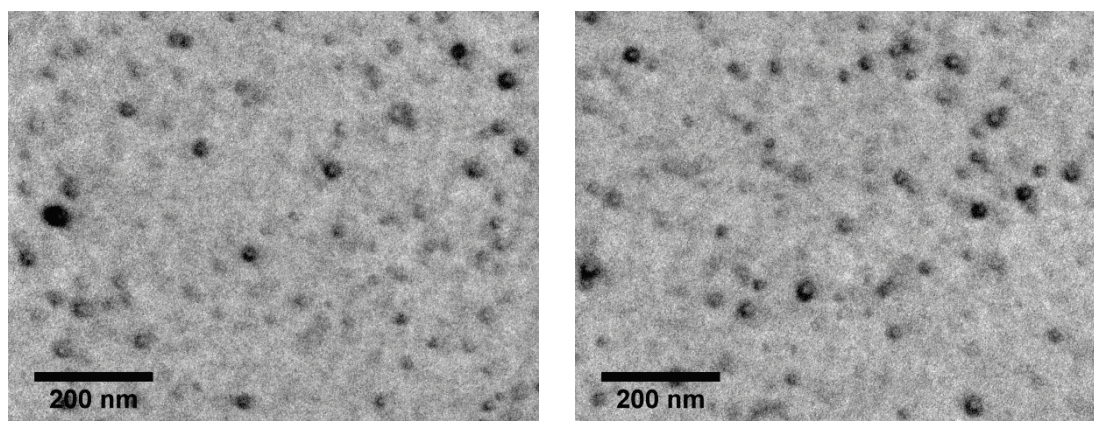


**Figure II.8: TEM micrographs of 95/5 PMMA/MAM blend stained by PTA. Micrographs shown the H (left) and V (right) planes.**



90/10 PMMA/MAM blends (Figure II.9) have a very similar appearance: micelles. Due to the 3-block “ABA” BCP structure, these “micelles” might be constituted by 3 layers: a PMMA core (not contrasted by PTA), a PBA shell (contrasted by PTA), and the outer one is soluble in the matrix and is not contrasted by PTA (PMMA layer) (Figure II. 10). Apparent diameter ( $r_m$ ) is 30 nm.  $H$  and  $V$  orientations are not completely equivalent. The  $V$  observation (injection flow direction) allows detecting an alignment effect (arrays or lines of micelles along the  $V$  direction).

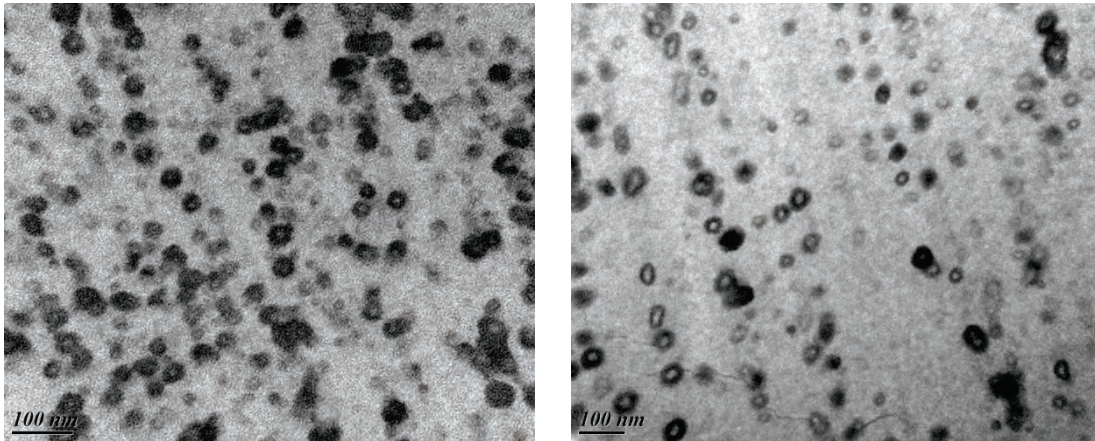


**Figure II.9: TEM micrographs of 90/10 PMMA/MAM blend stained by PTA. Micrographs shown the  $H$  (left) and  $V$  (right) planes.**

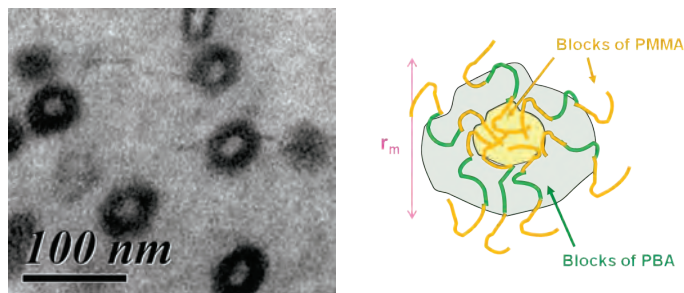


**Figure II.10: Core-shell structures from a TEM micrograph of 90/10 PMMA/MAM blend (left), and scheme (right) of these PMMA/MAM core-shell structures.**

75/25 PMMA/MAM blends (Figure II.11) show dispersed and elongated domains (called/known as worm-like), with the same core-shell (3 layers) as the micelles previously seen (i.e. an inner PMMA layer, an intermediate PBA layer, and an outer PMMA layer (Figure II.12)). Typical thickness of the domains is around 50-80 nm, while their length depends on the plane studied; domains in the  $H$  horizontal orientation present lengths between 100 and 250 nm, whereas in the  $V$  vertical orientation the domains present lengths higher than 300 nm and a preferred orientation into the injection direction.

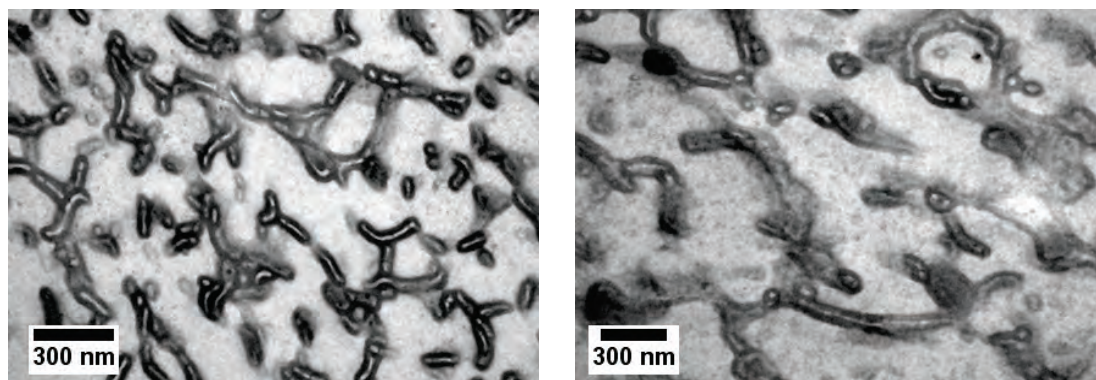


**Figure II.11: TEM micrographs of 75/25 PMMA/MAM blend stained by PTA. Micrographs shown the H (left) and V (right) planes.**

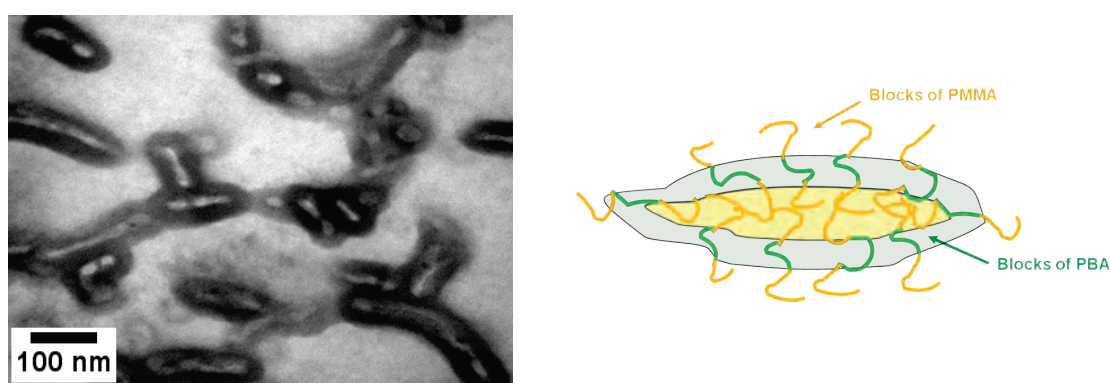


**Figure II.12: Core-shell structures from a TEM micrograph of 75/25 PMMA/MAM blend (left), and scheme (right) of these PMMA/MAM core-shell structures.**

50/50 PMMA/MAM blends (Figure II.13) show a great sensibility to the injection flow, i.e. horizontal H or vertical V orientations. 50/50 H orientation does not show clear structures, whereas only V-oriented samples are showing very clear nanostructures. Indeed on all injected 50/50 specimens, nano objects are characterized as worm-like or elongated micelles dispersed along the V direction. Typical thickness is around 40 nm, and a characteristic length of around 300 nm. Furthermore an inner structure is detected, i.e. black edges around these nano objects, and white inner cores (analogous to the structure shown in Figure II.12).



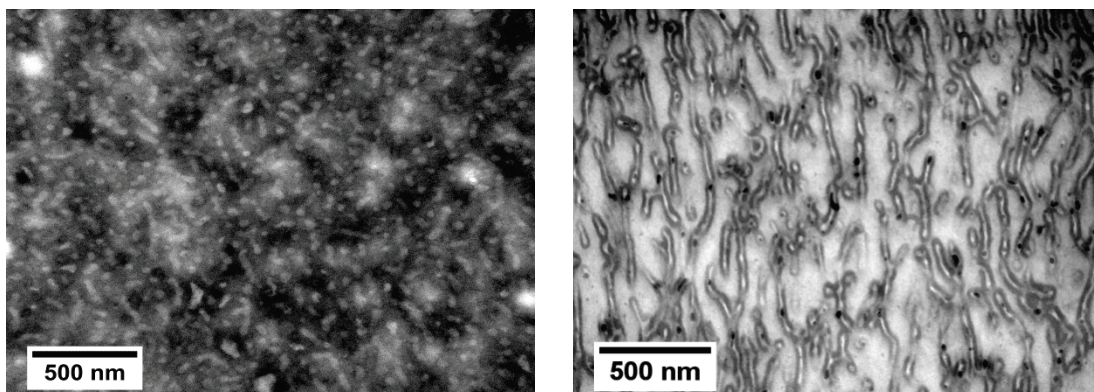


**Figure II.13: TEM micrographs of 50/50 PMMA/MAM blend stained by PTA. Micrographs shown the H (left) and V (right) planes.**

25/75 PMMA/MAM blends (Figure II.14) show a co-continuous nanostructuration with ill-defined lamellas with a thickness around 20-30 nm. No influence of the injection process is detected on these blends, probably due to the lower viscosity observed in the extrusion and injection of these blends, which can prevent the orientation of the nanostructuration during the injection process.

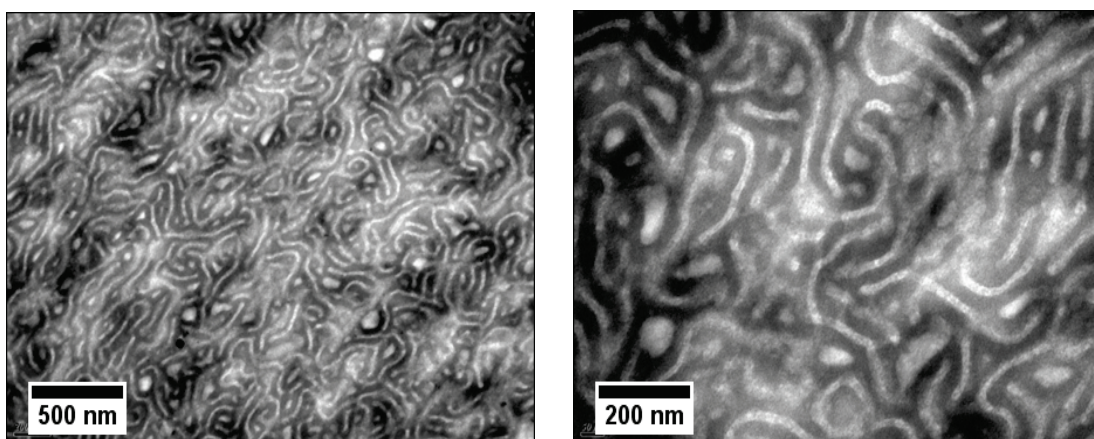


**Figure II.14: TEM micrographs of 25/75 PMMA/MAM blend stained by PTA. Micrographs shown the H (left) and V (right) planes.**

As a conclusion the MAM structures in PMMA blends are always present, being well or ill defined, even at very low content (5 wt%), even with a classical processing (e.g. single screw extruder with thermal treatment) the type of structures are rather classical and expected after the processing we used (extrusion + injection molding).

## II.5 Comparison between AFM and TEM results

Characterization of PMMA/MAM's nanostructuration by AFM and TEM will be compared for PMMA/MAM blends with low MAM (5 and 10 wt%), medium MAM (50 wt%) and high MAM contents (75 wt%). By performing this analysis we try to confirm the findings of the previous sections.

### II.5.1 Low MAM content:

In PMMA/MAM blends with low MAM contents both techniques allow identifying the nanostructuration with practically identical results. Shape, size and alignment can be equally detected by both techniques (Figure II.15). TEM micrographs show an apparent higher object density or higher dark area fraction, due to the characteristics of this technique explained in the previous section (projection in two dimensions of the full sample volume).

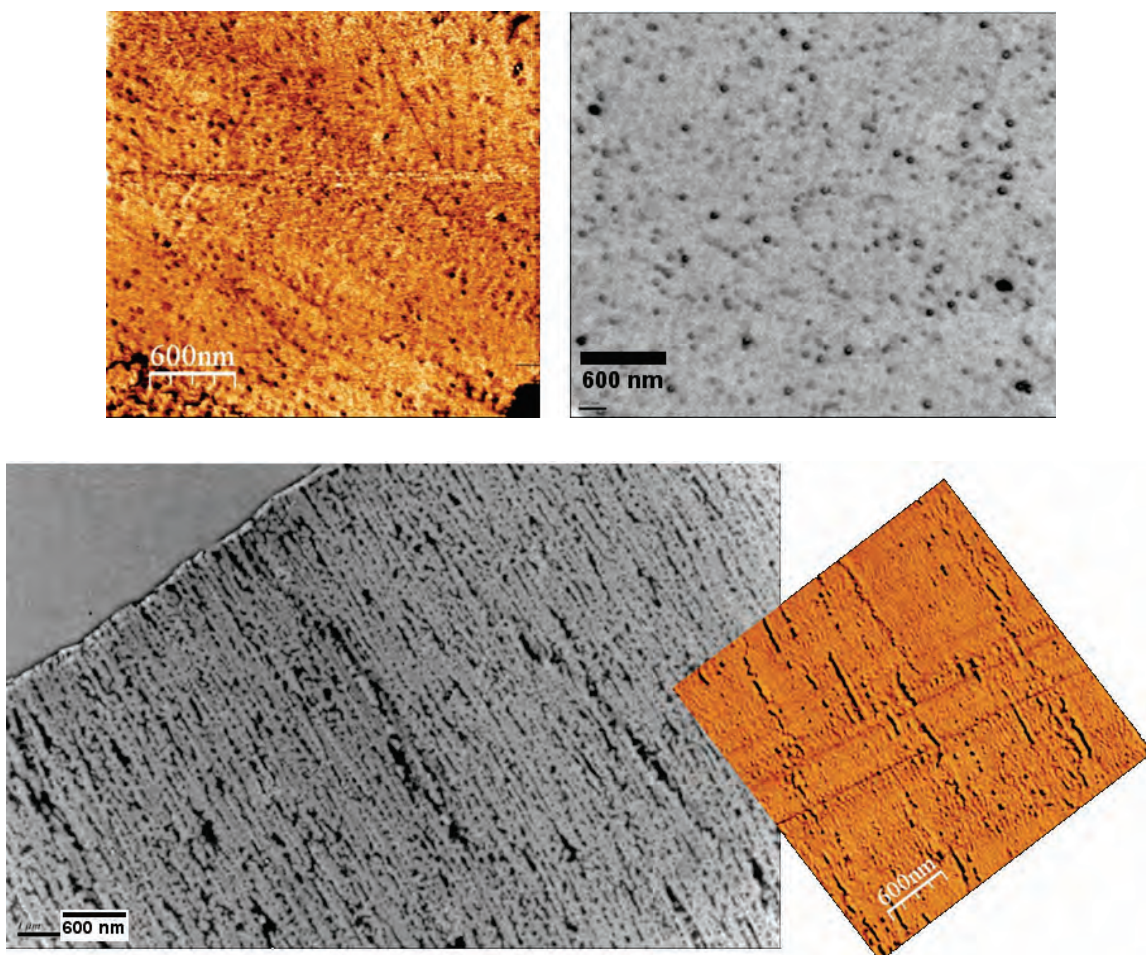
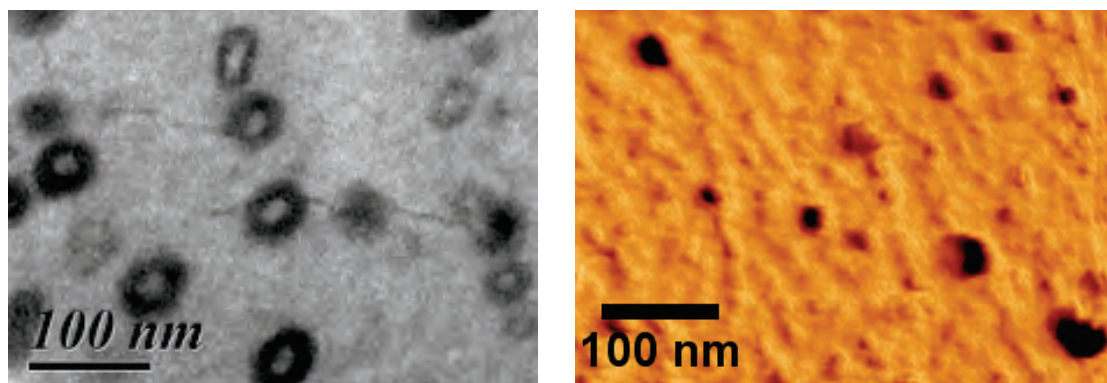


Figure II.15: Comparison between AFM (in color) and TEM (in gray scale) micrographs of 95/5 H (up) and 90/10 V (down) PMMA/MAM blends. Compared images have the same scale.



Nevertheless, only TEM micrographs show the inner structure as micelles/core-shells (Figure II.16). This inner structure is not detected by AFM.



**Figure II.16: Comparison between AFM (right, in color) and TEM (left, in gray scale) micrographs from a 90/10 PMMA/MAM blend. Inner structure is shown only in TEM micrographs.**

### II.5.2 Medium MAM content:

At medium MAM contents both techniques still reveals the nanostructuration (Figure II.17). However, TEM shows the worm-like domains and orientation with a better definition. Also, only on TEM micrographs the inner structure of the nodules can be identified.

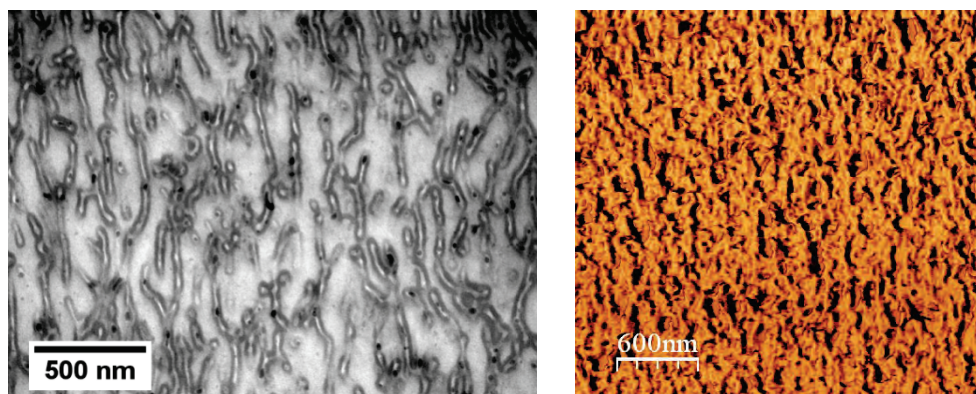


**Figure II.17: Comparison between AFM (right, in color) and TEM (left, in gray scale) micrographs of 50/50 PMMA/MAM blend.**

### II.5.3 High MAM content:

Finally, nanostructuration of PMMA/MAM blends with high amounts of MAM (i.e. 75 wt%) only can be studied by TEM. AFM micrographs of these blends do not show the characteristic lamellar structure of 25/75 PMMA/MAM blends (Figure II.18).

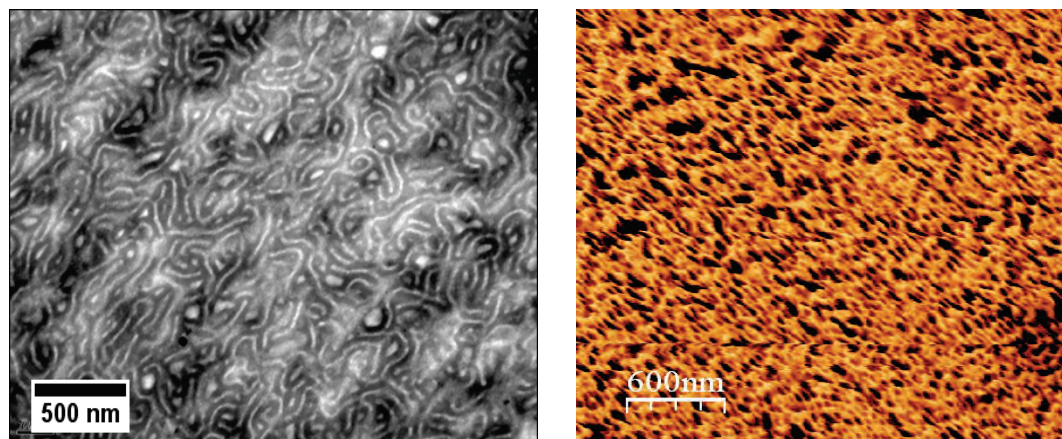


**Figure II.18: Comparison between AFM (right, in color) and TEM (left, in gray scale) micrographs of 25/75 H PMMA/MAM blend.**

However, lamellar structures of similar copolymers were studied using AFM in the literature [8]; therefore, this limitation must be due to the samples preparation and not to the AFM technique. Taking into account the samples preparation routes, the main difference that can be found resides in the knife used in the microtoming process. TEM samples were prepared with a diamond knife, while AFM samples were prepared using a glass knife.

As a conclusion, AFM and TEM techniques are appropriated to study the nanostructure of PMMA/MAM blends with low MAM amounts. Blends with medium-high MAM amounts present better resolution using TEM; however, AFM results could be improved by following an improved sample preparation route probably using a microtome diamond knife.

The main advantage of the TEM technique is the possibility to study the inner structure of the nanostructures. On the other hand, information about the PBA/nanostructure fraction obtained from AFM micrographs can be directly related to the PBA content of the sample, therefore this technique allows quantification (see Chapter I II); while TEM micrographs do not allow studying the PBA/nanostructure fraction due to the projection of three-dimensional information of the sample on a bidimensional micrograph.

Therefore, both techniques should be used in a complementary way to carry out a complete characterization of the PMMA/MAM nanostructure.

## II.6 Foams production route

Foams from neat PMMA, neat MAM, and PMMA/MAM blends with different MAM amounts (from 5 to 75 wt%) were produced by gas dissolution foaming, using  $\text{CO}_2$  as physical blowing agent. Two high pressure vessels were employed in the production of these foams.

The first one is a commercial high pressure vessel provided by TOP Industrie (Vaux Le Pénil, France), with a capacity of  $300 \text{ cm}^3$  and capable of operating at a maximum temperature of  $250^\circ \text{C}$  and maximum pressure of 40 MPa (Figure II.19). This pressure vessel is equipped with an accurate pressure pump controller provided by Teledyne ISCO (Lincoln NE, U.S.), and controlled automatically to keep the temperature, by means of external heaters, and pressure at the desired values (Figure II.19).



**Figure II.19: Teledyne ISCO pressure pump (left), and TOP Industrie high pressure vessel (right).**

Another high pressure vessel with glass windows self-designed at CellMat Laboratory has been used. This equipment has additional instrumentation (inner heaters and thermocouples, pressure control by means of a gas booster, control of the pressure release rate, etc.) with a capacity of  $500 \text{ cm}^3$  and maximum operation temperature and pressure of  $200^\circ \text{C}$  and 20 MPa, respectively (Figure II.20) [9].

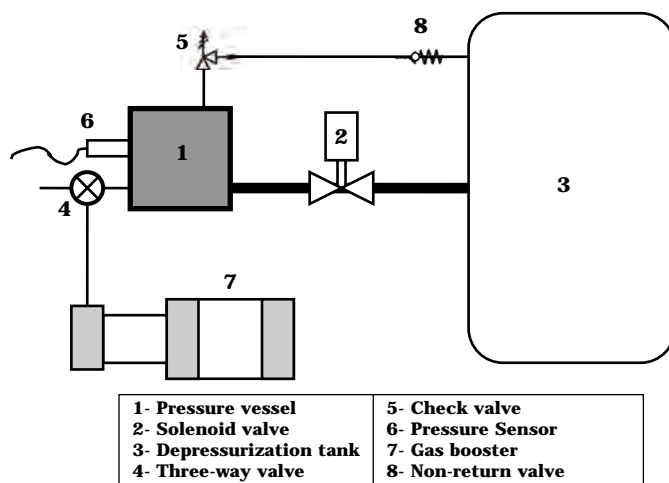


**Figure II.20: Scheme (up) and picture (down) of the self-designed at CellMat Laboratory high pressure vessel**

Both pressure vessels allow recording the pressure and temperature evolution during the entire process.

Saturation experiences in the TOP Industry high pressure vessel were carried out at pressures between 10 and 30 MPa, temperatures between room temperature and 70° C, and pressure release rates from 10 to 30 MPa/min. On the other hand, saturation experiences in our self-designed pressure vessel were carried out at room temperature and 7 MPa, while the average pressure release rate ranged from 1.4 to 45 MPa/min. In both pressure vessels the samples remained at controlled pressure and temperature for 24 h, to ensure that the dissolution of CO<sub>2</sub> into the polymer reaches its equilibrium/maximum value.

Depending on the saturation temperature (see Chapter IV) the cellular structure was triggered during or after the pressure drop.



## II.7 Nanostructuration evolution due to CO<sub>2</sub> saturation

During the foaming experiments of PMMA/MAM systems we found some unexpected results about the macroscopic expansion of the foams. Foams produced at saturation pressures and temperatures of 30 MPa and 60° C present a strong dependence of the MAM amount on their macroscopic expansion (Figure II.21). It should be noticed that these foams are produced by a free foaming process, i.e. not a constraint foaming neither mold foaming, and therefore the final shape and expansion of the foams are not fixed.



**Figure II.21: Macroscopic shape of foams produced at 30 MPa and 60° C from different PMMA/MAM blends compared to the solid precursors shape and dimensions (left). The saturation time was 24 hours and the depressurization rate was around 30 MPa/min.**

At this saturation conditions samples of neat PMMA or blends with low amounts of MAM (e.g. 95/5) present a similar expansion ratio in every direction, and creep in the gravity direction during the process. However, blends with medium amounts of MAM (from 10 to 50) present a significant decrease of their length, which is also aligned with the gravity direction, and creeping is not detected. Finally, blends with high amounts of MAM (e.g. 25/75) show neither creep nor significant expansion anisotropy.

These different macroscopic expansion behaviors can be a result of the foaming process or a result of an annealing of the solid samples during the saturation process (saturation annealing). Annealing is a thermally induced process that allows the polymer chains to reorganize themselves reaching a more energetically favorable organization. Commonly, in amorphous polymers this process is induced increasing the temperature of the polymer up to values near or over the glass transition temperature ( $T_g$ ). At these temperatures the polymer chains have an increased mobility that allows the reorganization.

Obviously, the temperature employed during these saturation processes ( $60^{\circ}\text{C}$ ) is far from the  $T_g$  of the PMMA ( $112^{\circ}\text{C}$  for the particular PMMA grade selected). However,  $T_g$  depletion induced by the  $\text{CO}_2$  sorption can decrease the  $T_{g,ef}$  of the PMMA down to values near or below room temperature [10, 11]. In addition, swelling induced by the  $\text{CO}_2$  sorption increases the mobility of the polymer chains. Therefore, the condition of the saturation process in the foaming tests may induce an annealing process of the PMMA/MAM samples due to the saturation with  $\text{CO}_2$ .

PMMA/MAM samples extracted from the pressure vessel after the saturation process at these conditions are already foamed, thus it is not easy to obtain information from these samples about the effect of annealing because foaming also modifies the sample volume.

Then, in order to detect if this behavior is produced by an annealing we carry out thermal annealing processes in PMMA/MAM blends; trying to reproduce this behavior. First attempts were carried out during 4 h at  $135^{\circ}\text{C}$  (about  $20^{\circ}\text{C}$  above the  $T_g$  of PMMA) without differences between different PMMA/MAM blends (Figure II.22). The modifications on dimensions were similar for all the analyzed samples.



**Figure II.22: PMMA (left) and PMMA/MAM samples (80/20, 75/25 and 25/75) after an annealing process at  $135^{\circ}\text{C}$  during 4 h.**

Temperature of the annealing process was progressively increased up to near  $T_{ODT}$ , until being able to reproduce the macroscopic changes seen after the saturation process. This behavior was finally reproduced after an annealing at  $165^{\circ}\text{C}$  during 4 h (Figure II.23). In this case neat PMMA and two PMMA/MAM blends, one with medium MAM content (75/25) and the other with high MAM content (25/75), were annealed to study the three different behaviors found in Figure II.21. As expected the neat PMMA sample presents creep, whereas the 75/25 PMMA/MAM sample decreases its length, and the 25/75 PMMA/MAM sample remains its dimensions almost constant (previous to the annealing the three samples present the same dimensions and geometry). It should be noticed that the bubbles inside the sample are produced by moisture present on the samples; also, samples with MAM probably present

thermal degradation, resulting in a color change, and the marker ink seems to diffuse in the samples with MAM.

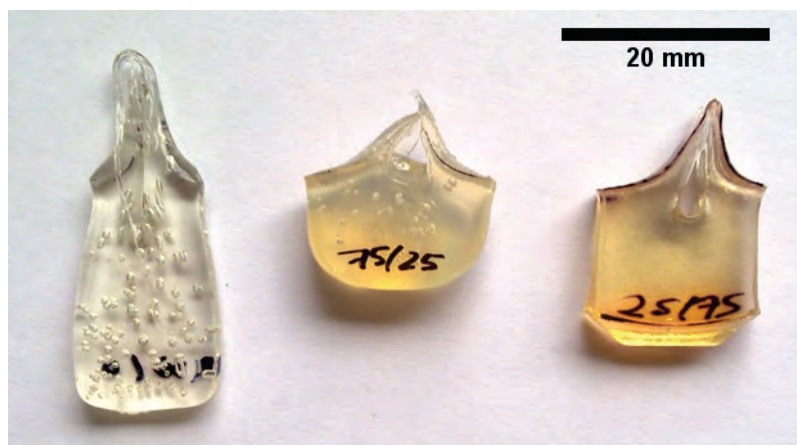


**Figure II.23: PMMA (left) and PMMA/MAM samples (75/25 and 25/75) after an annealing process at 165° C during 4 h. Before annealing the three samples had the same geometry and dimensions.**

Therefore, we make the hypothesis that the dimensional changes are due to an annealing induced by the CO<sub>2</sub> sorption during the saturation process. Secondly, looking for an explanation of the different evolutions of the samples it is possible to relate each kind of macroscopic evolution with different nanostructurations.

Samples without nanostructuration (neat PMMA) or micelles not aligned or elongated in the injection direction (95/5) are just creeping when the molecules have enough mobility.

Samples with micelles or nodules aligned and elongated in the injection direction (90/10, 80/20, 75/25, 50/50) present a significant decrease of their length and an increase of their width and thickness.

On the contrary samples with a co-continuous nanostructure and no orientation (25/75) do not present changes in their dimensions nor creep.

From these comparative qualitative observations between nanostructuration and macroscopic evolution during annealing we propose the following hypothesis:

During annealing (both thermal and CO<sub>2</sub> annealing) elongated micelles or nodules evolve in the direction of adopting their equilibrium shape (spherical). In this way the total length of the sample is decreased while their width and thickness are increased. Samples with no nanostructuration or spherical micelles (95/5) do not suffer this process and evolve in a normal way under annealing (creep). Finally, samples with a co-continuous local nanostructuration (such as 25/75) evolve into a clear three-dimensional

structuration in the mesoscale, which could avoid the appearance of creep (these mechanisms are proved in the following section). These mechanisms are schematically represented on Figure II.24.

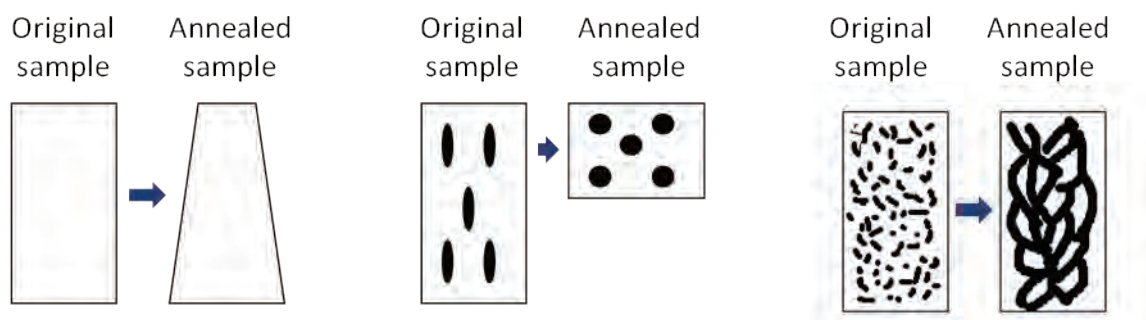


**Figure II.24: Evolution of macroscopic shape and nanostructuration during annealing of neat PMMA (left), PMMA/MAM blends with elongated micelles or nodules (middle), and PMMA/MAM blends with co-continuous nanostructuration (right).**

### II.7.1 Effect of CO<sub>2</sub> annealing on final morphology

In order to provide a demonstration of this hypothesis the nanostructuration of CO<sub>2</sub> annealed samples was studied by AFM and TEM. Annealed samples under CO<sub>2</sub> saturation (24 hours at 30 MPa and 60° C) were obtained from thin samples of 90/10 and 25/75 PMMA/MAM blends, carrying out an extremely slow pressure release (several hours) to avoid the foaming of the samples.

AFM phase images of 90/10 in the plane containing the injection direction (V) (Figure II.25) reveals that after annealing (24 hours at 30 MPa and 60° C) the elongated micelles decrease their length and increase their width. Anisotropy of the micelles does not completely disappear.

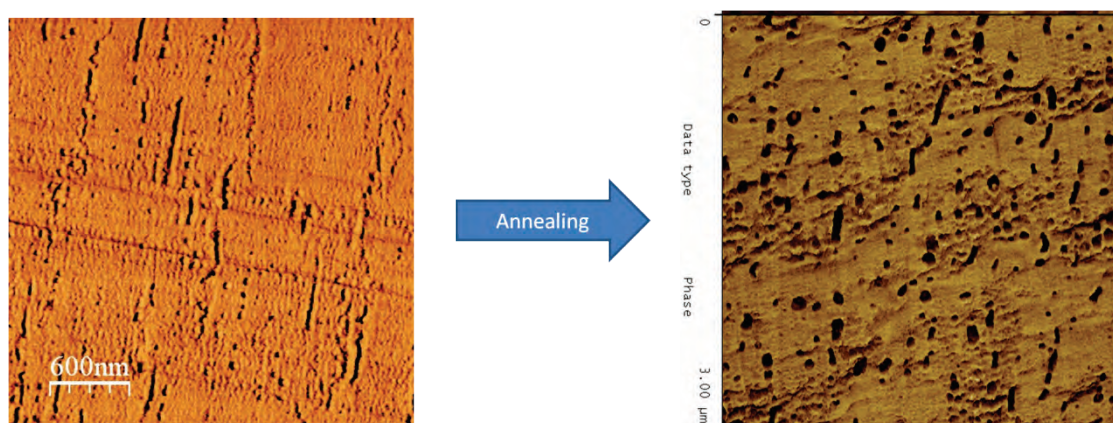


**Figure II.25: AFM phase images showing the evolution of the nanostructuration of 90/10 PMMA/MAM blends due to a CO<sub>2</sub> annealing (24 hours at 30 MPa and 60° C). Both AFM phase images have the same scale.**



Evolution of the nanostructuration of 25/75 PMMA/MAM blends was studied by TEM. TEM micrographs show a clear increase of the lamellas thickness (Figure II.26).

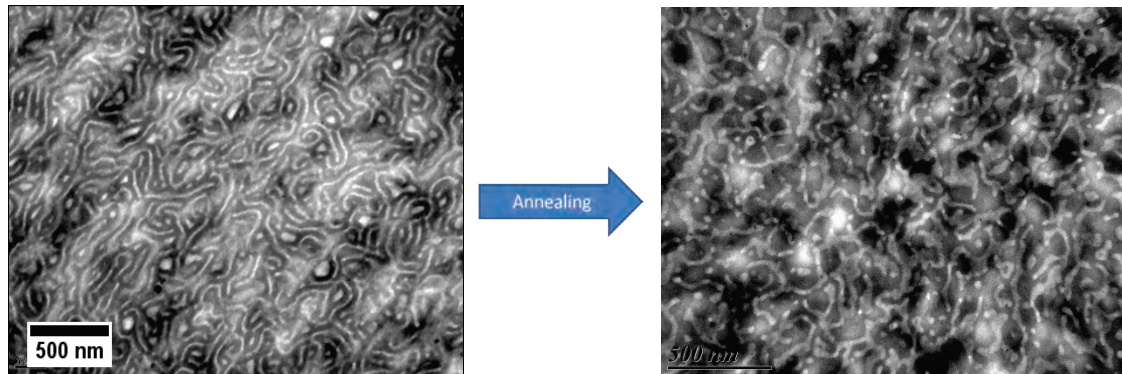


**Figure II.26: TEM micrographs showing the evolution of the nanostructuration of 25/75 PMMA/MAM blends due to an annealing process (24 hours at 30 MPa and 60° C).**

In addition, SEM micrographs from the 25/75 PMMA/MAM blends foamed at these conditions reveal the presence of a mesoscopic three-dimensional structuration, according to the previous hypothesis (Figure II.27). The mesoscopic structuration is composed of solid connected areas with thickness of 1-2  $\mu\text{m}$  (probably composed only by PMMA), and porous areas (probably composed both by PMMA and PBA).

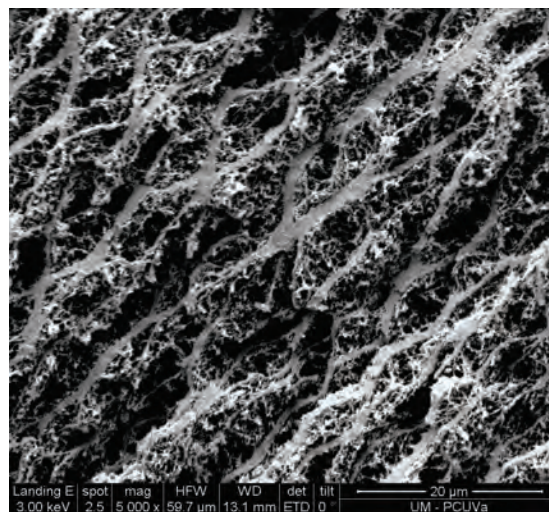


**Figure II.27: SEM micrograph from a 25/75 PMMA/MAM foam produced at 30 MPa and 60° C showing a mesoscopic structuration.**

As a conclusion, the nanostructuration presence and its particular morphology modify the macroscopic evolution of PMMA/MAM samples during the saturation and foaming processes at high temperatures has been demonstrated. We believe the process conditions and microstructure affect the dimensional changes upon foaming; we have shown a first benefit of nanostructuration: no macroscopic creep in some structures even above  $T_{g,ef}$ .

## II.8 Cellular structures of PMMA/MAM foams: general description and evolutions

Neat PMMA, neat MAM, and PMMA/MAM foams were studied by SEM in order to characterize their cellular structure. This section summarizes the typical cellular structures that can be obtained with the materials under study by modifying the amount of MAM in the PMMA and the processing conditions. We will show the tremendous variety of structures that can be produced (micro and nanocellular, closed and open cell, isotropic and anisotropic, etc.) without trying to explain the origin of each cellular structure produced. These explanations are included in the following chapters.

### II.8.1 Presence of solid skin-foamed core structure

In Chapter I it was explained that polymeric foams produced by gas dissolution foaming usually present an outer solid skin and a foamed inner core. SEM observations on some PMMA/MAM samples confirm that these foams can present this structure; however, it is not possible to study the thickness of the skin due to the nanometric size of the cellular structure (i.e. SEM micrographs with enough magnification to appreciate the cellular structure are too close to measure the skin thickness) (Figure II.28).

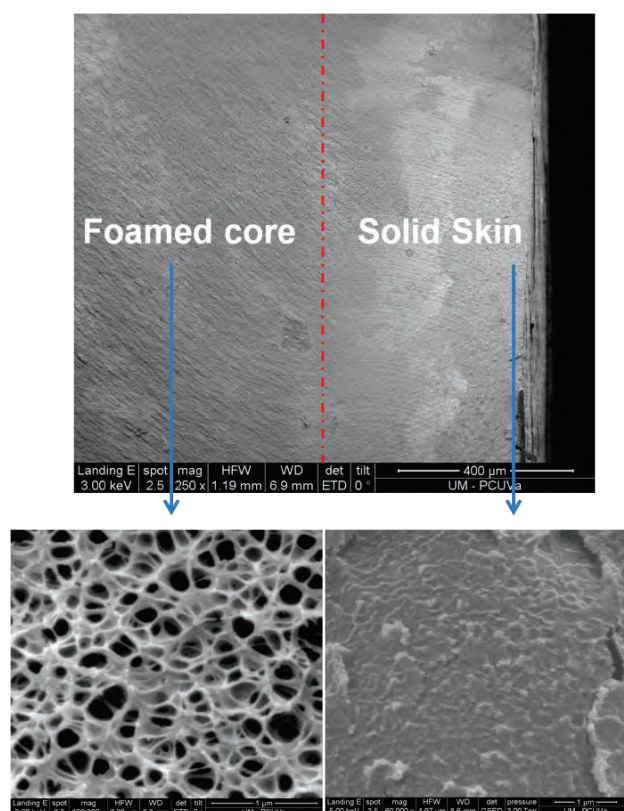


**Figure II.28: SEM micrographs of 90/10 PMMA/MAM foam produced at 30 MPa and RT. Upper micrograph was taken with the appropriate magnification to measure the skin thickness (overlaid in the micrograph). Lower micrographs show the structure of the foamed core (left) and the densified skin (right) with higher magnification.**





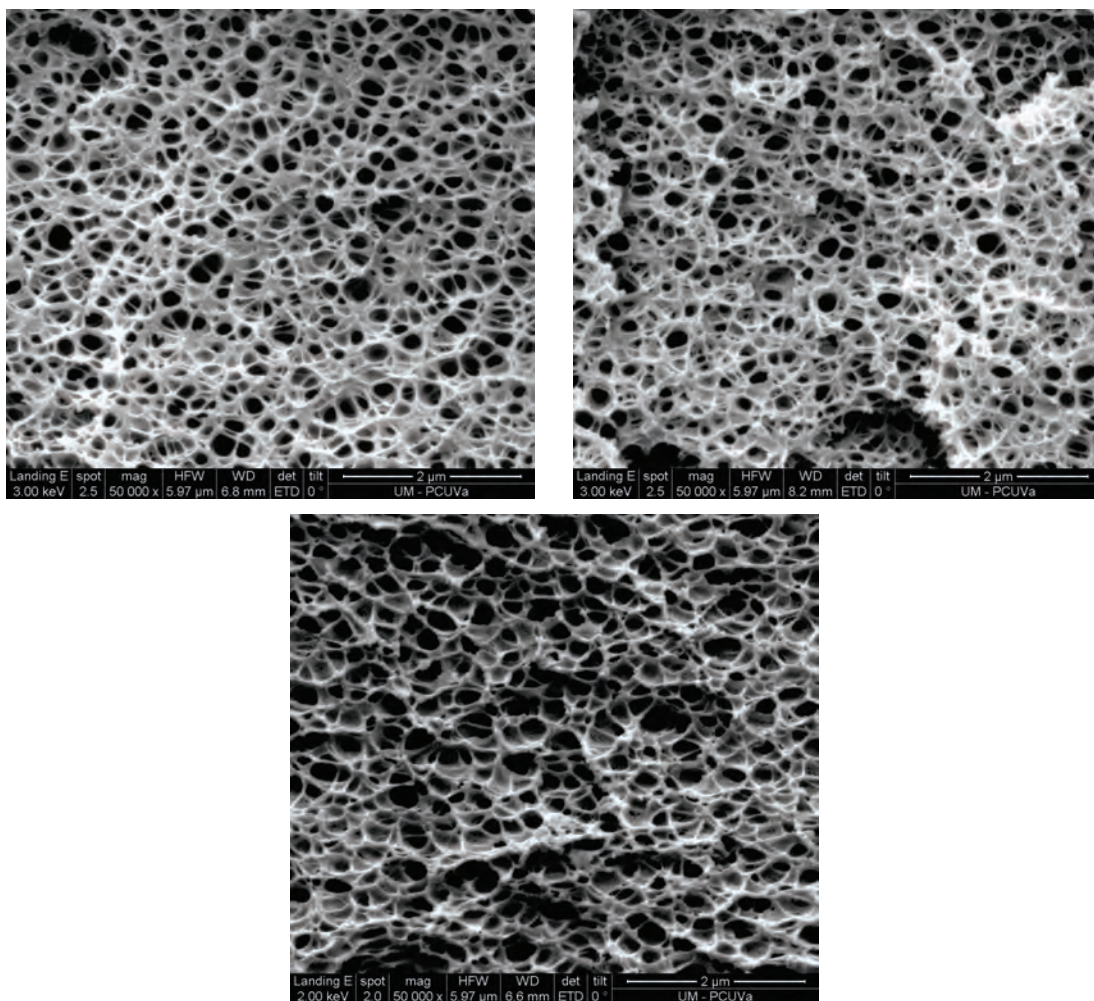


**Figure II.30: SEM micrographs of 90/10 PMMA/MAM blend foamed at 30 MPa and RT: areas H1 (upper left), H2 (upper right), and H3 (down).**



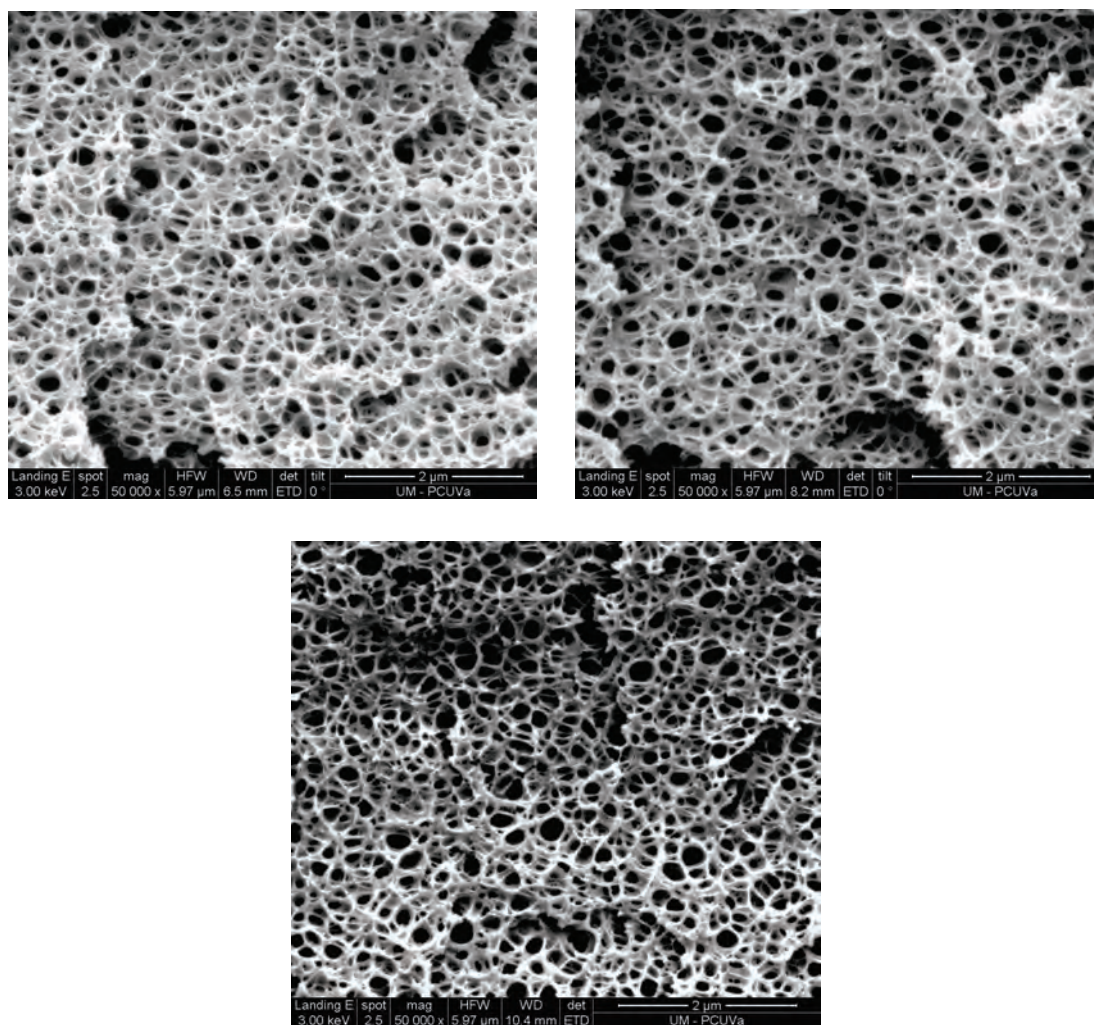
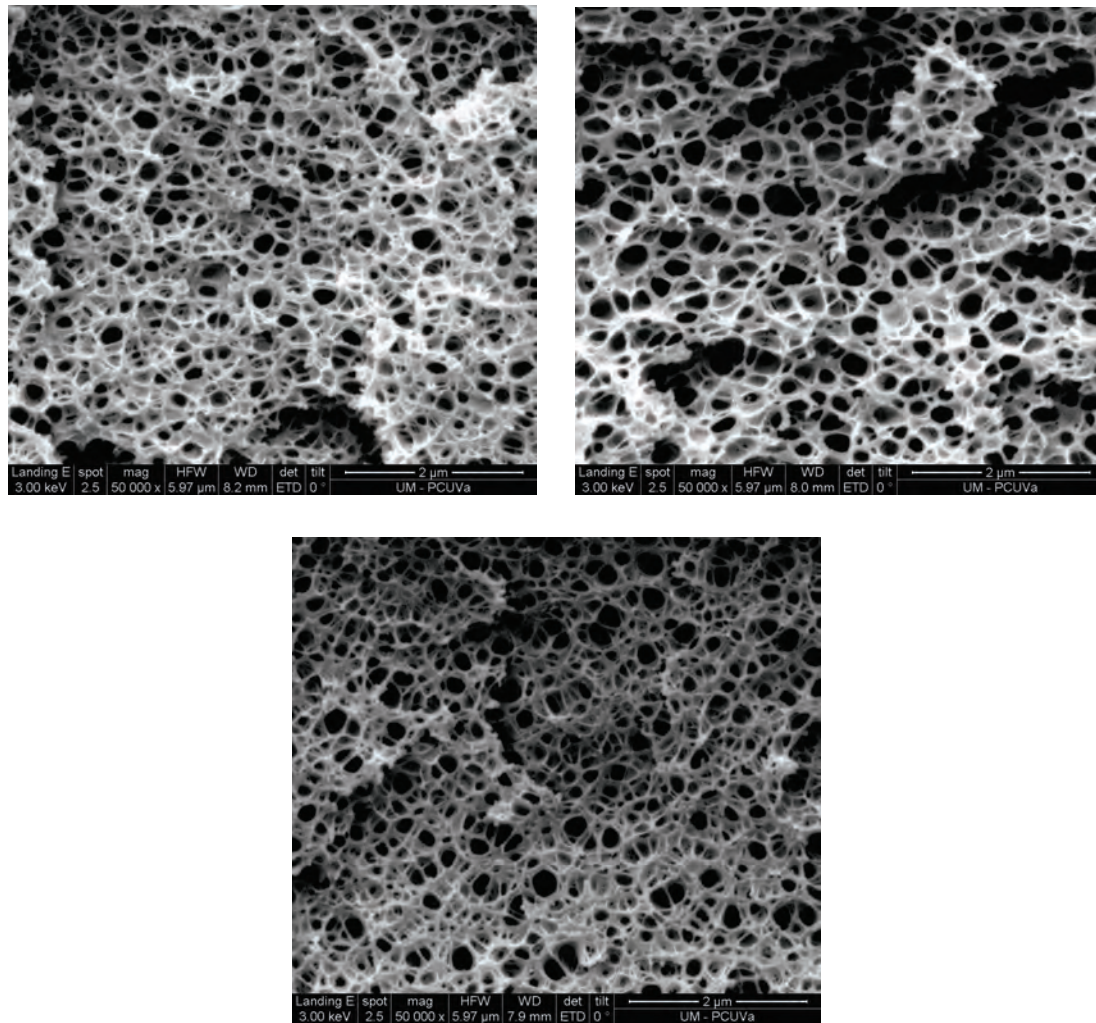


Figure II.31: SEM micrographs of 90/10 PMMA/MAM blend foamed at 30 MPa and RT: areas H4 (upper left), H2 (upper right), and H5 (down).



**Figure II.32: SEM micrographs of 90/10 PMMA/MAM blend foamed at 30 MPa and RT: area H2; zones B (upper left), C (upper right), and D (down).**

### II.8.3 Anisotropy of cells

Secondly, it was found that 90/10 PMA/MAM foams present an anisotropic cellular structure. As it can be observed in Figure II.33 the cells are completely different when they are observed in the vertical direction (V, parallel to the injection direction) than when they are observed in the perpendicular plane to the injection direction (H).



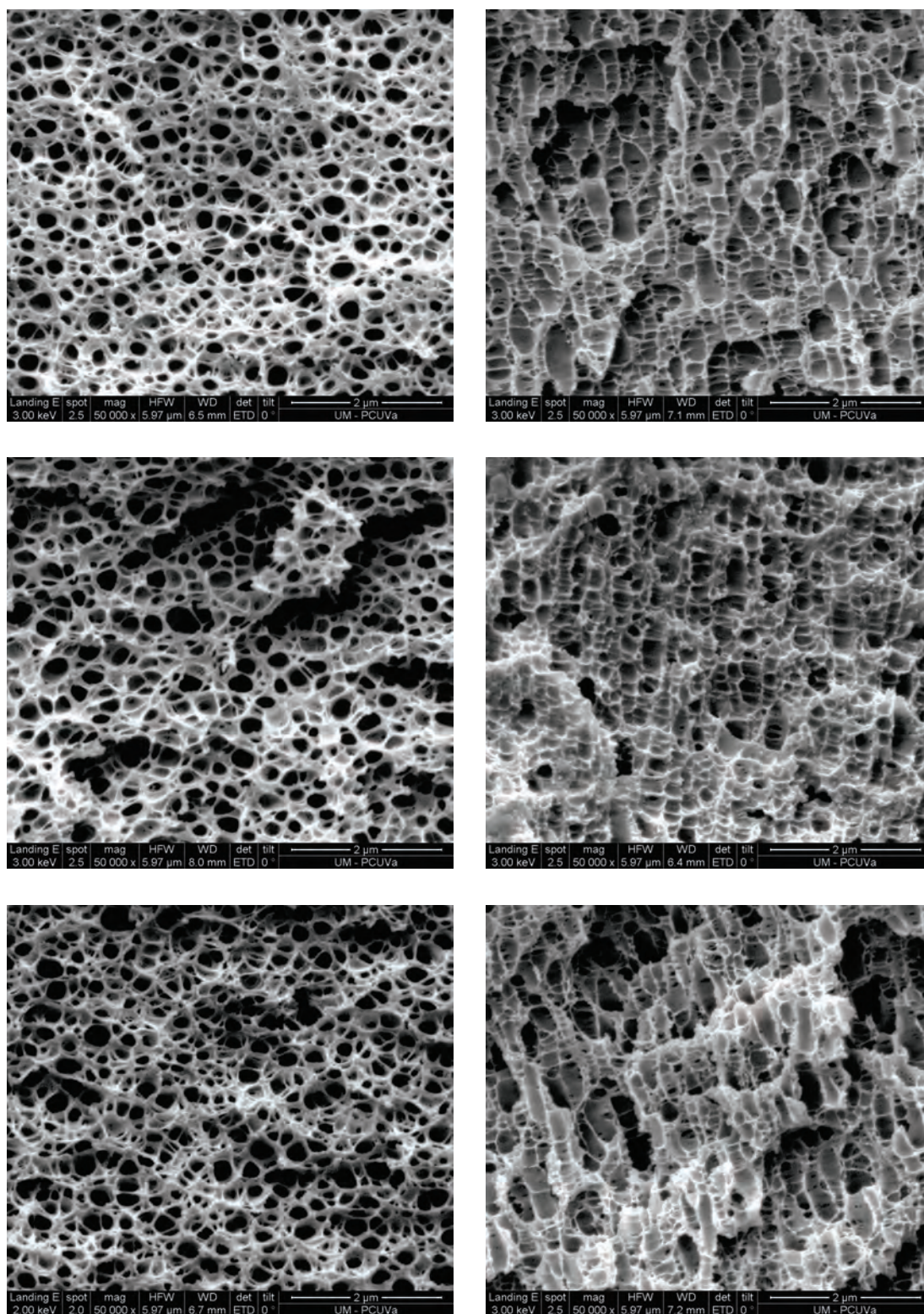


Figure II.33: SEM micrographs of 90/10 PMMA/MAM blends foamed at 30 MPa and RT: areas H1 (upper left), V1 (upper right), H2 (middle left), V2 (middle right), H3 (lower left), and V3 (lower right).



#### II.8.4 Cellular structure of different MAM content foams, evolution of cells morphology with the saturation temperature

Evolution of the cellular structure with the processing conditions and MAM amount can be studied from SEM micrographs taken from a selection of foams: neat PMMA, neat MAM, and some PMMA/MAM blends (95/5, 90/10, 75/25, and 25/75).

Neat PMMA foams produced at 30 MPa and different temperatures do not present elongated cells in the injection direction. In addition, the cellular size is significantly increased with the temperature (Figure II.34). In fact the material shows a transition from nanocellular to microcellular when the temperature is increased from RT to 40° C.

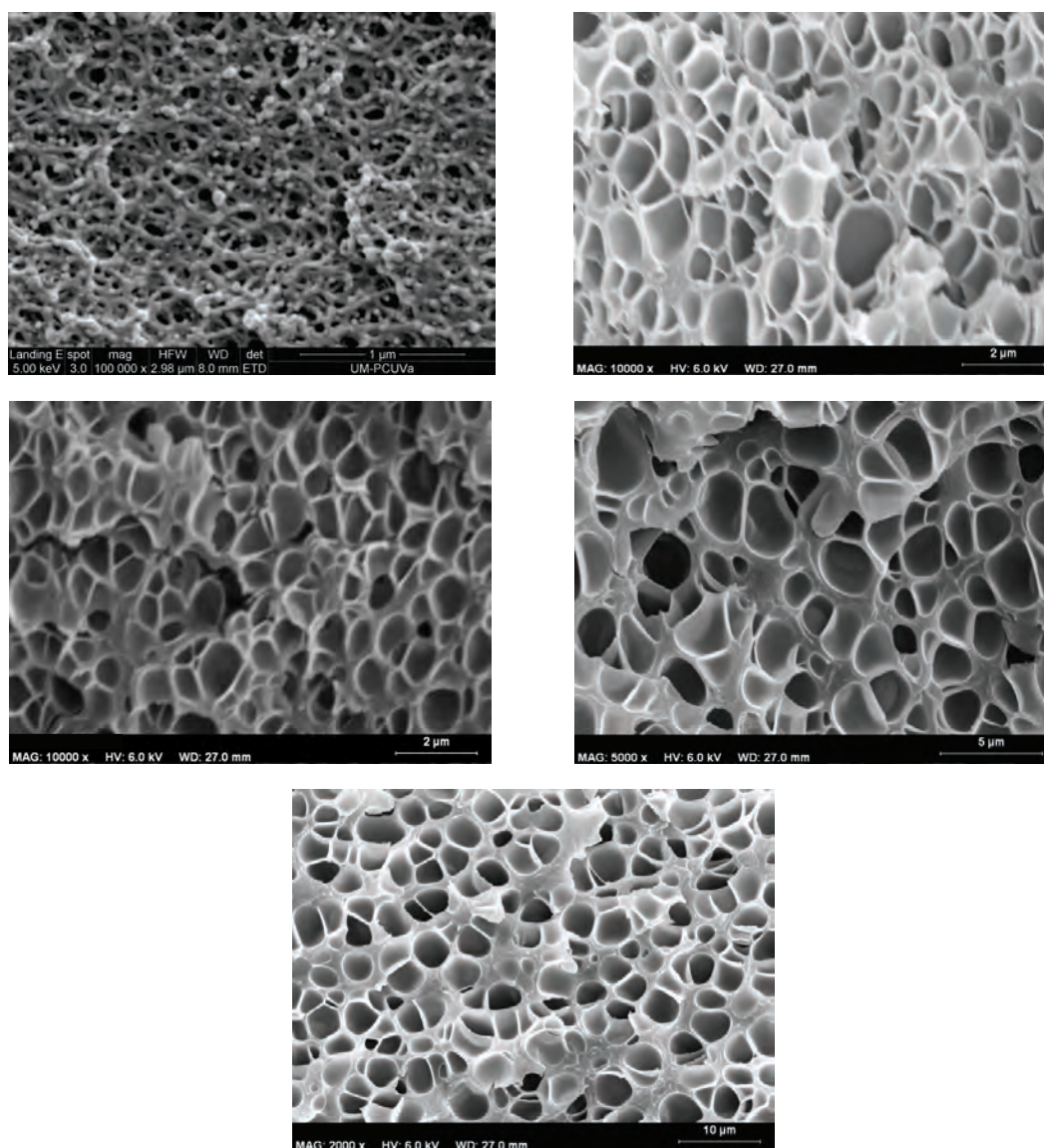
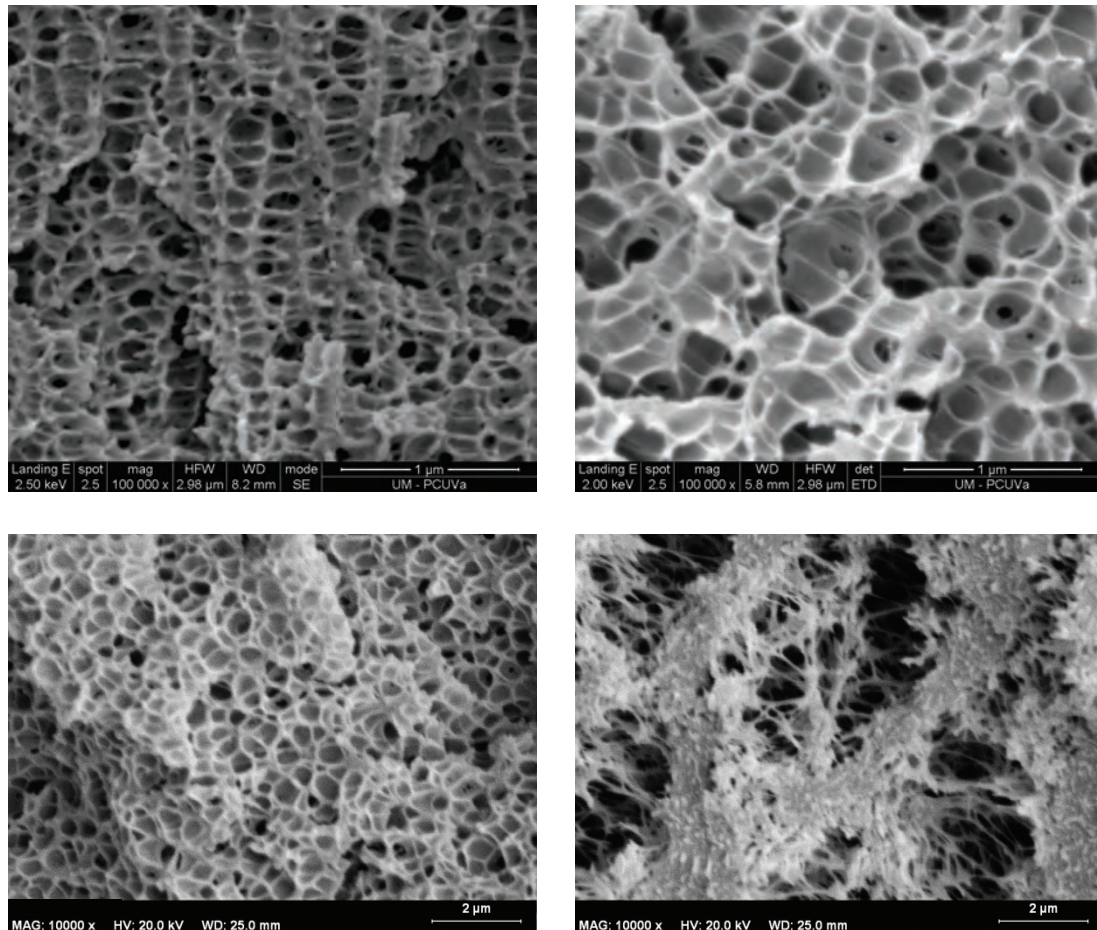


Figure II.34: SEM micrographs (V) of neat PMMA foamed at 30 MPa and different temperatures: RT (upper left), 40° C (upper right), 50° C (middle left), 60° C (middle right), 70° C (down).

95/5 PMMA/MAM foams produced at 30 MPa and RT present cells aligned in the injection direction, but with no elongation (Figure II.35). At higher temperatures up to 60° C, and the same pressure, alignment of cells disappears and the cell size is increased, while samples foamed at 70° C lose their well-defined cellular structure.



**Figure II.35: SEM micrographs (V) of 95/5 PMMA/MAM blends foamed at 30 MPa and different temperatures: RT (upper left), 40° C (upper right), 60° C (lower left), 70° C (lower right).**

90/10 PMMA/MAM foams produced at 30 MPa present a well-defined cellular structure in the entire range of temperatures from RT to 70° C (Figure II.36). Samples produced at RT present a clear alignment in the injection direction and also elongated nanocells. Both characteristics, alignment and elongation, tend to disappear when the temperature is increased, which could be related to the saturation annealing due to the combination of CO<sub>2</sub> sorption and temperature. Increment of the saturation temperature allows obtaining higher average cell sizes in the micrometric range.



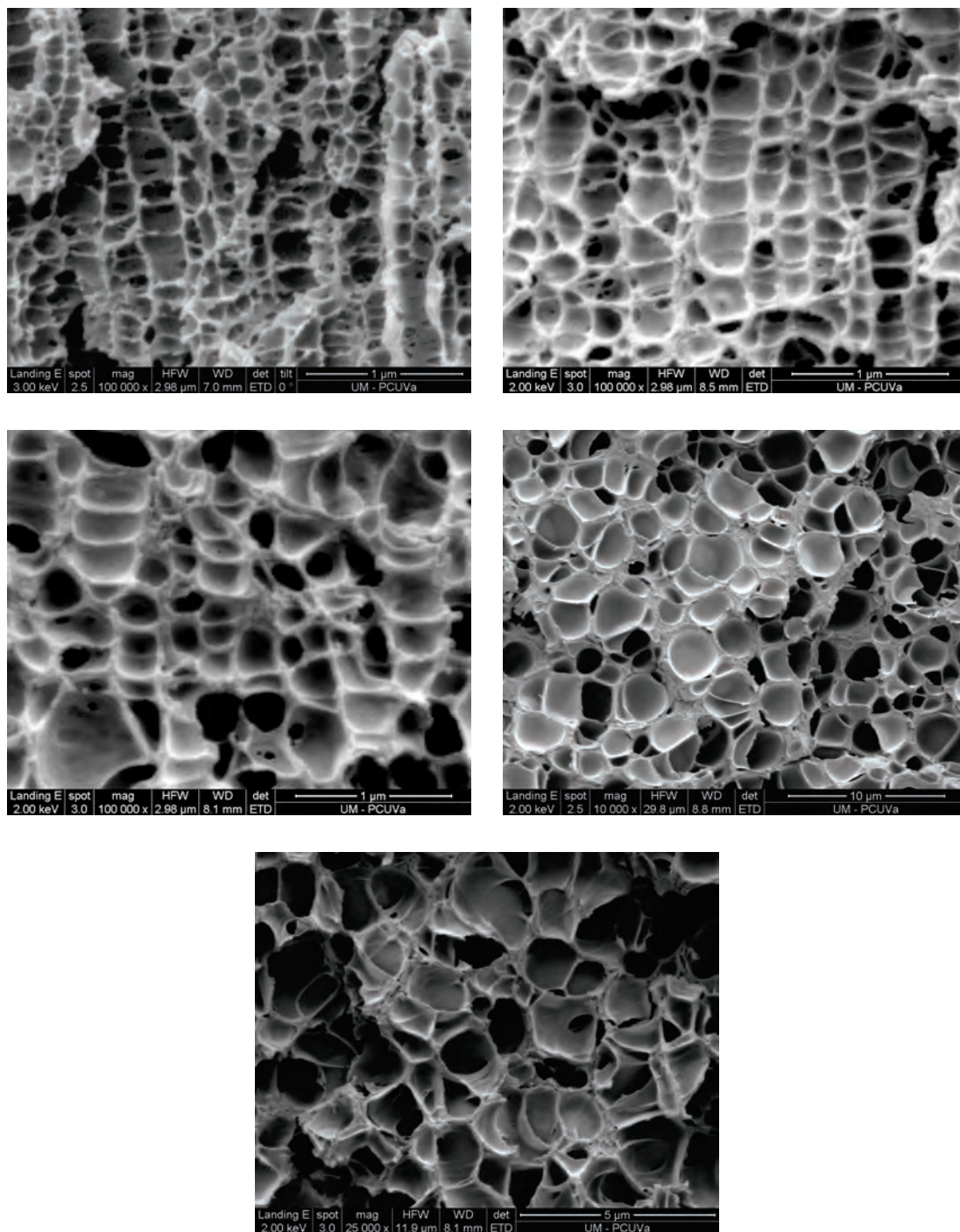


**Figure II.36: SEM micrographs (V) of 90/10 PMMA/MAM blends foamed at 30 MPa and different temperatures: RT (upper left), 40° C (upper right), 50° C (middle left), 60° C (middle right), 70° C (down).**

75/25 PMMA/MAM foams produced at 30 MPa present a well-defined and anisotropic cellular structure at RT and 40° C (Figure II.37). At temperatures between 50 and 60° C the nanocellular structure seems to become almost isotropic, probably due to the modification of the nanostructuration of the solid precursor previously explained (i.e. CO<sub>2</sub> saturation and annealing). Finally, at 70° C the cellular structure tends to be “semi co-continuous” without homogeneous distribution (i.e. areas with co-continuous cellular structure).

and areas without cells can be found in these foams; these solid areas could be related to the saturation annealing at these saturation conditions).

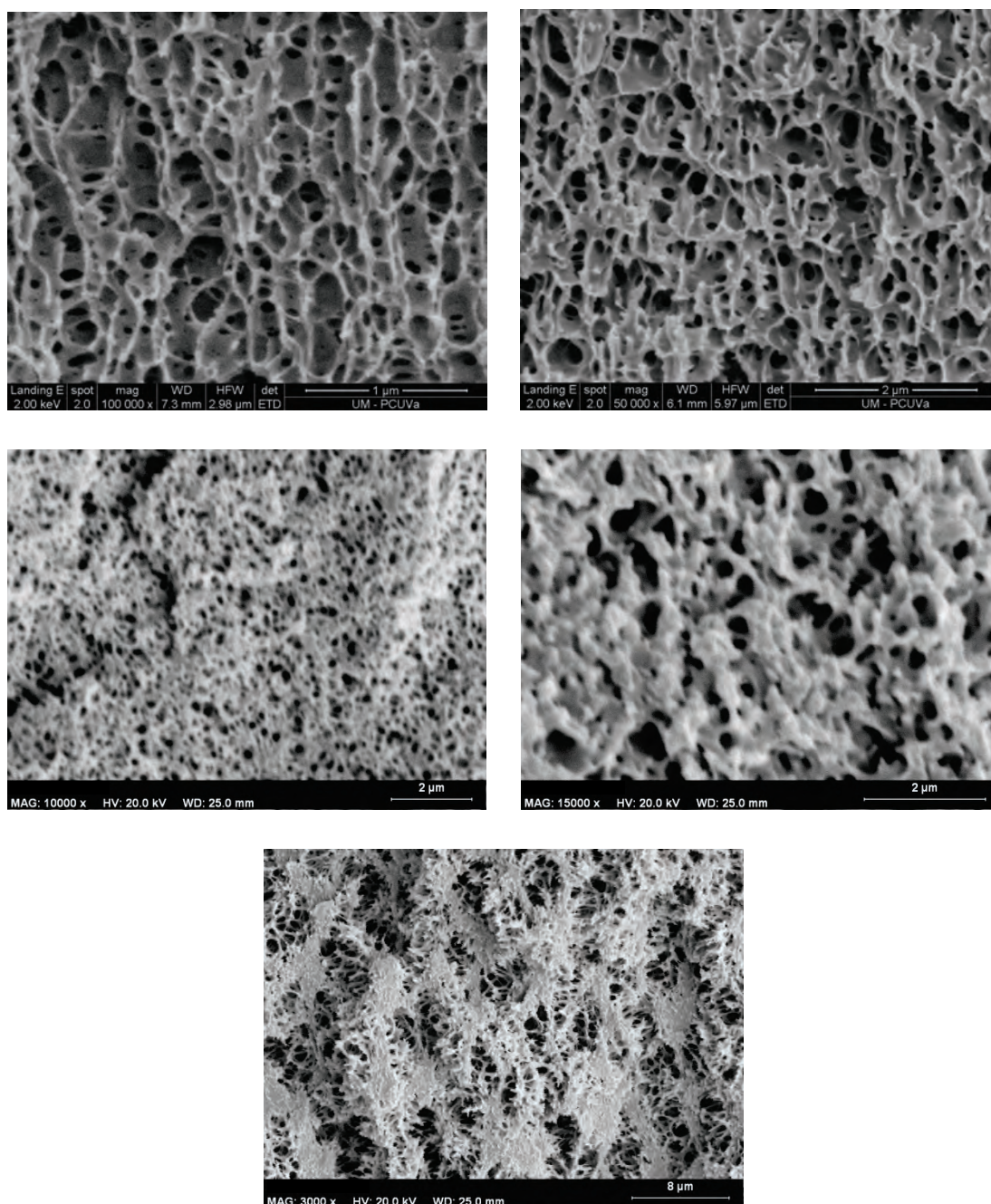


**Figure II.37: SEM micrographs (V) of 75/25 PMMA/MAM blends foamed at 30 MPa and different temperatures: RT (upper left), 40° C (upper right), 50° C (middle left), 60° C (middle right), 70° C (down).**

25/75 PMMA/MAM foams produced at 30 MPa present very different cellular morphologies depending on the saturation temperature (Figure II. 38), and no alignment of elongation effects on the injection direction. Foams produced at RT and 40° C present a co-continuous nanocellular structure (i.e. open cell structure with high connectivity). On the other hand foams produced at 50° C still present nanometric co-



continuous cells, but with an inhomogeneous structure containing solid areas, which could be related to the saturation annealing at these saturation conditions. On the contrary, foams produced at higher temperatures present a well-defined closed cell microcellular structure.

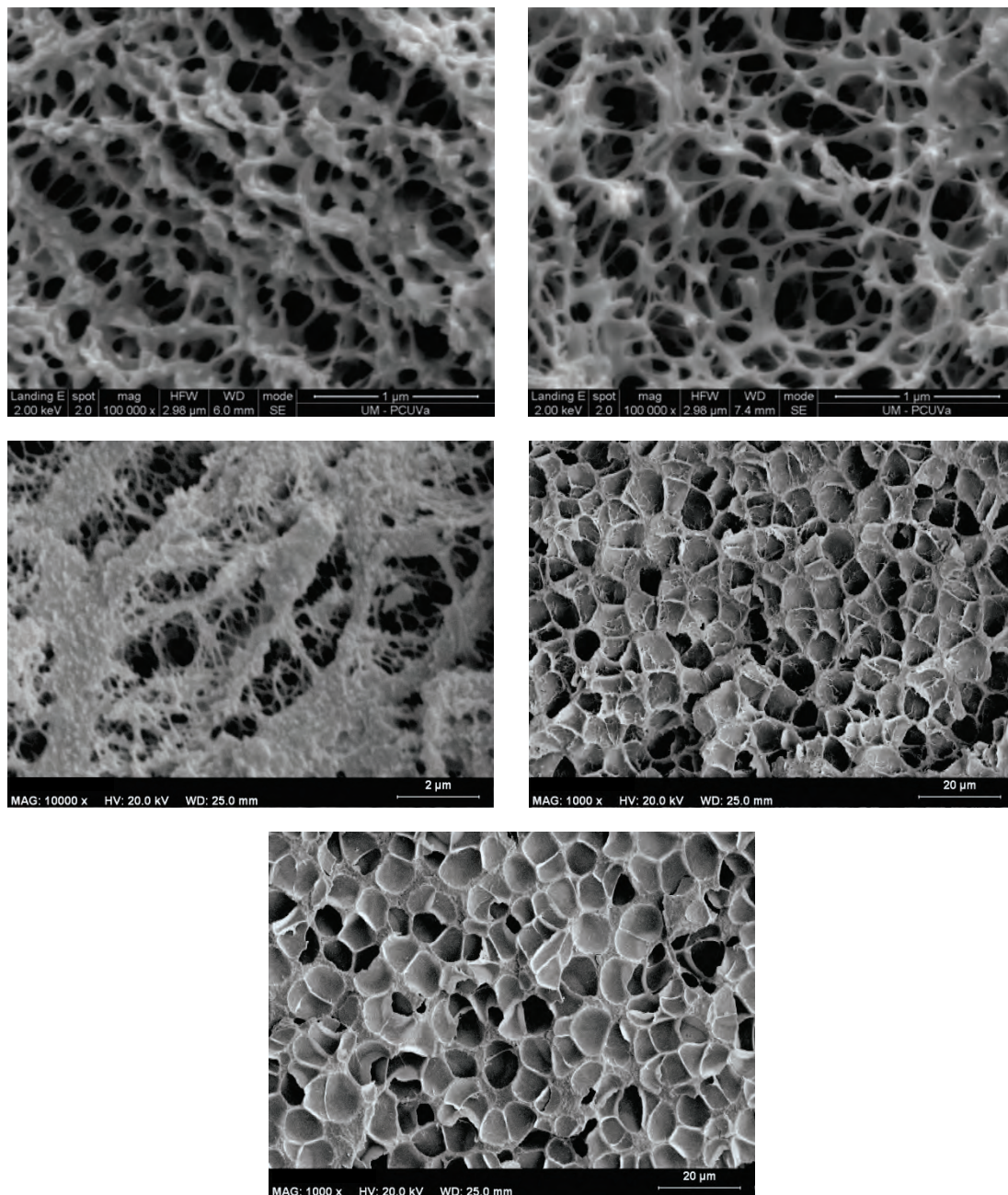


**Figure II.38: SEM micrographs (V) of 25/75 PMMA/MAM blends foamed at 30 MPa and different temperatures: RT (upper left), 40° C (upper right), 50° C (middle left), 60° C (middle right), 70° C (down).**

Neat MAM foams produced at 30 MPa present a similar behavior as 25/75 PMMA/MAM foams (Figure II.39). However, neat MAM only presents a co-continuous nanocellular structure when foaming is carried out at RT. At temperatures over 40° C, a rather constant closed microcellular structure is found.



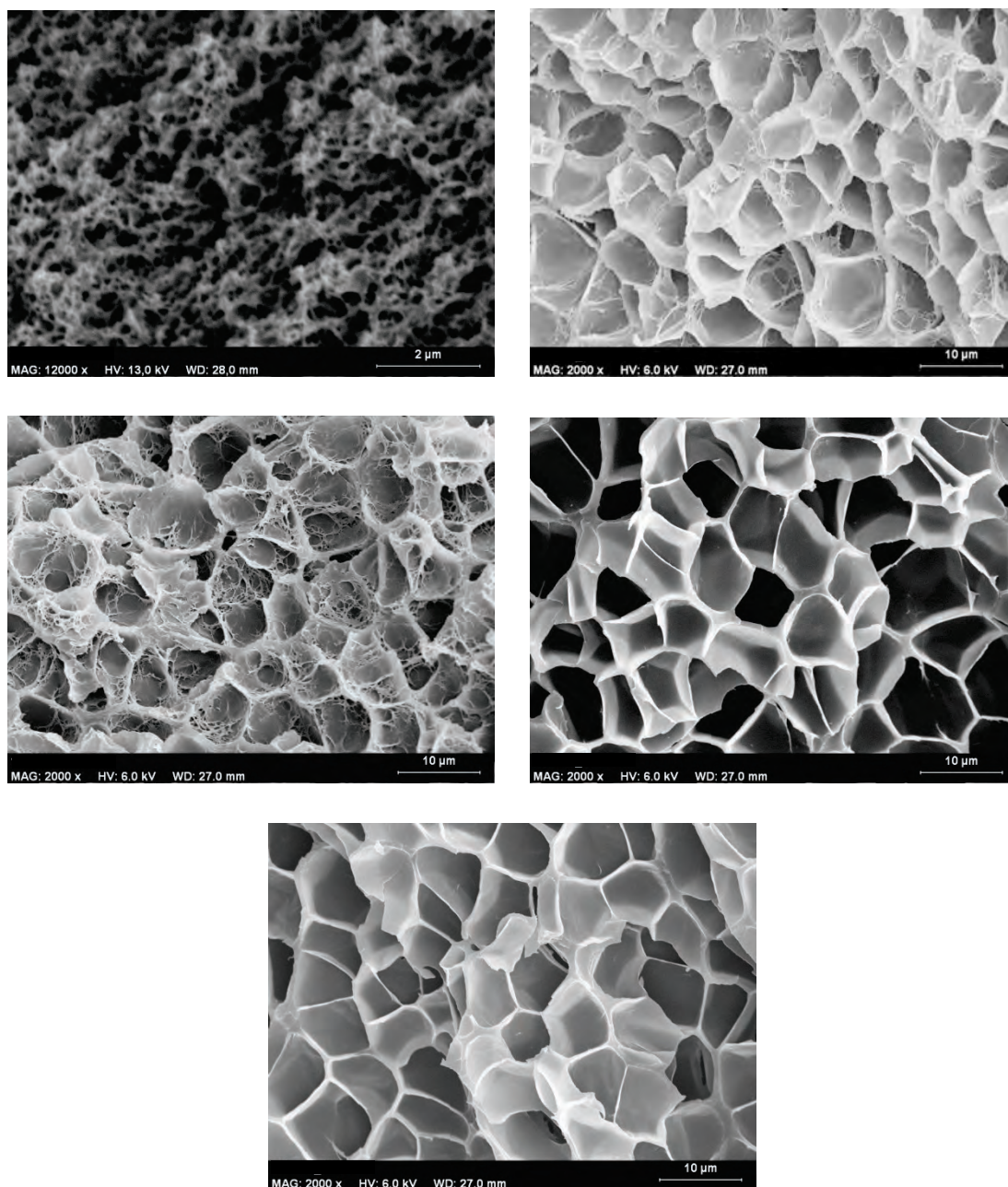


**Figure II.39: SEM micrographs (V) of neat MAM foamed at 30 MPa and different temperatures: RT (upper left), 40° C (upper right), 50° C (middle left), 60° C (middle right), 70° C (down).**

### II.8.5 Influence of saturation CO<sub>2</sub> pressure

The saturation temperature was not the only processing parameter studied in this research work. Influence of the saturation pressure on PMMA/MAM foams was also analyzed. Variation of the saturation pressure may or may not produce significant modifications of the cellular structure of PMMA based foams. For instance, neat PMMA and 90/10 PMMA/MAM foams present completely different behaviors according to the saturation pressure variation.

Neat PMMA foams produced at RT and pressures between 10 and 30 MPa show a clear dependence of the cell size with the saturation pressure (Figure II.32). Foams produced at pressures up to 20 MPa present microcellular structures, while at higher pressures the cell sizes lie under the micron; reaching an average size about 90 nm in foams produced at 30 MPa.

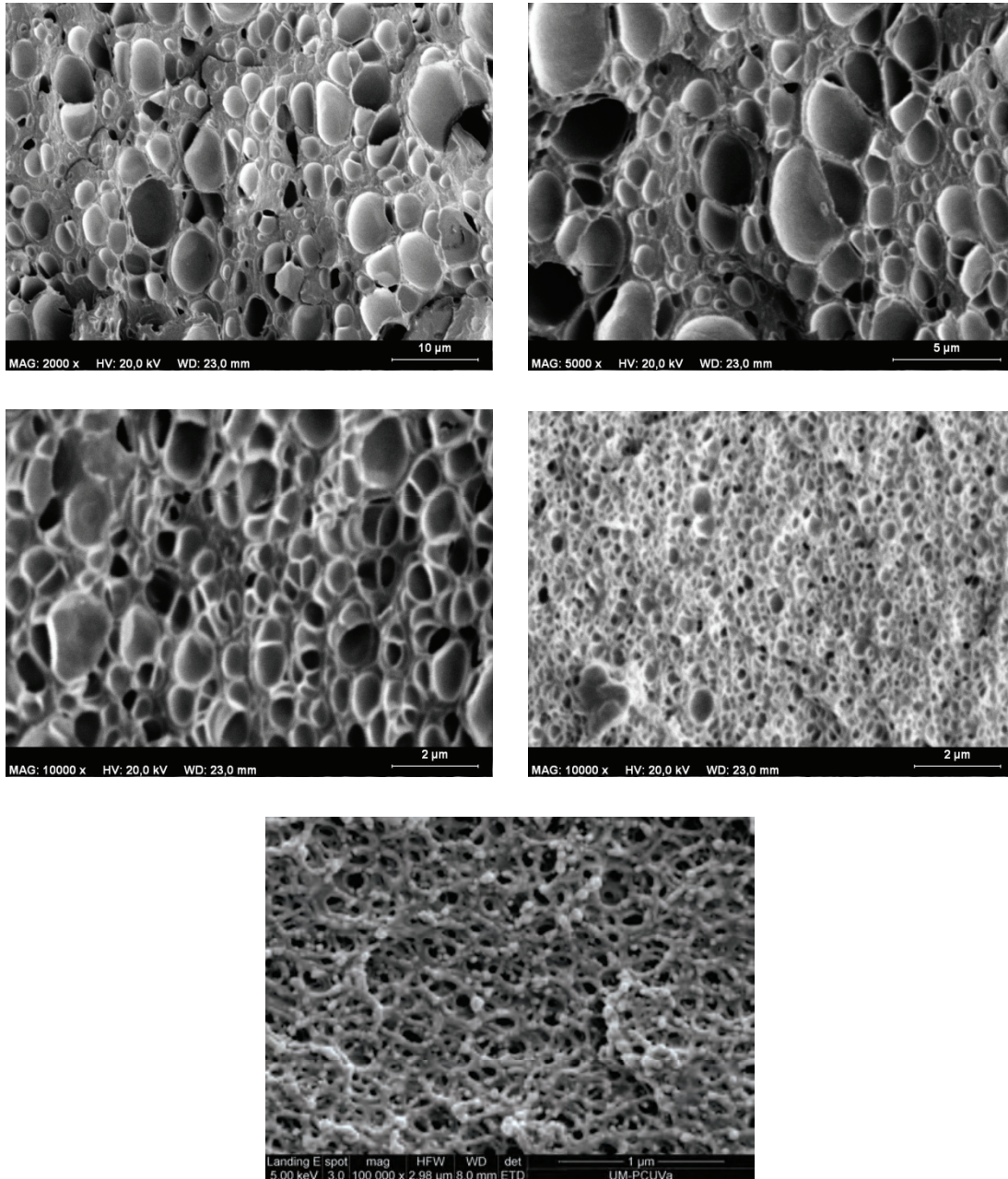


**Figure II.32: SEM micrographs (V) of neat PMMA foamed at room temperature and different pressures: 10 MPa (upper left), 15 MPa (upper right), 20 MPa (middle left), 25 MPa (middle right), 30 MPa (down).**



On the other hand, 90/10 PMMA/MAM foams produced at RT and different pressures (from 10 to 30 MPa) present nearly the same nanocellular structure, with only a small cell size increase with the increase of the saturation pressures (Figure II.33).

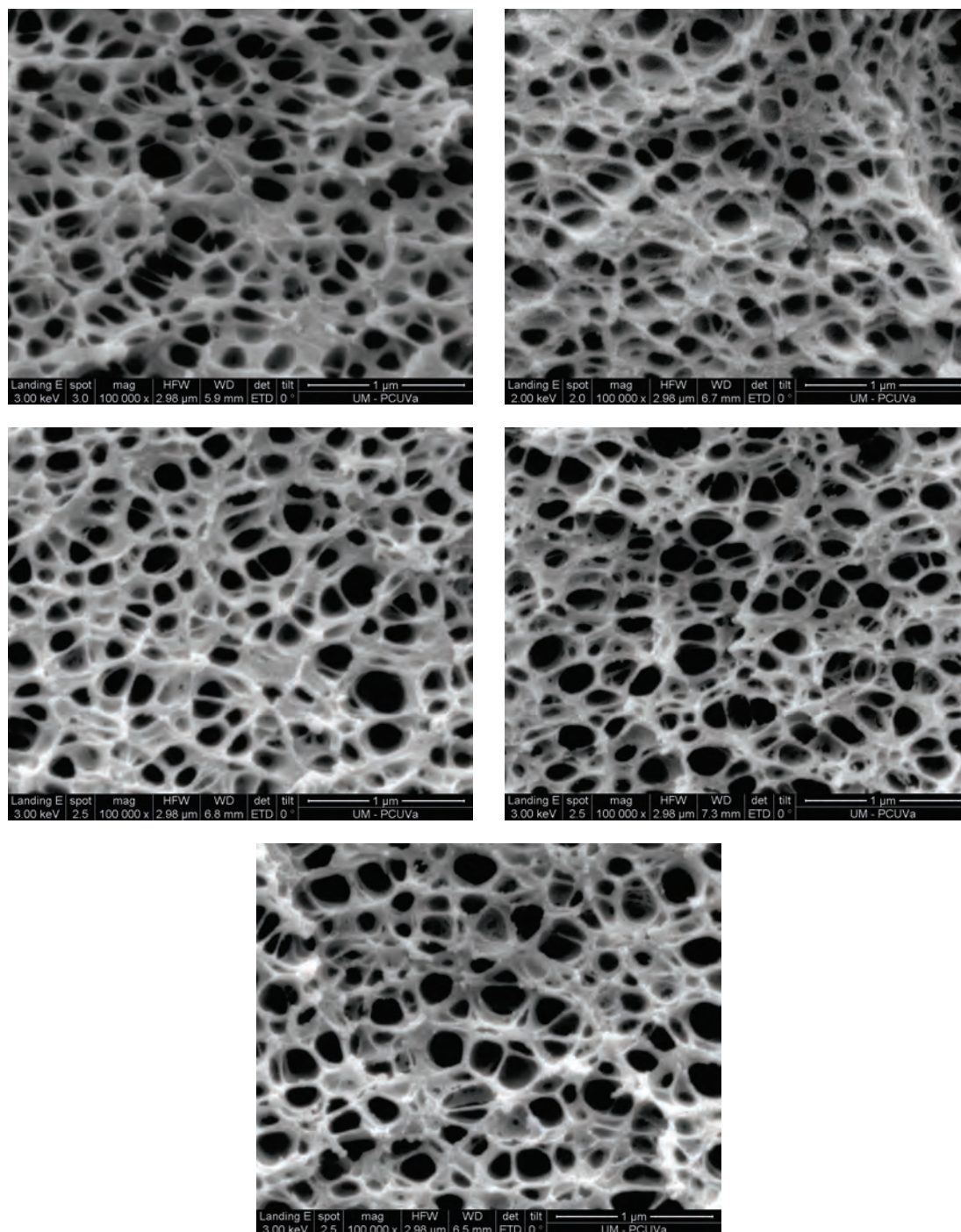


**Figure II.31: SEM micrographs (H) of 90/10 PMMA/MAM blends foamed at room temperature and different pressures: 10 MPa (upper left), 15 MPa (upper right), 20 MPa (middle left), 25 MPa (middle right), 30 MPa (down).**

As a conclusion, we found that the addition to PMMA of various MAM amounts generates a broad range of cellular structures, which are also dependent on the processing conditions; but this latter dependence is very sensitive (or related) to the MAM amount, whereas the processing conditions (i.e. saturation temperature, saturation pressure and foaming temperature) play a much more negligible role in the presence of MAM than in neat PMMA. The tremendous variety of structures produced in this system would be very helpful in the rest of the research, both for the analysis of foaming mechanisms and for the analysis of structure-property relationships.

A further study of these cellular structures, and moreover the relationship between the nanostructuration, cellular structure, and processing parameters is provided in the following chapters.

## II.9 References

1. Lalande, L., C.J.G. Plummer, J.-A.E. Manson and P. Gérard, *The influence of matrix modification on fracture mechanisms in rubber toughened polymethylmethacrylate*. Polymer, 2006. **47**(7): 2389-2401.
2. Lalande, L., C.J.G. Plummer, J.-A.E. Manson and P. Gérard, *Microdeformation mechanisms in rubber toughened PMMA and PMMA-based copolymers*. Engineering fracture mechanics, 2006. **73**(16): 2413-2426.
3. Lalande, L., *Structure et mécanismes de microdéformation de polyméthylméthacrylates renforcés au choc*, 2007, Ecole Polytechnique Federale de Lausanne.
4. Ruzette, A.-V., S. Tencé-Girault, L. Leibler, F. Chauvin, D. Bertin, O. Guerret and P. Gerard, *Molecular disorder and mesoscopic order in polydisperse acrylic block copolymers prepared by controlled radical polymerization*. Macromolecules, 2006. **39**(17): 5804-5814.
5. Corté, L., K. Yamauchi, F. Court, M. Cloître, T. Hashimoto and L. Leibler, *Annealing and defect trapping in lamellar phases of triblock terpolymers*. Macromolecules, 2003. **36**(20): 7695-7706.
6. Gerard, P., L. Couvreur, S. Magnet, J. Ness and S. Schmidt, *Controlled architecture polymers at Arkema: synthesis, morphology and properties of all-acrylic block copolymers*. Controlled/living radical polymerization: progress in RAFT, DT, NMP & OMRP, 2009: 361-373.
7. Maiez, S., *Relations entre la structure d'un copolymère à blocs et la nanostructuration d'un polymère réticulé*, 2007, INSA Lyon.
8. Tran, T.A., F. Leonardi, S. Bourrigaud, P. Gerard and C. Derail, *All acrylic block copolymers based on poly(methyl methacrylate) and poly(butyl acrylate). A link between the physico-chemical properties and the mechanical behaviour on impact tests*. Polymer Testing, 2008. **27**: 945-950.
9. Solórzano, E., J. Escudero, J. Pinto, M. A. Rodriguez-Perez and J. A. De Saja. *Evolution of Polymers during the Gas Dissolution Process*. in *International Conference on Diffusion in Solids and Liquids*. 2011. Algarve, Portugal.
10. Nawaby, A.V., Y.P. Handa, X. Liao, Y. Yoshitaka and M. Tomohiro, *Polymer-CO<sub>2</sub> systems exhibiting retrograde behavior and formation of nanofoams*. Polymer international, 2007. **56**(1): 67-73.
11. Goel, S.K. and E.J. Beckman, *Generation of microcellular polymers using supercritical CO<sub>2</sub>*. Cellular polymers, 1993. **12**(4): 251-274.



***Chapter III:***

***Relationship between PMMA/MAM blends nanostructuration and cellular structures. Foaming mechanisms***





## Chapter III. Relationship between PMMA/MAM blends nanostructures and cellular structures. Foaming mechanisms

In this chapter the cellular structures of foams produced from neat PMMA and PMMA/MAM blends produced by  $\text{CO}_2$  gas dissolution foaming are presented. A selection of samples to be foamed was undertaken taking into account the nanostructuration of PMMA/MAM blends (see Chapter II). Thus, PMMA/MAM blends with well-defined dispersed or co-continuous morphologies (micelles – core/shell nodules or lamellas) were selected to produce foams.

From the comparison between the characteristics of the cellular structure of foamed samples and the nanostructure of the solid samples used for foaming we focus the study on understanding the cells nucleation and growth mechanisms. Also the influence of foaming parameters (saturation temperature, saturation pressure, and pressure release drop rate) provides valuable information about the mechanisms involved in the formation of the cellular structure.

Experimental procedures employed to determine these mechanisms, as well as the results obtained and discussion are included in the journal articles included in this chapter that are briefly summarized in the following paragraphs.

The first article was published in **Chemical Engineering Journal 243C (2014)** and entitled *“Nanocellular  $\text{CO}_2$  foaming of PMMA assisted by block copolymer nanostructuration”*, explains the methodology used to determine the cell nucleation mechanism in PMMA/MAM blends. The nanostructuration of PMMA/MAM blends with low amounts of MAM (5, 10 and 20 wt%) was studied by AFM and TEM, relating directly the dark area fraction on AFM micrographs to the PBA amount in each blend. In addition, a nearly constant micelles volumetric density ( $N_n \approx 4 \times 10^{14}$  micelles/ $\text{cm}^3$  of the solid sample) was found on these blends both in AFM and TEM micrographs.

From the study of the  $\text{CO}_2$  sorption during the saturation process it was found that the  $\text{CO}_2$  uptake of the samples is increased with the MAM amount. This increment of the  $\text{CO}_2$  sorption is related to the higher  $\text{CO}_2$ -philicity of PBA, and therefore, the nanostructures formed by PBA enable a  $\text{CO}_2$  concentration higher than the PMMA matrix ( $\text{CO}_2$  is preferentially located in the PBA phase).

Neat PMMA and PMMA/MAM bulk samples were foamed at different saturation pressures (from 10 to 30 MPa) to study the influence of the saturation pressure on the cellular structure of the foams. Neat PMMA foams present a strong dependence on the saturation pressure: their average cell size and cell nucleation density ( $N_o$ , nuclei/ $\text{cm}^3$  of the unfoamed sample) varying in the studied pressure range from 3.3  $\mu\text{m}$  to 90 nm and from  $2.76 \times 10^{10}$  to  $2.94 \times 10^{15}$  cells/ $\text{cm}^3$ , respectively. However, PMMA/MAM foams present a constant cell nucleation density (about  $4 \times 10^{14}$  nuclei/ $\text{cm}^3$ , measured in the plane

perpendicular to the injection direction), and their average cell size is slightly increased from 150 to 190 nm with the saturation pressure. Those results show that neat PMMA foaming is controlled by a homogeneous cell nucleation, while PMMA/MAM foaming is controlled by a heterogeneous cell nucleation mechanism, the micelles being the agents that control cells nucleation. Moreover, the role of PMMA/MAM micelles as nucleating sites is supported by qualitative theoretical considerations about the nucleation energy barrier (expected to be lower in the PBA micelles than in the PMMA matrix).

The study about the relationship between the PMMA/MAM nanostructuration and cellular structures are continued in the second article, entitled *“Block Copolymers Self-Assembly Allows Obtaining Tunable Micro or Nanoporous Membranes and Depth Filters Based on PMMA; Fabrication Method and Nanostructures”* (published in **The Journal of Physical Chemistry C 118 (2014)**). This study is focused on the capacity of the PMMA/MAM nanostructure to be an exact pattern of the cellular structure, and not only the nucleation regulator, and it includes blends in a wider range than those showed in the first paper (i.e. includes materials with high MAM contents). Moreover, this article discusses the potential use of the obtained cellular structures for filtration processes with the possibility of producing membranes and depth filters.

The anisotropy of nanostructure of PMMA/MAM blends presenting micellar objects is related to the anisotropy of the cellular structure of the foams. It is found that PMMA/MAM blends with spherical micelles (95/5) result into foams with cells without a anisotropy, while PMMA/MAM blends with elongated micelles (90/10 and 80/20) result into foams with anisotropic pores and closed cell structures.

PMMA/MAM blends with high MAM amounts (25/75) exhibiting a co-continuous nanostructuration result into a co-continuous cellular structure (open cell foams).

Both types of cellular structures present a nucleation process located on the PBA nanostructures, without influence of the CO<sub>2</sub> saturation parameters. Therefore, the saturation parameters are only used to control the global porosity and the average pore size.

It should be noticed that the previous articles mention that the increase in the MAM amount in samples with micelles (5 to 20 wt% of MAM) produces an increment of the micelles average diameter, and not of the micelles volumetric density of the sample. These results suggest that the increment of the MAM amount increase the number of MAM molecules on each micelle (Figure III.1). However, in a micellar system is expected that the size of micelles remains nearly constant above the critical micellar concentration (CMC) in a fluid medium at equilibrium, thus the increment of concentration of the block

copolymer should result in an increment of the micelles volumetric density. Therefore, we can assume that the nanostructuration of PMMA/MAM blends is formed out of equilibrium, and the nanostructured domains observed are micellar objects/core-shell created in a viscous liquid.

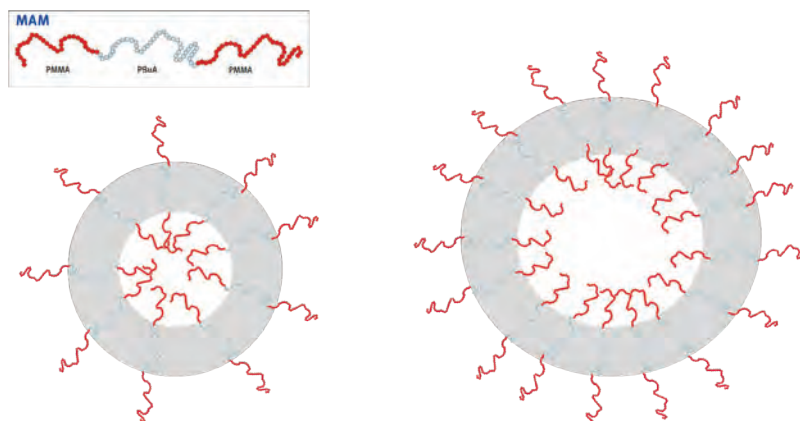


**Figure III.1: MAM structure and possible scheme about the micelles size increment related to the MAM amount increment**

The results of the two previous papers permitted to have a clear understanding of the cellular structure produced in each system and the key foaming mechanism taking place. Therefore, the inner cellular structure could be understood in terms of the concepts and ideas proposed in the two previous papers. However the foams produced by this process also can present a solid skin.

The last article, published in **Defect and Diffusion Forum Vols. 326-328 (2012)** and entitled “*Solid Skin Characterization of PMMA/MAM Foams Fabricated by Gas Dissolution Foaming over a Range of Pressures*”, is focused in the cells growth mechanism and in the understanding of the mechanisms creating the skin-core morphology of the foams under study.

The density profiles of neat PMMA and PMMA/MAM blends (with MAM amounts from 5 to 10 wt%) were obtained by X-ray radiography. From these density profiles it was possible to study the thickness and densification of the outer solid skin, a common characteristic of the foams produced by the solid state foaming process.

Neat PMMA foams present thicker solid skins than PMMA/MAM foams; also the skins of neat PMMA are completely densified and present a sharp transition between the foamed core and the solid skin, while PMMA/MAM skins are not completely densified, presenting a progressive densification from the core to the outside of the sample.

This behavior can be expected due to the different nucleation mechanisms of these materials. Neat PMMA, with a homogeneous nucleation mechanism, present typical solid skins, which are produced by the existence of a  $\text{CO}_2$  concentration threshold to trigger the nucleation process (Figure III.2). Areas of the neat PMMA samples with lower  $\text{CO}_2$  concentration than the threshold at the beginning of the foaming will not present nuclei, and thus no cells will appear on these areas.

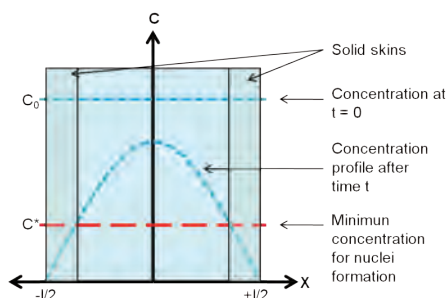


**Figure III.2: Schematic model of the solid skin formation on foams presenting homogeneous nucleation. Sample is extracted of the pressure vessel at time = 0 and foaming starts at time =  $t$ . Gas concentration is shown on axis Y, while the sample's width is shown on axis X (center of the sample corresponds to  $x = 0$ ).**

On the other hand, for the PMMA/MAM samples that present a heterogeneous nucleation mechanism the previous model is not valid. A new model for the cells growth and formation of outer skins on PMMA/MAM foams is presented in the article. The key idea is summarized in the following paragraphs and explained in detail in the paper.

Another important  $\text{CO}_2$  concentration threshold in PMMA/MAM foams corresponds to the  $\text{CO}_2$  concentration required for the PMMA matrix to be in a rubbery state at the foaming temperature (room temperature, RT). At the moment of the pressure release (time = 0) the  $\text{CO}_2$  concentration is constant in the entire PMMA/MAM sample, and the nucleation happens inside the PBA domains (Figure III.3).

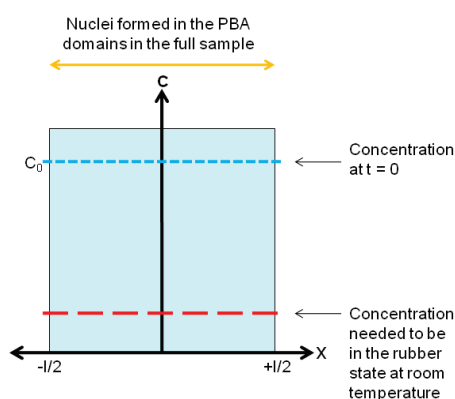


**Figure III.3: Schematic representation of the gas concentration profile at time = 0 and threshold concentration needed for the PMMA to be in a rubber state at RT. Gas concentration is shown on axis Y, while the sample's width is shown on axis X (center of the sample corresponds to  $x = 0$ ).**

However, after a time  $t$  (time needed for the sample to reach RT after the cooling produced by the pressure release) the concentration profile evolves, and the concentration of outer parts of the sample can fall under this concentration threshold. Nuclei are present on the PBA domains of the entire sample, but in the areas where the PMMA matrix is below their  $T_{g,ef}$  the cells growth will be hindered (Figure III.4). Main difference between both models is that the  $T_g$  is not a sharp threshold, but a continuous one, below this temperature the polymer chain mobility decreases significantly but some foaming is possible depending on the elastic properties of the polymer. That is why these foams present a progressive decrease of the porosity, but not a complete solid skin.

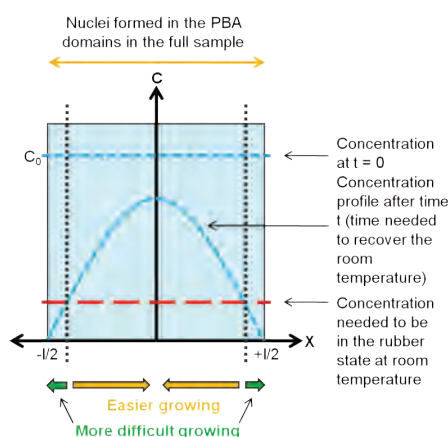


**Figure III.4: Schematic model of the solid skin formation on foams presenting heterogeneous nucleation.** Sample is extracted of the pressure vessel at time = 0 and foaming starts at time =  $t$ . Gas concentration is shown on axis Y, while the sample's width is shown on axis X (center of the sample corresponds to  $x = 0$ ).

As a conclusion, in these articles it is demonstrated that PMMA/MAM foams present a dissociated cell nucleation and growth mechanisms. Cell nucleation is controlled by the PBA domains, while cell growth is controlled by the plasticization of the PMMA matrix that surrounds the PBA domains. The knowledge developed allows predicting the type of cellular structure expected (open or closed cell), the cell size, the anisotropy, and the skin thickness as a function of the blend composition and the foaming parameters used.



## Nanocellular CO<sub>2</sub> foaming of PMMA assisted by block copolymer nanostructuration

Javier Pinto<sup>a,b,\*</sup>, Michel Dumon<sup>b</sup>, Matthieu Pedros<sup>c</sup>, José Reglero<sup>b</sup>, Miguel Angel Rodriguez-Perez<sup>a</sup>

<sup>a</sup> Cellular Materials Laboratory (CellMat), Condensed Matter Physics Department, University of Valladolid, 47011 Valladolid, Spain

<sup>b</sup> Laboratoire de Chimie des Polymères Organiques (LCPO), Université de Bordeaux, ENSCBP, 16 Avenue Pey Berland, 33607 Pessac-Cedex, France

<sup>c</sup> Département Science et Génie des Matériaux, IUT Université Bordeaux 1, 33175 Gradignan, France

### HIGHLIGHTS

- We obtain nanocellular foams by different nucleation mechanisms.
- We study the micelles present on PMMA/MAM blends.
- We found a clear relationship between the initial micelles and the final cells.
- We control the nucleation process with a self-assembled nanostructuration.

### ARTICLE INFO

#### Article history:

Received 26 September 2013

Received in revised form 7 January 2014

Accepted 9 January 2014

Available online 18 January 2014

#### Keywords:

Nanofoam

Block copolymer

Heterogeneous nucleation

### ABSTRACT

Polymer foams with closed cells in the range of 90–200 nm and relative densities between 0.4 and 0.6 have been produced by CO<sub>2</sub> gas dissolution foaming from neat poly(methyl methacrylate) (PMMA) and blends of PMMA and a triblock copolymer [poly(methyl methacrylate)-block poly(butyl acrylate)-block poly(methyl methacrylate), MAM]. Foams produced from these PMMA/MAM blends present a clear heterogeneous nucleation mechanism showing a clear relationship between the nanostructuration of the solid blend precursors and the nucleation efficiency of block copolymers during the saturation–expansion process. This paper discusses the role of the nanostructuration pattern of PMMA/MAM blends on the cells nucleation mechanism, showing that nucleation takes place preferably on the MAM nanostructures due to a combination of their high CO<sub>2</sub>-philicity, surface tension and morphology.

© 2014 Elsevier B.V. All rights reserved.

### 1. Introduction

One of the current horizons in the investigation of cellular materials is the development of low cost/easily accessible polymeric foams with cell sizes in the nanocellular range. These nanocellular foams are of great interest because they will present an unusual combination of properties.

First, they could have better mechanical properties than conventional foams, such as better toughness, fatigue life, stiffness and strength [1]. Secondly, when reducing the cell size below 75 nm, the contribution of gas to the thermal conductivity can be neglected due to the Knudsen effect [2]. This would allow producing cellular polymers with thermal conductivities much lower than those of the classical foams used nowadays for thermal insulation. Obviously, foams with these properties could be extremely interesting in several applications in construction, packaging, automo-

tive and aerospace sectors among others. Moreover, nanoporous morphologies will make these plastic materials good candidates for catalysis and filtration applications.

In the past years gas dissolution foaming using CO<sub>2</sub> has become one of the preferred routes to produce microcellular and nanocellular polymer foams [3–8]. This technique presents several advantages such as being industrially scalable and environmental friendly [9]. Development of polymer nanocellular foams by gas dissolution requires reaching very high cell nucleation ratios and reduced coalescence. Several approaches have been used to promote the nucleation up to the desired levels (typically higher than 10<sup>14</sup>–10<sup>15</sup> nuclei per cubic centimeter of un-foamed material).

However, these types of cellular structures are not easy to obtain because thermodynamics does not favor small cells, leading to a huge increment of the interfacial (surface) area and interfacial (surface) free energy.

It is known that the increase in the saturation pressure and the pressure drop rate increase the number of nuclei formed by homogeneous nucleation [10]. Also, increasing the potential nucleation sites can be achieved by the addition of several types of particles

\* Corresponding author at: Cellular Materials Laboratory (CellMat), Condensed Matter Physics Department, University of Valladolid, 47011 Valladolid, Spain.

E-mail addresses: [niarrod@fmc.uva.es](mailto:niarrod@fmc.uva.es), [jpinto@fmc.uva.es](mailto:jpinto@fmc.uva.es) (J. Pinto), [michel.dumon@u-bordeaux1.fr](mailto:michel.dumon@u-bordeaux1.fr) (M. Dumon).



(such as talc, titanium oxide, kaolin, nanosilica, and other nanoparticles) [11,12] that could act as nucleants agents. And finally, nucleation can be enhanced using copolymers, both random copolymers [13] and block copolymers [14–16]. This last method allows producing microcellular or submicrocellular foams with cell densities  $N_v > 10^9$  cells/cm<sup>3</sup>. A–B diblock or A–B–A triblock copolymers, at low contents (<15 wt.%), can self-assemble into a large number of spherical micelles up to  $10^{13}$ – $10^{14}$  micelles/cm<sup>3</sup>. The use of block copolymers with CO<sub>2</sub>-philic blocks can produce nanocellular porous structures as a blend with a homopolymer, in thin films or less frequently in bulk samples. However, up to date there are some important limitations in this procedure. First, the foaming process is achieved in thin film samples (thickness of 100 µm), and improved in some cases by reduction in the rate of CO<sub>2</sub> diffusion upon depressurization with barriers [17]. Second, a rather long and non-trivial chemical synthesis is needed to produce the CO<sub>2</sub>-philic block copolymers.

Influence of particles or nanostructures on the nucleation process has been widely studied. Classic Nucleation Theory (CNT) allows estimating the energy barrier that a nuclei should overcome to grow into a bubble (Gibbs free energy barrier), assuming homogeneous nucleation [12,14]:

$$\Delta G = \frac{16\pi}{3\Delta P^2} \gamma^3 \quad (1)$$

where  $\Delta P$  is the pressure difference between the bubble and the bulk (here assumed to be the saturation pressure) and  $\gamma$  is the surface tension of polymer matrix in the presence of CO<sub>2</sub> (i.e. between the bubble and the polymer phase). Following this equation (approximation) it is possible to obtain the critical value of the nuclei radius (i.e. the minimum nuclei radius needed to grow into a bubble) using the following expression [12]:

$$r^* = \frac{2\gamma}{\Delta P} \quad (2)$$

Therefore dispersed entities (particles, nanostructures, etc.) can act as effective nucleation agents when they provide a potential nucleation site with lower energy barrier than the surrounding polymeric matrix. Also, it is commonly assumed that effective nucleation agents should have a similar or higher size than the critical radius [12,14]. So, effectiveness of nucleation agents can be studied by comparison of their size and energy barrier with the corresponding values for homogeneous nucleation. It should be noticed that CNT presents limitations when the nuclei size falls into the nanometric range [12,18]. However, it can be used to provide a qualitatively estimation of nucleation in nanofoams [12].

Recently, several groups have made significant advances in the production of nanocellular foams with high porosity. Costeux and Zhu [12] fabricated nanocellular foams with cell sizes and relative density about 100 nm and 0.15 respectively, from acrylic copolymers by the addition of nanoparticles. Also Costeux et al. [19] produced foams from blends of styrenic and acrylic polymers with cell sizes below 100 nm and relative densities from 0.3 to 0.4, using gas saturation pressures up to 30 MPa. Foams with cell sizes between 40 and 100 nm and relative densities from 0.36 to 0.75 were obtained by Aher et al. [20], from homogeneous polyetherimide (PEI) saturated with CO<sub>2</sub> at 20 MPa during 100 h. Block copolymer poly(styrene-*b*-perfluorooctylethyl methacrylate) and homopolymer polystyrene were used by Shinkai et al. [21], obtaining films with pore sizes about 100 nm by quenching the films to –10 °C after the gas saturation process and using very low pressure release rates, in order to preserve the cellular structure.

In a previous work [15,16,22] we have obtained a new generation of nanocellular materials, which overcome most of the problems and difficulties exposed previously. Extruded blends of PMMA [poly(methyl methacrylate)] and MAM triblock copolymer

[poly(methyl methacrylate)-block poly(butyl acrylate)-block poly(methyl methacrylate)], both commercial materials, are easily nanostructured/self assembled. These blends can be foamed using CO<sub>2</sub> as blowing agent, even in parts with a significant thickness (several millimeters), and provide foams with an important density reduction (relative foam density, i.e. density of the foam divided by the density of the solid material,  $\rho_r \approx 0.5$ ), a nanosized cellular structure (cell sizes around or lower than 200 nm), and a high cell density up to  $10^{14}$  cells/cm<sup>3</sup>. However, in this initial work the relationship between the morphology of the solid blends and the cellular structure of the foams was not discussed. This is the main aim of this paper in which we present and discuss the nanostructure of the different solid blends. In addition, the cellular structure of the foams obtained from these blends by gas dissolution foaming using CO<sub>2</sub> has been characterized. Finally, the influence on the cellular structure of the processing parameters and the nanostructure has been determined. From these results and the measurements of the CO<sub>2</sub> sorption of neat PMMA and PMMA/MAM blends a block copolymer-assisted heterogeneous nucleation mechanism for these foams is proposed.

## 2. Experimental part

### 2.1. Materials

Poly(methyl methacrylate) (PMMA) and block copolymer poly(methylmethacrylate)-co-poly(butyl acrylate)-co-poly(methylmethacrylate) (MAM) were kindly supplied by Arkema Company (France). PMMA presents a density ( $\rho$ ) of 1.18 g/cm<sup>3</sup> and glass transition temperature ( $T_g$ ) of 112 °C. MAM triblock copolymer presents a density of 1.08 g/cm<sup>3</sup>. Both materials, obtained in the form of pellets, are optically transparent. Production details of MAM copolymers can be found in the literature [23,24].

The particular MAM in our study contains around 36 wt.% poly(butyl acrylate) (PBA), and the following molar mass characteristics, given by Arkema,  $M_n^{MAM} \approx 85,000$  g/mol (own SEC measurement at 85,000 g/mol),  $M_w^{MAM} \approx 180,000$  g/mol (our own measurement is at 170,000 g/mol), therefore  $M_w^{MAM} \approx 2$ . The PMMA used is a pure homopolymer (without impact modifier) with the following characteristics  $M_w \approx 83,000$  g/mol,  $M_n \approx 43,000$  g/mol,  $I_p \approx 1.9$ .

### 2.2. Blends production

Polymer blends of PMMA containing 5, 10, 15 and 20 wt.% of MAM were produced as follows. Both materials, PMMA and MAM, were dried in vacuum (680 mm Hg), at 80 °C during 4 h before processing. Mixing and extrusion were carried out using a Scamex CEO2 single-screw extruder ( $L/D = 28$   $d = 45$  mm), with a temperature profile from 165 to 225 °C at a screw speed of 60 rpm in the desired proportions. Pellets were produced using a continuous cutting machine operating at the end of the line at a constant speed of 240 rpm.

In a second step, the pellets produced were injected into pieces  $50 \times 15$  mm<sup>2</sup> with 3 mm thickness, using a small scale injection molding machine developed by DSM Xplore. The working temperature was fixed at 240 °C, whereas mold temperature was set at 60 °C. The injection pressure was fixed at 1 MPa. All samples are transparent and showed a good surface appearance as well a good injection behavior, without air bubbles inside the parts.

### 2.3. Foaming process and bulk foam production

Foaming experiments were carried out in a high pressure vessel provided by TOP Industry (France), with a capacity of 300 cm<sup>3</sup> and



capable of operating at maximum temperature of 250 °C and maximum pressure of 40 MPa. The reactor is equipped with an accurate pressure pump controller provided by Teledyne ISCO, and controlled automatically to keep the temperature and pressure at the desired values. The CO<sub>2</sub> vessel temperature and pressure were monitored in the course of the process. Thus a collection of experiments were performed in a modified solid state foaming process. The usual solid state foaming process with amorphous polymers has three stages, the saturation (under fixed gas pressure and temperature), gas desorption during and after the pressure release (to room pressure and temperature) and foaming of the sample (at a temperature over or around the  $T_g$  the plasticized polymer). However, the actual glass transition temperature of PMMA-CO<sub>2</sub> systems can reach values close to room temperature [25], even below room temperature in some particular conditions [4], so that the desorption (at room temperature) and foaming stages (at room temperature) are not well separated. Furthermore the samples temperature decreases to values clearly below room temperature during the pressure release (due to adiabatic depressurization), then foaming is induced when the sample temperature reaches room temperature.

In this study, samples were saturated at different pressures, from 10 to 30 MPa, and at room temperature during 24 h to assure the complete dissolution of CO<sub>2</sub> in the polymer. After this saturation process, foaming was triggered by releasing the pressure inside the vessel at a pressure drop rate between 10 and 30 MPa/min. This method allows foaming within the vessel in one-step ("pressure release foaming").

#### 2.4. Characterization

Foam and solid sample densities,  $\rho_f$  and  $\rho_s$ , respectively, were determined by water-displacement method, based on Archimedes' principle. At least three measurements were carried out for each sample produced.

The cellular structure of foamed samples was analyzed by means of scanning electron microscopy (SEM, model Quanta 200FEG, FEI). Foams were frozen in liquid nitrogen and fractured to assure that the microstructure remained intact. Surfaces were coated with gold using a sputter coater (model SCD 004, Balzers Union). The micrographs obtained were analyzed to measure cell sizes with a specific software [26] based on Fiji/ImageJ [27]. This software provides the cell size distribution, the average cell size, the cell anisotropy ratio distribution, the average cell anisotropy ratio, the cell density  $N_v$  (cells/cm<sup>3</sup>) and the cell nucleation density  $N_o$  (nucleation points/cm<sup>3</sup>), that can be calculated from  $N_v$  according to Eq. (3) [28]

$$N_o = \frac{N_v}{1 - V_f} \quad (3)$$

where  $V_f$  is the volume fraction of voids, which can be determined using Eq. (4).

$$V_f = 1 - \frac{\rho_f}{\rho_s} \quad (4)$$

Sorption of CO<sub>2</sub> in PMMA/MAM blends was studied measuring the CO<sub>2</sub> uptake during saturation. This value was calculated as the percentage of weight increment of the sample due to the CO<sub>2</sub> sorption. Samples were weighted before ( $m_0$ ) and just after the saturation ( $m_1$ , measured at RT after depressurization at 30 MPa/min), and the CO<sub>2</sub> uptake was calculated as follows:

$$\text{CO}_2 \text{ uptake} = \frac{(m_1 - m_0)}{m_0} \times 100 \quad (5)$$

Nanostructuration of PMMA/MAM blends was observed by Atomic Force Microscopy (AFM) and Transmission Electron Microscopy (TEM). AFM allows studying the nanostructuration of

the solid PMMA/MAM blends. The AFM images were obtained in tapping mode, with a super sharp silicon tip, cutting previously the samples using a microtome. The morphology analysis was carried out by image analysis from the obtained AFM phase images, and the nanostructure density  $N_n$  (number of dispersed nanosized domains/cm<sup>3</sup>) was calculated using Eq. (6).

$$N_n = \left(\frac{n}{A}\right)^{3/2} \quad (6)$$

where  $n$  is the number of nanostructures observed in an AFM phase image and  $A$  the area of the image in cm<sup>2</sup>. AFM was carried out in the Instituto de Microelectrónica de Madrid (INM, CSIC) using a Multimode AFM (Veeco Instruments).

In addition, morphologies of solid and foamed PMMA/MAM blends were observed by Transmission Electron Microscopy (TEM, model Hitachi H7650 with Orius camera). TEM thin cuts were obtained using a microtome with diamond knife operating at -50 °C and were treated by phosphotungstic acid (PTA). TEM was carried out in the Bordeaux Imaging Center BIC, Université Bordeaux Segalen.

### 3. Results and discussion

#### 3.1. Nanostructured morphology in PMMA/MAM blends

The detection of nanostructuration in PMMA/MAM blends was first attempted using AFM, obtaining relevant information about the composition and orientation of the nanostructures, but not about their inner structure.

As expected, AFM phase images from neat PMMA bulk samples show a homogeneous polymer matrix without multiple phases. In contrast images obtained from PMMA/MAM samples present two clearly differentiated phases (soft and rigid). Blends of PMMA containing 5, 10 and 20 wt.% MAM were prepared using a single-screw extrusion machine (see Experimental part), then, injection molding provided bulk nanostructured PMMA/MAM blends. Fig. 1 shows AFM phase images of the blend with 20 wt.% MAM in two different planes (containing the injection direction and perpendicular to the injection direction). It is clearly observed that the nanostructure (black area on the figures) is oriented in the injection direction, as often observed in bulk injected samples [8]. The images shown from now on will be from planes perpendicular to the injection direction, because the trends found comparing the materials are similar independently of the plane of the sample or the orientation of the nanostructures.

Fig. 2 shows the nanostructure of three blends at low MAM contents. The volume density ( $N_n$ ) and the area fraction ( $A_n$ ) of nanostructures in each blend were calculated by image analysis. Results are shown in Table 1, a similar density of dispersed domains is found in the three blends. Fig. 3 shows a clear correlation

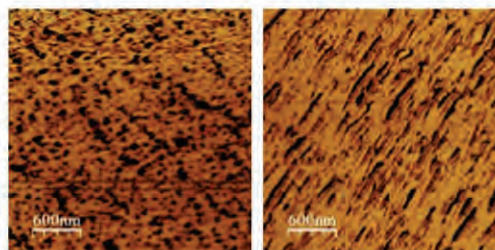


Fig. 1. AFM phase images of 80-PMMA/20-MAM. Plane perpendicular to the injection direction (left) and plane containing the injection direction (right).



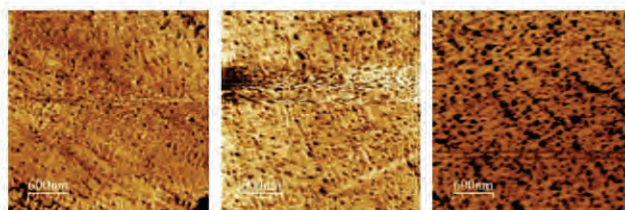


Fig. 2. AFM phase images of 95/5 (left), 90/10 (middle) and 80/20 (right) of PMMA/MAM blends in the plane perpendicular to the injection direction.

between the nanostructure fraction area and the nominal content of poly(butyl acrylate). The poly(butyl acrylate) (PBA) phase is the separated detected by AFM because it much softer than the PMMA matrix.

The nanostructures inner structure was revealed by TEM. TEM micrographs of samples treated by PTA show micellar objects at amounts of MAM between 5 and 20 wt.%. Fig. 4 shows an example of this, the nanostructure of the 90/10 PMMA/MAM blend.

Micelles appear as regular well dispersed nodules in the form of core-shell particles, appearing with a white PMMA core and a dark PBA layer (colored by PTA). Apparent two-layer nodules are embedded in a “white” matrix (probably PMMA coming both from the thermoplastic PMMA and from PMMA end blocks). Due to the 3-block “ABA” structure of the copolymer, these micelles might be constituted by 3 layers, the PMMA outer one is soluble in the matrix and is not contrasted by PTA.

A possible schematic representation of the overall micelles is shown in Fig. 5.

The average apparent size of micelles ( $r_m$ ) vary from 20 nm in 95/5 PMMA/MAM blends to 50 nm in 85/15 PMMA/MAM blends, the PMMA being core radius ( $r_c$ ) around 1/3 of the micelle size. The calculation of these means radii and the scheme in Fig. 5 shows that micelles may play the role of CO<sub>2</sub> concentrators of adequate size to act as organic nucleants.

Literature data shows that PBA homopolymer has a higher CO<sub>2</sub> solubility than PMMA homopolymer [29–31].

Also the PBA phase is in the rubbery phase whatever the temperature or pressure used. Thus these micelles are composed of a CO<sub>2</sub>-philic and soft PBA crown surrounded by a less CO<sub>2</sub>-philic and much more rigid PMMA phase. Both characteristics probably influence the foaming mechanism (e.g. CO<sub>2</sub> swelling, sorption, and cell expansion) as we'll describe in the next paragraphs.

### 3.2. CO<sub>2</sub> sorption of PMMA/MAM blends before foaming

CO<sub>2</sub> uptake of neat PMMA and three PMMA/MAM blends (95/5, 90/10, 85/15) saturated at RT at different pressures, between 10 and 30 MPa, are shown in Fig. 6.

Sorption of CO<sub>2</sub> in nanostructured blends increases with the addition of MAM. This behavior may have several explanations; MAM can present a higher CO<sub>2</sub>-philicity than PMMA [29–31], also the CO<sub>2</sub> solubility in PMMA blends can be increased by the presence of the soft-block, which allows a higher swelling during the CO<sub>2</sub> sorption process. Due to the significant increment of CO<sub>2</sub> even

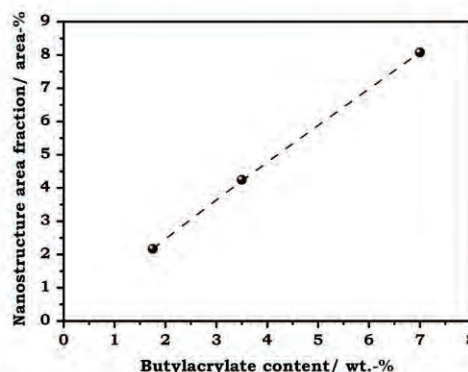


Fig. 3. Relationship between the nominal butylacrylate content of the blend and the nanostructure area fraction measured by image analysis on AFM images.

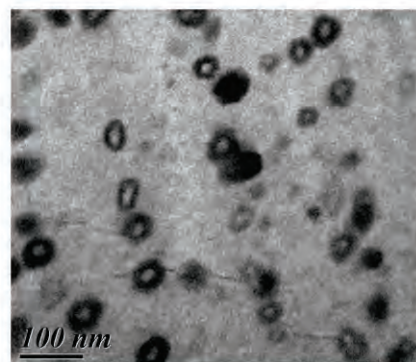


Fig. 4. TEM micrograph showing a core-shell structure of MAM copolymer in the 90/10 PMMA/MAM dense blend.

at low MAM amounts, it is reasonable to assume a combined contribution of both mechanisms. Then, nanostructures formed by PBA enable a CO<sub>2</sub> concentration higher than the PMMA matrix (a “localization” of CO<sub>2</sub>).

### 3.3. Effect of CO<sub>2</sub> saturation pressure on cellular structure

Samples of PMMA containing 10 wt.% of MAM and neat PMMA samples have been foamed together, using different saturation pressures between 10 and 30 MPa at room temperature. SEM images of neat PMMA and 90/10 foams obtained at the lower

**Table 1**  
Nanostructure characteristics of PMMA/MAM solid blend precursors ( $N_n$ : micelles density,  $A_n$ : area fraction from AFM).

Blend	$N_n$ (no./cm <sup>3</sup> )	$A_n$ (area-%)	Poly(butyl acrylate) content (wt.%)
95/5	$4.7 \times 10^{14}$	2.17	1.75
90/10	$4.7 \times 10^{14}$	4.25	3.50
80/20	$3.9 \times 10^{14}$	8.07	7.00



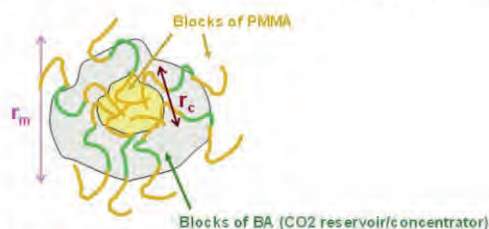


Fig. 5. Scheme of the MAM core-shell structure, showing PBA and PMMA 'crowns', PBA acting as a CO<sub>2</sub> concentrator in the middle shell.

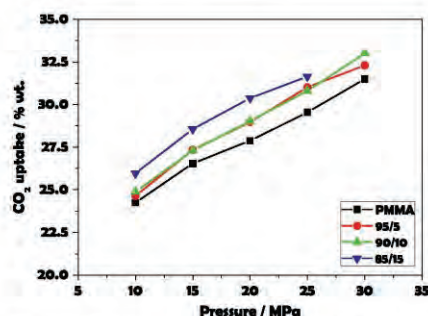


Fig. 6. CO<sub>2</sub> uptake of neat PMMA and PMMA/MAM blends after saturation at different pressures, at RT.

and higher saturation pressures (10 and 30 MPa) are shown in Fig. 7. The main characteristics of all the foams produced in this range of pressures can be found in Table 2 ( $P_{\text{sat}}$ ,  $\Phi_{\text{cell}}$ ,  $N_0$ , wt.%CO<sub>2</sub>uptake).

Neat PMMA foams present the expected behavior for materials with a homogeneous nucleation, where saturation pressure

controls the final relative density ( $\rho_r = \rho_f/\rho_s$ ) and the cell nucleation density ( $N_0$ ). As a consequence higher saturation pressures allow higher cell nucleation densities and lower densities. Increasing the saturation pressure up to 25–30 MPa allows producing nanocellular foams of neat PMMA with very high cell nucleation densities. It should be noticed that these nanocellular structures can only be obtained combining high pressures, rather 'low temperature' (room temperature or lower) and high pressure release rate (about 30 MPa/min or higher). Microcellular structures of neat PMMA foams have been reported previously with lower pressure release rates [15,22], where also an average cell size about 1  $\mu\text{m}$  has been found in PMMA foams produced at 30 MPa and 40 °C with pressure release rates about 30 MPa/min.

In contrast, 90%-PMMA/10%-MAM blend-foams (Table 2) present a behavior quite significantly different. Final relative density of the foams is also controlled by the saturation pressure, but a constant cell nucleation density (about  $4 \times 10^{14}$  nuclei/cm<sup>3</sup>) is found in every sample. The nucleation process seems to be decoupled from the saturation pressure, obtaining nanocellular foams even with the lowest saturation pressures (10 MPa). In addition, the values of the constant nucleation density of 90/10 PMMA/MAM foams virtually correspond to the density of dispersed micelles of the blends ( $4.7 \times 10^{14}$  micelles/cm<sup>3</sup>, Table 1), so in these foams the nucleation is dominated by the heterogeneous phase (poly(butyl acrylate) domains); for each micelle, a nanocell is produced.

Therefore, it is possible to obtain nanocellular foams from PMMA/MAM blends using low pressures, keeping nanocellular structures and modifying the density of the foam.

#### 3.4. Effect of MAM content on cellular structures

Different blends (95/5, 90/10 and 80/20) were foamed by saturation at room temperature and 30 MPa to study effect of the MAM content on the cellular structure. The main characteristics of resultant foams can be found in Table 3, also SEM images of the cellular structures of these foams are shown in Fig. 8.

Focusing on the nucleation of PMMA/MAM foams we found that the values of nucleation density are practically the same for the

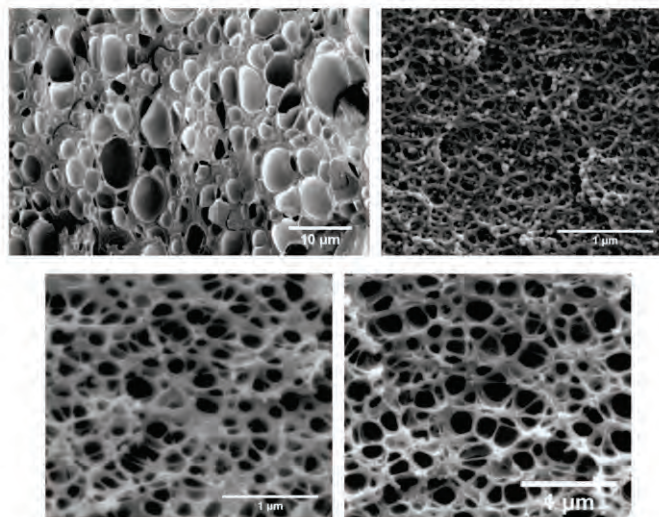


Fig. 7. SEM micrographs of foams from neat PMMA (up) and 90/10 PMMA/MAM (down) produced at room temperature and saturation pressures of 10 MPa (left) and 30 MPa (right).



**Table 2**

Comparative foams characteristics from neat PMMA (100/0) and PMMA/MAM blend (90/10) produced from different saturation pressures and room temperature (pressure release rate: around 30 MPa/min).

Blend	Saturation pressure (MPa)	$\rho_f$	Average cell size ( $\Phi_{cell}$ ) (nm)	$N_0$ (nuclei/cm <sup>3</sup> )	CO <sub>2</sub> Uptake (wt.%)
100/0	10	0.66	3290	$2.76 \times 10^{10}$	24.3
100/0	15	0.56	1460	$4.82 \times 10^{11}$	26.7
100/0	20	0.53	710	$4.73 \times 10^{12}$	28.1
100/0	25	0.49	200	$2.48 \times 10^{14}$	29.7
100/0	30	0.46	90	$2.94 \times 10^{15}$	31.5
90/10	10	0.58	150	$3.90 \times 10^{14}$	24.9
90/10	15	0.54	160	$3.81 \times 10^{14}$	27.5
90/10	20	0.49	170	$3.81 \times 10^{14}$	28.9
90/10	25	0.43	190	$3.68 \times 10^{14}$	30.6
90/10	30	0.44	180	$4.16 \times 10^{14}$	33.0

three blends, with values again about  $4 \times 10^{14}$  nuclei/cm<sup>3</sup>. Also, the increment of the MAM content is related to a higher CO<sub>2</sub> uptake and lower foam density. Consequently, assuming that the nucleation ratio is constant, the increment of MAM should induce an increment of the average cell size associated to a decrease in the foam density as shown in Fig. 9. However the variations are not large, due to the role of micelles whose structure probably limits the expansion by vitrification of the PMMA layers.

### 3.5. Heterogeneous nucleation mechanism

The previous results demonstrate the main role of the MAM micelles in the nucleation process. Apparently each micelle acts as a nucleus and grows into a cell. These results were obtained by simple comparison between the micelles density of solid blends and the cell nucleation density of foams.

A critical radius of the PMMA-CO<sub>2</sub> system can be estimated using Eq. (2). We used the saturation pressure as  $\Delta P$  and 38.5 mN/m as surface tension of PMMA-CO<sub>2</sub> [14,32]. Over the range of pressures of the study, 10–30 MPa,  $r^*$  takes values between 2.5 and 8 nm. Other estimations of the critical radius can be found in the literature. Costeux and Zhu [12] obtained values of 0.2 nm using CNT, and 2 nm taking into account other approximations claimed as more accurate, in both cases under processing conditions similar to ours. The micelles (taken as inner cores or first two layers, from 20 to 50 nm depending of the MAM content) are of much higher size than  $r^*_{estimated}$ —0.2 to 8 nm according to theories used, so it can be concluded that MAM micelles present appropriate sizes to promote the nucleation (higher than the critical radius). It should be noticed that the PMMA core of the

micelles have also an appropriate size to be a nucleation site (from about 7 nm to 17 nm).

Moreover, it is usually assumed that interfaces between phases provide a place energetically favorable for nucleation to take place. In PMMA/MAM blends two interfaces can be noticed according to the micelle morphology (see Fig. 5), one between the PBA shell and the PMMA matrix and other between the PMMA inner layer and the PBA shell. However, it is not clear that interfaces in our structures formed by “ABA” triblock copolymers show this behavior. In fact, the nucleation on an A–B interface necessitates vacating part in the interface to be occupied by the nucleated bubble, which would require additional energy in this type of block copolymers [14].

Therefore the most probable situation is that nucleation would take place in the PMMA or the PBA phase alone. It is possible to obtain a qualitative estimation about the magnitude of the nucleation energy barrier ( $\Delta G$ ) of each phase using the CNT equations. According to Eq. (1) the energy barrier is inversely proportional to the square of pressure difference between the bubble and the polymer phase ( $\Delta P$ ) and directly proportional to the surface tension ( $\gamma$ ) to the third power.

Pressure difference between the bubble and the polymer phase ( $\Delta P$ ) can be estimated as the difference between the initial and the final pressure of the gas-polymer system. Therefore, both PMMA and PBA should present similar values:  $\Delta P_{PMMA} \approx \Delta P_{MAM}$ .

In addition, surface tension of PBA has a value of 33.7 mN/m [33], lower than the PMMA one (38.5 mN/m):  $\gamma_{PBA} < \gamma_{PMMA}$ .

Taking into account both relationships it is concluded that neat PBA phase presents a homogeneous nucleation energy barrier significantly lower than that of neat PMMA phase.

**Table 3**

Comparative characteristics of PMMA/MAM foams produced from 30 MPa and room temperature at different MAM contents (in the low concentration range).

Blend	Temperature (°C)	$\rho_f$	Average cell size ( $\Phi_{cell}$ ) (nm)	$N_0$ (nuclei/cm <sup>3</sup> )	CO <sub>2</sub> uptake (wt.%)
95/5	23	0.46	170	$4.29 \times 10^{14}$	32.4
90/10	23	0.44	180	$4.16 \times 10^{14}$	33.0
80/20	23	0.41	190	$3.97 \times 10^{14}$	33.9

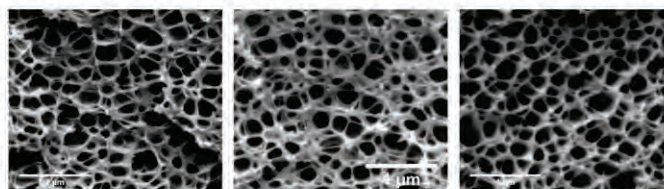


Fig. 8. SEM micrographs of 95/5 (left), 90/10 (middle) and 80/20 (right) PMMA/MAM foams.



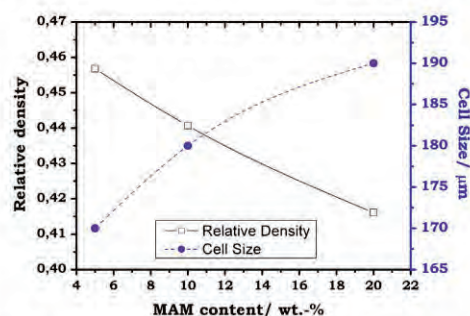


Fig. 9. Effect of the MAM content (low concentration range) on the relative density and average cell size of the foams.

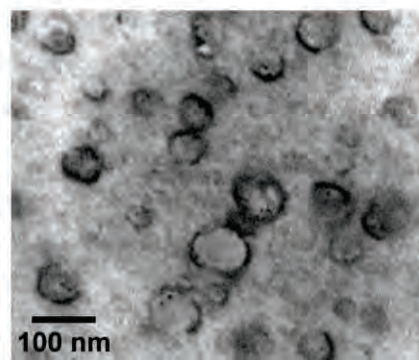


Fig. 11. TEM micrograph of 95/5 PMMA/MAM foam produced at 30 MPa and 10 °C.

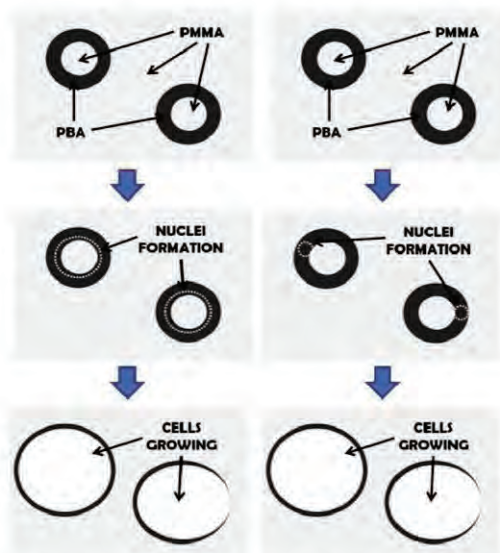


Fig. 10. Possible schemes of the heterogeneous nucleation foaming mechanism and cell growth in PMMA/MAM nanostructured blends.

Depending on the exact critical radius of PBA phase under the processing conditions, nucleation could happen around the PMMA inner core or inside the PBA shell, i.e. in both cases in the PBA phase (Fig. 10).

Both mechanisms imply the formation of the cell inside the micelle. After the nucleation process the growing of the cell is controlled by the plasticization of the surrounding PMMA matrix [34]. First attempts to check this hypothesis experimentally have been carried out. TEM images of foamed samples were obtained to analyze the possible nanostructure of foams. Unfortunately, in foams TEM micrographs voids cannot be directly observed, due to the filling of the voids with a sol–gel organic–inorganic solution in order to stiffen the foam.

Fig. 11 shows that micelles still can be detected in foams. If we compare TEM micrographs of solid (Fig. 4) and foamed samples is clear that the radius of the micelles is increased with the foaming

process. Then, growing of the cells seems to happen by blowing of the micelles. Thus in all cases the nucleation happens inside the micelle, according to the nucleation scheme presented in Fig. 10.

#### 4. Conclusions

PMMA-based nanocellular foams with very high nucleation ratios were produced by gas dissolution foaming by an appropriate combination of the process parameters for neat PMMA; or a choice of a compatible nanostructuring copolymer (e.g. a MAM block copolymer) blended with a polymer (e.g. PMMA). For example it was demonstrated that nanocellular foams with cell sizes around 100–200 nm and relative densities between 0.5 and 0.8 can be produced by CO<sub>2</sub> gas dissolution foaming from PMMA/MAM blends. These foams present the unique characteristic that their nucleation is controlled only by the nanostructure morphology of the solid precursor blend (it does not depend on the saturation process), with a conversion ratio micelles/nuclei close to unity.

The hypothesis of a heterogeneous nucleation controlled by the nanostructure of MAM [poly(methyl methacrylate)-block poly(butyl acrylate)-block poly(methyl methacrylate)] triblock copolymer is supported by TEM observation before and after foaming, CO<sub>2</sub> sorption measurements at variable pressures and variable MAM contents; the CO<sub>2</sub> uptake being preferably in the PBA phase.

This new kind of process allows producing polymer nanocellular foams with a well controlled cellular nanostructure independently of the foaming process parameters. So, it is possible to produce nanocellular foams using lower pressures of CO<sub>2</sub> than the usually employed in the production of this kind of materials. In addition, this process allows obtaining foams in a wide range of densities by varying these parameters and maintaining the same nanocellular structure.

#### Acknowledgments

Financial support from the Spanish Ministry of Science and Innovation and FEDER funds (MAT2009-14001 C02-01 and MAT 2012-34901), the European Spatial Agency (Project MAP AO-99-075), the Junta de Castile and Leon (Projects VA174A12-2 and VA035U13) are gratefully acknowledged. The help and expertise of Dr. Etienne Gontier, Dr. Soizic Lacampagne and Dr. Melina Petrel (BIC, Université Bordeaux Segalen) is indeed acknowledged for TEM observations and samples preparation and treatment. The help and expertise of Dr. Christian Dietz, and Dr. Ricardo García (INM, CSIC) is indeed acknowledged for AFM observations.

## References

- [1] D. Schmidt, V.I. Raman, C. Egger, C. Du Fresne, V. Schädler, Templated cross-linking reactions for designing nanoporous materials, *Mater. Sci. Eng. C* 27 (2007) 1487–1490.
- [2] X. Lu, R. Caps, J. Fricke, C.T. Alviso, R.W. Pekala, Correlation between structure and thermal conductivity of organic aerogels, *J. Non-Cryst. Solids* 188 (1995) 226–234.
- [3] H. Yokoyama, L. Li, T. Nemoto, K. Sugiyama, Tunable nanocellular polymeric monoliths using fluorinated block copolymer templates and supercritical carbon dioxide, *Adv. Mater.* 16 (2004) 1542–1546.
- [4] A.V. Nawaby, Y.P. Handa, X. Liao, Y. Yoshitaka, M. Tomohiro, Polymer- $\text{CO}_2$  systems exhibiting retrograde behavior and formation of nanofoams, *Polym. Int.* 56 (2007) 67–73.
- [5] D. Miller, P. Chatchaisucha, V. Kumar, Microcellular and nanocellular solid-state polyetherimide (PEI) foams using sub-critical carbon dioxide I, *Process Struct., Polym.* 50 (2009) 5576–5584.
- [6] H. Yokoyama, K. Sugiyama, Nanocellular structures in block copolymers with  $\text{CO}_2$ -philic blocks using  $\text{CO}_2$  as a blowing agent: crossover from micro- to nanocellular structures with depressurization temperature, *Macromolecules* 38 (2005) 10516–10522.
- [7] B. Krause, R. Mettrinkhof, N.F.A. van der Vegt, M. Wessling, Microcellular foaming of amorphous high- $T_g$  polymers using carbon dioxide, *Macromolecules* 34 (2001) 874–884.
- [8] T. Otsuka, K. Taki, M. Ohshima, Nanocellular foams of PS/PMMA polymer blends, *Macromol. Mater. Eng.* 293 (2008) 78–82.
- [9] L.J.M. Jacobs, M.F. Kemmere, J.T.F. Keurentjes, Sustainable polymer foaming using high pressure carbon dioxide: a review on fundamentals, processes and applications, *Green. Chem.* 10 (2008) 731–738.
- [10] I. Tsvintzelis, A.G. Angelopoulou, C. Panayiotou, Foaming of polymers with supercritical  $\text{CO}_2$ : an experimental and theoretical study, *Polymer* 48 (2007) 5928–5939.
- [11] S. Siripurapu, J.M. DeSimone, S.A. Khan, R.J. Spontak, Controlled foaming of polymer films through restricted surface diffusion and the addition of nanosilica particles or  $\text{CO}_2$ -philic surfactants, *Macromolecules* 38 (2005) 2271–2280.
- [12] S. Costeux, L. Zhu, Low density thermoplastic nanofoams nucleated by nanoparticles, *Polymer* 54 (2013) 2785–2795.
- [13] S. Costeux, H. Jeon, S. Bunker, I. Khan, Nanocellular foams from acrylic polymers: Experiments and modeling, in: *Proceedings of the SPE FOAMS 2012 Conference, Barcelona 2012*.
- [14] P. Spitzel, C.W. Macosko, R.B. McClurg, Block copolymer micelles for nucleation of microcellular thermoplastic foams, *Macromolecules* 37 (2004) 6874–6882.
- [15] J.A. Reglero Ruiz, M. Pedros, J.-M. Tallon, M. Dumon, Micro and nano cellular amorphous polymers (PMMA, PS) in supercritical  $\text{CO}_2$  assisted by nanostructured  $\text{CO}_2$ -philic block copolymers – One step foaming process, *J. Supercritical Fluids* 58 (2011) 168–176.
- [16] J.A. Reglero Ruiz, J.-M. Tallon, M. Pedros, M. Dumon, Two-step micro cellular foaming of amorphous polymers in supercritical  $\text{CO}_2$ , *J. Supercritical Fluids* 57 (2011) 87–94.
- [17] S. Siripurapu, J.M. DeSimone, S.A. Khan, R.J. Spontak, Low-temperature, surface-mediated foaming of polymer films, *Adv. Mater.* 16 (2004) 989–994.
- [18] Y. Kim, C.B. Park, P. Chen, R.B. Thompson, Origins of the failure of classical nucleation theory for nanocellular polymer foams, *Soft Matter* 7 (2011) 7351–7358.
- [19] S. Costeux, S.P. Bunker, H.K. Jeon, Homogeneous nanocellular foams from styrenic-acrylic polymer blends, *J. Mater. Res.* 28 (2013) 2351–2365.
- [20] B. Aher, N.M. Olson, V. Kumar, Production of bulk solid-state PEI nanofoams using supercritical  $\text{CO}_2$ , *J. Mater. Res.* 28 (2013) 2366–2373.
- [21] T. Shinkai, M. Ito, K. Sugiyama, K. Ito, H. Yokoyama, Ordered and foam structure of semifluorinated block copolymers in supercritical carbon dioxide, *Soft Matter* 8 (2012) 5811–5817.
- [22] J.A. Reglero Ruiz, M. Dumon, J. Pinto, M.A. Rodriguez-Perez, Low-density nanocellular foams produced by high-pressure carbon dioxide, *Macromol. Mater. Eng.* 296 (2011) 752–759.
- [23] L. Lalande, C.J.G. Plummer, J.A.E. Manson, P. Gerard, The influence of matrix modification on fracture mechanisms in rubber toughened polymethylmethacrylate, *Polymer* 47 (2006) 2389–2401.
- [24] L. Lalande, C.J.G. Plummer, J.A.E. Manson, P. Gerard, Microdeformation mechanisms in rubber toughened PMMA and PMMA-based copolymers, *Eng. Fract. Mech.* 73 (2006) 2413–2426.
- [25] S.K. Goel, E.J. Beckman, Generation of microcellular polymers using supercritical  $\text{CO}_2$ , *Cell. Polym.* 12 (1993) 251–274.
- [26] J. Pinto, E. Solórzano, M.A. Rodríguez-Perez, J.A. de Saja, Characterization of the cellular structure based on user-interactive image analysis procedures, *J. Cell. Polym.* 49 (2013) 555–575.
- [27] M.D. Abramoff, P.J. Magelhaes, S.J. Ram, Image processing with ImageJ, *Biophotonics Int.* 11 (2004) 36–42.
- [28] V. Kumar, N.P. Suh, A process for making microcellular thermoplastic parts, *Polym. Eng. Sci.* 30 (1990) 1323–1329.
- [29] F. Rindfleisch, T.P. DiNoia, M.A. McHugh, Solubility of polymers and copolymers in supercritical  $\text{CO}_2$ , *J. Chem. Phys.* 100 (1996) 15581–15587.
- [30] M. Lora, F. Rindfleisch, M.A. McHugh, Influence of the alkyl tail on the solubility of poly(alkyl acrylates) in ethylene and  $\text{CO}_2$  at high pressures: experiments and modeling, *J. Appl. Polym. Sci.* 73 (1999) 1979–1991.
- [31] T. Ribaut, J. Oberdisse, B. Annghofer, B. Fournel, S. Sarade, H. Haller, P. Lacroix-Desmazes, Solubility and self-assembly of amphiphilic gradient and block copolymers in supercritical  $\text{CO}_2$ , *J. Phys. Chem. B* 115 (2011) 836–843.
- [32] D.Y. Kwok, A. Leung, C.N.C. Lam, A. Li, R. Wu, A.W. Neumann, Low-rate dynamic contact angles on poly(methyl methacrylate) and the determination of solid surface tensions, *J. Coll. Int. Sci.* 206 (1998) 44–51.
- [33] J.E. Mark, *Physical Properties of Polymers Handbook*, second ed., Springer Science-Business Media, LLC, New York, 2007.
- [34] J. Pinto, S. Pardo, E. Solórzano, M.A. Rodríguez-Perez, M. Dumon, J.A. de Saja, Solid skin characterization of PMMA/MAM foams fabricated by gas dissolution foaming over a range of pressures, *Defect Diffus. Forum* 434 (2012) 326–328.



## Block Copolymers Self-Assembly Allows Obtaining Tunable Micro or Nanoporous Membranes or Depth Filters Based on PMMA; Fabrication Method and Nanostructures

Javier Pinto,<sup>\*,†,‡,§</sup> Michel Dumon,<sup>‡,§</sup> Miguel A. Rodriguez-Perez,<sup>\*,†</sup> Ricardo Garcia,<sup>||</sup> and Christian Dietz<sup>‡</sup>

<sup>†</sup>CellMat Laboratory, Condensed Matter Physics Department, University of Valladolid, Paseo de Belen no. 7, 47001 Valladolid, Spain

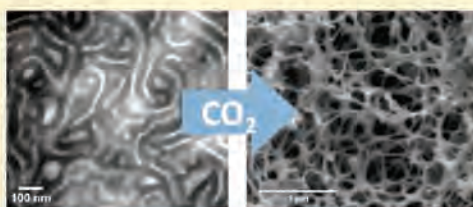
<sup>‡</sup>Laboratoire de Chimie des Polymères Organiques (LCPO), Université Bordeaux, LCPO, UMR 5629, F-33600 Pessac, France

<sup>§</sup>CNRS, LCPO, UMR 5629, F-33600 Pessac, France

<sup>||</sup>Instituto de Ciencia de Materiales de Madrid, CSIC, C/Sor Juana Inés de la Cruz no. 3, 28049 Madrid, Spain

<sup>‡</sup>Center of Smart Interfaces and Department of Materials Science, Technische Universität Darmstadt, Alaric-Weiss-Strasse 2, 64287 Darmstadt, Germany

**ABSTRACT:** An environmentally friendly method to produce tunable bulk micro or nanoporous structures is presented. Nano- and micro-porous structures are obtained by gas dissolution foaming using CO<sub>2</sub>, following the pattern of polymer blends between poly(methylmethacrylate) (PMMA) and a triblock copolymer, namely poly(methylmethacrylate)-*co*-poly(butyl acrylate)-*co*-poly(methyl methacrylate) (MAM) blends nanostructuration. Membranes or depth filters can be produced by this method, varying the amount of the triblock copolymer in the blend. Furthermore, main characteristics, such as the average pore size and porosity can be finely tuned by adjusting the process parameters (temperature or pressure) during gas foaming.



### 1. INTRODUCTION

Nowadays, particle filters are being used in a wide range of industrial applications, such as wastewater treatment, particles or biological samples collection, and desalination, among others.<sup>1,2</sup> Filtration processes and their potential applications can be classified by the size of the particles that could be separated, related to the pore size of the porous material. Particles with sizes higher than 1  $\mu\text{m}$  can be separated by usual particle filtration, from sizes of 50 to 500 nm the separation process is called microfiltration, for particles between 2 and 50 nm ultrafiltration filters are required, and lower particle sizes than 2 nm could be separated by nanofiltration.<sup>3</sup> Filters can also be classified by their thickness. On the one hand, depth filters have a significant physical depth and the particles to be retained are captured throughout the depth of the filter. Depth filters often have a labyrinthine three-dimensional structure, with multiple channels and heavy branching (high tortuous path), so that there is a large pathway through which the liquid must flow and by which the filter can retain particles.<sup>4</sup> On the other hand, membrane filters are porous media in which depth is not considered important. The membrane filter uses a relatively thin material with a well-defined maximum pore size, and the particle retaining effect takes place almost entirely at the surface. Membranes offer the advantage of having well-defined effective pore sizes, can be integrity tested more easily than depth filters, and can achieve filtration of smaller particles.<sup>5</sup>

Development of filters based on polymers has acquired relevance in recent years, mainly in microfiltration and

ultrafiltration processes. Focusing on the microfiltration, several fabrication methods to produce polymeric filters can be found in the literature: predefined patterns were transferred into a polymer film by lithographic and pattern-transfer techniques;<sup>6,7</sup> track etch technique can produce nanoporous membranes by irradiating polymers with high energy particles;<sup>7,8</sup> natural formation of nanostructured polymers via precipitation allows the use of solvent-based procedures;<sup>9,10</sup> biologically derived structures could act as porous membranes;<sup>11,12</sup> and in addition, nanoporous materials could also be obtained from self-assembly of block copolymers by the selective removal of one of the blocks.<sup>7,13–16</sup> Nanoporous structure templating from block copolymer morphologies has been studied since the 1990s on films (<1 mm) of generally high-T<sub>g</sub> polymers by thermal degradation of one part of the polymer/copolymer, or in other polymers by solvent effects or organization of surfactants.<sup>7,13,14,17,18</sup> Moreover, block copolymers have been used as structure-directing agents in the production of silica membranes by evaporation-induced self-assembly.<sup>19</sup>

Some attempts to use foaming process with supercritical CO<sub>2</sub> could be found in the literature with polymeric thin films,<sup>20,21</sup> but not on bulk samples. In general, each production route allows us to obtain just one kind of filter, membrane, or depth filter, and

Received: October 2, 2013

Revised: February 1, 2014

Published: February 6, 2014

requires the fabrication of different patterns to control the pore size.

In previous works, micro and nanoporous structures based on the self-assembly of block copolymers (MAM, SBM) in polymer blends were obtained using a different approach (for the pore generation) from those described above,<sup>22,23</sup> called gas solid state foaming technique, with CO<sub>2</sub> as the physical foaming agent.<sup>23</sup> This technique exhibits several advantages: it is industrially scalable and environmental friendly.<sup>25,26</sup> In this work, we prove that by an appropriate selection of PMMA/MAM blends and of process parameters, it is possible to produce nanoporous membranes and depth filters with tunable pore size, using the gas solid state foaming technique, with the additional advantage of the proven biocompatibility of PMMA.<sup>27,28</sup> In addition to this, a detailed study of the morphology of the initial dense precursors and the nanoporous structure of the filters is also presented.

## 2. EXPERIMENTAL SECTION

**2.1. Materials.** Transparent poly(methyl methacrylate) (PMMA) and poly(methyl methacrylate)-*co*-poly(butyl acrylate)-*co*-poly(methyl methacrylate) (MAM) were kindly supplied by the Arkema Company (France), in the form of pellets. PMMA homopolymer presents a glass transition temperature ( $T_g$ ) of 112 °C and density of 1.18 g/cm<sup>3</sup>. MAM triblock copolymer presents a density of 1.08 g/cm<sup>3</sup>. Details of production of MAM copolymer can be found elsewhere.<sup>29,30</sup>

The particular MAM in our study, 36 wt % poly(butyl acrylate) (PBA), has the following characteristics, given by Arkema,  $M_n^{\text{MAM}} \approx 85\,000$  g/mol (own SEC measurement at 85 000 g/mol),  $M_w^{\text{MAM}} \approx 180\,000$  g/mol (our own measure is at 165 000 g/mol), therefore  $I_p^{\text{MAM}} \approx 2.1$ .

The PMMA used is pure homopolymer (without impact modifier), with the following characteristics  $M_w \approx 83\,000$  g/mol,  $M_n \approx 43\,000$  g/mol,  $I_p \approx 1.9$ .

**2.2. Fabrication of Solid Samples.** Blends of PMMA and different amounts of MAM have been produced by the following route. First, both materials, PMMA and MAM, were dried in vacuum (680 mmHg) at 80 °C during 4 h. Then, blends with the appropriate amount of each polymer were produced by extrusion using a Scamex CE02 single screw extruder ( $L/D = 28$  d = 45 mm), with a temperature profile from 165 to 225 °C, at a screw speed of 60 rpm. Pellets from the produced blends were obtained using a continuous cutting machine operating at the end of the extrusion line.

In a second step, produced blends in the form of pellets were dried again, in the same conditions as the raw materials. Dry blends were injected into pieces (50 × 15 mm<sup>2</sup>) with 3 mm thickness, using a small scale injection molding machine developed by DSM Xplore. Melt temperature was fixed at 240 °C, whereas mold temperature was set at 60 °C. The injection pressure was fixed at 1 MPa during 8 s. Transparent solid samples were obtained with a good surface appearance and without injection defects (air bubbles inside the pieces, jetting, etc.).

**2.3. Fabrication of Porous Samples.** Production of porous materials was carried out by the solid state gas foaming process, in two high pressure vessels. One provided by TOP Industrie (Vaux Le Pénil, France), with a capacity of 300 cm<sup>3</sup> and maximum operation temperature and pressure of 250 °C and 40 MPa (400 bar), respectively. CO<sub>2</sub> pressure was supplied and controlled by an accurate pressure pump provided by Teledyne ISCO (Lincoln NE, U.S.). Another vessel is our self-designed vessel with glass windows and additional instrumentation (heaters, chillers, inner thermocouples, pressure control, control

of the pressure release drop rate, etc.) with a capacity of 500 cm<sup>3</sup> and maximum operation temperature and pressure of 200 °C and 20 MPa, respectively.<sup>31</sup> This vessel also allows observation of different processes at controlled temperatures and pressures.

During the entire process, pressure and temperature inside the vessels were monitored.

Solid samples were introduced into the pressure vessel, under controlled CO<sub>2</sub> pressure and temperature during 24 h. Different pressures (from 7 to 30 MPa) and temperatures (from 10 to 70 °C) were used. After 24 h, samples were completely saturated by CO<sub>2</sub>.<sup>22</sup> Then pressure was released, usually at pressure drop rates between 10 and 30 MPa/min with the TOP Industrie vessel, and between 1.4 and 45 MPa/min with the own-developed vessel. Porous structure was triggered during the pressure drop and stabilized at room temperature.

**2.4. Characterization.** Average molar masses of the MAM triblock copolymer were determined by Size Exclusion Chromatography (SEC) in a PL-GPC 50 Plus (Agilent Technologies) using THF (tetrahydrofuran) as a solvent with a polymer concentration of 3 mg/mL. Constant flow of 1.0 mL/min and a refraction index (RI) detector were employed. Calibration was made in THF with (homo)polystyrene calibration standards, being the molar mass values relative to the polystyrene standards.

Several characterization techniques were used in order to determine the main characteristics of the porous structure and the nanostructure of the PMMA/MAM blends.

**2.4.1. Porosity.** Density of nanoporous and solid samples were determined by water-displacement method, based on Archimedes' principle. Porosity (or volume fraction of voids,  $V_f$ ) was calculated from the relative density (obtained as the ratio between the density of the porous ( $\rho_f$ ) and the solid ( $\rho_s$ ) material) using eq 1.<sup>33</sup>

$$V_f = 1 - \frac{\rho_f}{\rho_s} \quad (1)$$

**2.4.2. Scanning Electron Microscopy (SEM).** Structure of nanoporous samples was studied using SEM (model Quanta 200FEG, FEI). Porous samples were immersed in liquid nitrogen and fractured to ensure that the microstructure remained intact. Surfaces were coated with gold using a sputter coater (model SCD 004, Balzers Union). The micrographs obtained were analyzed to measure the main pore size, pore density ( $N_p$ , pores per cubic centimeter in the porous material) and pore nucleation density ( $N_o$ , pore nucleation points per cubic centimeter of the solid material) with our developed specialized software based on FIJI/ImageJ.<sup>32,33</sup> The pore nucleation density can be calculated from the pore density and the porosity using eq 2.<sup>24</sup>

$$N_o = \frac{N_p}{1 - V_f} \quad (2)$$

This value represents the number of pores formed in a cubic centimeter of the solid material, assuming no coalescence between near pores during the stabilization of the porous structure. By comparison between the nucleation density ( $N_o$ ) and the potential nucleation sites in the solid material (i.e., dispersed nanostructures), it is possible to analyze the efficiency of the nanodomains as nucleating agents (conversion ratio between potential nucleation sites and developed pores).

**2.4.3. Atomic Force Microscopy (AFM).** Solid samples were prepared by microtome to obtain flat surfaces with differences in height lower than 100 nm, which could be analyzed by AFM



(Multimode AFM, Veeco Instruments, WSxM software).<sup>34</sup> The AFM was operated in the amplitude modulation mode (tapping mode AFM).<sup>35</sup> Both the topography and the phase shift signal were recorded. The AFM phase images show a better contrast on polymer blends than the topography images because they detect changes in the energy dissipated by the AFM.<sup>36</sup> Over the AFM phase images obtained, it is possible to differentiate the poly(butyl acrylate) domains (black in the images) and the poly(methyl methacrylate) matrix (gray in the images). In the case of dispersed nanostructures, the volumetric density of nanodomains (nanodomains/cm<sup>3</sup>) can be calculated from these images using eq 3.<sup>24</sup>

$$N_n = \left( \frac{n}{A} \right)^{3/2} \quad (3)$$

where  $n$  is the number of nanodomains observed in an AFM phase image, and  $A$  the area of the image in cm<sup>2</sup>.

**2.4.4. Transmission Electron Microscopy (TEM).** Transmission Electron Microscopy is carried out at the Bordeaux Imaging Center (BIC, Université Bordeaux 2 Segalen). TEM observations on solid and porous samples were performed between 60 to 80 kV, at magnifications from x30 000 to x330 000, using a TEM microscope Hitachi H7650 with Orius camera. Thin cuts (60–70 nm) of the solid samples were obtained by a microtome carried out at –50 °C with a diamond knife. Then, cuts were deposited on Formvar copper grids and treated by a water solution with 2 wt % phosphotungstic acid (PTA) + 2 wt % benzyl alcohol. As reported in literature,<sup>37–39</sup> PTA staining contrasts butyl acrylate selectively (black in the images) and no or little PMMA (white or gray in the images).

In order to stiffen the foamed materials, filling of the voids by a TEM-contrasting liquid hardening formulation was attempted. A sol–gel organic–inorganic solution of several siloxane reactive monomers (formulation remains confidential and not publishable) allowed the voids to be filled without solubilization of the PMMA. The overall system gelifies and hardens rapidly (<30 min).

In the case of dispersed nanostructures, the volumetric density of core–shell nodules (core–shell nodules/cm<sup>3</sup>) can be calculated from these images using eq 4.

$$N_n = \frac{n}{V} \quad (4)$$

where  $V$  is the volume of the sample in cm<sup>3</sup> (calculated from the area of the image and the thickness of the TEM sample), and  $n$  is the number of core–shell nodules observed in a TEM image. As the TEM image is a two-dimensional projection of the three-dimensional structure of the sample, some assumptions are needed to estimate the number of nanosized domains. Completely black structures in TEM images are assumed as core–shell structures completely contained in the sample and counted as units, and structures with a dark shell and gray core are assumed as core–shell nodules partially contained in the sample, because the gray core is due to the absence of the lower or upper part of the dark shell (not contained in the sample), and counted as halves.

**2.4.5. CO<sub>2</sub> wt. % Uptake.** CO<sub>2</sub> wt. % uptake by the polymer during saturation was measured for each sample by weighing the samples just after the pressure release.

### 3. RESULTS AND DISCUSSION

**3.1. Self-Assembled Nanostructures in the Foam-Precursor Polymer Blends (PMMA/MAM).** Self-assembling or nano structuration in polymer/block copolymer blends results from the microphase separation between different chemical blocks, which will act as a pattern for the porous structure.

**3.1.1. Low Contents of MAM in PMMA.** Each blend was analyzed from an injected bulk dense sample in two different planes, one containing the injection direction and another perpendicular to the injection direction.

TEM micrographs (only if samples are treated by phosphotungstic acid (PTA)) from 92.5-PMMA/7.5-MAM and 95-PMMA/5-MAM blends show regular well-dispersed nodules in the form of core–shell or micellar objects with a white PMMA core, and a black poly(butyl acrylate) (PBA) shell or layer, the apparent diameter of the objects is 20–25 nm (for generic example, see micrographs of Figure 1a). These nodules

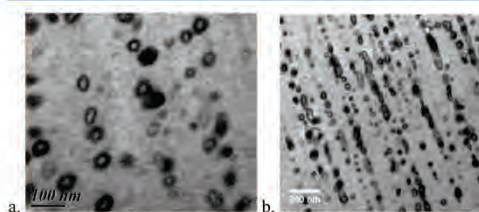


**Figure 1.** 90-PMMA/10-MAM blends (a) TEM micrograph, showing the core–shell structure of PBA domains. (b) TEM micrograph showing the alignment of the core–shell nodules.

are embedded in a “white” matrix (probably the PMMA matrix + the PMMA blocks) with no orientation effect.

90-PMMA/10-MAM blends have a very similar nodular appearance (Figure 1a). Due to the “ABA” structure of the MAM block copolymer, core–shell nodules might be constituted by 3 layers, the outer one (PMMA layer) is soluble in the matrix and is not contrasted by PTA. An apparent diameter of 30 nm is measured on TEM micrographs. The micrograph observation along the injection flow direction allows detection of a strong alignment effect (i.e., the presence of arrays or lines of core–shell nodules over several micrometers) (Figure 1b or Figure 2).

80-PMMA/20-MAM and 75-PMMA/25-MAM blends are still exhibiting nodular dispersed objects, analogous to the previous systems, although a more pronounced alignment effect is seen in Figure 2 (core–shell nodules become ellipsoids) and have a higher apparent diameter (30–50 nm).

As a conclusion, below 25 wt. % of MAM, all blends present nanosized micellar structures, with a clear orientation in the injection direction in 10, 20, and 25 wt. % MAM blends. Both techniques, AFM and TEM, agree about the core–shell nodules size, from 20 nm in 5 wt. % MAM blends to 50 nm in 20 wt. % MAM blends.

**3.1.2. High Contents of MAM in PMMA.** A different structure is observed in blends with 75 wt.-% of MAM. AFM phase images show no influence of the injection process on the orientation of the nanostructure (Figure 3). AFM is not enough to determine clearly the morphology whereas TEM images show a cocontinuous nanostructuration with poorly defined lamella of 20–30 nm apparent thickness (Figure 3).

A CO<sub>2</sub> saturation annealing was carried out at 50 °C, 30 MPa, 24 h, then releasing the pressure extremely slowly ( $\Delta P$  over 24 h) to prevent any foaming. Under this condition, the orientation sensitivity is erased and random curved lamellas develop all over the matrix, showing a completely volume-structured material; with the darker parts (PBA) having an apparent thickness larger than the annealed sample (i.e., the thickness of apparent dark + white parts of the lamella >90 nm).



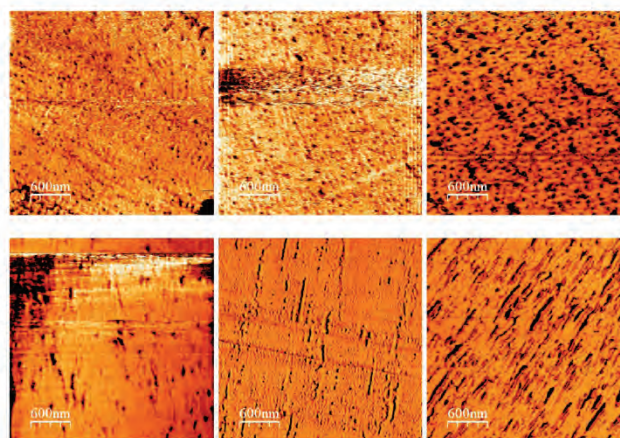


**Figure 2.** AFM phase images of PMMA/MAM blends 95/5 (left), 90/10 (middle), and 80/20 (right). Plane perpendicular to the injection direction (up) and plane containing the injection direction (down).

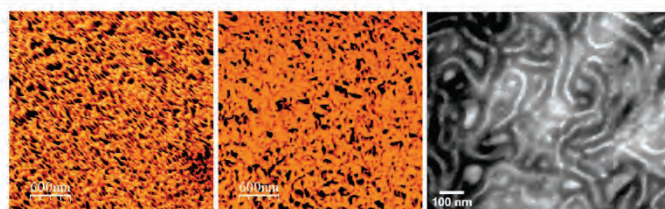


**Figure 3.** 2S-PMMA/7S-MAM blend. AFM phase image of the plane perpendicular to the injection direction (left), AFM phase image of the plane containing the injection direction (middle), and TEM image of PTA stained sample (right).

**3.2. Porous Structures.** The porous structures of the blends obtained by the solid state foaming process were analyzed by SEM. Pore formation by solid state gas foaming is usually governed by the process parameters, such as gas saturation pressure and temperature and pressure release drop rate;<sup>24</sup> however, PMMA/MAM blends could present a different behavior, with the nanostructure acting as a pattern for the porous structure.<sup>22,23,40</sup>

**3.2.1. Low Contents of MAM in PMMA.** Core-shell nodules in the solid blends have an appropriate size (20–50 nm) to act as nucleation sites of pores, i.e., higher than the critical nucleus radius ( $r^*$ ) in a PMMA matrix, calculated using eq 5.<sup>41</sup>

$$r^* = 2t/P \quad (5)$$

where  $P$  is the saturation pressure, and  $t$  is the surface tension of PMMA (38.5 mN/m),<sup>42</sup> over the range of pressures of the study, 10–30 MPa, and  $r^*$  takes values between 2.5 and 8 nm. Porous structures were analyzed by SEM, obtaining an equivalent average value of the pore nucleation density ( $N_o$ ) around  $4.05 \times 10^{14}$  nuclei/cm<sup>3</sup> for blends containing 5, 10, and 20 wt. %. Determination of the pore nucleation density was carried out from micrographs of the plane perpendicular to the injection direction, due to the fragility of the pore walls in the elongated pores fractured in the plane containing the injection direction (Figure 4 shows that the porous structure is missing when samples with highly elongated pores were fractured in that plane).

The value of the pore nucleation density ( $N_o$ ) has the same order of magnitude and a quite similar value as the average core-shell nodules/nanodomain density ( $N_n$ ) in these blends calculated from AFM images,  $N_n^{AFM} = 4.43 \times 10^{14}$  nanodomains/cm<sup>3</sup>,<sup>40</sup> and TEM images,  $N_n^{TEM} = 5.30 \times 10^{14}$  nanodomains/cm<sup>3</sup>.

Moreover, the shape of the porous structure can be analyzed in the same two planes as nanostructured dense samples, one containing the injection direction, and another perpendicular to the injection direction. Every sample presents pores with round shape in the plane perpendicular to the injection direction (Figure 4). But pores are clearly elongated in the injection direction (Figure 4) (10 and 20 wt. % of MAM). This corroborates the same previous observation in the dense precursor blends.

To ensure that the nucleation process is only or mainly governed by nanostructuration, it is needed to prove the decoupling of the process parameters, saturation pressure, and pressure release drop rate, from the nucleation process.

In a previous work, we found that saturation pressure (7 to 30 MPa) has no influence on porous structures working with these materials.<sup>40</sup> Here, the influence of the pressure release drop rate was characterized on samples of 90-PMMA/10-MAM, saturated at 7 MPa and room temperature, varying the pressure drop rate between 1.4 MPa/min to 45 MPa/min. Porous samples present a similar porous structure, and nucleation densities of  $4 \times 10^{14}$  and  $3.75 \times 10^{14}$  nuclei/cm<sup>3</sup> at drop rates of 45 and 1.4 MPa/min,



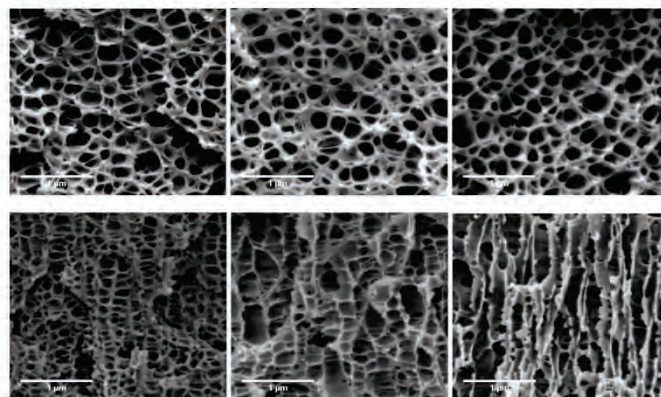


**Figure 4.** SEM images of porous PMMA/MAM blends 95/5 (left), 90/10 (middle), and 80/20 (right). Plane perpendicular to the injection direction (up) and plane containing the injection direction (down). Foaming conditions: 30 MPa, room temperature.

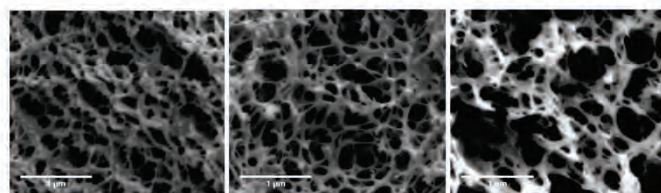


**Figure 5.** SEM images of porous 25-PMMA/75-MAM samples produced from saturation at 30 MPa and room temperature (left), 40 °C (middle), and 50 °C (right).

respectively. Thus, no influence of the pressure release drop rate on the nucleation process is found in the pressure drop rate range investigated.

So, a direct relationship between the solid blend nanostructure (e.g., core-shell nodules density) and the porous structure (e.g., pore density) is found in porous samples of PMMA/MAM blends containing 5, 10, and 20 wt. % of MAM, whose expansion is triggered by pressure release from saturation pressures between 10 to 30 MPa and room temperature saturation.

**3.2.2. High Contents of MAM in PMMA.** SEM images from porous samples of 25-PMMA/75-MAM produced at 30 MPa and temperatures from 23 to 50 °C show a cocontinuous porous structure (Figure 5), with edges mainly of 20–40 nm thickness, comparable to the apparent thickness of lamella in the solid blends. Co-continuous porous structures are not individual pores, then no information about the nucleation process could be obtained from these structures.

A different approach is needed to prove a morphological relationship between the nanostructure and the porous structure in blends with high contents of MAM.

Voids of the porous samples were attempted to be filled with a sol-gel organic-inorganic siloxane solution (see Experimental Section for details) in order to stiffen the material and reveal the Block Copolymer (BCP) location. As a result, the porous structure (light gray with black aggregates inside, coming from phase separation of the silica phase within the sol gel solution) could be differentiated from the polymer matrix (darker gray, without black aggregates) by the high contrast of a silica phase, which appears in the form of black aggregates, which are only

present in the voids filled by the sol-gel organic-inorganic solution (Figure 6).

The porous structure in Figure 6 seems to reproduce the nanostructure of the 25-PMMA/75-MAM solid blend (Figure 3).

Nevertheless, a clear nanostructure within the foams (i.e., pores + nanostructures, whatever the MAM content) cannot be evidenced by TEM so far, as though the core-shell nodules or the lamella had been blown up.

As a conclusion, nanostructuration of PMMA/MAM blends is the pattern of the porous structures obtained by gas dissolution foaming, both for low and high MAM contents. The higher CO<sub>2</sub>-philicity of PBA (compared to PMMA), and the difference between their glass transition temperatures ( $T_g$ ), −50 °C for PBA, 110 °C for PMMA, promotes that nucleation only happens in the nanostructures, particularly in the PBA phase. It should be noticed that the PBA shell of the core-shell nodules or the PBA lamellae present appropriate sizes for the nucleation process taking place inside them. PBA presents a surface tension of 33.7 mN/m,<sup>43</sup> thus, from eq 5, it is obtained that  $r^*$  takes values from 2.2 to 6.7 nm in the range of pressures used to produce these foams.

After the nucleation process, the CO<sub>2</sub>-swollen PMMA matrix allows growth of the porous structure, because the PMMA-CO<sub>2</sub> system is in the rubbery state even at low temperatures.<sup>44,45</sup> However, the small thickness of the PMMA walls and edges (a few nanometers) allows for rapid CO<sub>2</sub> desorption. As a consequence, PMMA enters the glassy state and constrains growth of the porous structure in the PBA phase, preventing coalescence of the pores.



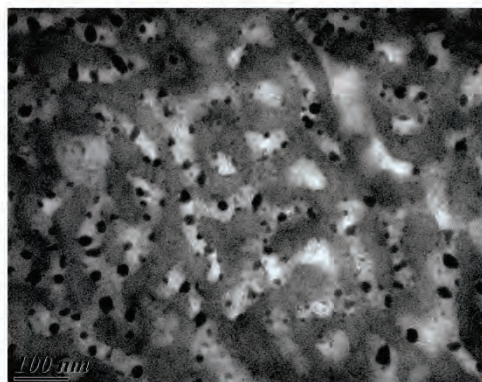


Figure 6. TEM image of “filled” porous 25-PMMA/75-MAM sample.

Influence of the core-shell morphology on the morphology of the pores cannot be strictly determined from the previous results. However, if the critical nucleation radius of the PBA phase is smaller than the size of the PMMA core of the dispersed copolymer objects, then the core can act as a nucleation point inside the PBA phase.

### 3.3. Control of Porosity and Average Pore Size.

Influence of blend composition and process parameters (saturation pressure and temperature) on the nucleation and morphology of the porous structure have been previously determined. Now, their influence on the pore growing is discussed.

**3.3.1. Low Contents of MAM in PMMA.** PMMA/MAM injected blends containing 10 and 20 wt. % of MAM were selected to produce porous structures that could be potentially used as membranes. Oriented nanostructuring of these materials acting as a pattern allows one to obtain elongated pores with a clear orientation.

Porous materials were produced after saturation at 30 MPa and room temperature from the selected blends, and also 95-PMMA/5-MAM blend, to study the influence of the MAM content on the porosity of the samples and their pore size (Figure 4). Direct relationships between the pore size and porosity evolution are expected due to the constant pore nucleation density previously mentioned.

Pore size was determined from the images obtained in the plane perpendicular to the injection direction, because this size will be the effective pore size to filtration processes.

First, for given processing parameters (pressure and temperature), the results show that pore size and porosity are increased with the amount of MAM (Figure 7), the increment in diameter and porosity is however small,  $V_f = 0.53$  to  $0.58$ ,  $\phi = 170$  to  $190$  nm. We expect that this is due to the higher  $\text{CO}_2$  sorption related to the MAM content.

Second, influence of the saturation pressure on porosity and pore size, was analyzed on samples of 90-PMMA/10-MAM produced at room temperature and increasing pressures between 10 and 30 MPa (Figure 8). As expected, pore size and porosity grow in parallel, but an asymptotic behavior seems to be reached at high pressures (especially for porosity), giving a further justification of the nucleation and gas location role of the PBA blocks.

This parallel behavior of pore size and porosity can be explained from the constant nucleation density controlled by the

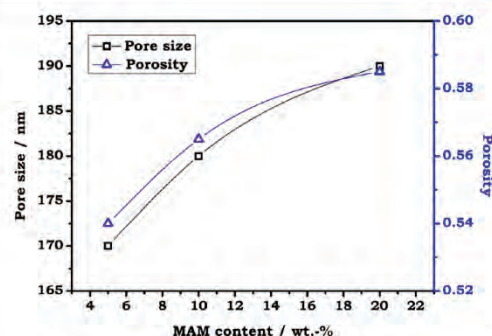


Figure 7. Effect of MAM content on the porosity and pore size in low MAM content blend porous materials. Foaming conditions: 30 MPa and room temperature.

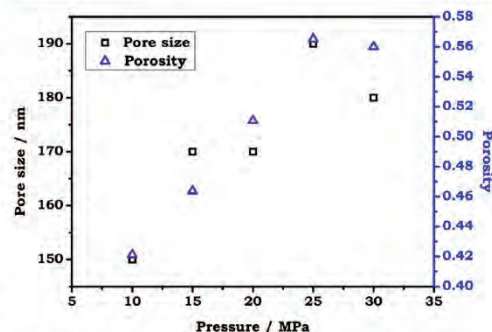


Figure 8. Effect of saturation pressure on the porosity and pore size in 90-PMMA/10-MAM porous blends. Saturation carried out at room temperature.

nanostructuring of these materials. The pore nucleation density of 90-PMMA/10-MAM blends produced from 10 to 30 MPa is nearly constant, with values between  $3.68 \times 10^{-14}$  and  $4.16 \times 10^{-14}$ .

Adding measurements of the  $\text{CO}_2$  uptake of the polymer blends during the saturation process were carried out to improve the understanding of the results obtained (Figure 9). As expected,  $\text{CO}_2$  uptake presents a direct linear relationship with the saturation pressure. Therefore, the increment of pore size with the saturation pressure is due to the higher internal pressure after the external pressure release, and the plasticization of the PMMA matrix.<sup>44,45</sup>

Thus, porous structures with the same morphology and different pore size and porosity could be obtained. Pore size and porosity are controlled by the amount of MAM or by the saturation pressure during the production process.

These porous structures produced in bulk, membranes of 60–100 nm thickness could be obtained using microtome at low temperatures. The membrane thickness is limited by the pore size in the injection direction, being probably too thin to support the pressure gradients needed for the filtration process without a structural failure. The use of a backside support with large openings could avoid this limitation and allow the use of these membranes in filtration processes.<sup>46</sup>



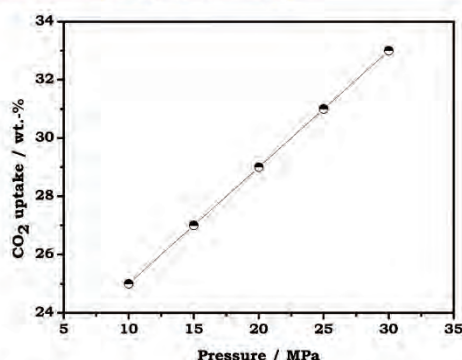


Figure 9. Relationship between the CO<sub>2</sub> saturation pressure and the CO<sub>2</sub> uptake for 90-PMMA/10-MAM samples.

**3.3.2. High Contents of MAM in PMMA.** As explained before, porous samples produced from the 25-PMMA/75-MAM blend allow a cocontinuous open porous structure to be obtained, which could be used as a depth filter.

Porous samples from this blend were produced at 30 MPa and temperatures between room temperature and 70 °C, in order to analyze the effect of the process temperature on the porosity of the samples, and the pore size (pore size means in this case the average size of the channels of the cocontinuous porous structure). Samples produced at 60 and 70 °C are discarded, due to the absence of the nanopores at these elaboration temperatures.

Morphologies of foamed samples produced between room temperature and 50 °C were given in Figure 5, while effect of CO<sub>2</sub> saturation temperature on the porosity and pore size in the 25-PMMA/75-MAM porous blends is shown in Figure 10.

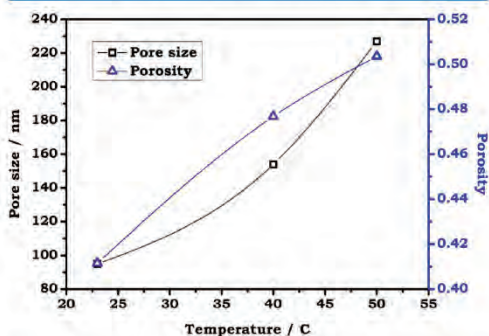


Figure 10. Effect of CO<sub>2</sub> saturation temperature on the porosity and pore size in 25-PMMA/75-MAM porous materials, saturation pressure = 30 MPa.

It is proven that (nano) pore size and porosity can be controlled by the process temperature, at temperatures up to 50 °C. Porosity of 25-PMMA/75-MAM blend foams present a lower variation than expected with temperature saturation (since porosity of neat MAM foams changes between 0.5 to 0.2 in the same temperature range), while the pore size increases, which

implies that the increment of the pore size is mainly due to coalescence between pores and not due to a higher expansion of the polymeric matrix.

These structures are also produced in bulk, the thickness of the samples to be used on filtration can be controlled by the thickness of the solid samples (taking into account the sample's expansion during the process), or just by cutting the bulk samples to the appropriate thickness. Then, preparation of filters from PMMA/MAM blends with high amounts of MAM can be simpler than from blends with low amounts of MAM. Also, these cocontinuous pore structures present the advantage that pore clogging will not be as severe as in a structure with well-defined closed pores, due to the high interconnection of the pores.

#### 4. CONCLUSIONS

A route to produce nanoporous structures, which could be used in filtration processes, has been presented. This route presents several advantages: it is based on an environmentally friendly process, the solid state foaming by CO<sub>2</sub>; this process is industrially scalable; the same route allows obtaining both membranes and depth filters. If the main component of the polymer matrix is PMMA in the presence of an adequate block copolymer (here MAM), then it presents a proven biocompatibility; and characteristics of the porous structures, such as the porosity and pore size, can be adjusted by composition and the process parameters.

This method is based on the particular behavior of nanostructured PMMA/MAM blends under the solid state foaming process. It has been demonstrated that nanoporous materials with pore sizes between 100 and 200 nm can be produced by a gas foaming process from PMMA/MAM blends. These materials present the unique characteristic that the pore nucleation process is controlled mainly by the nanostructure morphology of the initial solid blends.

Porous material morphology is governed by nanostructure, whereas process parameters control the overall porosity and the average pore size.

Further investigation on these PMMA/MAM systems, or other block copolymers with similar characteristics, could open a new way of fabrication of tunable nanoporous structures for microfiltration processes.

#### AUTHOR INFORMATION

##### Corresponding Author

\*Phone: +34 983 423572; e-mail: jpinto@fmc.uva.es (J.P.), marrod@fmc.uva.es (M.A.R.-P.).

##### Notes

The authors declare no competing financial interest.

#### ACKNOWLEDGMENTS

Financial assistance from MCINN (MAT2009-14001-C02-01 and MAT2012-34901), Junta of Castile and Leon (VA174A12-2 and VA035U13) and FPU grant AP2008-03603 (J.P.) from the Spanish Ministry of Education is gratefully acknowledged. The help and expertise of Dr. Etienne Gontier, Dr. Soizic Lacampagne, and Dr. Melina Petrel (BIC, Université Bordeaux Segalen) is acknowledged for TEM observations and samples preparation.

#### REFERENCES

- (1) Schafer, A. L.; Davey, J. *Appropriate Technologies for Environmental Protection in the Developing World*; Springer Science and Business Media B.V.: Edinburgh, U.K., 2009.

- (2) Eds: Nunes, S.; Peinemann, K.-V. *Membrane Technology in the Chemical Industry*; Wiley-VCH: Weinheim, Germany, 2001.
- (3) Ulbricht, M. Advanced Functional Polymer Membranes. *Polymer* **2006**, *47*, 2217–2262.
- (4) Yigzaw, Y.; Piper, R.; Tran, M.; Shukla, A. A. Exploitation of the Adsorptive Properties of Depth Filters for Host Cell Protein Removal during Monoclonal Antibody Purification. *Biotechnol. Prog.* **2006**, *22*, 288–296.
- (5) Li, L.; Schulte, L.; Clausen, L. D.; Hansen, K. M.; Jonsson, G. E.; Ndoni, S. Gyroid Nanoporous Membranes with Tunable Permeability. *ACS Nano* **2011**, *5*, 7754–7766.
- (6) Madou, M. J.; *Fundamentals of Microfabrication*, 2nd ed.; CRC Press: Boca Raton, FL, 2002.
- (7) Hillmyer, M. A. Nanoporous Materials from Block Copolymers Precursors. *Adv. Polym. Sci.* **2005**, *190*, 137–181.
- (8) Mehta, A.; Zydny, A. L. Permeability and Selectivity Analysis for Ultrafiltration Membranes. *J. Membr. Sci.* **2005**, *249*, 245–249.
- (9) Akthakul, A.; McDonald, W. F.; Mayes, A. M. Noncircular Pores on the Surface of Asymmetric Polymer Membranes: Evidence of Pore Formation via Spinodal Demixing. *J. Membr. Sci.* **2002**, *208*, 147–155.
- (10) Krause, B.; Diekmann, K.; van der Vegt, N. F. A.; Wessling, M. Open Nanoporous Morphologies from Polymeric Blends by Carbon Dioxide Foaming. *Macromolecules* **2002**, *35*, 1738–1745.
- (11) Sara, M.; Sleytr, U. B. S-Layer Proteins. *J. Bacteriol.* **2000**, *182*, 859–868.
- (12) Kamide, K.; *Cellulose and Cellulose Derivatives*; Elsevier Science: Amsterdam, Netherlands, 2005.
- (13) Hedrick, J. L.; Miller, R. D.; Hawker, C. J.; Carter, K. R.; Volksen, W.; Yoon, D. Y.; Trollsas, M. Templating Nanoporosity in Thin-Film Dielectric Insulators. *Adv. Mater.* **1998**, *10*, 1049–1053.
- (14) Hentze, H.-P.; Antonietti, M. Porous Polymers and Resins for Biotechnological and Biomedical Applications. *Rev. Mol. Biotechnol.* **2002**, *90*, 27–53.
- (15) Hentze, H.-P.; Antonietti, M. Template Synthesis of Porous Organic Polymers. *Curr. Opin. Solid State Mater. Sci.* **2001**, *5*, 343–353.
- (16) Jacson, E. A.; Hillmyer, M. A. Nanoporous Membranes Derived from Block Copolymers: From Drug Delivery to Water Filtration. *ACS Nano* **2010**, *4* (7), 3548–3553.
- (17) Lazzari, M.; Lopez-Quintela, M. A. Block Copolymers as a Tool for Nanomaterial Fabrication. *Adv. Mater.* **2003**, *15* (19), 1583–1594.
- (18) Park, C.; Yoon, J.; Thomas, E. L. Enabling Nanotechnology with Self Assembled Block Copolymer Patterns. *Polymer* **2003**, *44*, 6725–6760.
- (19) Smarsly, B.; Xomeritakis, G.; Yu, K.; Liu, N.; Fan, H.; Assink, R. A.; Drewien, C. A.; Ruland, W.; Brinker, C. J. Microstructural Characterization of Polystyrene-block-poly(ethylene oxide)-Templated Silica Films with Cubic-Ordered Spherical Mesopores. *Langmuir* **2003**, *19*, 7285–7301.
- (20) Li, L.; Yokoyama, H.; Nemoto, T.; Sugiyama, K. Facile Fabrication of Nanocellular Block Copolymer Thin Films using Supercritical Carbon Dioxide. *Adv. Mater.* **2004**, *16*, 1226–1229.
- (21) Yokoyama, H.; Li, L.; Sugiyama, K.; Nemoto, T. Tunable Nanocellular Polymeric Monoliths using Fluorinated Block Copolymer Templates and Supercritical Carbon Dioxide. *Adv. Mater.* **2004**, *16*, 1542–1546.
- (22) Reglero-Ruiz, J. A.; Pedros, M.; Tallon, J.-M.; Dumon, M. Micro and Nano Cellular Amorphous Polymers (PMMA, PS) in Supercritical CO<sub>2</sub> Assisted by Nanostructured CO<sub>2</sub>-Philic Block Copolymers—One Step Foaming Process. *J. Supercrit. Fluid.* **2011**, *58*, 168–176.
- (23) Dumon, M.; Reglero-Ruiz, J. A.; Pinto, J.; Rodriguez-Perez, M. A.; Tallon, J. M.; Pedros, M.; Viot, P. Block Copolymer-Assisted Microcellular Supercritical CO<sub>2</sub> Foaming of Polymers and Blends. *Cell. Polym.* **2012**, *31*, 207–222.
- (24) Kumar, V.; Suh, N. P. A Process for making Microcellular Thermoplastic Parts. *Polym. Eng. Sci.* **1990**, *30*, 1323–1329.
- (25) Jacobs, L. J. M.; Kemmere, M. F.; Keurentjes, J. T. F. Sustainable Polymer Foaming using High Pressure Carbon Dioxide: A Review on Fundamentals, Processes and Applications. *Green Chem.* **2008**, *10*, 731–738.
- (26) Wells, S. L.; DeSimone, J. CO<sub>2</sub> Technology Platform: An Important Tool for Environmental Problem Solving. *Angew. Chem., Int. Ed.* **2001**, *40*, 518–527.
- (27) Hollick, E. J.; Spalton, D. J.; Ursell, P. G.; Pande, M. V. Biocompatibility of Poly(methyl methacrylate), Silicone, and AcrySof Intraocular Lenses: Randomized Comparison of the Cellular Reaction on the Anterior Lens Surface. *J. Cataract Refr. Surg.* **1998**, *24*, 361–366.
- (28) Hakim, R. M.; Fearon, D. T.; Lazarus, J. M. Biocompatibility of Dialysis Membranes: Effects of Chronic Complement Activation. *Kidney Int.* **1984**, *26*, 194–200.
- (29) Lalande, L.; Plummer, C. J. G.; Manson, J.-A. E.; Gerard, P. The Influence of Matrix Modification on Fracture Mechanisms in Rubber Toughened Polymethylmethacrylate. *Polymer* **2006**, *47*, 2389–2401.
- (30) Lalande, L.; Plummer, C. J. G.; Manson, J.-A. E.; Gerard, P. Microdeformation Mechanisms in Rubber Toughened PMMA and PMMA-based Copolymers. *Eng. Fract. Mech.* **2006**, *73*, 2413–2426.
- (31) Solórzano, E.; Escudero, J.; Pinto, J.; Rodriguez-Perez, M. A.; de Saja, J. A. Evolution of Polymers during the Gas Dissolution Process. In *Proceedings International Conference on Diffusion in Solids and Liquids*; Algarve, Portugal, 2011.
- (32) Abramoff, M. D.; Magelhaes, P. J.; Ram, S. J. Image Processing with ImageJ. *Biophotonics Int.* **2004**, *11*, 36–42.
- (33) Pinto, J.; Solórzano, E.; Rodriguez-Perez, M. A.; de Saja, J. A. Characterization of the Cellular Structure based on User-Interactive Image Analysis Procedures. *J. Cell. Polym.* **2013**, *49*, 555–575.
- (34) Horcas, I.; Fernandez, R.; Gomez-Rodriguez, J. M.; Colchero, J.; Gomez-Herrero, J.; Baro, A. M. WSXM: A Software for Scanning Probe Microscopy and a Tool for Nanotechnology. *Rev. Sci. Instrum.* **2007**, *78* DOI: 10.1063/1.2432410.
- (35) Garcia, R.; San Paulo, A. Attractive and Repulsive Tip-Sample Interaction Regimes in Tapping-Mode Atomic Force Microscopy. *Phys. Rev. B* **1999**, *60*, 4961–4967.
- (36) Garcia, R.; Gómez, C. J.; Martínez, N. F.; Patil, S.; Dietz, C.; Magerle, R. Identification of Nanoscale Dissipation Processes by Dynamic Atomic Force Microscopy. *Phys. Rev. Lett.* **2006**, *97*, 016103.
- (37) Lalande, L. *Structure et Mécanismes de Microdéformation de Polyméthylmethacrylates Renforcés au Choc*; Ph. D. dissertation, Ecole Polytechnique Fédérale de Lausanne: France, 2007.
- (38) Chen, W.; Zhu, M.; Song, S.; Sun, B.; Chen, Y.; Adler, J. H. Morphological Characterization of PMMA/PAN Composite Particles in Nano to Submicro Size. *Macromol. Mater. Eng.* **2005**, *290*, 669–674.
- (39) Gallego Ferrer, G.; Salmeron Sanchez, M.; Gómez Ribelles, J. L.; Romero Colomer, F. J.; Monleón Pradas, M. Nanodomains in a Hydrophilic-Hydrophobic IPN base don Poly(2-hydroxyethyl acrylate) and Poly(ethyl acrylate). *Eur. Polym. J.* **2007**, *43*, 3136–3145.
- (40) Pinto, J.; Dumon, M.; Pedros, M.; Reglero, J.; Rodriguez-Perez, M. A. Nanocellular CO<sub>2</sub> Foaming of PMMA Assisted by Block Copolymer Nanostructure. *Chem. Eng. J.* **2014**, *243C*, 428–435.
- (41) Spital, P.; Macosko, C. W.; McClurg, R. B. Block Copolymer Micelles for Nucleation of the Microcellular Thermoplastic Foams. *Macromolecules* **2004**, *37* (7), 6874–6882.
- (42) Kwok, D. Y.; Leung, A.; Lam, C. N. C.; Li, A.; Wu, R.; Neumann, A. W. Low-Rate Dynamic Contact Angles on Poly(methyl methacrylate) and the Determination of Solid Surface Tensions. *J. Colloid Interface Sci.* **1998**, *206*, 44.
- (43) Mark, J. E. *Physical Properties of Polymers Handbook*, 2nd ed.; Springer Science-Business Media, LLC: New York, 2007.
- (44) Goel, S. K.; Beckman, E. J. Generation of Microcellular Polymers using Supercritical CO<sub>2</sub>. *Cell. Polym.* **1993**, *12*, 251–274.
- (45) Nawaby, A. V.; Handa, Y. P.; Liao, X.; Yoshitaka, Y.; Tomohiro, M. Polymer-CO<sub>2</sub> Systems Exhibiting Retrograde Behavior and Formation of Nanofoams. *Polym. Int.* **2007**, *56*, 67–73.
- (46) Warkiani, M. E.; Lou, C.-P.; Gong, H.-Q. Fabrication and Characterization of a Microporous Polymeric Micro-filter for Isolation of *Cryptosporidium parvum* oocysts. *J. Micromech. Microeng.* **2011**, *21* DOI: 10.1088/0960-1317/21/3/035002.

*Defect and Diffusion Forum Vols. 326-328 (2012) pp 434-439*  
 © (2012) Trans Tech Publications, Switzerland  
 doi:10.4028/www.scientific.net/DDF.326-328.434

## Solid Skin Characterization of PMMA/MAM Foams Fabricated by Gas Dissolution Foaming over a Range of Pressures

Javier Pinto<sup>1,a</sup>, Samuel Pardo<sup>1,b</sup>, E. Solorzano<sup>1,c</sup>, M. A. Rodriguez-Perez<sup>1,d</sup>,  
 M. Dumon<sup>2,e</sup> and J. A. de Saja<sup>1,f</sup>

<sup>1</sup>Cellular Materials Laboratory (CellMat), Condensed Matter Physics Department, University of Valladolid. c/ Prado de la Magdalena S/N. C.P.: 47011 Valladolid (Spain)

<sup>2</sup>Laboratoire de Chimie de Polymères Organiques (LCPO), Institut Polytechnique de Bordeaux (IPB)

<sup>a</sup>jpinto@fmc.uva.es, <sup>b</sup>samuelpardo.alonso@fmc.uva.es, <sup>c</sup>esolo@fmc.uva.es, <sup>d</sup>marrod@fmc.uva.es,  
<sup>e</sup>michel.dumon@iut.u-bordeaux1.fr, <sup>f</sup>sajasaez@fmc.uva.es

**Keywords:** foams; nanocellular; carbon dioxide; nanostructure; polymers; solid skin;

**Abstract.** A new model for solid skin formation on submicrocellular foams based on PMMA is presented. Structural foams has been produced by the solid state foaming technique using as precursor material a blend of poly(methyl methacrylate) PMMA and a triblock copolymer [poly(methyl methacrylate)-block poly(butyl acrylate)-block poly(methyl methacrylate), MAM].

An analysis on the skin thickness and densification has been carried based on x-ray high resolution radiography. The obtained results have been related to the fabrication parameters, i.e. MAM content of the blend and foaming pressure, and provide us a new vision about the processes that control the formation of a solid unfoamed, or partially unfoamed, skin in these materials.

## Introduction

The application of sandwich structural foams has rapidly increased in the last decade [1]. Structural foams are composed of two solid layers (skins) enclosing a foamed core. This kind of materials exhibit better mechanical properties, as strength and stiffness, compared to classical foams at an equivalent density. In addition the solid skin offers other advantages, a better surface quality and possibility of painting the surface.

Improvement of mechanical properties is directly correlated to the skin thickness. It could be possible to reach specific requirements by producing foams with the appropriate skin thickness [2]. Then, to understand the internal processes that cause the formation of the solid skin, and their relationship with the main parameters of the production method, is a key aspect to produce structural foams with the desired properties. In addition, the production of structural foams from materials with improved properties due to a special cellular structure, such as nanocellular foams [3], can have a synergistic improvements of the resultant foam properties.

In a previous work [4] we have obtained a new generation of nanocellular polymer materials using gas dissolution foaming method. Using blends of PMMA [poly(methyl methacrylate)] and MAM triblock copolymer [poly(methyl methacrylate)-block poly(butyl acrylate)-block poly(methyl methacrylate)], both commercial materials, we can obtain by extrusion a nanostructured material with a large number of micelles. These blends can be foamed by using CO<sub>2</sub> as blowing agent, even in parts with a significant thickness (several millimeters), not only thin film samples, and provide foams with an important density reduction (relative foam density [i.e., density of the foam divided by the density of the solid material]  $\rho_r \approx 0.5$ ), a nanosized cellular structure (cell sizes 200 nm), and a high cell density up to 10<sup>14</sup> cells/cm<sup>3</sup>.



A particular type of gas dissolution foaming method, the solid state foaming, can produce structural foams, whose solid skin formation process has been modelled [5].

In this model, it is assumed that there is a minimum amount of gas uptake that allows the formation of nuclei and growth of cells. Then, the gas concentration profile along the sample at the beginning of the foaming stage controls the solid skin formation. As this profile can be estimated using Fick's law [6] the final solid skin thickness can be predicted. This model predicts 100% dense solid skins.

It is important to remark that an essential property in this foaming process is the polymer glass transition temperature  $T_g$ . This property is substantially affected by the gas uptake [7,8], the relationship between  $T_g$  and the pressure of the gas  $p$  at equilibrium gives information on the extent of plasticization and changes in the thermal transitions. The usual behaviour is that the  $T_g$  decreases when the gas pressure increases.

In this study, we produce structural foams with a nanocellular structure based in nanostructured PMMA/MAM blends by using CO<sub>2</sub> as blowing agent in a modified solid state foaming process. Then, we analyze the correlation between the obtained skins and the model previously explained [5], and propose a modified model for this type of foams based in the  $T_g$  depletion of the plastized PMMA with CO<sub>2</sub>.

### Experimental part

**Materials.** Transparent PMMA was kindly supplied by Altuglas-Arkema Company (France), in the form of pellets. A transparent MAM triblock copolymer with 35 wt.-% methacrylate/30 wt.-% butylacrylate/35 wt.-% methacrylate was supplied by Arkema Company (France), in the form of pellets. The glass transition temperature ( $T_g$ ) value of the polymers employed were 112°C for the PMMA homopolymer, and +119°C and -49°C for the methacrylate and butyl acrylate blocks in the MAM triblock copolymer, respectively. Details of production of both PMMA and MAM polymers can be found elsewhere [9,10].

**Samples Production.** Polymer blends of PMMA containing 5, 7.5 and 10 wt.-% of MAM were produced as follows. Both materials, PMMA and MAM, were dried in vacuum (680 mm Hg), at 80°C during 4 h before processing. Mixing and extrusion were carried out using a Scamex CE02 single-screw extruder ( $L/D = 28$  d = 45 mm), with a temperature profile from 165 to 225°C, at a screw speed of 60 rpm, in the desired proportions. Pellets were produced using a continuous cutting machine operating at the end of the line at a constant speed of 240 rpm.

In a second step, pellets produced were injected into pieces (50 x 15 mm<sup>2</sup>) with 3 mm thickness, using a small scale injection molding machine developed by DSM Xplote. The working temperature was fixed at 240°C, whereas mold temperature was set at 60°C. The injection pressure was fixed at 1 MPa. Transparent samples obtained showed a good surface appearance as well a good injection behaviour, with no presence of air bubbles inside the parts.

**Foaming experiments.** Foaming experiments were carried out in a high pressure vessel provided by TOP Industry (France), with a capacity of 300 cm<sup>3</sup> and capable of operating at maximum temperature of 250°C and maximum pressure of 40 MPa. The reactor is equipped with an accurate pressure pump controller provided by Teledyne ISCO, and controlled automatically to keep the temperature and pressure at the desired values. The CO<sub>2</sub> vessel temperature and pressure were monitored during the process. Thus a collection of experiments were performed in a modified solid state foaming process. The usual solid state foaming process with amorphous polymers has three stages, the saturation (under fixed gas pressure and temperature), desorption (room pressure and temperature) and foaming of the sample (at temperature over the  $T_g$  of the polymer). However, the glass transition temperature of plastized PMMA with CO<sub>2</sub> can reach values near room temperature [11], even below room temperature in some particular conditions [12], then the

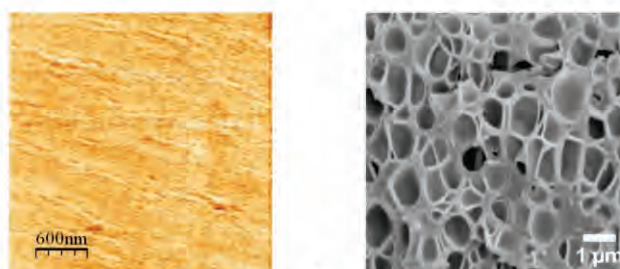


Figure 2. Neat PMMA, AFM phase image of solid material (left), and SEM image of foam produced at 30 MPa (right)

**Solid skin thickness.** First, it is necessary to check the accuracy of the measurement methods. We found that it is not possible to measure the skin thickness over a micrograph, because the magnification needed to appreciate the cellular structure is much higher than the magnification which allows to measuring the skin thickness. However, the x-ray high resolution radiography allow us to measure the skin thickness with accuracy. The main advantage of this method is that not only provides information about the skin thickness, but also an accurate measurement of the material density over the entire sample. So, the results shown from now on will be density profiles obtained by x-ray high resolution radiography.

In second place, the main parameters that control the solid skin formation in the model [5] should be analyzed in our experiments. The gas concentration profile can be calculated with equation 1 [6].

$$C = C_o \frac{4}{\pi} \sum_{n=0}^{\infty} \left[ \frac{(-1)^n}{2n+1} \exp\left(\frac{-D(2n+1)^2 \pi^2 t}{l^2}\right) \cos\left(\frac{(2n+1)\pi x}{l}\right) \right] \quad (1)$$

Where  $C$  is the concentration of gas at time  $t$  and distance  $x$ ,  $C_o$  is the initial gas concentration within the sample,  $D$  is the diffusion coefficient of the gas-polymer system,  $t$  is the desorption time,  $l$  is the thickness of the sample, and  $x$  the distance from the center of the sample. Based on this expression (Eq. 1) in our experiments the main parameters are as follows.

Desorption time: it is not possible to measure it in our foaming process since the second and third stages are not clearly differentiated as explained above, however it is the same time for experiments with similar conditions, i.e. similar saturation pressure and temperature.

Initial gas concentration, which is measured for each sample ( $\text{CO}_2$  wt.-% uptake).

Sample thickness, which is the same for every sample.

Diffusion coefficient, we assumed that the coefficient is the same for every blend. The amount of butylacrylate in every sample is very low ( $< 3.5$  %-wt.), and the gas diffusion out of the samples will be controlled by the methacrylate.

Then, the control parameter in our experiments will be the initial gas concentration. Higher amounts of  $\text{CO}_2$  uptake should result in lower skin thickness.

With the aim of validating the model in these samples the influence of the  $\text{CO}_2$  uptake on the skin thickness is analyzed. First, it is found that the influence of the MAM content on the  $\text{CO}_2$  uptake and skin thickness is not significant (Fig. 3). Then, it is possible to compare the relationship between the  $\text{CO}_2$  uptake and the skin thickness for all samples. As expected the results showed that the skin thickness decreases with the increase of the  $\text{CO}_2$  uptake (Fig. 4).



Then, the model seems to work with these PMMA/MAM blends. However, the formation of complete dense skins is predicted, with a clear nucleation threshold, but these complete dense skins only have been found in neat PMMA samples (Fig. 4). PMMA/MAM samples present a transitional skin (Fig. 4), without a clear nucleation threshold.

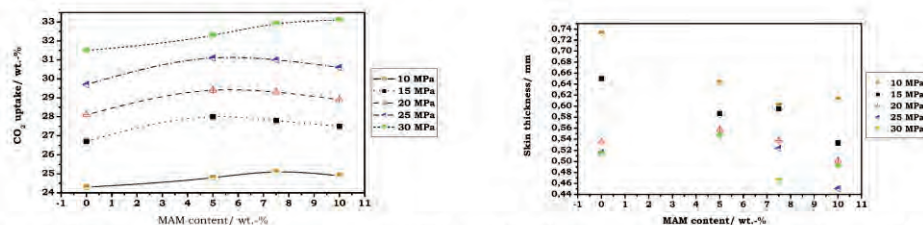


Figure 3. Effect of the MAM content on the CO<sub>2</sub> uptake (left) and the solid skin thickness (right)

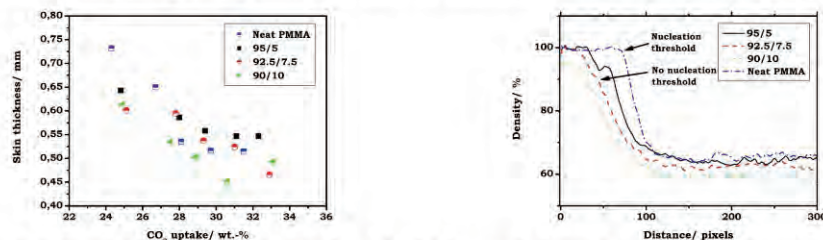


Figure 4. Effect of the CO<sub>2</sub> uptake on the skin thickness (left), and density profiles of neat PMMA and PMMA/MAM blends (right)

## Discussion

It is found that the model seems to work correctly in the neat PMMA samples; skin thickness is controlled by the amount of CO<sub>2</sub> uptake and presents a clear nucleation threshold. Neat PMMA are a homogeneous materials and it is possible to assume that the nucleation process is homogeneous, condition assumed in the model.

On the other hand, the skin formation of PMMA/MAM blends is controlled by the amount of CO<sub>2</sub>, but without a nucleation threshold. These blends are heterogeneous, homogeneous nucleation cannot be assumed, and the model cannot be applied.

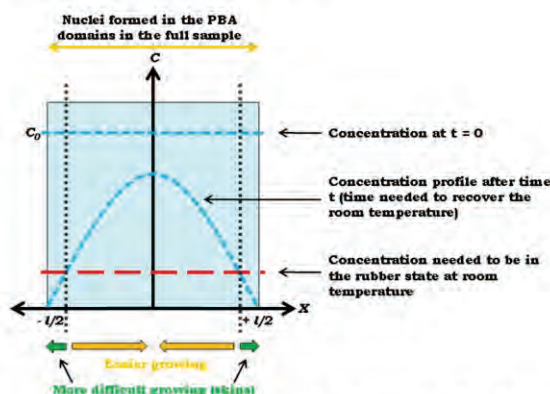


Figure 5. Schematic showing the development of a skin region

A qualitative modification of the model is proposed for PMMA/MAM blends (Fig. 5), heterogeneous nucleation is assumed; the nucleation happens mainly in the dispersed nanosized domains during the pressure release. These domains are supposed that are formed by butylacrylate. Our proposal is that the glass transition temperature  $T_g$  depletion of the continuous phase (PMMA) controls the solid skin formation, because the cells are nucleated in the butylacrylate domains over the entire sample, but they can grow only if the PMMA matrix around them is in the rubber state. In this model the amount of  $\text{CO}_2$  uptake control the skin thickness, because there is a minimum gas concentration  $C^*$  for the PMMA to be in a rubber state at room temperature, and the  $\text{CO}_2$  diffusion out of the sample after the pressure release controls the  $T_g$  depletion.

The main difference is that the  $T_g$  is not a threshold limit, under this temperature the chain mobility decreases significantly but is not completely avoided. Then, the foam has a continuous decrease of the porosity, but not a complete dense skin.

### Conclusions

It has been demonstrated that structural nanocellular foams with a transitional skin based in PMMA/MAM blends can be produced by a modified solid state foaming route. We found that the Kumar's model for solid skin formation is valid with neat PMMA foams, but not with PMMA/MAM blends. In this blends heterogeneous nucleation seems to dominate, controlled by the dispersed nanosized domains.

An alternative model for solid skin formation in heterogeneous blends has been proposed, based in the  $T_g$  depletion of the continuous phase (PMMA). This model for heterogeneous blends needs a pair of materials with a significantly difference between their glass transition temperatures and diffusion coefficients.

### Acknowledgments

Financial assistance from MCINN (MAT2009-14001-C02-01) and FPU grant AP2008-03603 (J. Pinto) from the Spanish Ministry of Education is gratefully acknowledged.

### References

- [1] D. Klemperer and V. Sendjarevic: *Polymeric Foams and Foam Technology* (Hanser Publisher, Munich 2004).
- [2] D. V. Khakhar, K. V. Joseph: *Polym. Eng. Sci.* Vol. 34-14 (1994), p. 726
- [3] C. Barlow, V. Kumar, B. Flinn, R. K. Bordia, J. Weller: *J. Eng. Mater. Technol.* Vol. 123-2 (2001), p. 329
- [4] J. A. R. Ruiz, M. Dumon, J. Pinto, M. A. Rodriguez-Perez: *Macromol. Mater. Eng.* Vol. 296 (2011), in press
- [5] V. Kumar, J. E. Weller: *Polym. Eng. Sci.* Vol. 34-3 (1994), p. 169
- [6] J. Crank: *The mathematics of diffusion* (Oxford University Press, United States 1989)
- [7] S. K. Goel, E. Beckman: *J. Polym. Eng. Sci.* Vol. 34 (1994), p. 1148
- [8] Y. P. Handa, Z. Zhang: *J. Polym. Sci. B: Polym. Phys.* Vol. 38 (2000), p. 716
- [9] L. Lalande, C. J. Plummer, J. Anders, E. Manson, P. Gerard: *Polymer* Vol. 47 (2006), p. 2389
- [10] L. Lalande, C. J. Plummer, J. Anders et al.: *Eng. Fract. Mech.* Vol. 73 (2006), p. 2413
- [11] S. K. Goel, E. J. Beckman: *Cell. Polym.* Vol. 12 (1993), p. 251
- [12] A. V. Nawaby, Y. P. Handa et al.: *Polym. Int.* Vol. 56 (2007), p. 67
- [13] J. Pinto, M. A. Rodriguez-Perez, J. A. De Saja: XI GEP Meeting (2009)
- [14] M. D. Abramoff, P. J. Magalhaes, S. J. Ram: *Biophotonics Int.* Vol. 11 (2004), p. 36
- [15] J. Escudero, E. Solórzano, M. A. Rodriguez-Perez, F. Garcia-Moreno, J. A. De Saja: *Journal. Cellular Polymers* Vol. 28 nº 4 (2009), p. 289

***Chapter IV:***  
***Influence of temperature on the  
foaming processes, mechanisms,  
and foams structures***





## Chapter IV. Influence of temperature on the foaming processes, mechanisms, and foams structures

In the previous chapter, it was demonstrated that some processing parameters, such as saturation pressure and pressure release rate, have or little influence on the *cell nucleation* process of PMMA/MAM. Thus foams with a cell nucleation density high enough to produce nanocellular structures can be produced in a wide range of processing conditions. So, the next challenge is to produce nanocellular foams from PMMA/MAM blends with lower relative densities ( $\rho_r$ ). Due to the constant cell nucleation density of these materials, the key to reduce the density is to understand and to have a better control of the cells growth.

We know that PMMA/MAM blends with low amounts of MAM present a rather low decrease (-10 %) of their density by increasing the MAM amount between 5 and 20 wt%. Also the saturation pressure can produce a decrease (down to -25 %) for 90/10 PMMA/MAM foams produced at 10 and 30 MPa. It was explained that the main factor controlling the cells growth is the plasticization of the PMMA matrix. A possible strategy to increase the cells growth can be to perform the expansion at higher temperatures, so the sample lies in the rubbery state more time during the foaming stage.

Therefore, in this chapter the influence of the temperature on the foaming process and on the foam structure of PMMA/MAM blends will be studied with the goal of reducing the overall density.

First, the influence of the saturation temperature (i.e. the temperature during the saturation process) on the cellular structure and density of neat PMMA, neat MAM and 90/10 PMMA/MAM blends is studied. Moreover, the foaming behavior of these materials at different temperatures will allow differentiating between foaming process with desorption stage between the pressure release and the foaming (i.e. *solid state foaming*) and without desorption stage (i.e. *batch foaming*).

Secondly, the influence of the foaming temperature (i.e. the temperature at which the solid sample is subjected after the pressure release in solid state foaming processes) and the post-foaming temperature (i.e. the temperature at which the foamed sample is subjected after the pressure release in batch foaming processes) on the cellular structure and density of 90/10 PMMA/MAM blends and neat PMMA is determined.

## IV.1 Influence of the CO<sub>2</sub> saturation temperature on foaming process, morphology and density of PMMA/MAM foams

The analysis of the influence of the saturation temperature on the foaming process, and the cellular structure of PMMA, MAM, and 90/10 PMMA/MAM blends has been summarized in the journal article entitled *“Temperature Influence and CO<sub>2</sub> Transport in Foaming Processes of Poly(methyl methacrylate)-Block Copolymer Nanocellular and Microcellular Foams”* (submitted to *Journal of Supercritical Fluids*, acceptance pending).

In order to estimate the plastification evolution of these materials, the CO<sub>2</sub> desorption of PMMA, MAM and 90/10 PMMA/MAM blend was measured after the pressure release at 30 MPa/min.

The PMMA and 90/10 systems presented the same behavior: a slow CO<sub>2</sub> diffusion out of the sample, leaving nearly all the CO<sub>2</sub> inside the polymer matrix. On the contrary, MAM alone loses the gas very quickly. PMMA/MAM blends with low amounts of MAM present dispersed nanodomains, thus the CO<sub>2</sub> absorbed both by the PMMA matrix and the PBA domains should diffuse through the PMMA matrix to go out of the sample. Therefore these low content blends will present a similar desorption behavior as neat PMMA. On the contrary, neat MAM and PMMA/MAM blends with medium and high amounts of MAM present “co-continuous or semi co-continuous” PBA domains that allow the CO<sub>2</sub> to diffuse out of the sample mainly through the nanostructures.

Foams were produced at 30 MPa and saturation temperatures between room temperature (RT) and 70° C. At RT all samples present nanocellular structure (cell sizes below 200 nm) and similar relative density (about 0.45). But when temperature is increased to 40° C, that quasi stable density completely disappears. Density of PMMA foams remains constant, while 90/10 and MAM foams densities decrease by -10 % and -50 %, respectively. Above this temperature, density of the three materials does not show any more significant variations.

However, the evolution of the average cell size is quite different. Neat PMMA increase its average cell size steadily with the temperature from nanometric to micrometric ranges; cells of 90/10 PMMA/MAM blends remains in the nanometric range (below 300 nm) up to 50° C, increasing to 1 μm due to coalescence at 60° and 70° C; and neat MAM present a sharp change between RT and 40° C, from nanocellular (below 200 nm) to micrometric (about 8 μm), remaining constant over 40° C.

Therefore, only 90/10 PMMA/MAM blends present a significant density reduction (about 10%) keeping the nanocellular structure. Neat PMMA present no significant density reductions, whereas neat MAM foams present a high density reduction but lose their nanocellular structure.

These behaviors are difficult to explain. In the following journal article an hypothesis about the foaming processes of the PMMA/MAM systems is provided taking into account the previous observations (i.e. important differences between RT and 40° C), the evolution of pressure and temperature during the pressure release, and some observations about the samples state when are extracted from the pressure vessel. Gas dissolution foaming processes, with and without desorption stage, are suggested.

## TEMPERATURE INFLUENCE AND CO<sub>2</sub> TRANSPORT IN FOAMING PROCESSES OF POLY(METHYL METHACRYLATE)-BLOCK COPOLYMER NANOCELLULAR AND MICROCELLULAR FOAMS

*Javier Pinto<sup>1,2</sup>, José A. Reglero-Ruiz<sup>2</sup>, Michel Dumon<sup>2</sup>, Miguel A. Rodriguez-Perez<sup>1</sup>*

1: Cellular Materials Laboratory (CellMat), Condensed Matter Physics Department, University of Valladolid, 47011, Valladolid, Spain, email: [jpinto@fmc.uva.es](mailto:jpinto@fmc.uva.es), [marrod@fmc.uva.es](mailto:marrod@fmc.uva.es), Phone: + 34 983 423572, Fax: + 34 983 423192

2: Laboratoire de Chimie des Polymères Organiques (LCPO). Université de Bordeaux. ENSCBP, 16 Avenue Pey Berland, 33607 Pessac-Cedex, France

### Abstract

Fabricated by high-pressure or supercritical CO<sub>2</sub> gas dissolution foaming process, nanocellular and microcellular foams based on poly(methyl methacrylate) (PMMA) present a controlled nucleation mechanism by the addition of a Methylmethacrylate-ButylAcrylate-Methylmethacrylate (MAM) block copolymer, leading to defined nanocellular morphologies templated by the nanostructuration of the PMMA/MAM blends. Influence of the saturation temperature on the foaming mechanism and on the foam structure has been studied in 90/10 PMMA/MAM blends and also in the neat PMMA or MAM, in order to understand the role of the MAM nanostructuration in the cell growing and coalescence phenomena. CO<sub>2</sub> uptake and desorption measurements on series of block copolymer/homopolymer blend samples show a competitive behavior of the soft, rubbery, and CO<sub>2</sub>-philic block of PBA (poly(butyl acrylate)): fast desorption kinetics but higher initial saturation. This competition nevertheless is strongly influenced by the type of dispersion of PBA (e.g. micellar, lamellar) and a very consequent influence on foaming.

CO<sub>2</sub> sorption and desorption were characterized in order to provide a better understanding of the role of the block copolymer on the foaming stages. Poly(butyl acrylate) blocks are shown to have a faster CO<sub>2</sub> diffusion rate than poly(methyl methacrylate) but are more CO<sub>2</sub>-philic. Thus gas saturation and cell nucleation (heterogeneous) are more affected by the PBA block while cell coalescence is more affected by the PMMA phases (in the copolymer blocks + in the matrix).

**Keywords:** nanocellular polymer foams, microcellular foams, poly(methyl methacrylate), CO<sub>2</sub> diffusion, gas dissolution foaming, block copolymer

## Introduction

Development of nanocellular polymeric materials arouses a significant interest during the last years. Open pores in the nanometric range (20 to 100 nm) allows using these materials in micro and nanofiltration processes [1], where different particles can be selectively removed by an accurate control of the pore size distribution and the overall porosity of the material. Furthermore, when the pore size reaches values around the free path of the gas molecules contained in the pores (e.g.  $\sim 75$  nm in case of air), the conduction contribution of the gas to the thermal conductivity of the material is drastically decreased due to the Knudsen effect [2]. The combination of this effect with a high porosity content allow obtaining materials with very low thermal conductivity [3], with significant applications in thermal insulation industry. Other applications due to the high surface area of these materials is their use as catalyst or as scaffolds.

Nanocellular polymer foams can be produced by different processes. Such materials were obtained by the selective removal of one component in nanostructured polymers [4-7] or by pattern-transfer techniques [4, 8]. However, from a “production” point of view, one of the most promising techniques to obtain nanocellular polymer foams is the high-pressure or supercritical CO<sub>2</sub> gas dissolution foaming, where CO<sub>2</sub> is used as physical blowing agent.

Commonly, the plasticization effect of CO<sub>2</sub> on amorphous polymers decreases the effective value of the polymer glass transition ( $T_{g,ef}$ ) [9-11]. Considering this, two main types of process can be described, according to effective temperature at the moment of the foam trigger. On one hand, at saturation temperatures higher than the  $T_{g,ef}$  (i.e. the polymer is in the rubbery state) the foaming process occurs during the pressure release. This process is usually called *one-step* or *batch* foaming [12, 13]. On the other hand, when the saturation temperature is lower than the  $T_{g,ef}$  (i.e. the polymer is in the glassy state) the foaming process is triggered in a second stage by heating the sample above its  $T_{g,ef}$ . This process is called *two-step* or *solid state foaming* [14].

First attempts to produce nanocellular foams using CO<sub>2</sub> gas dissolution foaming were carried out in thin films or sheets [15-18], obtaining high relative densities ( $>0.4$  g/cm<sup>3</sup>). However, different approaches have appeared in the last years to increase the cell nucleation density, with the aim of fabricating nanocellular foams with medium to low relative densities in bulk polymers (high thickness).

Main issue to produce nanocellular foams is to increase the nucleation ratio to values high enough to produce cells in the nanometric range. Addition of particles that could act as nucleating agents (both common inorganic additives and nanoparticles) has been used to increase the potential nucleation sites in several works [19, 20]. Also the use of copolymers, both random copolymers [21] and block copolymers [22-24] can promote the nucleation up to values appropriate to produce nanocellular foams. Recently,

different approaches have been used with significant results. Nanocellular foams with cell sizes below 100 nm and relative densities from 0.3 to 0.4 were obtained using blends of styrenic and acrylic polymers [25]. Also foams with cell sizes between 40 and 100 nm and relative densities between 0.36 and 0.75 were produced from homogeneous polyetherimide (PEI) [26].

Using the block copolymer approach micro and nanocellular foams can be obtained from blends of PMMA and a tri block copolymer (i.e. Methylmethacrylate-ButylAcrylate-Methylmethacrylate (MAM)) [24, 27-29]. Previous results showed that these materials present a decoupling between the cell nucleation and some process parameters such as the saturation pressure and the pressure release rate [24]. This particular behavior allows the production of nanocellular foams even at relative low CO<sub>2</sub> pressures (about 10 MPa, when nanocellular foams production usually requires saturation pressures from 20 to 40 MPa). Furthermore, the constant nucleation ratio allows to study separately the influence of the processing parameters on other foaming phenomena (cells growth or coalescence).

Up to date no information about the influence of the saturation temperature on the foaming process of these materials has been provided. As these blends show a self-assembled nanostructuration a significant influence is expected on the gas saturation and foaming.

The present study is an investigation about the influence of the saturation temperature and of the final cellular structure. The role of the block copolymer on the high-pressure CO<sub>2</sub> sorption and desorption behavior is studied.

## Experimental section

### *Materials*

Poly(methyl methacrylate) (PMMA) and block copolymer (BCP) Methylmethacrylate-ButylAcrylate-Methylmethacrylate (MAM) were kindly supplied by Arkema Company (France). Both materials are obtained in the form of pellets, and are optically transparent.

PMMA is a homopolymer ( $M_n = 43000$  g/mol,  $M_w = 83000$  g/mol) without impact modifier, with a density ( $\rho$ ) of 1.18 g/cm<sup>3</sup> and glass transition temperature ( $T_g$ ) of 112° C. The MAM BCP used in our study ( $M_n = 85000$  g/mol,  $M_w = 170000$  g/mol) presents a density of 1.08 g/cm<sup>3</sup>, and has 36 % wt. of the soft block, poly(butyl acrylate) (PBA) which  $T_g$  is about -50° C. Production details of this kind of MAM copolymers can be found in the literature [30, 31].



### *Fabrication of bulk solid blends*

PMMA/MAM blend with 10% wt. of MAM was produced by extrusion. First, both polymers were dried in vacuum (680 mm Hg) at 80° C during 4 h. A Scamex CE02 single screw extruder (L/D = 28, d = 45 mm), with a temperature profile from 165 to 225° C and screw speed of 60 rpm, was sufficient to generate macroscopically homogeneous transparent blends. Pellets from each blend were obtained using a continuous cutting machine operating at the end of the extrusion line.

Solid samples of neat polymers and PMMA/MAM blends were injection molded. Pellets, both raw materials and blends, were first dried in the same conditions as the extrusion process. Then, dried pellets were injected into bulk pieces (50 x 15 x 3 mm<sup>3</sup>) using a small scale injection molding machine (DSM Xplore). Process parameters were set at 240° C for the melt temperature, 60° C for the mold temperature and 1 MPa during 8 seconds for the injection pressure. Obtained pieces were optically transparent, both for raw materials and blends, and without injection defects. These bulk specimens were subsequently foamed under different temperature and pressure conditions.

### *Foaming route*

Foamed samples were produced following a gas dissolution foaming technique, i.e. a CO<sub>2</sub> saturation step (at fixed pressure and fixed temperature) followed by a foaming step (depressurization step, with or without external heating). Solid samples of both neat materials and PMMA/MAM blends were saturated with high-pressure or supercritical CO<sub>2</sub> using a pressure vessel with temperature control provided by TOP Industrie (France), which has a capacity of 300 cm<sup>3</sup> and can operate up to 40 MPa and 250° C. Pressure was set at 30 MPa (300 bar) during 24 h for every foaming experiment, while different temperatures were fixed between room temperature (RT) and 70° C. The period of 24 h was enough to complete saturation of the gas in the polymer (maximum and homogeneous gas uptake). Then, pressure was quickly released at the (uncontrolled) maximum drop rate allowed for the device considered (i.e. at an average of 30 MPa/min). Pressure and temperature were monitored during the entire process.

### *Characterization techniques*

Sorption of CO<sub>2</sub> on PMMA was studied measuring the CO<sub>2</sub> uptake during saturation. This value was calculated as the percentage of weight increment of the sample due to the CO<sub>2</sub> sorption. Samples were weighted before ( $m_0$ ) and just after the saturation ( $m_1$ ), and the CO<sub>2</sub> uptake was calculated using equation 1.

$$CO_2 uptake = \frac{(m_1 - m_0)}{m_0} \cdot 100 \quad [1]$$

Time needed to extract the samples from the pressure vessel after the pressure release, around three minutes, can be a significant source of inaccuracy of these measurements. To determine the deviation of these values from the real CO<sub>2</sub> uptake a study of the CO<sub>2</sub> desorption was carried out by weighting several samples every minute during ten minutes after the samples extraction.

Nanostructuration of solid samples was determined by Transmission Electron Microscopy (TEM, model Hitachi H 7650 with Orius camera) at BIC (Bordeaux Imaging Center, Université Bordeaux Segalen). TEM observations were performed between 60 to 80 kV, at magnifications from x30000 to x330000. TEM samples were obtained from solid materials using a microtome with diamond knife operating at -50° C. Then, the thin cuts (60-70 nm) were treated by a water solution of 2 % wt. phosphotungstic acid (PTA) and 2 % wt. benzyl alcohol. After 10 minutes at 60° C samples were rinsed 3 times on a drop of distilled water. After this treatment the selective staining of poly(butyl acrylate) by PTA reveals the nanostructuration.

Density of both solids ( $\rho_s$ ) and foams ( $\rho_f$ ) were determined by the water-displacement method, based on Archimedes' principle, obtaining an average value from at least three measurements of each sample. Relative density ( $\rho_r$ ) of foamed samples was obtained dividing their density ( $\rho_f$ ) by the solid density ( $\rho_s$ ). Due to the presence of an outer solid skin in some samples, density measurements were carried out after removing this skin mechanically.

Micrographs of the cellular structure were taken by Scanning Electron Microscopy (SEM, model Quanta 200FEG, FEI) at magnifications between 10000x and 100000x. Samples were immersed in liquid nitrogen to freeze the cellular structure, and then were fractured to assure that the microstructure remained intact. Fractured surfaces within the cellular structure were coated with gold, using a sputter coater model SC 004 provided by Balzers Union. Characterization of the micrographs was carried out by an own-developed software [32] based on FIJI/ImageJ [32, 33]. Main parameters of the cellular structure were obtained, such as the average cell size ( $\Phi$ ) and the volumetric cell nucleation density ( $N_o$ ), defined as the number of cells nucleated (or nuclei) per cubic centimeter of the unfoamed sample [14]. The volumetric cell nucleation density is calculated from the volumetric cell density ( $N_v$ , defined as the number of cells per cubic centimeter of the foamed sample) taking into account the expansion of the foam. This calculation only provides accurate values when there is no coalescence between cells. In this work this magnitude will be calculated both in foams with and without coalescence effects with the aim to compare the values and then to estimate the magnitude of the coalescence. Therefore, it will be called as apparent cell nucleation density.

Glass transition temperature ( $T_g$ ) of neat materials and blends were obtained by Differential Scanning Calorimetry (DSC, model DSC 862, Mettler). The  $T_g$  was measured at the second heating, from 20° C to 160° C with the heating rate of 10° C/min in a N<sub>2</sub> environment (flow rate 60 ml/min).

## Results and discussion

### *CO<sub>2</sub> sorption and desorption behavior*

Several saturation tests with neat PMMA and MAM, and 90/10 PMMA/MAM blend were performed at 30 MPa and at RT. Desorption behavior after the depressurization stage was measured as a function of time for at least two samples of each material with identical results. Typical desorption curves are shown in Figure 1, where time is measured from the pressure release (30 MPa/min). Samples were dense unfoamed materials.

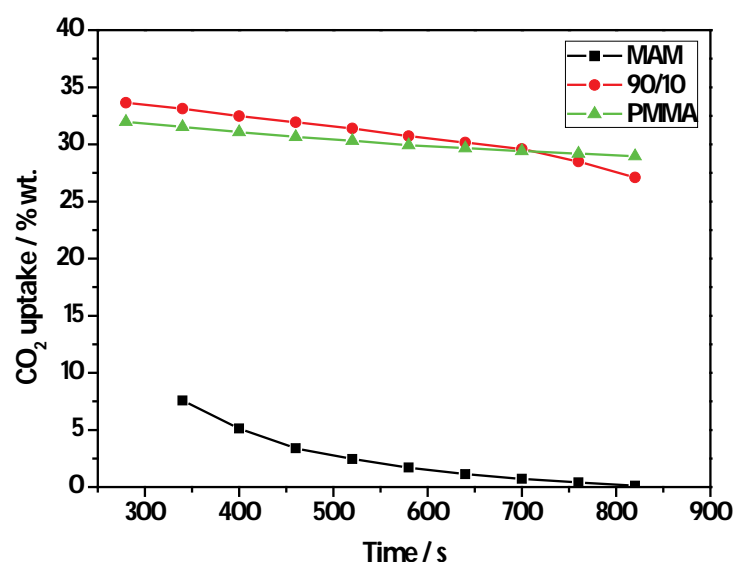


**Figure 1. Desorption curves of neat PMMA and MAM, and 90/10 PMMA/MAM. (Initial saturation conditions: 30 MPa and RT, all are dense unfoamed materials).**

A simple estimation of the CO<sub>2</sub> uptake at the saturation conditions can be obtained by a linear extrapolation to  $t = 0$  s of the first part of the desorption curves which is almost linear. Following this procedure, a small deviation of the CO<sub>2</sub> uptake measurements from the estimated values by extrapolation was found (around a 5% over the total amount of CO<sub>2</sub> uptake) for PMMA and 90/10 samples. Due to the good accuracy of the simple measurement, this value was used in the following discussions for samples with low MAM contents. However, neat MAM presents a different desorption behavior (see Figure 1), and the deviation of the measurements can be higher than 70-90%. MAM has much faster desorption kinetics. Depending upon the type of phase separated structure, the PBA desorption is more or less

constrained. The phase separation of the PBA phase is either a core/shell or micellar object or a lamellar structure (i.e. blend nanostructuration), which is presented in the TEM images of Figure 2. The lamellar structure of this block copolymer allows a higher CO<sub>2</sub> diffusivity through the soft block phase. Also it was checked that blends with high MAM contents (50 to 75 % wt., results not included in this paper) present a similar behavior as neat MAM. As a consequence CO<sub>2</sub> uptake in pure MAM cannot be measured within 3 minutes because during this time there is a strong desorption. Thus MAM bulk neat copolymer is discarded to further analysis of the CO<sub>2</sub> sorption and desorption behavior but kept for the cellular structure analysis.

In previous works [27, 29] lower values of the CO<sub>2</sub> uptake of PMMA and 90/10 samples have been obtained due to the different pressure release rates employed (15 MPa/min), being the measurements taken at longer times from the initial pressure release and might be consequently less quantitative. Also estimations of neat MAM CO<sub>2</sub> uptake were provided, however the present study about the CO<sub>2</sub> desorption behavior of MAM shows that these estimations could be not accurate.

In contrast, the dispersed objects of 90/10 PMMA/MAM (Figure 2) allows the PMMA matrix to control the CO<sub>2</sub> desorption, and consequently PMMA/MAM blends with dispersed nanostructuration present a similar desorption behavior than neat PMMA.

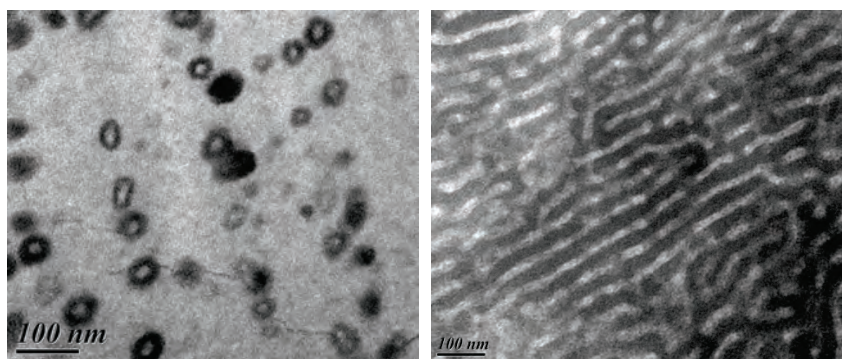


**Figure 2. Morphology (TEM image) of the 90/10 PMMA/MAM blend (left) and neat MAM (right) showing the nanostructuration**

Influence of the saturation temperature on the sorption behavior of PMMA and 90/10 PMMA/MAM was studied at a saturation pressure of 30 MPa. Figure 3 shows the CO<sub>2</sub> uptake at temperatures between RT and 70° C. As expected, the CO<sub>2</sub> sorption is decreased with the increase of temperature [34]. It should be noticed that samples produced over 40° C are already foamed at the moment of the measurement. However, these samples present a similar desorption behavior as un-foamed samples (produced at RT and measured before the foaming process starts) due to their closed cell structure (gas should diffuse through

the PMMA matrix to get out of the sample). Therefore, accurate measurements of the CO<sub>2</sub> uptake in these samples can be carried out.

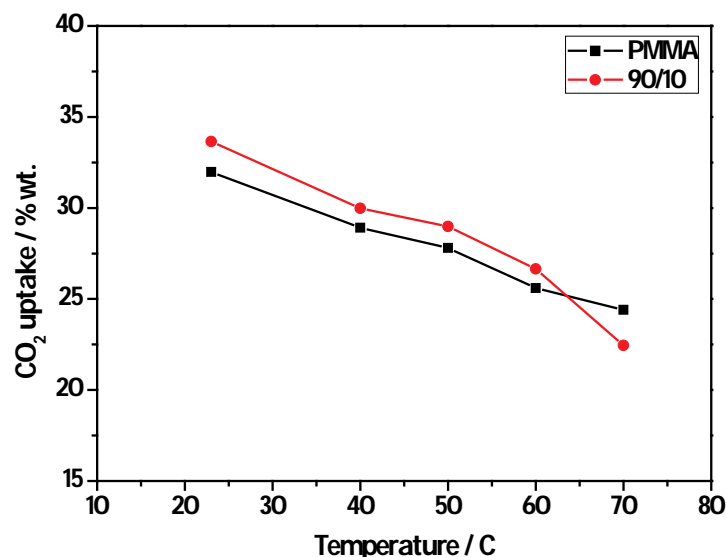


**Figure 3. CO<sub>2</sub> uptake of PMMA and 90/10 PMMA/MAM blend CO<sub>2</sub>-saturated under 30 MPa and at different saturation temperatures ranging between room temperature and 70° C**

In spite of a faster desorption (Figure 3) shows that the addition of MAM increases the CO<sub>2</sub> uptake up to 60° C. At higher temperatures the assumption of an equal diffusion behavior between neat PMMA and 90/10 PMMA/MAM blends starts to fail. CO<sub>2</sub> diffusion starts to be too fast in blends to provide accurate results with the measurement method employed.

These results, showing an increase of the CO<sub>2</sub> uptake due to the addition of MAM in a temperature range up to 70° C are in good agreement with a concomitant study of the CO<sub>2</sub> sorption of neat PMMA and PMMA/MAM blends where saturation pressure is varied in a range of pressures (from 10 to 30 MPa) [24]. Values for CO<sub>2</sub>/polymer cloud points found in the work of Rindfleisch et al. [35] on PBA and PMMA although of different molar masses are quite consistent with our measurements.

So independently of the foaming conditions (pressure or temperature) the CO<sub>2</sub> uptake increases with the amount of MAM added to the blends, due to the higher CO<sub>2</sub> solubility in PBA and its higher swelling compared to PMMA.

#### *Influence of the saturation temperature on the foam properties*

Foamed samples of neat PMMA and MAM, and the 90/10 PMMA/MAM blend, have been produced to study the influence of the saturation temperature on the relative density and the cellular structure of the

foams. Saturation pressure was set at 30 MPa, with different saturation temperatures from room temperature (RT) to 70° C.

First, it is noticed a significant difference between foams produced at room temperature and foams produced at temperatures over 40° C. After saturation stages carried out at room temperature the samples were extracted in a solid state from the pressure vessel (samples remain transparent), and start to foam a few minutes after the extraction (increasing their volume and becoming opaque). On the contrary, after saturation stages carried out at temperatures over 40° C the samples were extracted already foamed. Therefore, it can be expected important differences between the properties of the foams produced at room temperature and the foams produced above 40° C.

Figure 4 presents the evolution of the relative density with saturation temperature. As it can be seen, at room temperature the three materials present practically the same relative density. When temperature is increasing up to 40° C a sharp change is found, neat PMMA presents no changes in its relative density, however relative density of 90/10 PMMA/MAM blend and neat MAM decrease by about 10% and 50% respectively.

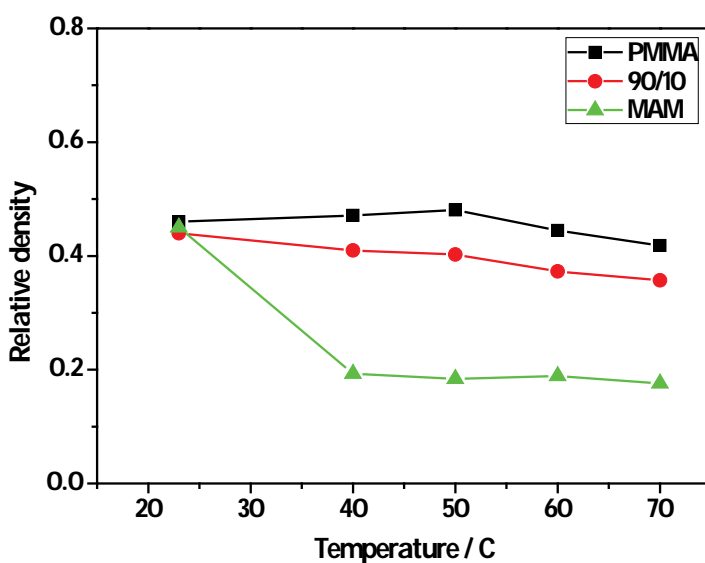


**Figure 4. Relative density of neat PMMA and MAM, and 90/10 PMMA/MAM foams. Saturation pressure is fixed at 30 MPa with saturation temperatures between RT and 70° C.**

Over 40° C relative density does not present significant changes as a function of the saturation temperature, with only a small reduction in PMMA and 90/10 PMMA/MAM foams as temperature increases. Expansion ratio of neat MAM foams is higher than that of neat PMMA ones, as expected due to the lower  $T_g$  and the higher CO<sub>2</sub> sorption of the PBA. Addition of MAM to PMMA also decreases the



foams density. At low amounts of MAM (like 90/10) this reduction can be explained by the higher CO<sub>2</sub> sorption of the PBA micelles which act as reservoirs [29].

Influence of the saturation temperature on the cellular structure has been studied over SEM micrographs of the foams. Some of the most representative micrographs are shown in Figure 5.

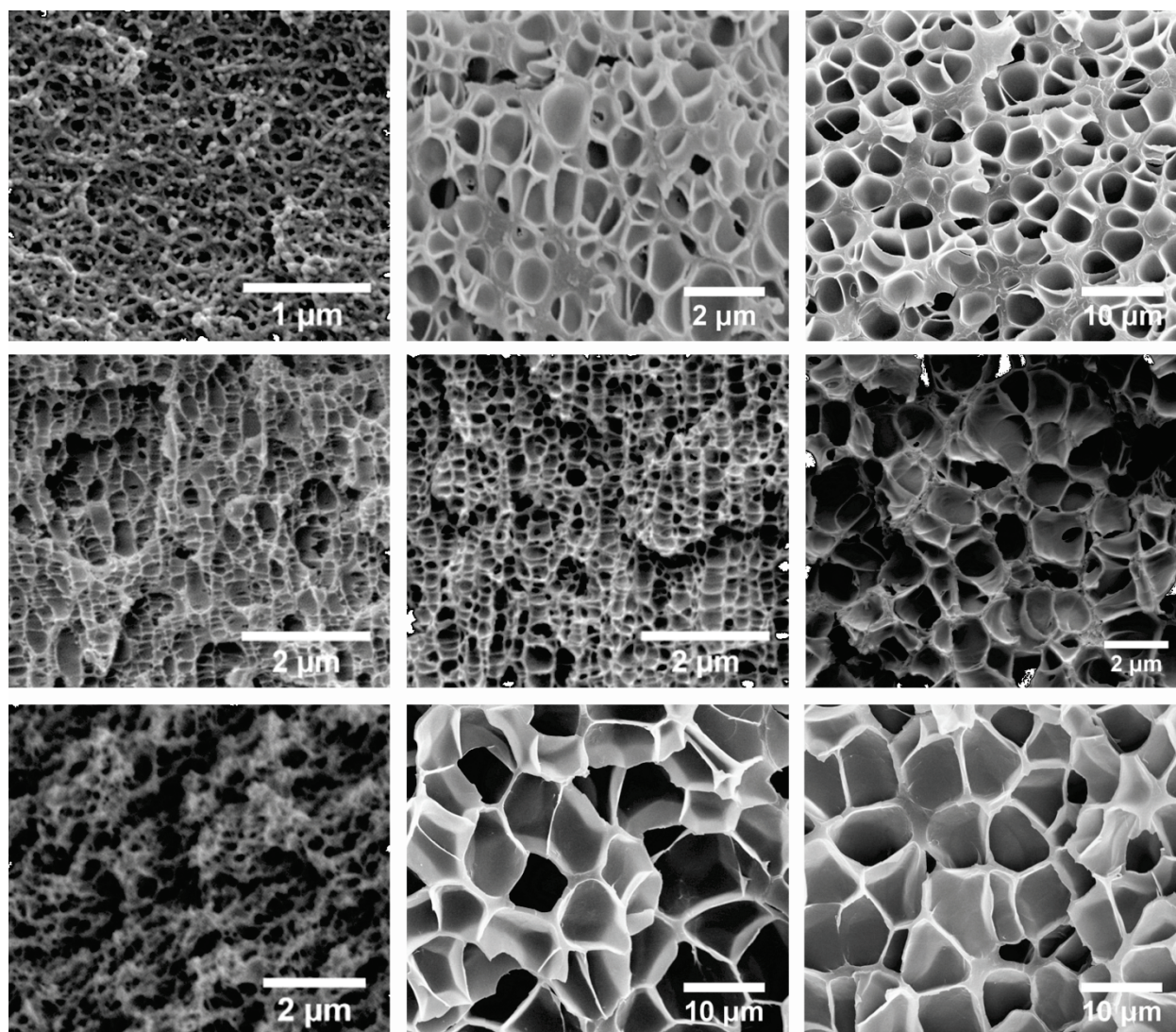


**Figure 5. Cellular structure of several foams produced at 30 MPa and RT (left), 40° C (middle) or 70° C (right) from neat PMMA (up), 90/10 PMMA/MAM (middle) and neat MAM (down).**

Figure 6 shows the average cell size as a function of saturation temperature. A clear threshold between foams produced at room temperature and foams produced over 40° C is found again in neat PMMA and MAM foams; on the contrary, 90/10 PMMA/MAM foams present a rather constant average cell size up to 50° C, being the threshold in this case over 60° C.

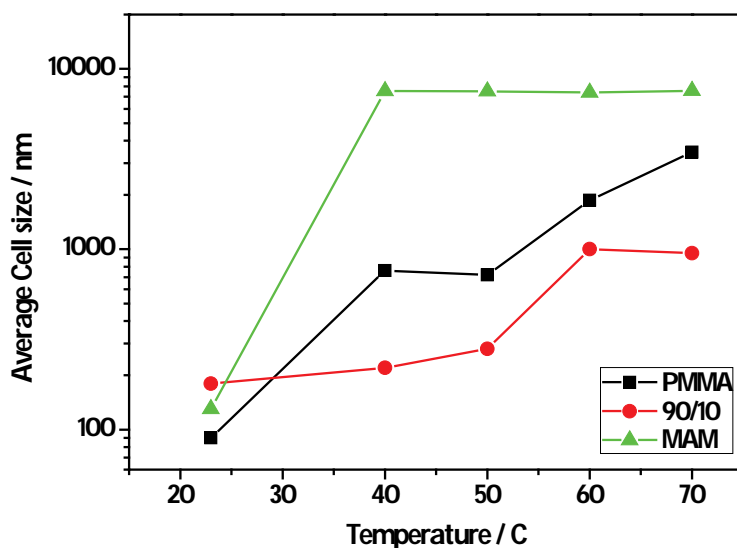


**Figure 6. Cell size of neat PMMA and MAM, and 90/10 PMMA/MAM foams. Produced at 30 MPa and temperatures between RT and 70° C. All foams are triggered by depressurization at  $\approx 30$  MPa/min.**

Foams produced at room temperature present a nanocellular structure with cell sizes under 200 nm independently of their composition. However, there is an important difference in the cells connectivity between the neat polymers and the blend. Neat PMMA and MAM show an open or partially connected cell structure, while 90/10 PMMA/MAM blend presents a closed cell structure. Explanation for the different cell structures can be found in the nucleation and cell growing. In previous studies, it was demonstrated that 90/10 PMMA/MAM blends present a heterogeneous nucleation controlled by the micelles, being the growing of the cells controlled by the plasticization of the PMMA matrix [24]. These mechanisms prevent the coalescence and the formation of an open cell structure.

On the other hand, foams produced at temperatures over 40° C present a closed cell structure. Saturation temperature has a great influence on the cellular structure of PMMA and 90/10 foams, with a significant change between 40° C and 70° C. Average cell size of neat PMMA foams vary from values close to one micron to a few microns, and cells of 90/10 PMMA/MAM foams increase their sizes from nanometric to micrometric range. On the contrary, the microcellular structure of neat MAM foams presents a noticeable thermal constancy; with no significant morphological changes between 40 and 70° C. A higher sensibility of the MAM foams to the temperature could be expected due to the lower glass transition temperature of their soft-block. This thermal stability during foaming is also related to the fast CO<sub>2</sub> diffusion after the pressure release. Loss of the CO<sub>2</sub> inside the developing cellular structure stops the cellular growing and coalescence due to the reduction of the internal pressure. Besides, loss of CO<sub>2</sub> solved into the polymer matrix increases the effective glass transition temperature of the polymer matrix, avoiding the cell growth

and coalescence. In conclusion, MAM foaming over 40° C is controlled by their quick CO<sub>2</sub> desorption, independently of the saturation temperature.

Focusing on PMMA and 90/10 PMMA/MAM foams, there is no obvious correlation between their variation of the cell size (figure 5) and density (figure 4). Increment of the cell size without a reduction of the density when the processing temperature is increased can be explained by two phenomena: the cell nucleation ratio can decrease due to the reduction of the CO<sub>2</sub> uptake and the coalescence of the cells due to the lower stiffness of the cell walls. In figure 6, 90/10 PMMA/MAM curve is not in between PMMA and MAM curves, this non linearity is a sign of the role of nano dispersed reservoirs acted by PBA objects.

As explained before, 90/10 PMMA/MAM blend presents a constant nucleation ratio independently of the processing conditions [24]. This constant nucleation ratio is controlled by the micelles volumetric density (about  $4 \times 10^{14}$  micelles/cm<sup>3</sup>). Therefore, by studying the evolution of the apparent cell nucleation density of these foams it will be possible to identify the presence, or not, of coalescence. Figure 7 shows the evolution of the apparent cell nucleation density of neat PMMA and 90/10 PMMA/MAM foams.

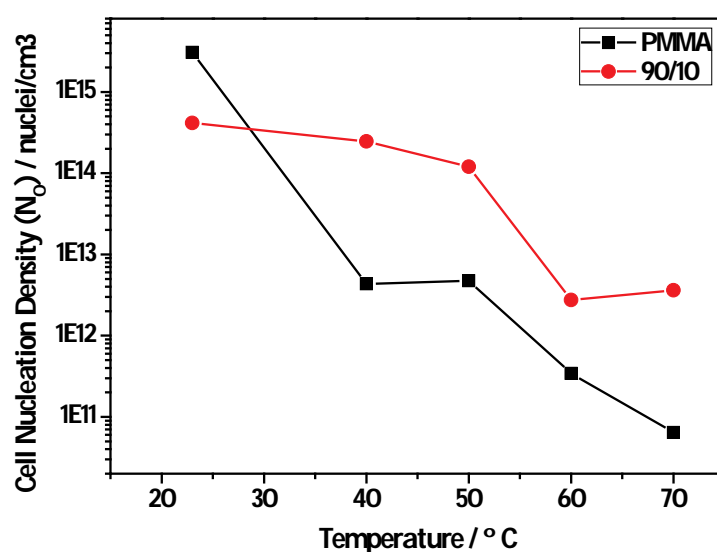


**Figure 7. Cell nucleation density of neat PMMA and 90/10 PMMA/MAM foams. Produced at 30 MPa and saturation temperatures between RT and 70° C.**

Cell nucleation density of 90/10 PMMA/MAM foams produced at RT ( $N_0 = 4.17 \times 10^{14}$ ) corresponds to the micelles density of this materials (heterogeneous cell nucleation), then, no coalescence happens at this temperature and this value can be taken as a reference value. Based on this reference it is possible to estimate the magnitude of the coalescence as the temperature is increased. At temperatures of 40° and 50°

Coalescence has a small influence, with an average value of 1.7 and 3.5 cells becoming one, respectively. However, at higher temperatures coalescence starts to have a strong effect, with more than 100 cells becoming one at temperatures of 60° and 70° C. Growing of the cells and therefore coalescence are controlled mainly by the properties of the PMMA matrix of the PMMA/MAM blends. A similar behavior can be expected in neat PMMA foams, with the supplementary effect of a homogeneous nucleation ratio variation depending upon the saturation temperature.

It can be concluded that 90/10 PMMA/MAM foams presents a significant thermal stability between saturation temperatures from room temperature to 50° C, allowing to obtain nanocellular foams with cell sizes below 300 nm in this range of temperatures. On the other hand, nanocellular foams can be produced from neat PMMA and MAM foams just at room temperature.

#### *Foaming mechanisms of PMMA/MAM blends*

According to the previous results it is possible to differentiate two foaming mechanisms for the neat PMMA and MAM, and PMMA/MAM blends in the range of temperatures studied. In the first one, with the saturation process carried out at room temperature, samples started to foam after being extracted of the pressure vessel. In the second one, with saturation temperatures over 40° C, samples foamed before being extracted of the pressure vessel. In addition, this variation of the foaming process involves important changes on the foams structure. Then, an explanation about this threshold in the foaming processes and schemes of the complete foaming process of PMMA/MAM blends, taking into account their particular nucleation behavior, is as follows.

Figure 8 shows the evolution of pressure and temperature during the depressurization process when the initial saturation temperature is either RT (23°C) or 40° C with an initial saturation pressure of 30 MPa. At these high pressure drop ratios the temperature of the vessel decreases during the process, and can reach values down to -30° C (from RT) or -10° C (from 40° C), eventually inducing vitrification of the material or even of some part of the micro phase separated system.



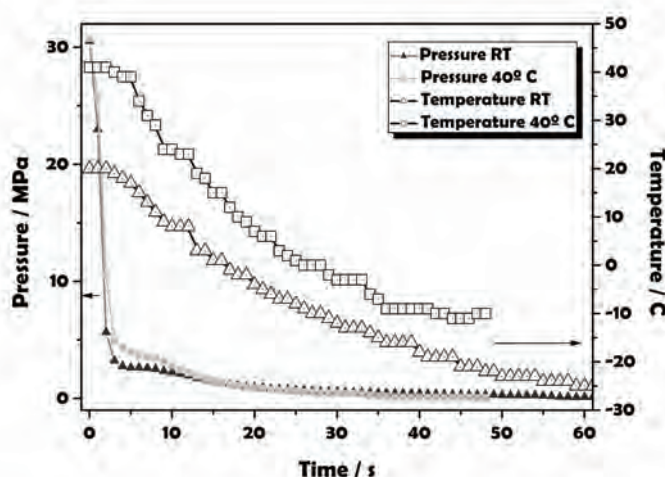


**Figure 8: Pressure and temperature evolution during the depressurization process. (Saturation pressure 30 MPa and saturation temperatures: RT and 40° C).**

Under CO<sub>2</sub> pressure, PMMA can be in the rubbery state at room temperature, even at saturation pressures lower than 30 MPa [15, 36-38], so it is expected that foaming takes place during the pressure release at saturation temperatures equal or higher to room temperature (batch foaming process). However, depending on the pressure release rates and the saturation temperatures used, the cooling of the system may limit foaming due to vitrification and quenching of cell growth (see Fig. 8 for temperature evolution).

An equivalent high pressure drop rate is used for all blends saturated at the same pressure (pressure is completely released in about one minute), but depending on the saturation temperature, samples may remain transparent ( $T_{sat} \leq RT$ ) when they are taken out of the pressure vessel, keeping nearly “all the CO<sub>2</sub> inside” and they will be foamed in a second stage by increasing the temperature. On the other hand, when the saturation temperature is higher ( $T_{sat} \geq 40^\circ\text{C}$ ) the foaming occurs during the pressure release. The temperature at which samples start to foam is not known, but this foaming is probably triggered near room temperature.

In both cases, it is expected that the cell nucleation, located in the micelles [24], occurs during the pressure release. Thus, the main difference between the two foaming processes lies in the cell growing controlled by the plasticization of the PMMA matrix [39]. Nuclei of samples saturated at room temperature cannot grow into cells until the samples reach an appropriate temperature (after the cooling due to the pressure release, some time is necessary after releasing pressure). On the other hand, nuclei in samples saturated at higher temperatures can grow just after, or during, the pressure release. Finally, both foaming processes are stopped when the CO<sub>2</sub> desorption from the polymer matrix increases the  $T_{g,ef}$  of the sample above the room temperature. Both mechanisms are shown in Figure 9.

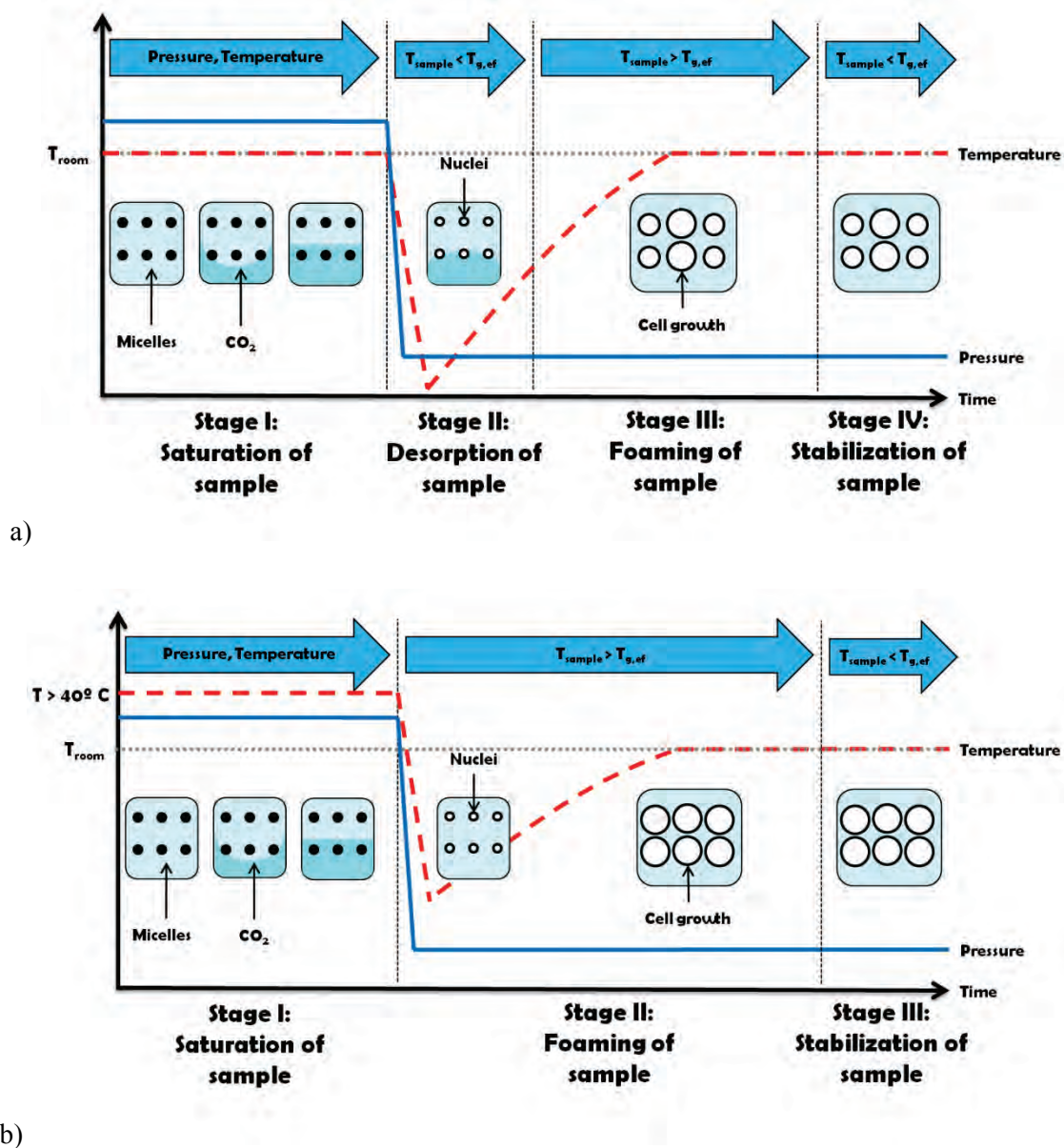


Figure 9: Foaming schemes / mechanisms for PMMA/MAM blend samples. a) With desorption stage due to the cooling of the system. b) Without desorption stage.

Presence of a desorption stage in the foaming process at room temperature explains the presence of solid skins in neat PMMA foams and the semi-solid skins in 90/10 PMMA/MAM foams found in previous work [39].

Foaming carried out at temperatures between RT and 40° C presents an intermediate behavior.



## Conclusions

Nanocellular and microcellular polymers from neat PMMA, neat MAM and a 90/10 PMMA/MAM blend have been produced by means of high-pressure CO<sub>2</sub> saturation process. The influence of the saturation temperature has been studied, allowing the description of two types of gas dissolution foaming processes in the range of temperatures studied. Significant differences in the foam structures were found between both processes. On one hand, foaming experiments carried out at room temperature allows obtaining nanocellular foams with different pore connectivity, open or semi-open cell structures are obtained from neat polymers, while well defined closed cell structures are obtained from the 90/10 PMMA/MAM blend. On the other hand, higher saturation temperatures produce microcellular foams from neat polymers and allow studying coalescence in 90/10 PMMA/MAM foams; and shows that cells of these foams hardly collapse, remaining nanocellular and with a small density variation from RT to 50° C. Moreover, the morphology of MAM based-foams showed remarkable thermal cell size and morphology stability from 40° to 70° C, with no cell size or density variations. On the other hand, PMMA present a high sensibility of their cell size upon saturation temperature on their cell size, but not on the density.

The role of PBA chains in the CO<sub>2</sub> sorption and desorption behavior of PMMA/MAM blends has been determined, leading to a better understanding of the foaming process. It was found that nanostructuration of the PBA block affects the CO<sub>2</sub> diffusion in PMMA/MAM blends. Co-continuous structures of PBA allow a higher diffusivity of the CO<sub>2</sub> out of the sample. On the other hand, isolated nanodomains of PBA surrounded by the PMMA matrix increase the CO<sub>2</sub> uptake without influence on the diffusivity.

### **Acknowledgements**

Financial assistance from MCINN (MAT2009-14001-C02-01 and MAT 2012-34901), the Junta of Castile and Leon (VA035U13), and FPU grant AP2008-03603 (J. Pinto) from the Spanish Ministry of Education is gratefully acknowledged. The help and expertise of Dr. Etienne Gontier, Dr. Soizic Lacampagne and Dr. Melina Petrel (BIC, Université Bordeaux Segalen) is indeed acknowledged for TEM observations and samples preparation.

## References

- [1] M. Ulbricht, Advanced functional polymer membranes, *Polymer*, 47 (2006) 2217-2262.
- [2] D. Schmidt, V.I. Raman, C. Egger, C. du Fresne, V. Schädler, Templated cross-linking reactions for designing nanoporous materials, *Materials Science and Engineering: C*, 27 (2007) 1487-1490.
- [3] J. Pinto, E. Solórzano, M.A. Rodriguez Perez, M. Dumon, Thermal Conductivity Transition Between Microcellular and Nanocellular Polymeric Foams: Experimental Validation of the Knudsen Effect, in: *SPE FOAMS 2012 Conference*, Barcelona (Spain), 2012.
- [4] M.A. Hillmyer, Nanoporous materials from block copolymer precursors, in: *Block Copolymers II*, Springer, 2005, pp. 137-181.
- [5] H.P. Hentze, M. Antonietti, Porous polymers and resins for biotechnological and biomedical applications, *Reviews in molecular biotechnology*, 90 (2002) 27-53.
- [6] E.A. Jackson, M.A. Hillmyer, Nanoporous membranes derived from block copolymers: From drug delivery to water filtration, *ACS nano*, 4 (2010) 3548-3553.
- [7] J.L. Hedrick, K.R. Carter, J.W. Labadie, R.D. Miller, W. Volksen, C.J. Hawker, D.Y. Yoon, T.P. Russell, J.E. McGrath, R.M. Briber, Nanoporous polyimides, in: *Progress in Polyimide Chemistry II*, Springer, 1999, pp. 1-43.
- [8] M.J. Madou, *Fundamentals of Microfabrication: The Science of Miniaturization*, Second Edition, CRC, Boca Raton, 2002.
- [9] Y. Dong Hwang, S. Woon Cha, The relationship between gas absorption and the glass transition temperature in a batch microcellular foaming process, *Polymer Testing*, 21 (2002) 269-275.
- [10] P. Alessi, A. Cortesi, I. Kikic, F. Vecchione, Plasticization of polymers with supercritical carbon dioxide: Experimental determination of glass-transition temperatures, *Journal of Applied Polymer Science*, 88 (2003) 2189-2193.
- [11] Z. Zhang, Y.P. Handa, An in-situ study of plasticization of polymers by high-pressure gases, *Journal of Polymer Science Part B: Polymer Physics*, 36 (1998) 977-982.
- [12] I. Tsivintzelis, A.G. Angelopoulou, C. Panayiotou, Foaming of polymers with supercritical CO<sub>2</sub>: An experimental and theoretical study, *Polymer*, 48 (2007) 5928-5939.

- [13] J.A. Reglero Ruiz, P. Viot, M. Dumon, Microcellular foaming of polymethylmethacrylate in a batch supercritical CO<sub>2</sub> process: Effect of microstructure on compression behavior, *Journal of Applied Polymer Science*, 118 (2010) 320-331.
- [14] V. Kumar, N.P. Suh, A process for making microcellular thermoplastic parts, *Polymer Engineering & Science*, 30 (1990) 1323-1329.
- [15] A.V. Nawaby, Y.P. Handa, X. Liao, Y. Yoshitaka, M. Tomohiro, Polymer–CO<sub>2</sub> systems exhibiting retrograde behavior and formation of nanofoams, *Polymer international*, 56 (2007) 67-73.
- [16] B. Krause, R. Mettinkhof, N.F.A. Van der Vegt, M. Wessling, Microcellular foaming of amorphous high-T<sub>g</sub> polymers using carbon dioxide, *Macromolecules*, 34 (2001) 874-884.
- [17] D. Miller, P. Chatchaisucha, V. Kumar, Microcellular and nanocellular solid-state polyetherimide (PEI) foams using sub-critical carbon dioxide I. Processing and structure, *Polymer*, 50 (2009) 5576-5584.
- [18] D. Miller, V. Kumar, Microcellular and nanocellular solid-state polyetherimide (PEI) foams using sub-critical carbon dioxide II. Tensile and impact properties, *Polymer*, 52 (2011) 2910-2919.
- [19] S. Siripurapu, J.M. DeSimone, S.A. Khan, R.J. Spontak, Controlled foaming of polymer films through restricted surface diffusion and the addition of nanosilica particles or CO<sub>2</sub>-philic surfactants, *Macromolecules*, 38 (2005) 2271-2280.
- [20] S. Costeux, L. Zhu, Low density thermoplastic nanofoams nucleated by nanoparticles, *Polymer*, 54 (2013) 2785-2795.
- [21] S. Costeux, H. Jeon, S. Bunker, I. Khan, Nanocellular foams from acrylic polymers: Experiments and modeling, in: *SPE FOAMS 2012 Conference*, Barcelona, Spain, 2012.
- [22] P. Spitael, C.W. Macosko, R.B. McClurg, Block copolymer micelles for nucleation of microcellular thermoplastic foams, *Macromolecules*, 37 (2004) 6874-6882.
- [23] T. Shinkai, M. Ito, K. Sugiyama, K. Ito, H. Yokoyama, Ordered and foam structures of semifluorinated block copolymers in supercritical carbon dioxide, *Soft Matter*, 8 (2012) 5811-5817.
- [24] J. Pinto, M. Dumon, M. Pedros, J.A. Reglero, M.A. Rodriguez-Perez, Nanocellular CO<sub>2</sub> foaming of PMMA assisted by block copolymer nanostructuration, *Chemical Engineering Journal*, 243C (2014) 428-435.
- [25] S. Costeux, S.P. Bunker, H.K. Jeon, Homogeneous nanocellular foams from styrenic-acrylic polymer blends, *Journal of Materials Research*, 28 (2013) 2351-2365.

- [26] B. Aher, N.M. Olson, V. Kumar, Production of bulk solid-state PEI nanofoams using supercritical CO<sub>2</sub>, *Journal of Materials Research*, 28 (2013) 2366-2373
- [27] J.A. Reglero Ruiz, M. Dumon, J. Pinto, M.A. Rodriguez-Pérez, Low-Density Nanocellular Foams Produced by High-Pressure Carbon Dioxide, *Macromolecular Materials and Engineering*, 296 (2011) 752-759.
- [28] J.A.R. Ruiz, M. Pedros, J.-M. Tallon, M. Dumon, Micro and nano cellular amorphous polymers (PMMA, PS) in supercritical CO<sub>2</sub> assisted by nanostructured CO<sub>2</sub>-philic block copolymers – One step foaming process, *The Journal of Supercritical Fluids*, 58 (2011) 168-176.
- [29] M. Dumon, J.A. Reglero Ruiz, J. Pinto Sanz, M.A. Rodriguez Perez, J.M. Tallon, M. Pedros, E. Cloutet, P. Viot, Block Copolymer-Assisted Microcellular Supercritical CO<sub>2</sub> Foaming of Polymers and Blends, *Cellular polymers*, 31 (2012) 207-222.
- [30] L. Lalande, C.J.G. Plummer, J.-A.E. Manson, P. Gérard, The influence of matrix modification on fracture mechanisms in rubber toughened polymethylmethacrylate, *Polymer*, 47 (2006) 2389-2401.
- [31] L. Lalande, C.J.G. Plummer, J.-A.E. Manson, P. Gérard, Microdeformation mechanisms in rubber toughened PMMA and PMMA-based copolymers, *Engineering fracture mechanics*, 73 (2006) 2413-2426.
- [32] J. Pinto, E. Solórzano, M.A. Rodriguez-Perez, J.A. de Saja, Characterization of the cellular structure based on user-interactive image analysis procedures, *Journal of Cellular Plastics*, 49 (2013) 555-575.
- [33] M.D. Abràmoff, P.J. Magalhães, S.J. Ram, Image processing with ImageJ, *Biophotonics international*, 11 (2004) 36-42.
- [34] S. Hilic, S.A.E. Boyer, A.A.H. Pádua, J.-P.E. Grolier, Simultaneous measurement of the solubility of nitrogen and carbon dioxide in polystyrene and of the associated polymer swelling, *Journal of Polymer Science Part B: Polymer Physics*, 39 (2001) 2063-2070.
- [35] F. Rindfleisch, T.P. DiNoia, M.A. McHugh, Solubility of polymers and copolymers in supercritical CO<sub>2</sub>, *The Journal of Physical Chemistry*, 100 (1996) 15581-15587.
- [36] S.K. Goel, E.J. Beckman, Generation of microcellular polymers using supercritical CO<sub>2</sub>, *Cellular polymers*, 12 (1993) 251-274.
- [37] Y.P. Handa, Z. Zhang, A new technique for measuring retrograde vitrification in polymer–gas systems and for making ultramicrocellular foams from the retrograde phase, *Journal of Polymer Science Part B: Polymer Physics*, 38 (2000) 716-725.

[38] P.D. Condo, I.C. Sanchez, C.G. Panayiotou, K.P. Johnston, Glass transition behavior including retrograde vitrification of polymers with compressed fluid diluents, *Macromolecules*, 25 (1992) 6119-6127.

[39] J. Pinto, S. Pardo, E. Solórzano, M.A. Rodríguez-Pérez, M. Dumon, J.A. de Saja, Solid Skin Characterization of PMMA/MAM Foams Fabricated by Gas Dissolution Foaming over a Range of Pressures, *Defect and Diffusion Forum*, 326-328 (2012) 434-439.



## IV.2 Influence of the foaming temperature and post-foaming on the morphology and density of PMMA/MAM foams

The study of the influence of the foaming temperature on the properties of PMMA/MAM foams was carried out with samples that hold nearly all the CO<sub>2</sub> inside after the pressure release. Thus, samples of 90/10 and 80/20 PMMA/MAM foams were selected.

In order to obtain saturated samples with high levels of CO<sub>2</sub> uptake the samples were saturated at the maximum pressure (30 MPa) and low temperatures (between RT and 50° C). The foaming or post-foaming temperature (in a second step) was controlled with a thermostatic water bath, in which the samples were introduced after being extracted of the pressure vessel (about 3 minutes from the beginning of the pressure release).

First, the foaming stage was carried out on samples saturated at RT (presenting desorption stage) at temperatures between 60° and 90° C, during times in general between 60 and 180 seconds. Samples foamed at 70° C were studied also at foaming times of 15 and 30 seconds. The maximum foaming time, 180 seconds, was fixed due to the absence of gas diffusion out of the sample at this time. At lower times gas bubbles appears on the water bath from the gas diffusion out of the sample; therefore, the absence of bubbles/gas diffusion implies that no more gas is contained inside the sample, and the cells growth process has finished.

Density evolution of the 90/10 PMMA/MAM samples with the foaming temperature and time is shown in Figure IV.1. Taking into account that the relative density of 90/10 foams produced at RT is about 0.44 we found that no density reductions are obtained at any conditions. Best results, just a small density increase, are found for the lower temperatures (60° and 70° C) at times between 60 and 120 seconds.

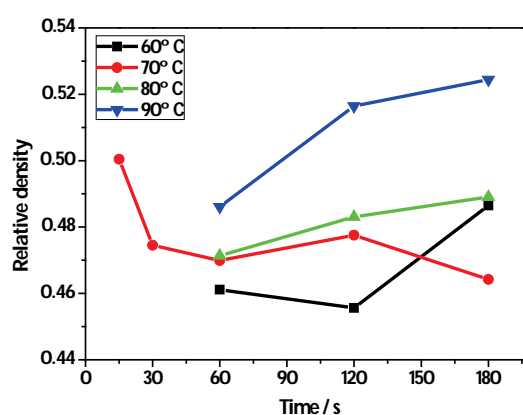


**Figure IV.1: Relative density of 90/10 PMMA/MAM foams at different foaming temperatures and times. Saturation stage: 30 MPa and RT.**

80/20 PMMA/MAM foams produced at RT present a relative density near 0.41. Results from the 80/20 foaming at higher temperatures can be found on Figure IV.2; in this case, significant density increments are found in the entire range of temperatures and times studied. Rather in contradiction to the density of 90/10 system the general tendency is an increase of density with time and temperature: there is no sign of asymptotic behavior.

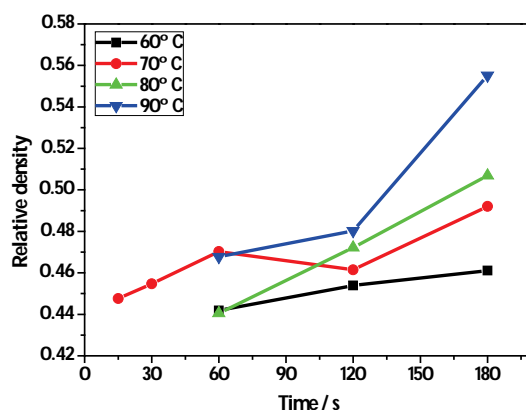


**Figure IV.2: Relative density of 80/20 PMMA/MAM foams at different foaming temperatures and times.**  
**Saturation stage: 30 MPa and RT.**

In general, the density values (0.44 to 0.55) present small differences between adjacent temperatures and times. These small differences may be within the experimental error, and then it is difficult to obtain clear conclusions from these results. However, it seems that the lower densities can be obtained using the lower foaming temperature (and low-intermediate foaming times). More experiments at lower temperatures (below 60° C) should be done trying to find better foaming conditions, which allow decreasing the density.

#### IV.2.1 Post-foaming vs. two-step foaming

Previous results were obtained by a foaming process –saturation at RT– with a desorption stage (as the solid state foaming process, see Chapter I II), therefore the samples were extracted from the pressure vessel in solid state and foamed at the selected temperatures and times.

On the contrary, samples saturated at higher temperatures (40° and 50° C) do not present a desorption stage (as the batch foaming process, see Chapter III); and the foaming stage happens just after the pressure release, being the samples already foamed when they are extracted from the pressure vessel. In this case, some samples were nevertheless subjected to a post-foaming step into the thermostatic water bath to establish some initial trends about the possibility of reducing the density by this method.

Samples of 90/10 and 80/20 PMMA/MAM blends were produced at a saturation pressure of 30 MPa and saturation temperatures of 40° C and 50° C. Then, the post-foaming stage was carried out at 70° C during 120 seconds.

Table IV-1 shows the relative densities of 90/10 and 80/20 foams saturated at 30 MPa and 40°/50° C, with and without post-foaming stage.

**Table IV-1. Relative densities of PMMA/MAM foams with and without post-foaming. Saturation stage: 30 MPa and 40°/50° C. Post-foaming stage: 70° C and 120 seconds**

PMMA/MAM	40° C	40° C + PF	50° C	50° C + PF
90/10	0.41	0.39	0.40	0.40
80/20	0.52	0.48	0.60	0.48

Foams produced from 80/20 present a rather significant density reduction due to the post-foaming (about 10-20 %); even so, density of the post-foamed foams is higher than the density of the 80/20 foams produced with the saturation stage carried out at RT. Therefore, this strategy is not able to produce 80/20 foams with lower relative densities than those produced by saturating at RT.

On the contrary, small density reductions (about a 5%) are found in 90/10 samples saturated at 40° C and post-foamed. While no differences between post-foamed and non post-foamed samples can be found in 90/10 samples saturated at 50° C.

Then, the best result obtained by post-foaming was a 5% density reduction on 90/10 PMMA/MAM nanocellular foams. Taking into account the results of the previous study, maybe lower post-foaming temperatures and/or times can produce lower densities.

#### IV.2.2 Comparison of PMMA and PMMA/MAM post-foaming

In order to understand the difficulties found in the reduction of the density of nanocellular PMMA/MAM foams, neat PMMA was subjected to the same processing conditions as the lowest density previously obtained. PMMA samples were saturated at 30 MPa and 40° C, and post-foamed at 70° C during 120 seconds. Surprisingly, neat PMMA samples present a density decrease of about 55 % , from a relative density of **0.47** (before post-foaming) to a relative density of **0.21** (after post-foaming).

Then, a study of the cellular structure of neat PMMA and 90/10 PMMA/MAM foams, produced at 30 MPa/40° C and with or without post-foaming at 70° C during 120 seconds, was carried out. SEM images obtained from these foams are shown in Figure IV.3.

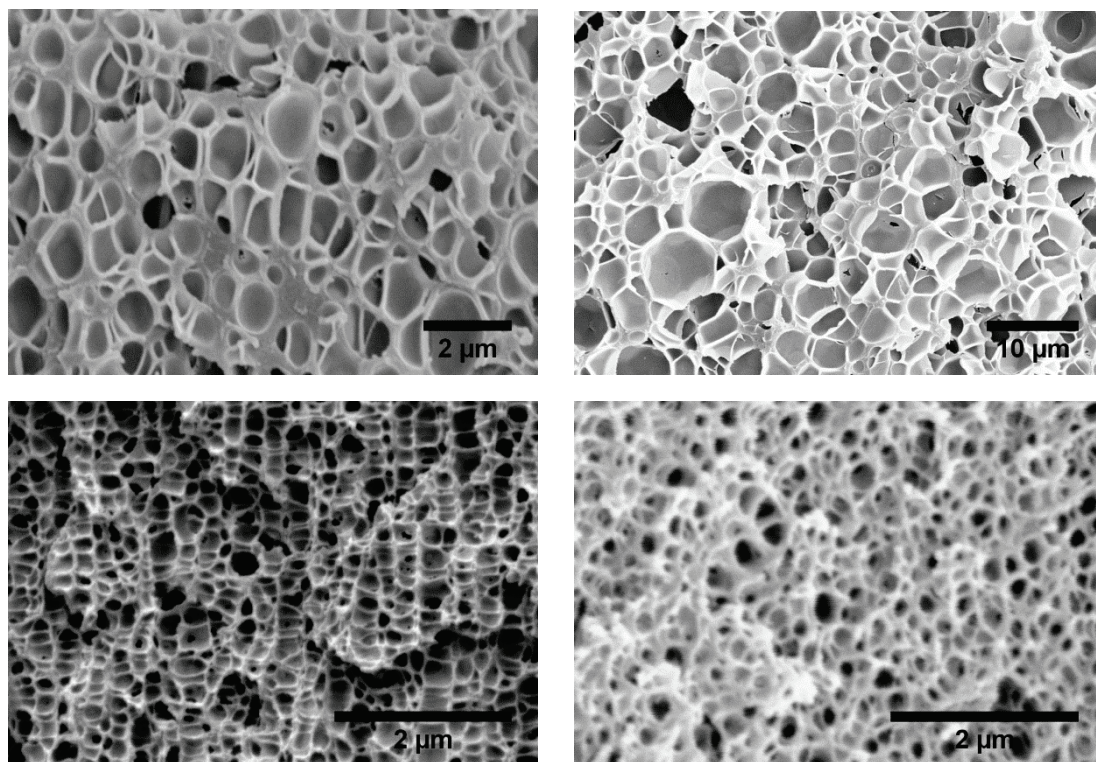


**Figure IV.3: SEM micrographs of neat PMMA (up) and 90/10 PMMA/MAM (down) foams. Saturation stage: 30 MPa and 40° C. Post-foaming: none (left) and 70° C during 120 seconds (right)**

Neat PMMA foams increased their average cell size from 0.75 to 3.14 μm due to the post-foaming (in terms of the cells average volume, this represents an increase of 73 times). Distribution of the cell size of these foams is shown on Figure IV.4.

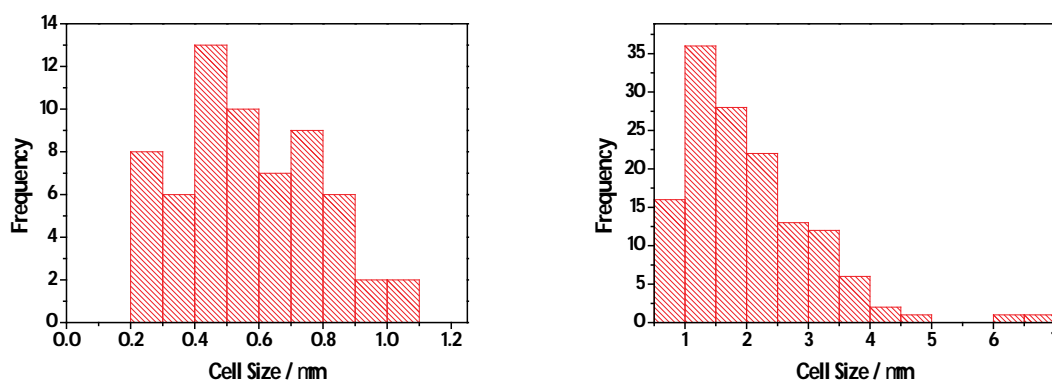


**Figure IV.4: Cell size distribution of neat PMMA foams produced at 30 MPa and 40° C. Before (left) and after the post-foaming (right).**

Along with the increase in the average cell size it is also observed that the cell size distribution becomes wider, resulting in a less homogeneous cellular structure. Moreover, their apparent cell nucleation density decreases 23 times from  $5.21 \times 10^{12}$  to  $2.31 \times 10^{11}$  nuclei/cm<sup>3</sup> ( $N_o$ , cells nuclei per cubic centimeter of the

unfoamed material; see the journal article included in this chapter for more details). Therefore, due to the coalescence 23 cells converge in one on average during the post-foaming. In addition to the coalescence the cells should increase their volume about 3 times more to reach their final volume. This cell volume increment corresponds to the macroscopic relative density reduction of the foam from 0.47 to 0.21.

On the other hand, 90/10 PMMA/MAM foams presents small changes. Their average cell size is increased by the post-foaming from 210 to 220 nm, while their cell nucleation density remains practically constant from  $3.03 \times 10^{14}$  to  $2.71 \times 10^{14}$  nuclei/cm<sup>3</sup>. Thus, no significant influence of the post-foaming process on the cell size distribution can be found on these foams (Figure IV.5). 90/10 foams present the advantage that no coalescence is induced by the post-foaming. However, also no significant expansion is obtained; the average cell volume is only increased 1.15 times, corresponding to the small relative density reduction found in these foams.

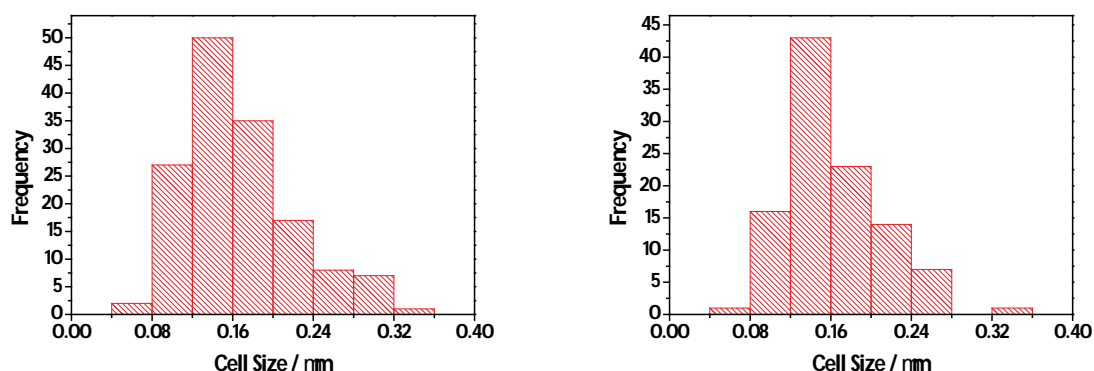


**Figure IV.5: Cell size distribution of 90/10 PMMA/MAM foams produced at 30 MPa and 40° C. Before (left), and after (right) the post-foaming.**

A possible explanation of the different post-foaming behavior between neat PMMA and 90/10 PMMA/MAM can be found in the thickness of their cell walls. Cell walls of PMMA foams have thickness in the order of hundreds of nanometers, while 90/10 cell walls present thicknesses of about tens of nanometers. That difference allows a faster CO<sub>2</sub> diffusion out of the cell walls in the 90/10 foams, resulting in a quick decrease of the PMMA matrix plasticization that stops the cells growth.

### IV.3 Conclusions

As a conclusion of this chapter, we found that the cellular structure of neat PMMA and MAM foams present a clear threshold between RT and 40° C as saturation temperatures. Both materials presented a nanocellular structure when the saturation stage was carried out at RT, whereas at higher temperatures microcellular structures were obtained. In addition, the density of neat PMMA foams remained rather constant for the entire range of saturation temperatures studied, while the density of neat MAM foams presents once again a threshold between RT and 40° C as saturation temperatures. Neat MAM foams presented relative densities about 0.45 at RT and about 0.2 at temperatures over 40° C.

On the contrary, we have observed that there is a small effect of the saturation and foaming temperatures of PMMA/MAM blends with low MAM amounts on the final foam density. Also there is a small incidence of coalescence for these foams, which is a consequence of the nanocellular structure. Variation of the saturation temperature only provides a density decrease of about 10 % keeping the nanocellular structure, whereas no density decrease is obtained by modifying the foaming temperature in the range studied, and post-foaming process can decrease the density just a 5 % keeping the nanocells. Foaming and post-foaming parameters could be improved, but the results obtained comparing the post-foaming effects on 90/10 PMMA/MAM nanocellular foams with the effects on neat PMMA microcellular foams show that, even optimizing these parameters, no significant density reductions can be expected, due to the quick CO<sub>2</sub> diffusion out of the thick cell walls of nanocellular foams.

A possible strategy to avoid early CO<sub>2</sub> diffusion could be carrying out a foaming or post-foaming stage in a CO<sub>2</sub>-rich environment. For instance, after the saturation stage at 30 MPa the pressure release can be stopped at 5-10 MPa. Pressure difference between the sample and the environment may be enough to induce the cell nucleation on the PBA domains and promote the cells growth. Then, the temperature could be increased to a post-foaming temperature and the remaining pressure released to promote cell growth.

By selecting an appropriate combination of the remaining CO<sub>2</sub> pressure and the post-foaming temperature (inside the pressure vessel, just after the pressure release) the PMMA matrix could be maintained in the rubbery state, and perhaps nanocellular foams with lower densities could be obtained.



***Chapter V:***  
***Transition between microcellular and  
nanocellular foams; consequences  
on mechanical and thermal  
properties***



## Chapter V. Transition between microcellular and nanocellular foams; consequences on mechanical and thermal properties

As explained in the introduction chapter it is expected that nanocellular foams will present improved properties compared to conventional ones [1-5]. Although the main focus of this research work is to understand the phenomena leading to nanocellular PMMA-based structures induced by block copolymer and gas dissolution foaming, a study was also performed on the evolution of some properties when the cells are modified from the micrometric to the nanometric scale. In particular, the system under study, PMMA/MAM blends, is very convenient for this purpose because as we have seen in the previous chapters by modifying the processing conditions it is possible to produce nanocellular and microcellular materials with similar composition and density.

In particular, the influence of the cell size is presented on the following characteristics *i*) the Young's modulus (measured by a three-point bending DMA test), *ii*) glass transition temperature ( $T_g$ ) of the polymer matrix, and *iii*) thermal conductivity of the foams.

Earlier indications of this influence on the Young's modulus and on the glass transition temperature were shown on the article published in **Macromolecular Materials and Engineering** **296 (2011)**, entitled ***“Low-Density Nanocellular Foams Produced by High-Pressure Carbon Dioxide”***. In this article the first PMMA/MAM nanocellular foams obtained were presented. They were produced from a 90/10 PMMA/MAM blend at room temperature (RT) and different pressures between 10 and 30 MPa.

Focusing on the properties, the article suggests that the low thickness of the pore walls, near or below 100 nm, leads to a reduction of the PMMA chains mobility; resulting in an increment of  $T_g$  of the PMMA/MAM nanocellular foams in comparison with the solid material.

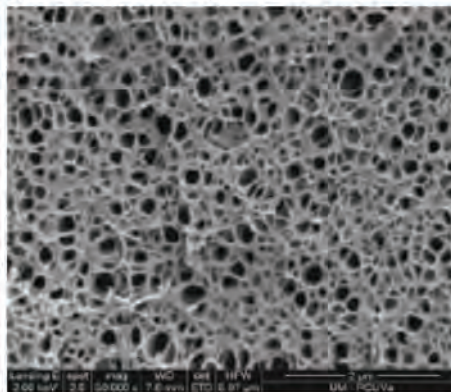
Next, a mechanical characterization is presented. 90/10 PMMA/MAM foams are studied by DMA three-point bending, to measure their Young's modulus ( $E$ ). It is shown that 90/10 PMMA/MAM foams present higher values of  $E$  than experimental results for conventional PMMA foams from the literature [3].

Both studies, about  $T_g$  and  $E$ , are continued and extended in sections V.1 and V.2 of chapter V, after the included article. In addition, results about the thermal conductivity are included in section V.3.

# Low-Density Nanocellular Foams Produced by High-Pressure Carbon Dioxide

Jose Antonio Reglero Ruiz,\* Michel Dumon, Javier Pinto,  
Miguel Angel Rodriguez-Pérez

A new type of nanocellular polymeric material based on PMMA and a MAM triblock copolymer is presented. The production avoids the use of physical additives and leads to completely homogeneous nanostructured polymers with a large number of CO<sub>2</sub> nucleation sites. The foamed materials show average cell sizes <200 nm and relative foam densities of 0.4, presenting a homogeneous cell structure. A physical effect not measured before in nanocellular materials is demonstrated, which leads to an increase of the glass transition temperature due to the confining effect of PMMA chains in the cell walls of the nanocellular foam. The effects of changing saturation pressure and MAM content in the cellular structure are described, together with three-point bending Young's modulus measured using DMA.



## Introduction

In the last years, the use of supercritical carbon dioxide (scCO<sub>2</sub>) to produce microcellular materials has greatly increased.<sup>[1,2]</sup> Foams with cell sizes in the microcellular range (from 1 to 100 μm) have been fabricated using classical or commodity amorphous polymers such as polystyrene (PS) and poly(methyl methacrylate) (PMMA), leading to excellent

results in thermal and mechanical properties.<sup>[3,4]</sup> Reducing cell size down to nanocellular range (i.e., below 1 μm) has become one of the most important objectives in this area of materials science, due to the improvement in several mechanical properties such as impact energy absorption and compression strength.<sup>[5]</sup> In addition, a nanocellular foam based on amorphous polymers presents two specific properties which could be extremely interesting in several applications in the construction, packaging, automotive and aerospace sectors.<sup>[6]</sup> First, a well-defined nanocellular foam based in amorphous polymers such as PMMA and PS could present transparency, a key factor for using these materials in a significant number of applications in which good mechanical properties, reduced density and transparency are essential. Secondly, when reducing the cell size below 50 nm, the contribution of the gas to the thermal conductivity can be neglected due to the Knudsen effect, which is a consequence of the low vibration of the gas molecules in

J. A. Reglero Ruiz, M. Dumon  
Laboratoire de Chimie de Polymères Organiques, LCPO Institute  
Polytechnique de Bordeaux – IPB16, Avenue Pey Berland, Pessac  
33607, France  
E-mail: jareglero@gmail.com  
J. Pinto, M. A. Rodriguez-Pérez  
Cellular Materials Laboratory (CellMat), Condensed Matter  
Physics Department School of Sciences, University of Valladolid C/  
Prado de la Magdalena, s/n, Valladolid 47010, Spain



such a low range of cell sizes.<sup>[7]</sup> This would allow producing cellular materials with thermal conductivities much lower than those of the best foams used nowadays for thermal insulation. However obtaining these types of materials is not a simple task because thermodynamics does not favor small nuclei, leading to a huge increment of the interfacial (surface) area and interfacial (surface) free energy.

Obviously, these materials would present a combination of properties not found before, creating a new generation of cellular polymer materials. Although several efforts have been developed in this topic, a well-defined homogeneous nanocellular structure has not been achieved using  $\text{ScCO}_2$  as blowing agent. For example, foaming of amorphous polymers adding small amounts of additives, mainly clay nanoparticles, has been carried out. These particles play a multifunctional role acting as nucleating agents, improving the melt strength and cellular structure, increasing the thermal stability and the mechanical properties.<sup>[8]</sup> Furthermore, a very good dispersion and exfoliation of the nanoclays is needed. For this reason, complex chemical treatments are necessary to modify the nanoclay before the dispersion and exfoliation into the polymer matrix. This procedure permits the production of microcellular foams with cell sizes in the range of 2–20  $\mu\text{m}$ , together with densities reductions compared to solid material up to 50%.<sup>[9,10]</sup> From a different point of view, nanocellular porous structures have been fabricated using as base polymers block copolymers (BCPs) with  $\text{CO}_2$  philic blocks, specially a fluorinated block or a methacrylate block and  $\text{CO}_2$  as blowing agent.<sup>[11,12]</sup> Following this strategy, a preliminary polymer synthesis is carried out, by means of sequential anionic polymerization, to produce a diblock copolymer, e.g., formed by an amorphous PS block and a perfluorinated (PFMA) or methacrylate block (PMMA). In both cases, defined closed cell porous nanostructures have been produced. However, there are several important limitations in this procedure. First, foaming process is only achieved on thin film samples, with thickness below 200  $\mu\text{m}$ , which makes the analysis of thermal and mechanical properties difficult. Second, a rather long and nontrivial chemical synthesis is needed to produce the  $\text{CO}_2$ -philic diblock fluoropolymers, which involves the use of several monomers under well-controlled synthesis conditions. Finally, using this method only small density reductions have been reached [relative foam density (i.e., density of the foam divided by the density of the solid material) ( $\rho_r$ ) values are above 0.8], which limits greatly the range of applications of these materials. Other approximation was based on the foaming of PMMA ultra-thin films using as surface confinement for  $\text{CO}_2$  nanosilica particles.<sup>[13]</sup> In this system, average cell size values obtained are close to 1  $\mu\text{m}$ , but a limitation in the density reduction is also found ( $\rho_r > 0.7$ ), together with the low thickness of the samples investigated. These materials were closed-cell foams.

Parallel to these investigations, the development in the study of BCPs has reached a well recognized status. These copolymers can be structured at an appropriate scale, usually less than 1  $\mu\text{m}$ , and local segregation of the different polymer blocks leads to molecular scale aggregates of nanometer size.<sup>[14,15]</sup> A lot of diblock and triblock copolymers present self-assembly in the nanoscale range, offering different distribution possibilities depending of the relative chain length and proportion of each block (e.g., commercial copolymers based on PS and PMMA units).<sup>[16]</sup> One of the most important application is focused in the use of these nanostructured copolymers as additives in several polymer matrixes. The addition of small proportions of diblock or triblock copolymers lead to nanostructured materials in which the additive is dispersed at a nanometric scale depending on the mixing conditions, the additive quantity and the chemical composition of matrix and copolymer.

In this study, we show a completely new generation of nanocellular polymer materials, which overcome most of the problems and difficulties exposed previously. We have been able to fabricate, by using supercritical  $\text{CO}_2$  as blowing agent, nanocellular foams with physical characteristics not achieved before. The materials obtained in this work combine a homogeneous and well-defined open cell nanocellular structure, together with a great density reduction ( $\rho_r \approx 0.4$ ). In addition, the raw materials used are commercial polymers and due to this reason the fabrication process of the starting materials is extremely simple, based on blending and extrusion of polymers, leading to samples with an adequate size to characterize mechanical, thermal and acoustic properties, avoiding the problems of working with thin films samples. The extrusion process provides a homogeneous nanostructured network, and no dispersion or aggregation problems which are often presented when using nanoclays as nucleating agents, were observed. The nanocellular structure obtained is directly related to the nanostructuring of the polymeric matrix, derived from the use of a triblock copolymer, [poly(methyl methacrylate)-*block*-poly(butyl acrylate)-*block*-poly(methyl methacrylate), MAM] as an additive in an amorphous PMMA matrix. The nanostructured matrix was foamed using  $\text{ScCO}_2$  in a batch single-step process, then analyzing the average cell size and the foam cell morphology.

## Experimental Part

### Materials

Transparent PMMA was kindly supplied by Altuglas-Arkema Company (France), in the form of pellets. The PMMA chosen contains nearly no additive in order not to extract any additive during the  $\text{CO}_2$  uptake. A transparent MAM triblock terpolymer with 35 wt.-% methacrylate/30 wt.-% butylacrylate/35 wt.-% methacrylate was supplied by Arkema company (France) in the



form of pellets. The physical properties of the polymers employed were as follows: glass transition temperature ( $T_g$ ) midpoint value of PMMA homopolymer was 112 °C, with values of +119 and -49 °C for the methacrylate and butyl acrylate blocks in the MAM triblock copolymer, respectively. The weight-average molar mass of PMMA was  $\bar{M}_w = 85\,000\text{ g}\cdot\text{mol}^{-1}$ , with values of 90 000 and 70 000  $\text{g}\cdot\text{mol}^{-1}$  for the methacrylate and butyl acrylate blocks in the MAM triblock copolymer, respectively. Details of production of both PMMA and MAM polymers can be found elsewhere.<sup>[17,18]</sup>

Polymer blends were produced as follows. Both materials, PMMA and MAM, were dried in vacuum (680 mm Hg), at 80 °C during 4 h before processing. Mixing and extrusion were carried out using a Scamex CE02 single-screw extruder ( $L/D = 28$ ), with a temperature profile from 165 to 225 °C, at a screw speed of 60 rpm, in the desired proportion. Pellets were produced using a continuous cutting machine operating at the end of the line at a constant speed of 240 rpm.

In a second step, pellets produced were injected into pieces ( $50 \times 15\text{ mm}^2$ ) with 3 mm thickness, using a small scale injection molding machine developed by DSM Xplore. The working temperature was fixed at 240 °C, whereas mold temperature was set at 60 °C. The injection pressure was fixed at 1 MPa. Transparent samples obtained showed a good surface appearance as well as a good injection behavior, with no presence of air bubbles inside the parts.

### Foaming Experiments

Foaming experiments were carried out in a high pressure reactor provided by TOP Industry (France), with a capacity of 300  $\text{cm}^3$  and capable of operating at maximum temperature of 250 °C and maximum pressure of 40 MPa. The reactor is equipped with an accurate pressure pump controller provided by Teledyne ISCO, and controlled automatically to keep the temperature and pressure at the desired values. The  $\text{CO}_2$  vessel temperature and pressure were monitored in the course of the process. Thus a collection of experiments were performed in a single-step batch process. Samples were saturated at different pressures, from 10 to 30 MPa, at room temperature during 16 h to assure an equilibrium dissolution of  $\text{CO}_2$  in the polymer. After the saturation process, foaming was carried out by releasing the pressure inside the reactor at a constant depressurization rate of 15  $\text{MPa}\cdot\text{min}^{-1}$ . Foamed samples were extracted from the reactor and the foam structure was fixed in an ice-water bath.

### Characterization

Foam density  $\rho_f$  was determined by water-displacement method, based on Archimedes' principle. At least three measurements were carried out for each sample produced.

The nanostructure of the solid material was analyzed by high-resolution scanning electron microscopy (model JEOL JSM 6700F), treating previously the samples with  $\text{RuO}_4$  vapor for 150 min. The cellular structure in foamed samples was analyzed by means of scanning electron microscopy (SEM, model HITACHI S-3000N). In this case, foams were frozen in liquid nitrogen and fractured to assure that the microstructure remained intact. Surfaces were

coated with gold using a sputter coater (model EMScope SC 500), in argon atmosphere. The micrographs obtained were analyzed to measure cell sizes. The cell size  $\phi$  was obtained from direct observation, using a minimum of 100 cells in each calculation, whereas the cell density  $N_c$  ( $\text{cells}\cdot\text{cm}^{-3}$ ) was calculated according to<sup>[19]</sup>

$$N_c \cong \left( \frac{nM^2}{A} \right)^{3/2} \quad (1)$$

where  $n$  is the number of cells observed in a SEM micrograph,  $A$  the area of the micrograph in  $\text{cm}^2$  and  $M$  is the magnification factor.

Dynamical mechanical analysis (DMA) was performed using a Mettler DMA instrument (model DMA-861e), working in three-point bending, to evaluate Young's modulus. All tests were carried out at room temperature at a frequency of 1 Hz.

## Results and Discussion

### Analysis of the PMMA/MAM (90/10) blend

Blends of PMMA containing 10 wt.-% of MAM were prepared using a single-screw extrusion machine (see Experimental Part), then injection molding provides bulk nanostructured PMMA. Figure 1 shows a high-resolution SEM image of an injected sample obtained after a staining with  $\text{RuO}_4$ . As it can be observed, the addition of 10 wt.-% of MAM into the PMMA matrix leads to a nanostructured polymer. In the self-assembly process, methacrylate blocks are miscible into the PMMA matrix, and butyl acrylate groups appear as short worm-like micelles which are short enough to avoid the light scattering, and thus the modified network is perfectly transparent. The nanostructured

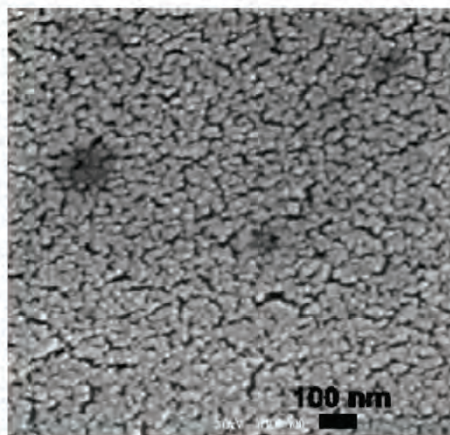


Figure 1. High-resolution SEM image of PMMA/MAM (90/10) blend.



network (PMMA/MAM) depends on two main factors. First, the proportion and molecular weight of methacrylate and butyl acrylate groups in the MAM triblock, and secondly the quantity of additive in the blend. In this case, the miscibility of methacrylate groups of MAM into the PMMA matrix is assured due to the similar molecular weight (85 000 and 90 000 g·mol<sup>-1</sup>, respectively). For an additive percentage of 10 wt.-%, the immiscible butyl acrylate blocks are presented in such proportion into the PMMA matrix as worm-like micelles with less than 100 nm length.

PMMA/MAM nanostructured blends were foamed at room temperature at a saturation pressure of ScCO<sub>2</sub> of 30 MPa. Figure 2a and b show the foam cell morphology of the samples obtained (Figure 2). Values of average cell size were 200 nm, with cell densities values of  $4.50 \times 10^{14}$  cells·cm<sup>-3</sup>, obtained from Equation (1) (see Experimental Part). These values are typically in the range of ultramicrocellular foams or nanofoams depending on the nomenclature of each scientific community. Relative foam densities reached were 0.4, values much lower than those presented in previous papers, which can be considered a remarkable result. Compared to other conventional microcellular foams, values of average cell size and cell densities are in the nanocellular range, showing a homogeneous open cell structure which differs to that obtained in previous investigations. As it is well known from the classical nucleation theory,<sup>[20,21]</sup> CO<sub>2</sub> presents much higher solubility in PMMA than in other polymers<sup>[22]</sup> because of the strong interaction between CO<sub>2</sub> and the carbonyl groups presented in PMMA matrix, which increases greatly the homogeneous nucleation. Moreover, in this study the effect of the MAM additive in the PMMA matrix is the increase of the heterogeneous nucleation. The combination of both effects, together with high saturation pressure and time leads to the nanocellular structures showed in Figure 2. It must be noticed that the homogeneity of the cellular structure is directly related to the remarkable dispersion of the MAM additive in the PMMA matrix during the extrusion process, overcoming the problems derived from the dispersion of particles, such as the apparition of agglomerates that usually occur working with physical additives, for example nanoclays. To illustrate clearly the effect of the additive in the main foam characteristics, neat PMMA foams were produced in the same conditions. The morphology resultant is showed in Figure 3. In this case, a closed cell morphology is observed, with values of average cell size of 5  $\mu$ m and cell densities values of  $1.60 \times 10^{10}$  cells·cm<sup>-3</sup>, obtained from Equation (1). The relative foam densities were much higher than in the

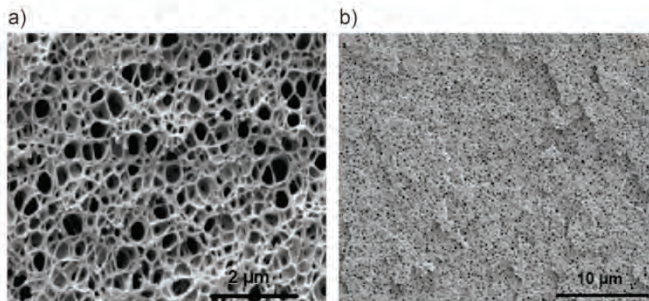


Figure 2. Scanning electron microscopy (SEM) images of PMMA/MAM (90/10) foams saturated at 300 bar.

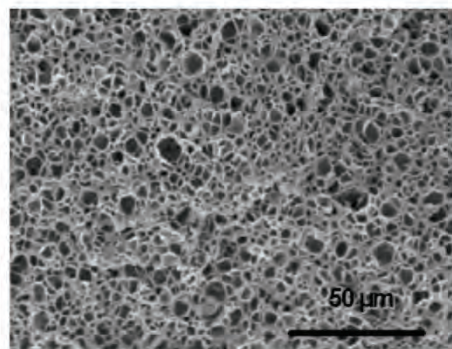


Figure 3. Scanning electron microscopy (SEM) image of neat PMMA foam.

PMMA/MAM materials, with values above 0.70. The comparative results are shown in Table 1, which lists also the CO<sub>2</sub> uptake after saturation at 30 MPa, measured at 20 °C just after the sample was removed from the CO<sub>2</sub> vessel (samples are in a supersaturated, glassy state).

It can be seen that the addition of 10 wt.-% of MAM into the PMMA matrix has a remarkable effect in the foaming characteristics. The average cell size is reduced to nanometric scale, whereas cell density increases in three orders of magnitude. In addition, the relative density is also reduced to values of 0.4. This drastic improvement in foam characteristics can be explained by physical-chemical mechanisms active during the blending process. First, an increase of the number of nucleating sites appears due to the presence of the nanostructured polymer formed by the butyl acrylate groups, which are not miscible in the PMMA matrix. Furthermore, during the saturation process, the CO<sub>2</sub> molecules can localize within these rubbery blocks, which present great affinity with the CO<sub>2</sub>. In the depressurization process, the CO<sub>2</sub> inside the butyl acrylate groups can expand



Table 1. Comparative foam characteristics in neat PMMA foams and PMMA/MAM (90/10) foams.

Material	Relative density	Average cell size	Cell density	CO <sub>2</sub> uptake
		[ $\mu\text{m}$ ]	[cells · cm <sup>-3</sup> ]	[wt.-%]
PMMA	0.7	2	$1.60 \times 10^{10}$	18.1
PMMA + 10% MAM	0.4	0.2	$4.50 \times 10^{14}$	25.6

easily, due to the low  $T_g$  ( $-50^\circ\text{C}$ ), but this expansion is avoided by the surrounding methacrylate matrix, which has a higher  $T_g$  ( $+50^\circ\text{C}$  for a saturation pressure of 30 MPa.<sup>[23]</sup>) This combines CO<sub>2</sub>/polymer interactions and rubbery CO<sub>2</sub>-philic sites dispersed at a nanoscale.

To show one example of the new and interesting properties observed in these materials, we present a remarkable physical effect concerning the thermal properties of foamed PMMA/MAM, as a result of the average cell size reduction and the increase of cell density. This effect was observed analyzing the influence of the foaming process in the glass transition temperature. As a result of the foaming process, the polymer is confined in the cell walls, with only 140 nm thickness. This confining effect has an influence in the mobility of the PMMA chains, leading to an increase in the glass transition temperature compared to bulk polymer. Figure 4 presents the DSC diagram of both foamed and solid samples, together with a SEM micrograph showing the typical thickness of a cell wall (Figure 4). The DSC diagram show an appreciable increase in the glass transition temperature, from  $112^\circ\text{C}$  in the bulk material to  $123^\circ\text{C}$  in the PMMA confined in the cell wall. Both values are constant on first and second heating process. This result has been predicted theoretically and has great interest in the analysis of two-dimensional polymer systems, for example thin films.<sup>[24]</sup>

An indication of the presence of nanometric pore dimensions within the foams is the significative increase in the observed  $T_g$ . Such an evolution is non classical. Indeed contradictory effects are observed on the  $T_g$  evolution of PMMA confined either to thin polymer films (film

thickness  $< 50\text{ nm}$ ) or to nano pores (often silica pores with size  $< 15\text{ nm}$ ).

In both cases PMMA chains are confined but nevertheless this does not necessarily restrict the chain motions or segmental mobility. Thus  $T_g$  may either show an increase or a decrease depending on the surface type, the film thickness and the pore size.<sup>[25–29]</sup>

For example, PMMA film deposition on gold involves a  $T_g$  decrease whereas films deposited on a silica surface show an increase of typically  $+15^\circ\text{C}$ , due the surface/polymer chains interaction and strong adsorption. The stronger the interactions, the higher the  $T_g$  increases. On the other hand, the  $T_g$  modification in any confinement is classically suppressed as soon as a solvent or a diluent is introduced. Classically for PMMA, the most frequent tendency seems to be a  $T_g$  decrease except in the case of thin films on silica surfaces. Our case is somehow different because confinement is provided neither in films nor in silica pores but confinement arises from walls whose thicknesses vary but may lie in the range of nanometers. If  $T_g$  increase (measured at mid point by DSC,  $10^\circ\text{C} \cdot \text{min}^{-1}$ ) is evidenced,  $\Delta T_g$  does not change. Neat PMMA unfoamed is set at  $T_g = 108\text{--}112^\circ\text{C}$  (measured or given by supplier) while  $T_g$  of the PMMA block is even lower ( $T_g = 95\text{--}100^\circ\text{C}$ ) and could be thought to be responsible for a  $T_g$  decrease of the matrix.<sup>[30]</sup> Nevertheless, the measured  $T_g$  here at  $123^\circ\text{C}$  is far greater. Such values are still in accordance with  $T_g$  values of PMMA chains (range from  $100$  to  $130^\circ\text{C}$ ) depending primarily on molar mass, comonomer content, chain entanglement, tacticity and, secondary, on surface effects. In this sense, the observation of a  $T_g$  increase in PMMA is interesting and we suggest to

attribute this effect to chain mobility restriction in the thinnest wall layers and maybe to another effect: a partial chain elongation in the course of foaming.

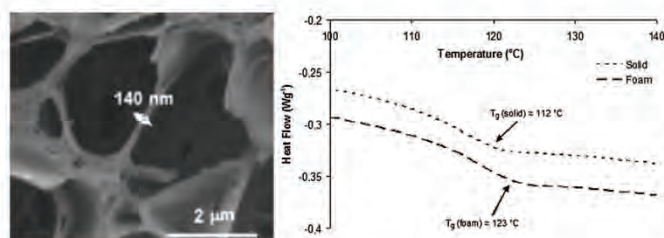


Figure 4. Glass transition increase due to confining effect of PMMA chains in the cell walls.

#### Effect of the Saturation Pressure on Cellular Structure and Three-Point Bending DMA Tests

To analyze the effect of the saturation pressure in the foaming behavior, a collection of PMMA/MAM (90/10) foams was obtained varying the saturation



pressure from 10 to 25 MPa, keeping constant the rest of the foaming parameters. As expected, the obtained relative densities decrease with saturation pressure, from 0.7 to  $0.5 \text{ g} \cdot \text{cm}^{-3}$  (Figure 5), which is directly related to the decrease in the  $\text{CO}_2$  uptake, from 23.1 wt.% at 25 MPa to 14.1 wt.% at 10 MPa. Concerning the cellular structure, it can be seen that the average cell size shows no great variation in all the foams produced, which indicates that saturation pressure has not a great influence in the cellular structure (Figure 6). The main foam characteristics are summarized in Table 2.

Three-point bending tests were carried out to evaluate the mechanical properties of the nanocellular foams produced. At least three different tests were performed in all the samples produced using different saturation pressures. Young's modulus obtained varied between 0.5 and 1.2 GPa, and increased with foam density (Figure 7). On the other hand, Young's modulus of the solid material, measured in the same procedure, was 3.4 GPa. For similar densities, Fu et al. found lower values for Young's modulus in neat PMMA microcellular foams, with higher cell sizes.<sup>[31]</sup> Thus, it can be concluded that, for a given foam density, reducing cell size up to nanometric scale derives directly in an improvement of the mechanical properties.

#### Effect of MAM Content on Cellular Structure

The effect of the MAM content on the cellular structure was also analyzed. To evaluate this effect, two additional samples were fabricated, with 5 wt.% of MAM and

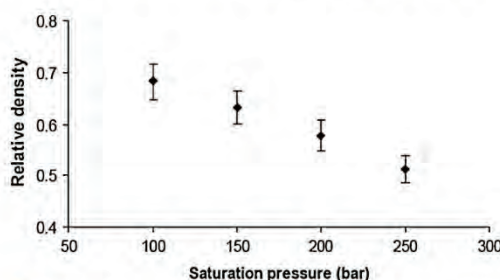


Figure 5. Effect of the saturation pressure on the relative foam density.

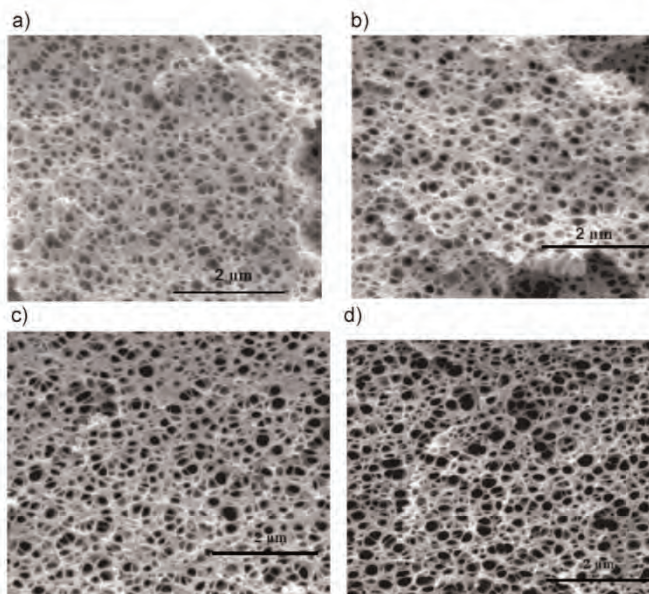


Figure 6. SEM micrographs of the PMMA/MAM (90/10) foams produced at different saturation pressures (a) 100 bar (b) 150 bar (c) 200 bar (d) 250 bar.

20 wt.% of MAM, respectively. The cellular structure of both samples is presented in Figure 8. As it can be seen in the SEM micrographs, the cellular morphology observed in these samples is completely different from that of the samples with 10 wt.% MAM (see Figure 2). This fact can be due to the nanostructuration which is observed in the PMMA/MAM (90/10) blend (Figure 1), which it is not observed in both blends, PMMA/MAM (95/5) and PMMA/MAM (80/20). This indicates that polymer nanostructuration is a key factor to control the cell morphology and to obtain low-density nanocellular foams with a regular and homogeneous cellular structure.

#### Conclusion

A new kind of nanocellular materials has been developed, using a nanostructured polymer matrix as base material and foaming it using supercritical  $\text{CO}_2$ . It has been demonstrated that the addition of small quantities of a triblock copolymer to an amorphous polymer matrix in a simple blending process, leads to a nanostructured polymer, with an excellent homogeneity. The resulting nanocellular foam was produced by means of a clean physical foaming process at room temperature, avoiding the use of chemical foaming agents. The resulting material



Table 2. Characteristics of the PMMA/MAM (90/10) foams produced by varying the saturation pressure.

Saturation pressure	Relative density	Average cell size	Cell density	CO <sub>2</sub> uptake
[MPa]		[ $\mu\text{m}$ ]	[cells $\cdot \text{cm}^{-3}$ ]	[wt.-%]
100	0.70	0.3	$7.60 \times 10^{13}$	14.1
150	0.60	0.2	$2.99 \times 10^{14}$	17.6
200	0.55	0.2	$3.27 \times 10^{14}$	21.2
250	0.51	0.2	$3.52 \times 10^{14}$	23.1

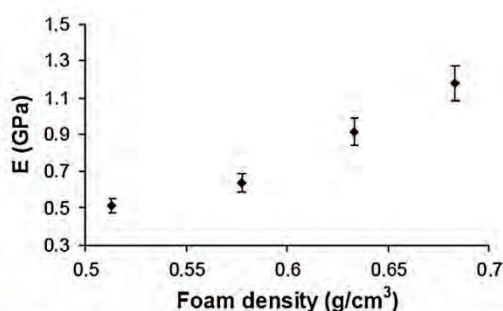


Figure 7. Young's modulus obtained in three-point bending DMA tests for the foams produced at different saturation pressures.

Acknowledgements: Financial support from MICINN (Spanish Government) through the project MAT 2009-14001-C02-01 and a doctoral grant (Javier Pinto, FPU Grant Ref-AP-2008-03603) is gratefully acknowledged.

Received: September 21, 2010; Revised: January 26, 2011;  
Published online: DOI: 10.1002/mame.201000346

Keywords: carbon dioxide; foams; morphology; nanocellular; polymers

presented an average cell size around 200 nm, with an open cell homogeneous structure and cell densities values close to  $10^{14}$  cells  $\cdot \text{cm}^{-3}$ . This new kind of materials not only offers excellent mechanical and thermal properties due to the cellular structure, but also presents interesting physical properties due to the confining effect of the polymer during the formation of the nanocellular structure.

- [1] A. I. Cooper, *J. Mater. Chem.* **2000**, *10*, 207.
- [2] I. Tsivintzelis, A. G. Angelopoulou, C. Panayiotou, *Polymer* **2007**, *48*, 5928.
- [3] A. K. Arora, A. J. Lesser, T. J. McCarthy, *Polym. Eng. Sci.* **1998**, *38*, 707.
- [4] J. Fu, C. Jo, H. E. Nagueib, *Cellular Polym.* **2005**, *24*, 177.
- [5] C. Barlow, V. Kumar, B. Flinn, R. K. Bordia, J. Weller, *J. Eng. Mater. Technol.* **2001**, *123*, 329.
- [6] M. Y. S. Ahmed, P. C. Lee, C. B. Park, N. Atalla, *ANTEC Proc.* **2006**, *1*, 27.
- [7] D. Schmidt, V. I. Raman, C. Egger, C. du Fresne, V. Schaedler, *Mater. Sci. Eng. C* **2007**, *27*, 1487.
- [8] Y. Ito, M. Yamashita, M. Okamoto, *Macromol. Mater. Eng.* **2006**, *291*, 773.
- [9] C. Zeng, X. Han, L. J. Lee, K. W. Koelling, D. L. Tomasko, *Adv. Mater.* **2003**, *15*, 1743.
- [10] J.-M. Yeh, K.-C. Chang, C.-W. Peng, M.-C. Lai, C.-B. Hung, S.-C. Hsu, S.-S. Hwang, H.-R. Lin, *Mater. Chem. Phys.* **2009**, *115*, 744.
- [11] H. Yokoyama, K. Sugiyama, *Macromolecules* **2005**, *38*, 10516.
- [12] T. Otsuka, K. Taki, M. Ohshima, *Macromol. Mater. Eng.* **2008**, *293*, 78.
- [13] S. Siripurapu, J. M. DeSimone, S. A. Khan, R. J. Spontak, *Adv. Mater.* **2004**, *16*, 989.
- [14] A.-V. Ruzette, L. Leibler, *Nat. Mater.* **2005**, *4*, 19.
- [15] L. Leibler, *Prog. Polym. Sci.* **2005**, *30*, 898.
- [16] T. A. Tran, F. Leonardi, S. Bourrigaud, P. Gerard, C. Derail, *Polym. Test.* **2008**, *27*, 945.

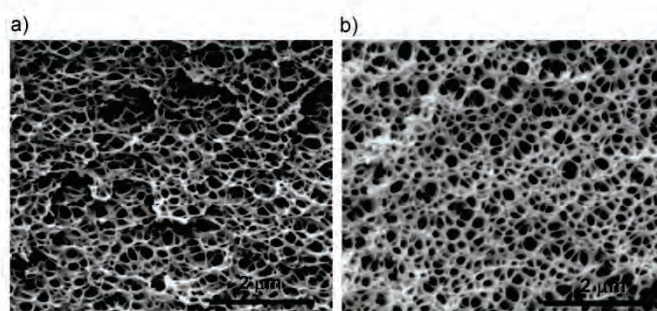


Figure 8. SEM micrographs of PMMA/MAM foams varying the weight percentage of MAM (a) 5 wt.-% MAM (b) 20 wt.-% MAM.

- [17] L. Lalande, C. J. G. Plummer, J. Anders, E. Manson, P. Gerard, *Polymer* **2001**, 47, 2389.
- [18] L. Lalande, J. G. Plummer, J. Anders, E. Manson, P. Gerard, *Eng. Fract. Mech.* **2006**, 73, 2413.
- [19] V. Kumar, N. P. Suh, *Polym. Eng. Sci.* **1990**, 30, 1323.
- [20] C. B. Murray, D. J. Norris, M. G. Bawendi, *J. Am. Chem. Soc.* **1993**, 115, 8706.
- [21] J. S. Colton, N. P. Suh, *Polym. Eng. Sci.* **1987**, 27, 500.
- [22] F. Rindfleisch, T. P. DiNoia, M. A. McHugh, *J. Phys. Chem.* **1996**, 100, 15581.
- [23] A. V. Nawaby, Y. P. Handa, X. Liao, Y. Yoshitaka, M. Tomohiro, *Polym. Int.* **2006**, 56, 67.
- [24] C. B. Roth, J. R. Dutcher, *J. Electroanal. Chem.* **2005**, 584, 13.
- [25] S. Kim, *Macromolecules* **2010**, 43, 5158.
- [26] I. Ioannis, *Acta Mater.* **2005**, 53, 1621.
- [27] I. M. Kalogeras, *Eur. Polym. J.* **2004**, 40, 193.
- [28] S. Siripurapu, *Macromolecules* **2005**, 41, 2271.
- [29] H. Oh, *Macromolecules* **2008**, 41, 2561.
- [30] L. Lalande, *Polymer* **2006**, 47, 2389.
- [31] J. Fu, C. Jo, H. E. Naguib, *Cellular Polym.* **2005**, 47, 177.

## V.1 Young's Modulus

In order to study some mechanical properties neat PMMA foams and 90/10 PMMA/MAM blends foams were produced at different processing conditions (Table V-1). Four measurements were carried out for each foam, using a three-point bending set-up in a Dynamic Mechanical Analyzer (Perkin-Elmer, Mod. DMA-7), to determine the Young's modulus ( $E$ ) at room temperature. Samples for DMA tests were prepared using a precision saw (mod. 1000, Isomet), with dimensions  $15 \times 2 \times 2 \text{ mm}^3$ . DMA experiments were carried out at room temperature, using a static force of 1293 mN and a dynamic force of 1077 mN with a frequency of 1 Hz.

**Table V-1. Processing conditions and properties of the produced foams**

Sample	Saturation Pressure (MPa)	Saturation Temperature (° C)	Cell size (nm)	$\rho_r$	E (Pa)
90/10 PMMA/MAM	10	23	150	0.58	$7.82 \times 10^8$
90/10 PMMA/MAM	15	23	160	0.54	$9.15 \times 10^8$
90/10 PMMA/MAM	20	23	170	0.49	$6.38 \times 10^8$
90/10 PMMA/MAM	25	23	190	0.43	$5.15 \times 10^8$
90/10 PMMA/MAM	30	23	180	0.44	$7.25 \times 10^8$
90/10 PMMA/MAM	30	40	220	0.41	$5.01 \times 10^8$
90/10 PMMA/MAM	30	50	280	0.40	$4.69 \times 10^8$
90/10 PMMA/MAM	30	60	1000	0.37	$4.80 \times 10^8$
90/10 PMMA/MAM	30	70	950	0.36	$4.70 \times 10^8$
Neat PMMA	30	40	760	0.47	$4.09 \times 10^8$
Neat PMMA	30	50	720	0.48	$2.90 \times 10^8$
Neat PMMA	30	60	1870	0.44	$3.41 \times 10^8$

Mechanical properties of foams are strongly related to the apparent macroscopic density. In particular, the Young's modulus of foams ( $E_f$ ) can be estimated from the value of the solid precursor ( $E_s$ ) using the following expression (Equation V-1) [6].

$$E_f = E_s \cdot \rho_r^n \quad [\text{V-1}]$$

Where  $\rho_r$  is the relative density of foam and the exponent  $n$  takes values between 1 and 2. Solid neat PMMA and 90/10 PMMA/MAM blend present Young's moduli about 3.1 GPa, which are in good agreement with the value provided for the PMMA by the supplier. Then, we can compare the predictions



calculated by the previous equation together with the experimental values. Comparison is shown in Figure V.1.

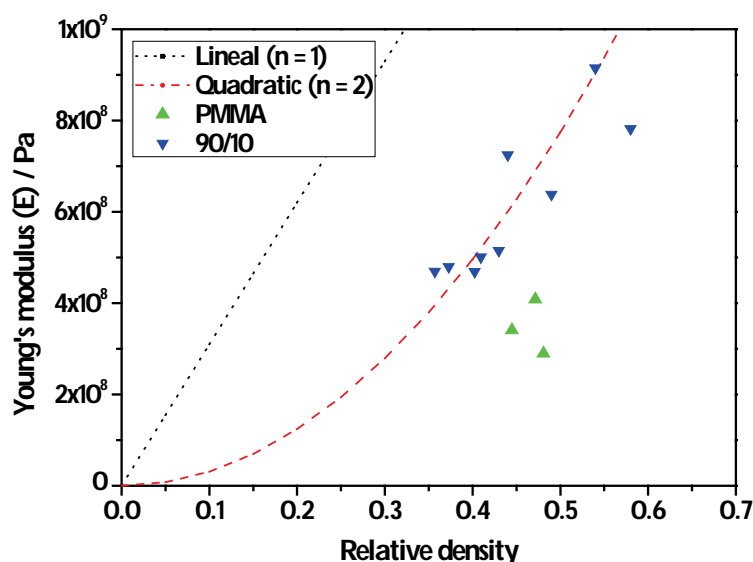


**Figure V.1: Young's modulus of PMMA and PMMA/MAM foams as a function of relative density**

Results show that 90/10 PMMA/MAM blend foams fit the theoretical predictions with  $n = 2$ . On the contrary, neat PMMA samples present lower values than the expected, even with  $n = 2$ . Taking into account the cell size of these foams (Table V-1) this difference cannot be attributed to the cell size, because several 90/10 foams present cell sizes with the same order of magnitude as neat PMMA ones (near to 1  $\mu\text{m}$ ).

In the previous chapter it was showed that the high structural stability of 90/10 PMMA/MAM avoids coalescence, and their controlled nucleation process results in cellular structures with higher homogeneity than that of neat PMMA foams. Therefore, the better mechanical behavior of 90/10 PMMA/MAM foams could be related to the homogeneity of their cellular structure.

In addition, cells of 90/10 PMMA/MAM foams present anisotropy, with the cells elongated along the injection direction. It is known that the anisotropy of the cells has a great influence on the Young's modulus. Foams with anisotropic cells present enhanced values of  $E$  in the direction of the long axis of the cells; on the contrary, values of  $E$  measured in a direction perpendicular to the long axis of the cells are significantly lower than the expected [6].

In this study, determination of  $E$  on 90/10 PMMA/MAM foams was carried out in a direction perpendicular to the long axis of their cells (dimensions of PMMA/MAM foamed samples did not allow

preparing samples to measure  $E$  in the direction of the long axis of the cells with appropriate dimensions to our DMA measurement system); therefore it can be expected that these foams present higher values of  $E$  in the direction of the long axis of their cells, whereas neat PMMA foams present an isotropic cellular structures and their  $E$  should be the same independently of the measured direction.

As the previous results show a quadratic dependence of the Young's modulus with the relative density, the influence of the cell size on  $E$  for the 90/10 foams can be analyzed by representing  $E$  normalized by the square of the relative density versus the cell size (Figure V.2).

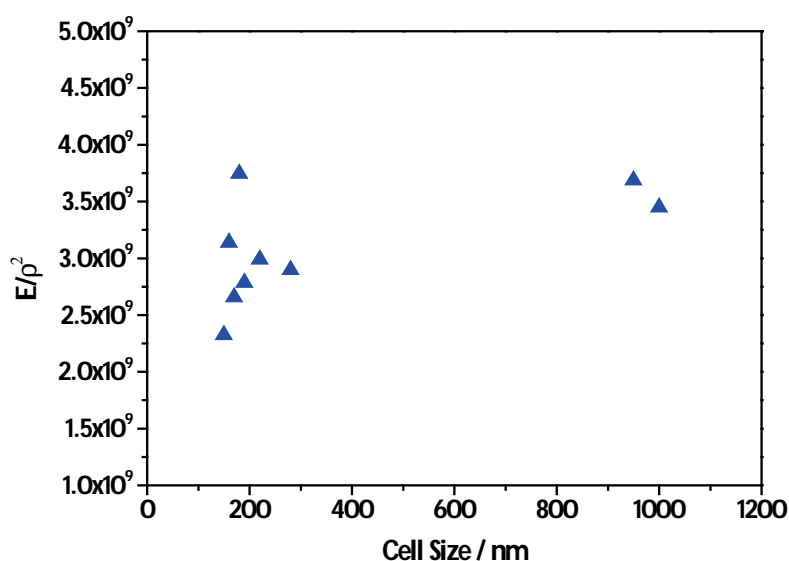


**Figure V.2: Influence of the cell size of 90/10 PMMA/MAM foams on the normalized Young's modulus**

No relationship between the cell size and the normalized Young's modulus is found. This result is in good agreement with previous works, which shown that cell size (in the microcellular range) has no influence on the Young's modulus [7, 8].

Therefore the Young's modulus of 90/10 PMMA/MAM foams seems to depend on the relative density and also on other structural characteristics such as the homogeneity of the cellular structure, anisotropy, etc., but not on the cell size. Because of the narrow range of cell sizes under study, we cannot make a definitive conclusion on this topic. Optimization of the post-foaming processes should allow producing PMMA/MAM foams with higher cell sizes, which would be appropriate to extend this study in the future. Also, characterization of other mechanical properties and the study of the influence of the anisotropy of the cells on these properties could provide valuable information about the advantages of nanocellular foams.

## V.2 Glass Transition Temperature

Increment of the  $T_g$  of 90/10 PMMA/MAM nanocellular foams is first related to the confinement of the PMMA chains inside the walls of the cells when they fall into the nanometric range. This confinement effect has been widely studied in the literature on films of amorphous polymers such as PMMA or polystyrene (PS) [9-14], and some evidences has been found on PEI nanofoams [5]. Results from the literature demonstrate the existence of this confinement effect, but rather few explanations about its phenomenon are provided. We give arguments coherent with our system and some literature data and interpretation, but there also are contradictory arguments in literature so we stay at the hypothesis state.

Some studies related the increment of  $T_g$  to the reduction of the free volume/polymer chains mobility [9, 10], and the existence of hydrogen bonds [10]. With the aim to estimate the range of dimensions (for the confinement) which can influence the polymer chain mobility of PMMA, we calculated the theoretical length of a PMMA chain ( $L$ , assuming the chain completely stretched). This length can be estimated from an average degree of polymerization of the PMMA chain ( $X_n = M_n/M_o$ , where  $M_n = 43000$  g/mol is the number average molecular mass of our PMMA and  $M_o = 100.12$  g/mol is the molecular mass of the MMA unit), the number of C-C bonds of the MMA backbone ( $N_{C-C\ bonds} = 2$ ), and the length and angle of the C-C bonds ( $d_{C-C\ bond} = 0.154$  nm,  $\theta_{C-C\ bond} = 109^\circ$ ), using the following expression (Equation V-2).

$$L = X_n \cdot N \cdot d \cdot \sin\left(\frac{\theta}{2}\right) \quad [V-2]$$

Obtained PMMA chain length is about 107 nm. Although the polymer chains are never completely stretched inside the polymer matrix, it can be expected that confinement of the polymer chains below these dimensions can have a significant influence on the chain mobility, and therefore on the  $T_g$ .

In order to provide more experimental evidences of this effect two sets of measurements were carried out.

First, the  $T_g$  was measured in samples produced at constant pressure (30 MPa) and different saturation temperatures (from 10 to 70° C), from 95/5 and 75/25 PMMA/MAM blends.  $T_g$  of foams and solid blends (an example can be found in Figure V.3) were determined by DSC using the midpoint (more details about the DSC measurements can be found in Chapter II), and the average cell size of foams was measured using the specific software, explained in Chapter I.

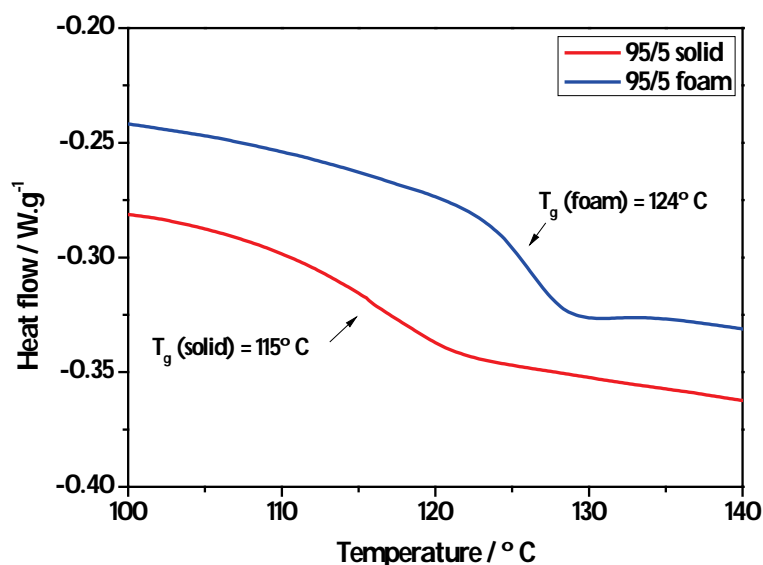


**Figure V.3: Comparison between the DSC curves of a 95/5 foamed and solid blends. Foamed sample shows a higher  $T_g$ .**

No real influence of the saturation temperature was found, and all the foams present values of their  $T_g$  higher than the corresponding value of their solid precursor (Figure V.4). It should be noticed that all the cell sizes of these foams are below the micron, and that the  $T_g$  is increased when the cell size is decreased.

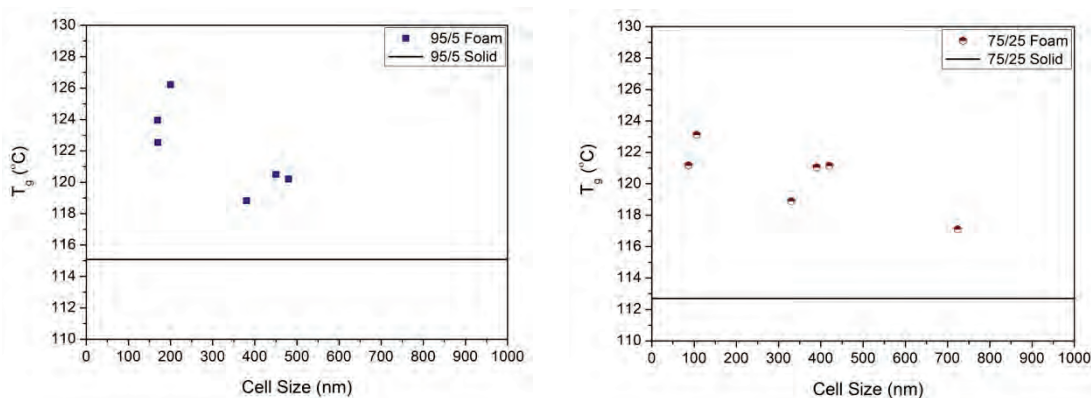


**Figure V.4: Experimental  $T_g$  values from 95/5 (left) and 75/25 (right) foams compared to their solid precursors**

Second  $T_g$ 's measurements were carried out in samples produced at the same temperature (RT) and different pressures (from 10 to 25 MPa), from neat PMMA, 92.5/7.5 and 85/15 PMMA/MAM blends.

It is found that saturation pressure does not show any direct influence on the  $T_g$ 's evolution. Foams with cell sizes below the micron present significant increments of their  $T_g$  in comparison with the solid precursors, while foams with higher cell sizes present values close to that of the solid precursors (Figure V.5). Once again the  $T_g$  is increased when the cell size is decreased.

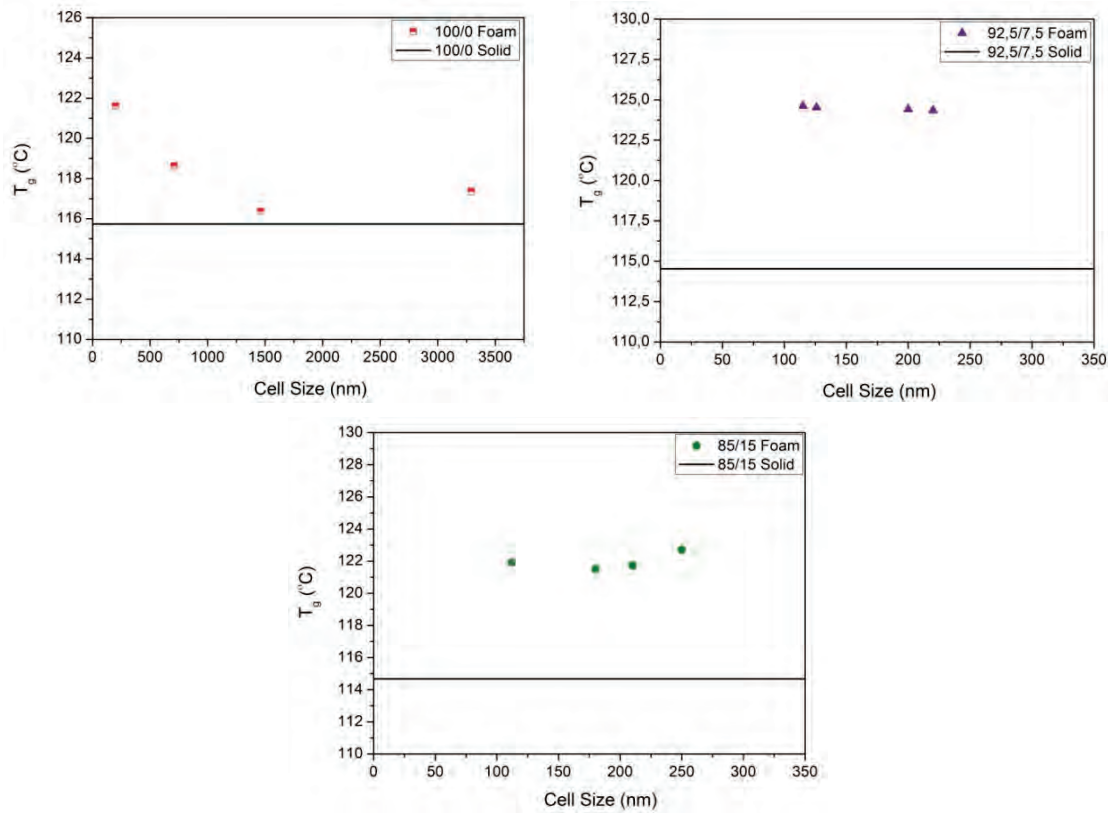


**Figure V.5: Experimental  $T_g$  values from neat PMMA (upper left), 92.5/7.5 (upper left) and 85/15 (down). The values are compared with those of their solid precursors.**

Although the cell size of the foams and the evolution of their  $T_g$  seems to be related, it was explained before that this effect should be related to the cell walls thickness, and not necessarily to the cell size. Cell walls thickness ( $\delta$ ) can be estimated from the cell size ( $\Phi$ ) and the relative density ( $\rho_r$ ) using the following expression (Equation V-3) [6].

$$\delta = \rho_r \cdot \Phi \cdot \frac{(1-f_s)}{C} \quad [\text{V-3}]$$

Where  $f_s$  is the fraction of polymer mass in the edges, and  $C$  is a constant that depends in the cell shape. Assuming  $f_s$  as a constant the cell wall thickness should be proportional to the product of the relative density and the cell size. Then, in order to estimate the influence of the cell wall thickness on the  $T_g$  evolution, the measured temperature increment ( $\Delta T_g = T_{g, \text{foam}} - T_{g, \text{solid}}$ ) can be represented as a function of the variable  $\rho_r \cdot \Phi$  (Figure V.6).

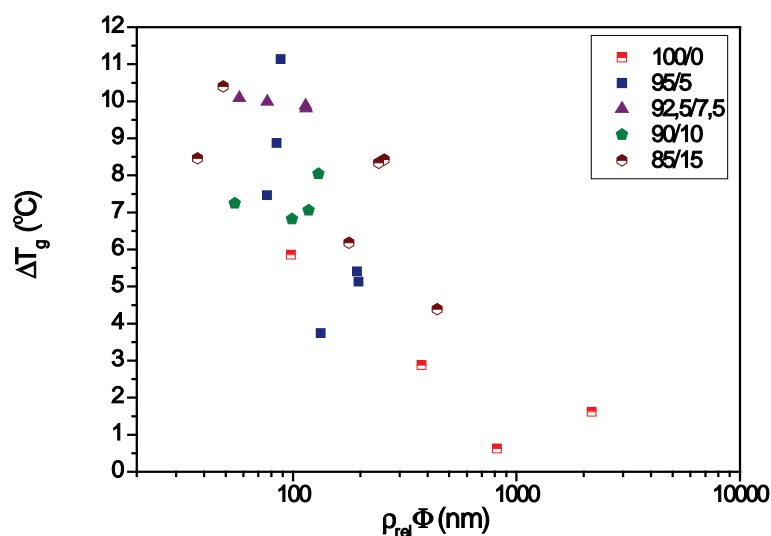


**Figure V.6:** Experimental increment of the glass transition temperature of neat PMMA and PMMA/MAM blends as a function of the product between their relative density and cell size.

As expected a relationship between the increment of the  $T_g$  and the reduction of this product, related to the cell wall thickness, is found. With the aim to obtain a further proof of this behavior the average cell wall thickness of these foams was estimated by measuring at least one hundred walls from each foam over SEM micrographs. Results of the  $T_g$  increase as a function of the measured cell wall thickness are shown on Figure V.7. The results show that below cell wall thickness of 100 nm there is a clear increase of the glass transition temperature in the foams.

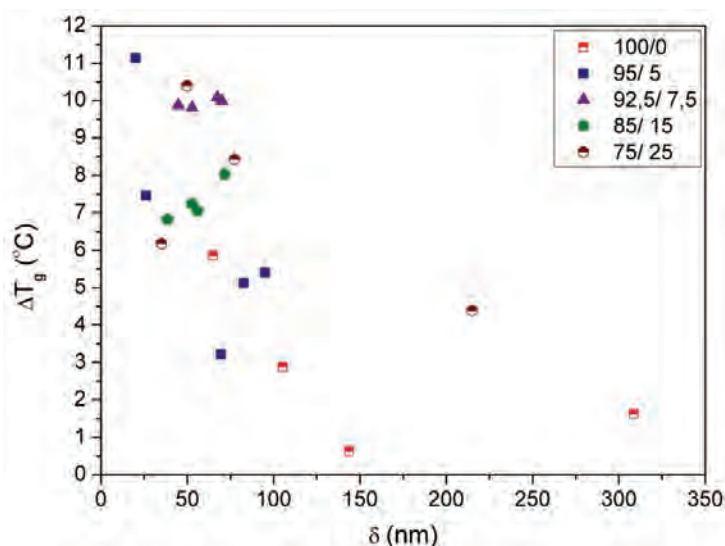


**Figure V.7:** Experimental  $T_g$  increment from neat PMMA and PMMA/MAM blends foams vs. to their cell wall thickness.



Therefore we can make the hypothesis that P MMA and P MMA/MAM foams present a confinement effect when cell sizes lie below the micron, due to the associated reduction of their cell walls (below 100 nm for these cell sizes). Reduction of the P MMA chains mobility under these circumstances allows obtaining an increment of the glass transition temperature up to 11° C. Figure V.8 shows a detail of the cell walls from foams presenting this 11° C increment of their  $T_g$ . The thickness of the walls is clearly below 100 nm.

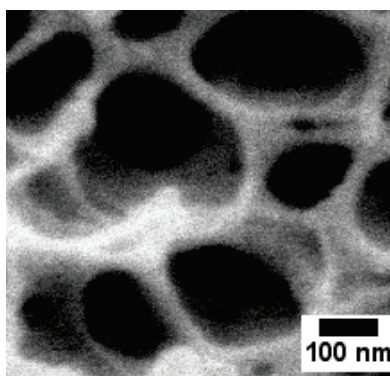


**Figure V.8:** SEM micrograph showing cell walls of a 95/5 PMMA/MAM foam with a  $T_g$  of 126° C

### V.3 Thermal Conductivity

One of the most extended applications of cellular polymers is thermal insulation (buildings, pipes, fridges, transport, cryogenic applications...), with a high social, environmental, and economic impact. It is estimated that about 13 % of the total energy consumption in the European Union is related to the climatization of residential buildings. Some studies about thermal insulation obtain that an optimal thermal insulation (with current technology and materials) results in a 75 % power consumption and CO<sub>2</sub> emissions savings (Dynamic simulation from BASF (Passiv Haus Institut)).

Therefore, development of improved thermal insulation materials can have a significant impact on the economy and on the environmental problems associated to the CO<sub>2</sub> emissions.

The main advantage of cellular materials as thermal insulators is that the thermal conductivity of the polymer matrix, usually not so high, is reduced by the addition of the gaseous phase (with a much lower thermal conductivity). However, the contribution of the gaseous phase becomes the main component of the foam thermal conductivity at the relative densities usually employed in thermal insulation (below 0.1), as Figure V.9 shows. For instance for a relative density of 0.1 the gas phase contribution is around 60%, the solid phase contributes with 30%, and the radiation term accounts for around 10% of the total conductivity.

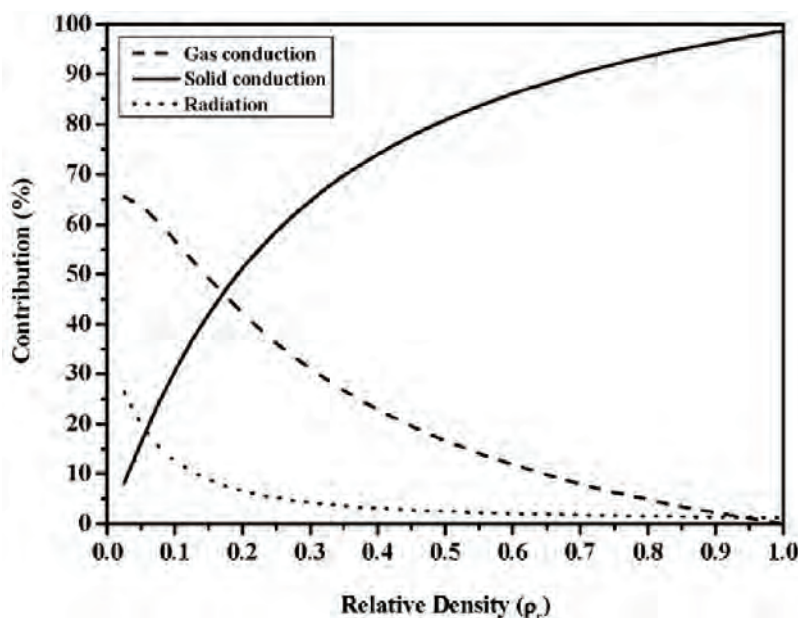


**Figure V.9: Contribution (in percentage) of the solid phase, gaseous phase and radiation term to the thermal conductivity of a polymer foam (adapted from E. Solórzano et al., *Adv. Eng. Mater*, 11, 818 (2009)).**

Then, the main challenge in thermal insulation with foams is to reduce the thermal conductivity of the gaseous phase. One of the approaches employed is to substitute the gas inside the cells, usually air whose

thermal conductivity is about 0.026 W/m·K, by gases with lower thermal conductivity. But this approach presents the disadvantages that this gas should be retained inside the foam (which is in fact very difficult in the long-term), avoiding diffusion or interchange with the environment, otherwise the foam will lose their improved insulation performance. Another disadvantage of this approach is that the typical gases with good performance are not very convenient from the environmental point of view, because they contribute to the global warming and/or to the ozone depletion.

A second approach to reduce the thermal conductivity is the use of nanocellular foams, because it is expected that nanocellular foams will present the so called Knudsen effect [1, 4]. This effect implies that when the cell size is comparable or smaller than the mean free path of the liquid or gas, the molecules of the latter collide more often with the molecules forming the solid part than among them. A schematic representation of this effect can be found in Figure V.10, where the gas molecules are represented by a sphere with radius equal to their mean free path ( $l_g$ ).

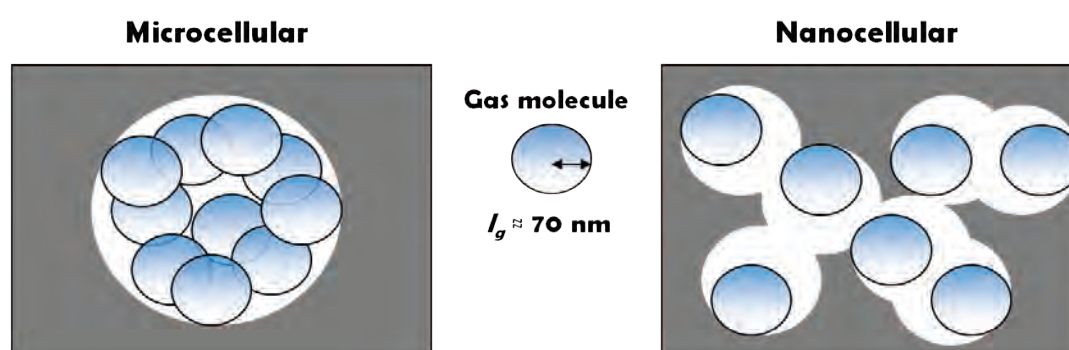


**Figure V.10: Behavior of gas molecules of air in microcellular foams (left) and in nanocellular foams with pore diameter about the mean free path  $l_g$  (right). Gas molecules interact between them in the microcellular foams, allowing the heat transmission; whereas no interaction, or a reduced one, is found between the gas molecules on the nanocellular foam.**

Theoretical reduction of the thermal conductivity at room temperature of the gas phase (assuming air as the gas in the cells) due to the Knudsen effect is shown in Figure V.11, together with the range of cell sizes obtained from the PMMA/MAM blends selected for this study: 25, 50 and 75 wt% of MAM. These blends were selected in order to provide a co-continuous or semi co-continuous cellular structures, which allow extracting the gas inside the foams in order to perform the measurements, explained in Chapter I (thermal conductivity in vacuum).

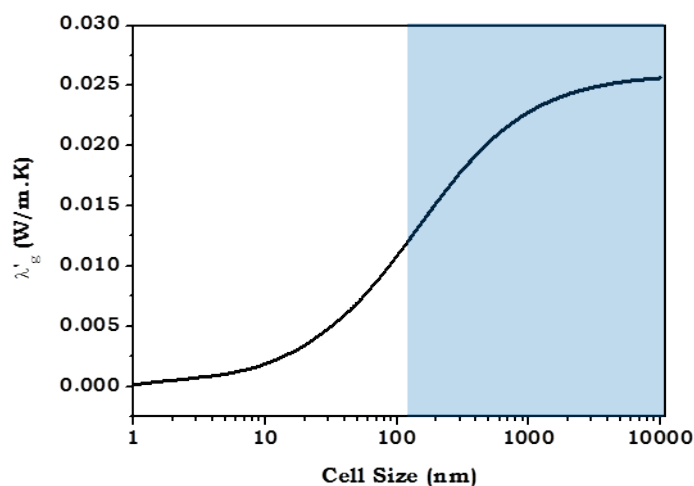


**Figure V.11: Predicted relationship between the air thermal conductivity and the cell size due to the Knudsen effect. Cell size range of selected PMMA/MAM foams for this study is overlaid in blue.**

As Figure V.9 shows, our PMMA/MAM nanocellular and microcellular foams cover an appropriate range to be able to show the Knudsen effect. A study about this phenomenon was carried out and published as a proceeding in the **10<sup>th</sup> International Conference on Foam Materials & Technology (FOAMS 2012, Barcelona)** with the title *“Thermal Conductivity Transition Between Microcellular and Nanocellular Polymeric Foams: Experimental Validation of the Knudsen Effect”*.

The measurement of the solid precursors shows that the thermal conductivity is not affected by the MAM amount; thus the thermal conductivity of all the foams under study can be analyzed just according to their relative density and cell size. When the normalized thermal conductivity (calculated as the relative thermal conductivity divided by the relative density) is represented as a function of the cell size a clear threshold is found between the nanocellular and the microcellular foams, being the conductivity of the nanocellular foams smaller. Taking into account the relative density of the analyzed materials (around 0.5) the thermal conductivity by radiation can be neglected (Figure V.9) and then our study can be focused on the two remaining mechanisms (conductivity through the gas and solid phase).

That difference is explained in terms of an increment of the polymer matrix tortuosity (Figure V.12), which reduces the thermal conductivity of the solid phase, and the contribution of the Knudsen effect.

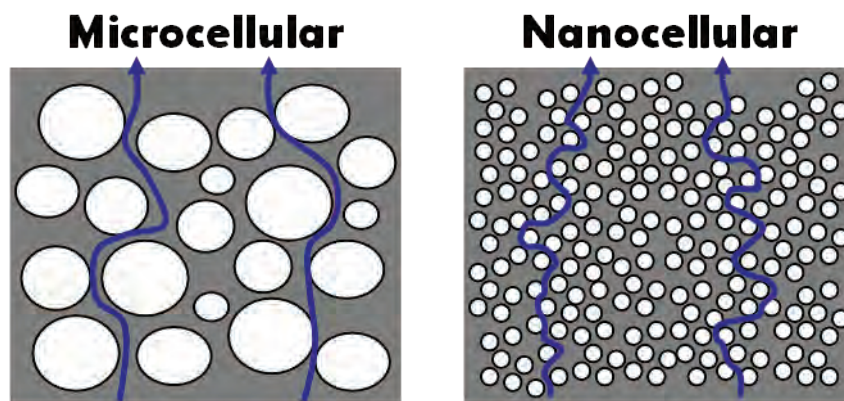


**Figure V.12: Schematic representation of the solid phase tortuosity increase from microcellular to nanocellular foams**

Both mechanisms are checked. Determination of the contribution of the gaseous phase shows a decrease when the cell size is decreased, fitting the predictions of the theoretical expressions of the Knudsen effect. Also, the fitting of the contribution of the solid phase to usual models requires the introduction of a structural factor ( $g$ ) different for microcellular foams and for nanocellular foams that accounts for the different tortuosity of the materials.

## THERMAL CONDUCTIVITY TRANSITION BETWEEN MICROCELLULAR AND NANOCELLULAR POLYMERIC FOAMS: EXPERIMENTAL VALIDATION OF THE KNUDSEN EFFECT

*Javier Pinto, Cellular Materials Laboratory (CellMat), Condensed Matter Physics Department, University of Valladolid and Laboratoire de Chimie de Polymères Organiques (LCPO), Institut Polytechnique de Bordeaux (IPB); email: jpinto@fmc.uva.es*  
*Eusebio Solórzano, Miguel A. Rodríguez-Pérez and Jose A. de Saja, Cellular Materials Laboratory (CellMat), Condensed Matter Physics Department, University of Valladolid;*  
*Michel Dumon, Laboratoire de Chimie de Polymères Organiques (LCPO), Institut Polytechnique de Bordeaux (IPB)*

### Abstract

In this paper the thermal conductivity of polymeric foams with cell sizes from 100 nm to several microns and relative densities between 0.3 and 0.6 has been characterized. Samples have been produced by the batch dissolution foaming technique using as precursor material a blend of poly(methyl methacrylate) PMMA and a triblock copolymer [poly(methyl methacrylate)-block poly(butyl acrylate)-block poly(methyl methacrylate), MAM].

It has been demonstrated the existence of a clear transition in the experimental results of thermal conductivity between polymeric foams with cell sizes in the microcellular and the nanocellular range. Furthermore, this behavior has been modeled using theoretical models and in particular the equations of the pore size influence over the gas thermal conductivity (Knudsen effect).

It has been obtained a good agreement between the experimental results and the theoretical predictions, proving the validity of the Knudsen effect equations for nanocellular polymeric foams.

### Introduction

Nanocellular polymeric foams have become one of the most promising topics in cellular materials science, due to the potential improvement of several properties in comparison with conventional foams that is assumed<sup>[1,2]</sup>.

One of the main expected advantages is a significant improvement of the thermal insulation. The evaluation of the thermal conductivity of cellular materials from the conductivity data of the two component phases and the structure of the material is an interesting subject that has been approached by different authors<sup>[3-10]</sup>. It is assumed that there are four different contributions to the thermal

conductivity of a cellular material ( $\lambda_c$ ): conduction through the gas phase ( $\lambda_g$ ), conduction along the cell walls and struts of the solid material ( $\lambda_s$ ), convection within the cells ( $\lambda_c$ ) and the thermal radiation ( $\lambda_r$ ). It is widely accepted that convection plays a minor role in closed cell materials with cell sizes below 4 mm in diameter<sup>[11]</sup>, and in open cell materials with cell sizes lower than 2 mm<sup>[12]</sup>. Also, the contribution of the radiation mechanism could be neglected for foams with relative densities over 0.2<sup>[3]</sup>. So, in our case, with cell sizes in the nano and micrometric range and relative densities over 0.3 the contribution of the convection and radiation terms can be considered as negligible.

The effective thermal conductivity of the gas in air-filled cellular structures can be described by the Knudsen equation<sup>[13]</sup>:

$$\lambda'_g = \lambda'_{g0} / (1 + \beta Kn) \quad (1)$$

Where  $\lambda'_{g0}$  is the thermal conductivity of free air (0.026 W/m.K at room temperature),  $\beta$  is a parameter that takes into account the energy transfer between gas molecules and the limiting solid structure, (about 2 for air), and  $Kn$  is the Knudsen number that is obtained by dividing the mean free path of the gas molecules ( $l_g \approx 70$  nm at room temperature) and the average pore diameter ( $\Phi$ ):

$$Kn = l_g / \Phi \quad (2)$$

Then, for cell sizes in the nanocellular range a reduction of the gaseous contribution on the thermal conductivity of the foams could be expected, this behavior is called Knudsen effect<sup>[1,13]</sup> (Figure 1).



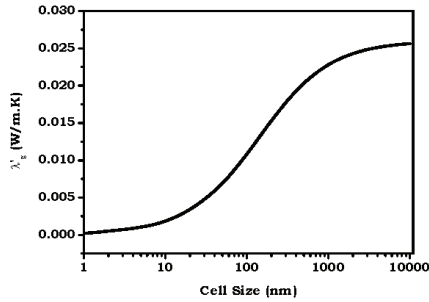


Figure 1: Predicted relationship between the air thermal conductivity and the cell size due to the Knudsen effect

This effect have been previously demonstrated in aerogels<sup>[13,14]</sup>, but as far as we know there are not experimental results in polymeric foams produced by conventional methods showing the Knudsen effect.

In previous works<sup>[15-16]</sup> we presented a method to produce nanocellular and microcellular polymeric foams with homogeneous cellular structures and significant thickness (several millimeters) and relative densities of above 0.2. Foams with these characteristics are appropriate to check the Knudsen effect, due to the range of cell sizes obtained and the homogeneous cellular structure.

Moreover, the thermal conductivity of foams with similar relative densities and based on the copolymer MAM has been previously studied<sup>[17]</sup>. The results for these materials showed shown that their thermal conductivity behavior could be predicted by the Ashby model:

$$\lambda_t = \lambda_s + \lambda_g = g\lambda'_s(1 - V_f) + \lambda'_g V_f \quad (3)$$

Where  $V_f$  is the volume fraction of voids and  $g$  is an efficiency factor which allows for the tortuous shape of the cell walls and which ranges between 1/3 and 1. For this material the model fits the experimental results with  $g = 1$ <sup>[17]</sup>.

In this study foams with homogeneous cellular structures with different cell sizes from 130 nm to 8500 nm and relative densities from 0.3 to 0.6 have been produced using the same materials and production route that the previously mentioned works<sup>[15-16]</sup>. A characterization of the thermal conductivity of these foams has been carried out to provide an experimental validation of Knudsen effect in polymeric foams.

## Experimental part

### Materials

Transparent PMMA was kindly supplied by Altuglas-Arkema Company (France), in the form of pellets. A transparent MAM triblock copolymer with 35 wt.-% methacrylate/30 wt.-% butylacrylate/35 wt.-% methacrylate was supplied by Arkema Company (France), in the form of pellets. The glass transition temperature ( $T_g$ ) value of the polymers employed were 112° C for the PMMA homopolymer, and +119° C and -49° C for the methacrylate and butyl acrylate blocks in the MAM triblock copolymer, respectively. Details of production of both PMMA and MAM polymers can be found elsewhere.<sup>[18,19]</sup>

### Samples Production

Polymer blends of PMMA containing 25, 50 and 75 wt.-% of MAM were produced as follows. Both materials, PMMA and MAM, were dried in vacuum (680 mm Hg), at 80° C during 4 h before processing. Mixing and extrusion were carried out using a Scamex CE02 single-screw extruder ( $L/D = 28$  d = 45 mm), with a temperature profile from 165 to 225° C, at a screw speed of 60 rpm, in the desired proportions. Pellets were produced using a continuous cutting machine operating at the end of the line at a constant speed of 240 rpm.

In a second step, pellets produced were injected into pieces (50 x 15 mm<sup>2</sup>) with 3 mm thickness, using a small scale injection molding machine developed by DSM Xplote. The working temperature was fixed at 240° C, whereas mold temperature was set at 60° C. The injection pressure was fixed at 1 MPa. Transparent samples obtained showed a good surface appearance as well a good injection behavior, with no presence of air bubbles inside the parts.

### Foaming Experiments

Foaming experiments were carried out in a high pressure vessel provided by TOP Industry (France), with a capacity of 300 cm<sup>3</sup> and capable of operating at maximum temperature of 250° C and maximum pressure of 40 MPa. The reactor is equipped with an accurate pressure pump controller provided by Teledyne ISCO, and controlled automatically to keep the temperature and pressure at the desired values. The CO<sub>2</sub> vessel temperature and pressure were monitored in the course of the process. Thus a collection of experiments were performed in a modified solid state foaming process. The usual solid state foaming process with amorphous polymers has three stages, the saturation (under fixed gas

pressure and temperature), desorption (room pressure and temperature) and foaming of the sample (at a temperature over the  $T_g$  the polymer). However, the glass transition temperature of plastized PMMA with  $\text{CO}_2$  can reach values near to room temperature<sup>[20]</sup>, even below room temperature in some particular conditions<sup>[21]</sup>, then the desorption (at room temperature) and foaming stage (at room temperature) can not be well differentiated. The samples temperature decrease to values clearly below room temperature during the pressure release (adiabatic depressurization), and the materials start to foam when reach again a temperature near room temperature.

In this study, samples were saturated at 30 MPa, and different temperatures between room temperature and 70 Celsius during 16 h to assure an equilibrium dissolution of  $\text{CO}_2$  in the polymer. After the saturation process, foaming was carried out by releasing the pressure inside the vessel at an average pressure drop rate of 30 MPa/min.

### Characterization

In first place foamed samples have been analyzed by x-ray radiography<sup>[22]</sup> to exclude those materials presenting defects or inhomogeneities that could be an important source of inaccuracy in the thermal conductivity measurements (Figure 2).

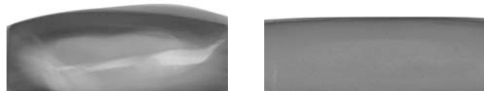


Figure 2: X-ray radiographs of foam with structural defects (left) and homogeneous foam (right)

Foam and solid sample densities,  $\rho_f$  and  $\rho_s$ , respectively, were determined by water-displacement method, based on Archimedes' principle. At least three measurements were carried out for each sample produced.

The cellular structure in foamed samples was analyzed by means of scanning electron microscopy (model Quanta 200FEG, FEI). In this case foams were frozen in liquid nitrogen and fractured to assure that the microstructure remained intact. Surfaces were coated with gold using a sputter coater (model SCD 004, Balzers Union). The micrographs obtained were analyzed to measure cell sizes with a specialized software<sup>[23]</sup> based on ImageJ<sup>[24]</sup> developed by the author. This software provides the cell size distribution, the average cell size, the cell anisotropy ratio distribution, the average cell anisotropy ratio, the cell density  $N_v$  (cells/cm<sup>3</sup>) and the nucleation density  $N_p$  (nucleation points/cm<sup>3</sup>), that can be calculated from  $N_v$  according to equation 4<sup>[25]</sup>

$$N_o = \frac{N_v}{1 - V_f} \quad (4)$$

Where  $V_f$  is the volume fraction of voids, which can be determined using equation 5.

$$V_f = 1 - \frac{\rho_f}{\rho_s} \quad (5)$$

The thermal conductivity has been characterized using the Transient Plane Source (TPS) technique<sup>[26]</sup>. In the TPS method, a round and plane heat source is used. It behaves as a transient plane source working simultaneously as a temperature sensor. The TPS element is located between two samples with both sensor faces in contact with the two sample surfaces. Samples have been prepared by polishing to obtain homogeneous surfaces to assure an appropriate contact with the sensor faces. This technique has been used previously on this kind of materials with good results<sup>[17]</sup>.

This method provides a measurement of the total thermal conductivity of the foams, so to be able to evaluate the contribution of the gaseous phase two sets of measurements have been carried out. One of them at atmospheric pressure that provides the value of the total thermal conductivity ( $\lambda_t$ ), and another in vacuum conditions (around 50 mbar, enough to ensure the gas desorption from cells and cancel the gaseous phase contribution<sup>[14]</sup>). Measures under vacuum conditions are taken each hour during 12 hours. These samples present a fast desorption, then, a constant value is reached in the first hours, this constant value provides the contribution of the solid phase ( $\lambda_s$ ) (table 1). Difference between the two sets of measurements provides us the contribution of the gaseous phase to the thermal conductivity.

### Results and Discussion

From the fabricated samples (see Experimental part) seven foams without structural defects or inhomogeneities have been selected to be characterized with the techniques explained before, also the solid samples for the different blends have been characterized (Table 1).

The characterization of solid samples of the three different blends show that there are not significant differences between them, as expected because the major component is the PMMA in every blend (blend with 25 % of neat PMMA and 75 % of MAM triblock copolymer is composed by 85 % of PMMA and only 15 % of PBA (poly(butyl acrylate))). So, it is possible to compare results from different blends without a significant influence of the composition.

Characterization of the foamed samples cellular structure shows two groups of clearly differentiated foams: nanocellular and microcellular foams. Each group presents very similar cellular structures, however the cellular structure of nanocellular and microcellular foams is completely different as it is shown in Figure 3.

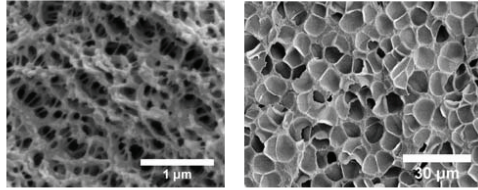


Figure 3: SEM images from the cellular structure of nanocellular (left) and microcellular (right) PMMA/MAM foams

Density of foamed samples have a main role on the thermal conductivity, then the normalized thermal conductivity (the relative thermal conductivity ( $\lambda_{foam}/\lambda_{solid}$ ) divided by the relative density ( $\rho_{foam}/\rho_{solid}$ ) of the foam) is shown in Figure 4 to analyze the influence of the cellular structure.

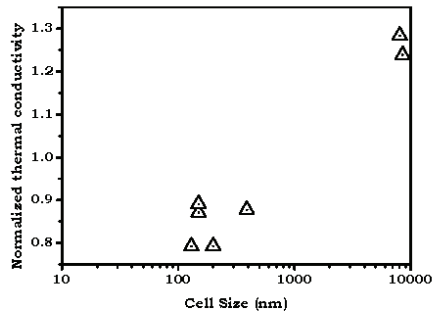


Figure 4: Relationship between the relative thermal conductivity of foamed samples and the cellular structure

These results show that there is a clear transition in the values of the thermal conductivity between microcellular and nanocellular foams. This reduction of the thermal conductivity in the transition from microcellular to nanocellular foams could be produced by the Knudsen effect, an increment of the solid phase tortuosity, or a combination of both effects.

Using the measured values for the thermal conductivity of the foamed samples at ambient pressure ( $\lambda_r$ ) and vacuum ( $\lambda_v$ ) (table 1), and the equation 3 it is possible to calculate the gas thermal conductivity ( $\lambda'_g$ ).

The obtained results are shown in Figure 5 as a function of the cell size, together with the values predicted by the Knudsen effect equation (equations 1 and 2).

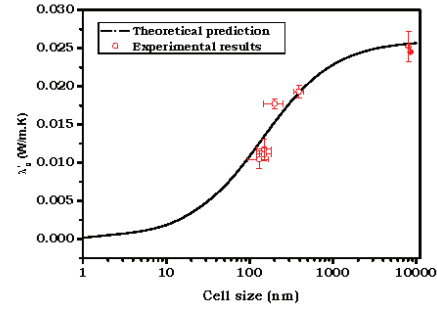


Figure 5: Effect of the cell size on the gas thermal conductivity

The experimental results are consistent with the theoretical predictions of the Knudsen effect, with only small differences between the experimental and theoretical values, probably due to nanometrics local defects (not detected by the x-ray radiography) or cell size inhomogeneities.

Finally, the results can be described by a combination of the Ashby model (equation 3) and Knudsen equations (equations 1 and 2):

$$\lambda_r = g\lambda'_s(1 - V_f) + \lambda'_{g0}V_f / (1 + \beta l_g / \phi) \quad (6)$$

An accurate fitting (Figure 6) is obtained using a structural factor ( $g$ ) of 1 for microcellular foams and 0.8 for nanocellular foams that present a higher tortuosity of the solid phase.

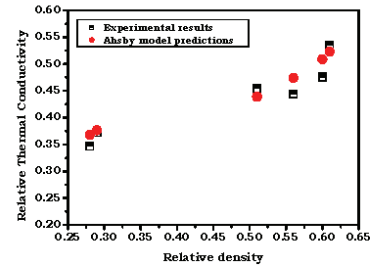


Figure 6: Comparison between experimental results and Ashby theoretical model combined with the Knudsen equation

### Conclusions

It has been demonstrated that nanocellular polymeric foams produced by the batch dissolution foaming from PMMA/MAM blends present a significant decrease of their thermal conductivity due to the influence of the pore size over the thermal conductivity of the gaseous phase as predicted the equations of the Knudsen Effect.

These results have been obtained with samples of a significant thickness (4-5 mm) and produced by an industrially scalable process. Therefore the potential benefits of nanocellular foams compared to microcellular foams in thermal insulation applications have been demonstrated.

### Acknowledgments

Financial assistance from MCINN (MAT2009-14001-C02-01), Juan de la Cierva E. Solorzano (JCI-2011-09775) and FPU grant AP2008-03603 (J. Pinto) from the Spanish Ministry of Education is gratefully acknowledged.

### References

1. D. Schmidt, V. I. Raman, C. Egger, C. Du Fresne, V. Schaedler, *Mater. Sci. Eng. C*, **27**, 1487 (2007)
2. H. Yokoyama, L. Li, T. Nemoto, K. Sugiyama, *Adv. Mater.*, **16**, 1542 (2004)
3. E. Solórzano, M. A. Rodríguez-Pérez, J. Lazaro, J. A. de Saja, *Adv. Eng. Mater.*, **11**, 818 (2009)
4. R. H. Russel, *J. Am. Ceram. Soc.*, **18**, 1 (1935)
5. A. G. Leach, *J. Phys. D: Appl. Phys.*, **26**, 733 (1993)
6. D. Bedeaux, R. Kapral, *J. Chem. Phys.*, **79**, 1793 (1983)
7. P. G. Collishaw, J. R. G. Evans, *J. Mater. Sci.*, **29**, 486 (1983)
8. J. Kuhn, H. P. Ebert, M. C. Arduini-Schuster, D. Büttner, J. Fricke, *Int. J. Heat Mass Transf.*, **35**, 1795 (1992)
9. A. Cunningham, *Proc. Int. Cent. Heat Mass Trans.*, **24**, 32 (1987)
10. M. A. Schuetz, L. R. Glicksman, *J. Cell. Plast.*, **20**, 114 (1984)
11. Ed: J. P. Holman, *Heat Transfer*, McGraw-Hill, New York, **Ch. 1** (1981)
12. M. Alvarez-Lainez, M. A. Rodríguez-Pérez, J. A. de Saja, *J. Polym. Sci. Part B: Polym. Phys.*, **46**, 212 (2008)
13. X. Lu, R. Caps, J. Fricke, C. T. Alviso, R. W. Pekala, *J. Non-Cryst. Solids*, **188**, 226 (1995)
14. L. W. Hrubesh, R. W. Pekala, *J. Mater. Res.*, **9**, 731 (1994)
15. J. A. R. Ruiz, M. Dumon, J. Pinto, M. A. Rodríguez-Pérez, *Macromol. Mater. Eng.*, **296**, (2011)
16. J. Pinto, M. A. Rodríguez-Pérez, J. A. de Saja, M. Dumon, C. Dietz, R. Garcia, in Proceedings of the SPE FOAMS 2011 Conference, Iselin, NJ (2011)
17. J. A. Reglero-Ruiz, C. Saiz-Arroyo, M. Dumon, M. A. Rodríguez-Pérez, L. Gonzalez, *Polym. Int.*, **60**, 146 (2010)
18. L. Lalande, C. J. Plummer, J. Anders, E. Manson, P. Gerard, *Polymer*, **47**, 2389 (2006)
19. L. Lalande, C. J. Plummer, J. Anders, E. Manson, P. Gerard, *Eng. Fract. Mech.*, **73**, 2413 (2006)
20. S. K. Goel, E. J. Beckman, *Cell. Polym.*, **12**, 251 (1993)
21. A. V. Nawaby, Y. P. Handa, X. Liao, Y. Yoshitaka, M. Tomohira, *Polym. Int.*, **56**, 67 (2007)
22. J. Escudero, E. Solorzano, M. A. Rodríguez-Pérez, F. Garcia-Moreno, J. A. De Saja, *J. Cell. Polym.*, **28**, 289 (2009)
23. J. Pinto, E. Solorzano, M. A. Rodríguez-Pérez, J. A. de Saja, *Materials Characterization*, Submitted 2012
24. M. D. Abramoff, P. J. Magelhaes, S. J. Ram, *Biophotonics Int.*, **11**, 36 (2004)
25. V. Kumar, N. P. Suh, *Polymer. Eng. Sci.*, **30**, 1323 (1990)
26. E. Solorzano, J. A. Reglero, M. A. Rodríguez-Pérez, D. Lemus, M. Wichmann, J. A. de Saja, *Int. J. Heat Mass Trans.*, **51**, 6259 (2008)

Key Words: foams; Knudsen Effect; nanocellular; carbon dioxide; thermal conductivity; polymers

Table 1: Results of foamed and solid samples characterization

Blend (PMMA/MAM)	Foaming P(MPa)/ T (° C)	$\rho$ (g/cm <sup>3</sup> )	$V_f$	$\Phi$ (nm)	$\lambda_t$ (W/m.K)	$\lambda_s$ (W/m.K)
75/25	-	1.16	0	-	0.2150	-
50/50	-	1.16	0	-	0.2134	-
25/75	-	1.14	0	-	0.2101	-
75/25	30 / 60	0.71	0.39	390	0.1151	0.1077
50/50	30 / 23	0.59	0.49	150	0.0948	0.0900
50/50	30 / 40	0.65	0.44	130	0.0947	0.0901
50/50	30 / 50	0.69	0.40	200	0.1015	0.0944
25/75	30 / 23	0.58	0.49	150	0.0955	0.0900
25/75	30 / 60	0.33	0.71	8070	0.07825	0.0604
25/75	30 / 70	0.32	0.72	8530	0.0729	0.0552

## V.4 References

1. Lu, X., et al., *Correlation between structure and thermal conductivity of organic aerogels*. Journal of non-crystalline solids, 1995. **188**(3): p. 226-234.
2. Roth, C.B. and J.R. Dutcher, *Glass transition and chain mobility in thin polymer films*. Journal of Electroanalytical Chemistry, 2005. **584**(1): p. 13-22.
3. Jo, C., J. Fu, and H.E. Naguib, *Constitutive modeling for mechanical behavior of PMMA microcellular foams*. Polymer, 2005. **46**(25): p. 11896-11903.
4. Schmidt, D., et al., *Templated cross-linking reactions for designing nanoporous materials*. Materials Science and Engineering: C, 2007. **27**(5–8): p. 1487-1490.
5. Miller, D. and V. Kumar, *Microcellular and nanocellular solid-state polyetherimide (PEI) foams using sub-critical carbon dioxide II. Tensile and impact properties*. Polymer, 2011. **52**(13): p. 2910-2919.
6. Gibson, L.J. and M.F. Ashby, *Cellular Solids: Structure and Properties*. 2nd ed1997, Cambridge: Cambridge University Press.
7. Rodríguez Pérez, M.Á., et al., *Mechanical Behaviour at Low Strains of LDPE Foams with Cell Sizes in the Microcellular Range: Advantages of Using these Materials in Structural Elements*. Cellular polymers, 2008. **27**(6): p. 347-362.
8. Rodriguez-Perez, M.A., et al., *The effect of cell size on the physical properties of crosslinked closed cell polyethylene foams produced by a high pressure nitrogen solution process*. Cellular polymers, 2002. **21**(3): p. 165-194.
9. Fox, T.G. and P.J. Flory, *The Glass Temperature and Related Properties of Poly-styrene. Influence of the Molecular Weight*. Journal of Polymer Science, 1954. **14**: p. 315.
10. Mundra, M.K., et al., *Fluorescence studies of confinement in polymer films and nanocomposited: Glass transition temperature, plasticz effects and sensitivity to stress relaxation and local polarity*. European Physical Journal - Special Topics, 2007. **141**: p. 143-151.
11. Kraus, J., et al., *Confinement effects on the chain conformation in thin polymer films*. Europhysics Letters, 2000. **49**: p. 210-216.
12. Yong-Park, J. and G.B. McKenna, *Size and confinement effects on the glass transition behavior of polystyrene/o-terphenyl polymer solutions*. Physical Review B, 2000. **61**.
13. Forrest, J.A., K. Dalnoki-Veress, and J.R. Dutcher, *Interface and chain confinement effects on the glass transition temperature of thin polymer films*. Physical Review E, 1997. **56**.
14. Anastasiadis, S.H., K. Karatasos, and G. Vlachos, *Nanosopic-Confinemente Effects on Local Dynamics*. Physical Review Letters, 2000. **84**.



## ***Conclusions and Perspectives***



## Conclusions and Perspectives

This final section summarizes all the main conclusions and remarkable achievements of this research work. The section is written according to the scope and objectives of this thesis. The conclusions cover the optimization of experimental techniques, the study of nanostructured polymers and nanocellular PMMA-based polymer foams, the understanding of the phenomena involved in the elaboration of these materials, and the main properties of these systems.

As a general conclusion, PMMA/MAM blends have proven to be exceptional materials for the production and study of nanocellular foams. These materials allow obtaining foams with different cellular structures in the nanometric range, presenting significant density reductions (down to around  $0.4 \text{ g/cm}^3$ ). In addition, they exhibit well defined and controlled cell nucleation and growth mechanisms, which enable the production of nanocellular foams in a range of processing conditions wider than other polymers studied previously in the literature. Both nanocellular and microcellular foams are produced from these blends with a tunable cell size, cell interconnectivity (open and closed cells are possible), and density.

First, the advances on some experimental techniques are listed. And then the principal conclusions according the three main objectives of this research are presented (i.e. production of nanocellular foams, understanding of the foaming mechanisms, and properties of nanocellular foams).

### Improved experimental techniques or technological progress for characterization:

The study of the PMMA/MAM system has required the improvement or adaptation of some experimental techniques. Main novelties on this topic are as follows:

- Procedures to study the PMMA/MAM nanostructuration by AFM and TEM have been established. It has been determined the range of application (i.e. MAM amount on the PMMA/MAM blend) of each technique, and how both techniques can complement each other when both techniques are applicable. Also, quantification procedures to measure the nanodomains volumetric density have been developed for both techniques, obtaining comparable results.
- Specific software for the cellular structure characterization has been developed. It has been demonstrated that it enables the analysis of SEM micrographs from materials with different cellular structures and densities. This software provides a detailed characterization of the cellular structure of porous materials. This methodology combines a better accuracy than the standard

methods with a short processing time, presenting significant advantages to become a useful tool in the cellular materials science.

- A TPS thermal conductivimeter was adapted to develop a procedure that allows determining the contribution of the gaseous phase to the thermal conductivity of cellular materials. The methodology employed also involves the use of X-ray radiography as a non-destructive technique to analyze the homogeneity of the samples.

These optimized techniques have demonstrated their suitability to improve the characterization of our materials. They have provided essential information to be able to achieve the objectives of this research.

### **Production of nanocellular foams:**

A new route to produce nanocellular foams has been established using PMMA/MAM blends precursors. Our materials present several advantages.

- Blends of PMMA and MAM, both commercial grades, can be easily produced by extrusion and injection obtaining bulk pieces with a well defined nanostructure. Self-assembly of PMMA/MAM blends appears for each MAM amount of the blend. The morphology depends on the amount of the soft-block (PBA), evolving from nodular independent objects, such as micelles/core shells, to lamellas/worm like or quasi co-continuous structures.
- Gas dissolution foaming provided nanocellular foams from neat PMMA and MAM, together with PMMA/MAM blends. Nanocellular foams from the neat materials can only be obtained with a selection of specific processing parameters (i.e. near the maximum saturation pressure available (30 MPa) and temperatures near or below room temperature); while PMMA/MAM foams with cell sizes in the nanometric range can be produced in the large range of pressures (from 10 to 30 MPa) and several temperatures (up to 50° C).
- No specific or uncommon procedure had to be used to obtain these nanocellular foams. Requirements such as extremely high pressures (over 40 MPa), high pressure release rates (GPa/second), or quenching of the sample after or prior the pressure release, are not needed to obtain PMMA/MAM nanofoams.
- Nanocellular PMMA/MAM foams with significant density reduction (over 50 %) were obtained in a wide range of processing conditions (pressure and temperature). Also, different MAM

amounts allow obtaining nanocellular foams with different pore morphologies, from closed cell spherical or elongated pores to open cell co-continuous pores.

- Some evidence of saturation annealing of the PMMA/MAM blends during the foaming process was found. This process could avoid macroscopic creep of the samples and produce a homogenization of the nanostructuration, avoiding defects or inhomogeneities resulting from the production route of the solid precursors. The resulting nanofoams are reproducible and homogeneous.

Therefore we have been able to obtain a wide range of nanocellular foams with different characteristics overcoming the main difficulties of the production of this kind of materials. We just use commercial polymers and conventional industrially scalable techniques to produce these nanocellular foams. Therefore, we think that our work is a significant advance in the development of these materials, decreasing the gap between the laboratory scale and the industrial production.

#### Understanding of the foaming mechanisms:

From the study of the nanostructures of solid samples, the cellular structures of foamed samples, and the foaming behavior of these materials we have characterized the foaming process and understood the phenomena involved in the production of these materials.

- It was demonstrated that PMMA/MAM blends present a heterogeneous nucleation process, controlled by the soft-block (PBA) domains inside the PMMA matrix. This behavior is due to several factors:
  - PBA is more CO<sub>2</sub>-philic than PMMA.
  - PBA is in the rubbery state during the entire process, due to its low  $T_g$  about -50° C.
  - PBA probably presents a lower energy barrier for the nucleation process than PMMA due to their intrinsic characteristics.
- No influence of the processing parameters (i.e. saturation pressure and temperature, pressure release ratio) was found over the nucleation process.

- PBA domains of the solid samples act as an exact pattern of the cellular structures of the foamed samples:
  - o PMMA/MAM blends presenting dispersed nanostructures (i.e. micelles or nodules) shown a nucleation efficiency ratio close to unity, which implies that each nucleating agent (dispersed nanostructure) becomes a cell. In addition, cell morphology reproduced the shape of the nanostructure: micelles become spherical cells, while elongated nodules result in anisotropic cells. Attempts to study the nanostructuration on the foams suggest that the nucleation process happens inside the PBA phase of the core-shell structure of the micelles/nodules. We reach this conclusion because the PBA shell appears swollen in the foamed samples with an inner diameter of similar size as the average cell size of these foams.
  - o PMMA/MAM blends with co-continuous morphologies result in co-continuous cellular structures. No information about the PBA domains after foaming can be derived from these materials. However, it is expected that the nucleation happens also inside the PBA domains.
- Increment of the MAM amount (between 5 to 20 wt%) seems to increase the CO<sub>2</sub> uptake and therefore increases the cell size and decrease the relative density, remaining constant a high cell nucleation density close to  $4 \times 10^{14}$  nuclei/cm<sup>3</sup>. At higher MAM contents a similar behavior can be expected about the CO<sub>2</sub> sorption, however, the co-continuous or semi co-continuous nanostructure allows a quicker diffusion of the gas out of the sample after the pressure release, avoiding the study of the CO<sub>2</sub> sorption by the gravimetric method employed in this work.
- Cell growth in PMMA/MAM blends is controlled by the plasticization of the PMMA matrix. Nucleation happens in the PBA domains along the entire sample, but these nuclei only can grow into a cell if the surrounding PMMA is plasticized enough to allow the growth of the nuclei. Therefore, nucleation and cell growth in PMMA/MAM blends are independent processes, and can be controlled separately.
- As a consequence of the heterogeneous nucleation mechanism of PMMA/MAM blends, the formation of the solid skins, typical of solid state foaming processes, does not fit the model used on conventional foams with homogeneous nucleation. Therefore, a new qualitative model that explains the formation of the solid or semi-solid skins on PMMA/MAM blends has been



proposed, taking into account the nucleation and cell growth mechanisms previously determined. This model is based on the evolution of the plasticization of the PMMA matrix due to the desorption of CO<sub>2</sub>, and how this evolution controls the growth of the nuclei present on the PBA domains.

- It was found that the saturation temperature, and the evolution of the sample's temperature during the pressure release, control the presence of a desorption stage on the foaming process. Thus, quenching of the samples due to the pressure release from saturation temperatures near room temperature causes a desorption stage (like in the two-steps route or the solid state foaming process); while higher saturation temperatures (over 40° C) avoid this desorption stage (like in the one-step or batch foaming).

Differences between both processes are huge on the neat PMMA and MAM polymers. In fact, nanocellular foams from the neat polymers can be only obtained by the two-step foaming process. On the contrary, PMMA/MAM blends present "*a higher thermal stability*", with small differences between both processes and a negligible incidence of the coalescence phenomena up to a saturation temperature over 60° C. This thermal stability of PMMA/MAM foams is a great advantage to obtain nanocellular foams in a wide range of processing conditions.

- On the other hand, the thermal stability of PMMA/MAM foams makes difficult obtaining nanocellular foams with lower relative densities than 0.4 g/cm<sup>3</sup>. Saturation temperature just allowed a density decrease by about a 10 %; while some attempts to reduce the density by post-foaming only decreased the density by another 5 %. This limitation on the cell growth/density reduction is related to a quick diffusion of CO<sub>2</sub> out of the very thin cell walls, reducing the PMMA plasticization and limiting the cell growth.

### Properties of PMMA/MAM foams:

The unique characteristics of PMMA/MAM foams, their easy production, and the variety of possible cellular structures make them ideal materials for the study of the foam's properties evolution from the microcellular to the nanocellular range. Efforts performed on this topic provided several results of significant interest.

- 90/10 PMMA/MAM foams present an improved mechanical behavior (higher Young's modulus) than neat PMMA foams. Although PMMA foams present in general microcellular structures and PMMA/MAM foams present in general nanocellular structures, no evidences of a relation/link

between the enhancement of the mechanical properties and the reduction of the cell size was found in the range of cell sizes studied (from 100 nm to 2  $\mu$ m). It is suggested that the better mechanical performance is a result of the higher homogeneity of the cellular structure of the PMMA/MAM foams, due to their controlled nucleation mechanism.

- It has been demonstrated that the glass transition temperature of the PMMA matrix of nanocellular foams increases when the average cell size lies under the micron. Different studies about the influence of the saturation pressure and temperature have been carried out, resulting in the absence of influence of the processing parameters on this property. On the contrary, a clear relationship between the glass transition temperature and the average cell wall thickness of the foams has been found. This behavior is related to the confinement of the PMMA chains inside the cell wall. Finally, it is concluded that the glass transition temperature is significantly increased when the cell wall thickness lies below 100 nm.
- Study of the thermal conductivity of PMMA/MAM microcellular and nanocellular foams shows a clear threshold between the two cell size ranges. Nanocellular foams present a lower thermal conductivity than microcellular foams. This reduction of the thermal conductivity was related to the phenomenon called Knudsen effect. Experimental measurements allow validating the theoretical predictions (obtained by Knudsen equation) of the dependence of the thermal conductivity of the gaseous phase with the average cell size.

Therefore, the existence of a property threshold between microcellular and nanocellular foams has been demonstrated for the thermal conductivity, and for the glass transition temperature; however the values of the Young's modulus seems to show an enhancement, which is more related to another property of the cellular structure, such as their homogeneity, than to a decrease of the cell size.

### Future Perspectives

This is the first Ph.D. investigation in CellMat and LCPO about nanocellular foams. That is the reason why this research has been mainly focused in the understanding of the phenomena leading to the production of nanocellular foams by CO<sub>2</sub> dissolution with medium densities.

As nanocellular foams are one of the current frontiers on cellular materials science, and raising great expectations due to their potential properties and applications, we expect that the knowledge acquired

during this research could be a starting point for new research works, some of which could be focused on the following topics.

- Research on PMMA/MAM blends:
  - To analyze in detail the characteristics of PMMA/MAM foams with medium amounts of MAM.
  - To extend the study of the post-foaming process on PMMA/MAM foams, trying to reach significant density reductions. Two approaches have been mentioned, post-foaming at low temperatures than those used, and post-foaming under pressure.
  - To study the influence of the MAM amount on the CO<sub>2</sub> diffusion and PMMA swelling during the saturation process by optical means.
  - To try to produce PMMA/MAM nanocellular foams without integral skin by modifying the production route.
  - To try to develop filtration devices based on PMMA/MAM nanofoams and characterize them.
  - To look for other potential applications of PMMA/MAM foams.
- Transition between microcellular and nanocellular foams:
  - To extend the study of the mechanical properties to other properties such as impact strength, toughness, fatigue, etc. (not only the Young's modulus), and to a wider range of cell sizes and relative densities. To be able to determine if nanocellular foams present improved mechanical properties as it is predicted in the literature.
  - To extend the study of the thermal conductivity to a wider range of cell sizes and relative densities. To be able to provide an accurate validation and understanding of the Knudsen effect on polymer nanofoams.

- To study the evolution of other properties, such as electrical conductivity, dielectric permittivity, acoustic insulation, matrix tortuosity, etc., between microcellular and nanocellular foams.
  - To analyze and understand the implications of the confinement of the polymer chains detected in this thesis.
- Looking for other polymers with similar characteristics: other block copolymers with CO<sub>2</sub>-philic soft blocks can lead to the production of nanocellular foams with higher nucleation densities if the block copolymer allows higher nanodomains density than MAM. From the accumulated knowledge on this research new block copolymers with optimal properties to enhance the nucleation can be looked for.
- Continuous production route: current production route requires long processing times (i.e. saturation times about 16-24 h) in a non-continuous production route. Then, the development of a continuous and fast production route of nanocellular foams is the main issue required for the industrial production of these materials.